University of Southampton

Faculty of Engineering and Physical Sciences

School of Engineering

Low-cycle Fatigue Assessment of Mooring Chains Based on The Critical Plane Approach

By

Gilang Muhammad Gemilang

ORCID ID: https://orcid.org/0000-0001-9641-9495

Thesis for the degree of Doctor of Philosophy

October 2020

University of Southampton

Abstract

Faculty of Engineering and Physical Sciences

School of Engineering

Doctor of Philosophy

Low-cycle Fatigue Assessment of Mooring Chains Based on The Critical Plane Approach

by

Gilang Muhammad Gemilang

The integrity of mooring chains is important to the safety of a range of offshore platforms for the exploitation of natural resources, including oil, gas, wind, and wave energy sources. However, mooring line failures have been occurring earlier than they are designed for with a high number of these failures occurring due to fatigue. The failures occur in the first three years, when operating in harsh sea environments, indicating that the failure mechanism could be attributed to low-cycle fatigue, where the fatigue hotspot is sensitive to the mean load and there is plastic strain accumulation from the multiaxial stress-strain responses of the material, leading to cyclic plastic damage accumulation.

However, the traditional SN approach, suggested by mooring standards, does not consider these effects, and it is proposed that the lack of this consideration under low-cycle fatigue conditions is the reason for the current non-conservative fatigue assessments of mooring chains. Therefore, this thesis aims to develop a fatigue approach, based on a critical plane multiaxial fatigue criterion. This method is capable of accounting for the mean load and cyclic plasticity effects on the fatigue damage, which governs the low-cycle fatigue of mooring chains. This allows for an investigation into how fatigue damage prediction changes with a more accurate representation of the low-cycle fatigue regime under stochastic tension loading in service for intact mooring chains.

A finite element model with explicit solver is developed and shown to be robust for modelling representative stresses in mooring chains when compared with

other finite element models available in the literature. Using the determined finite element model, the critical plane approach is developed based on the multiaxial stress-strain conditions at the hotspot and this is correlated with the fatigue life derived from tests taken from the mooring standards. Subsequently, the developed critical plane approach is compared with the traditional SN approach using a mooring line simulation of an FPSO as a case study.

The result found that the critical plane approach predicts significantly higher proportions of low-cycle fatigue than the traditional SN approach in the mooring line loading. This is because the mean load effect is detrimental when it is above 20% of the minimum breaking load, shown to make up a large proportion of the loads in high sea-states. However, the effect of the cyclic plasticity is limited as the mechanisms are only applied when the tension load exceeds 70% of the minimum breaking load due to the strain hardening from the proof load application during the first cycle. The traditional SN approach is shown to be conservative when the mean load is below 20% of the minimum breaking load, but after this, it is non-conservative, which is observed in harsh environments where the majority of mooring chain failures were witnessed. The low-cycle fatigue analysis in this study explains why current fatigue assessment in mooring chain applications is non-conservative and demonstrates that the critical plane approach should be accounted for in mooring line design.

Table of Contents

Table of Contents ..... **i**
List of Tables ..... **v**
List of Figures ..... **vii**
Research Thesis: Declaration of Authorship ..... **xiii**
Acknowledgements ..... **xv**
Abbreviations ..... **xvii**
Nomenclatures ..... **xix**
Chapter 1: Introduction **1**

1.1 Mooring chain fatigue failures 1
1.2 Research aim and objectives 6
1.3 Research novelty 6
1.4 Scope of work 7
1.5 Thesis structure 7
1.6 Publications 8

Chapter 2: Literature review **9**

2.1 Outline of the literature review 9
2.2 Manufacture of mooring chains 9
2.2.1 Manufacturing process 9
2.2.2 Proof load test 10
2.3 Mooring chain failure scenarios 12
2.4 Mooring line loading in service 15
2.5 Chain models 17
2.6 Fatigue of mooring chains 19
2.6.1 Fatigue in metallic materials 19
2.6.2 Fatigue hotspots 23
2.6.3 Fatigue design approach in the industry 26
2.6.4 Fracture mechanics analysis of mooring chains 29
2.6.5 Fatigue tests of mooring chains 29
2.6.6 Quantification of mean load effects of mooring chains 31

2.7 Fatigue of steel structures 32
2.7.1 Critical plane based multiaxial fatigue criteria 32
2.7.2 Material response under fatigue loading 36
2.7.3 Material models 38
2.8 Summary from the literature 40
Chapter 3: Methodology 45
3.1 Development of chain FE model 45
3.2 Calibration of the critical plane approach 46
3.3 Mooring line simulation 48
Chapter 4: Selection of appropriate numerical models for modelling stresses in mooring chains 51
4.1 The criticality of accurate structural modelling in mooring chain failure analysis 51
4.2 Finite element model definition 53
4.3 Definition and calibration of the numerical models 59
4.3.1 Elastic model with pressure distribution, 20 node brick element with reduced integration (EP20R) 59
4.3.2 Elastoplastic model with pressure distribution, 20 node brick element with reduced integration (P20R) 60
4.3.3 Elastoplastic model with contact interaction, 20 node brick element with reduced integration (C20R) 62
4.3.4 Elastoplastic model with contact interaction, 8 node brick element with incompatible mode (C8I) 63
4.3.5 Elastoplastic model with contact interaction, explicit solver 8 node brick element with reduced integration (CEx8R) .64
4.4 Model selection 66
4.4.1 Validation of the numerical models 67
4.4.2 Benchmarking of the numerical models 70
4.5 Discussion 76

4.6 Summary 80

Chapter 5: Low-cycle Fatigue Assessment of Mooring Chains Under Service Loading 83

5.1 Introduction 83
5.2 Development of a representative chain model 84
5.3 Material Models 85
5.4 Development of the critical plane fatigue assessment for mooring chains 90
5.4.1 The Smith Watson Topper Critical Plane Approach 90
5.4.2 Calibration of the critical plane approach 91
5.5 Fatigue Simulations 97
5.5.1 Mooring Chain loading 97
5.5.2 Fatigue Damage Comparison 99
5.5.3 Parametric study for fatigue in different sea-states 104
5.6 Discussion 107
5.7 Summary 112

Chapter 6: Discussion and limitations 115

6.1 Potential increase in proportion of low-cycle fatigue events in the mooring line loading 116
6.2 Potential increase in low-cycle fatigue proportion from the critical plane approach 118
6.3 Recommendations for application 119
6.4 Future work 124

Chapter 7: Conclusion 125
Appendix A List of Early Mooring Chain Failure Scenarios 129
Appendix B Mesh convergence analysis 133

Appendix B.1 Mesh convergence analysis referred in section 4.4.1 133

Appendix B.2 Mesh convergence analysis referred in section 4.4.2 138
Appendix B.3 Mesh convergence analysis referred in section 5.2 143

Appendix C Calibration results of *SWT* damage parameters 147
Appendix D Wave scatter diagram in the North Sea..... 151
Appendix E Gemilang et al. [186] (Published)..... 155
Appendix F Gemilang et al. [207] (Published)..... 171
List of References..... 187

List of Tables

Table 1: Formulas for the minimum breaking load (MBL) of studless link for different steel grades [20] [22]. 10

Table 2: Different numerical methods for modelling mooring chains in the open literature. 17

Table 3: The quantification of the mean load effect found in the literature 31

Table 4: Different material models used in the literature for fatigue analysis of mooring chains. 38

Table 5: Summary of fatigue studies for mooring chains in the literature.. 41

Table 6: Summary of numerical analyses for mooring chains in the literature. 52

Table 7: Minimum mechanical properties for chain materials [19]. 54

Table 8: Original inputs for the elastic model with pressure distribution (EP20R). 59

Table 9: Original inputs for the elastoplastic model with pressure distribution (P20R). 61

Table 10: Original inputs for the elastoplastic model with contact (C20R). 62

Table 11: Original inputs for the elastoplastic model with contact interaction (C8I)..... 64

Table 12: Differences in modelling between the different FE models. 67

Table 13: Summary of appropriate models for predicting stress-strain parameters in mooring chains. 77

Table 14: The computational costs and memory for the different FE models normalised against the explicit model. 80

Table 15: Parameters for the monotonic and cyclic material models. 87

Table 16: Main particulars of the FPSO taken from Flexcom [183]. 97

Table 17: Mooring component principals [183]. 98

Table 18: The wave parameters for the nine representative partitions of the North Sea..... 105

List of Figures

Figure 1: The Usan FPSO operating in the West African oil field [3]. 1

Figure 2: (a) cumulative failure events versus the number of mooring leg exposure years per year; (b) single line annual failure rate per line by each year [1]..... 4

Figure 3: Types of failure modes for mooring chains by the proportion of occurrence [1]..... 5

Figure 4: Logarithmic plot of load amplitude versus fatigue life for different proof load levels at a mean load of 20% of the minimum breaking load [30]..... 12

Figure 5: Schematic view of potential breaking locations of chains along a mooring line..... 14

Figure 6: The components in tension time series of a mooring line [18]. .. 16

Figure 7: Interlink loading method in FEA: (a) a model with pressure distribution [27] and (b) a model with contact interaction [42]. 18

Figure 8: A rough surface consisting of hills and valleys in form of extrusion and intrusion, respectively [13]..... 20

Figure 9: A schematic illustration of the sinusoidal waveform with nonzero mean stress [86]..... 21

Figure 10: A schematic distinction between high-cycle fatigue loading cycles and low-cycle fatigue loading cycles [89]. 23

Figure 11: Identified fatigue hotspots in the literature. 24

Figure 12: Illustrations of failed mooring chains in two distinct locations of fatigue hotspots: (a) the K_t point and (b) the crown point [91]. 25

Figure 13: Mooring fatigue design SN curves, according to DNV-OS-E301 [7]. 27

Figure 14: Illustrations of cyclic plasticity effect on a material: (a) a cyclically hardening material and (b) a cyclically softening material [144].....36

Figure 15: Evolution of yield surface in the principal stress space: (a) isotropic hardening (b) kinematic hardening (c) combination of both hardening [146].37

Figure 16: Illustrations of each material model: (a) the bilinear material model under monotonic loading, showing the bilinear stress-strain relationship [28] (b) the Ramberg-Osgood material model under monotonic loading, showing the stress-strain curves [73] (c) the cyclic material model under cyclic loading, showing the softening evolution of the maximum and minimum values of the peak stresses with the number of cycles [75].....39

Figure 17: Flowchart of the model developed to study low-cycle fatigue behaviour of mooring chains in the present study. 45

Figure 18: The calibration methodology of the critical plane approach. 47

Figure 19: The model of the mooring system connecting an FPSO on the water level to anchor points on the seabed.....48

Figure 20: Mooring line simulation methodology. 49

Figure 21: The IACS specification for the design of a studless chain link [20]. 53

Figure 22: Stress-strain diagrams of R3 and R4S grade steel.....55

Figure 23: Finite element definition for a model with pressure distribution method.....56

Figure 24: Finite element definition for a model with contact interaction method. 57

Figure 25: Finite element definition for symmetric boundary conditions in the chain model.....58

Figure 26: Key paths for stress-strain field prediction for a chain: (a) path-1, (b) path-2 and (c) path-3. 58

Figure 27: Calibration of H along a part of path-2 for the longitudinal stress.60

Figure 28: Verification of H=11.3mm for the P20R model along path-2 for the longitudinal stress. 61

Figure 29: Calibration of the Initial Boundary Condition (IBC) for the maximum absolute principal stress along path-1..... 63

Figure 30: Stress-strain relationship used in the current simulation derived from the tensile tests [31]. 68

Figure 31: The predicted permanent elongations of the different FE models normalised against experimental tests. 69

Figure 32: Comparison of the von Mises stresses for the different FE models in the validation study under 50% of the minimum breaking load along path-1.71

Figure 33: Comparison of the stress range and mean stress for the different FE models at both fatigue hotspots..... 73

Figure 34: Comparison of the maximum principal stress for the different FE models under 50% of the minimum breaking load along (a) path-2 and (b) path-3. 74

Figure 35: Comparison of the equivalent plastic strains (PEEQ) for the different FE models under 50% of the minimum breaking load along path-1..... 76

Figure 36: The standardised dimensions for a studless chain, taken from IACS, and the critical fatigue locations. 84

Figure 37: The finite element model of the chain-link used in this analysis, where the left part is the master and the right part is the slave. 85

Figure 38: Comparison between each model under monotonic loading, showing the stress-strain curves..... 88

Figure 39: Comparison between each model under cyclic loading, (a) showing the stress-strain relationship in the hysteresis loop, (b) showing the evolution of the maximum and minimum values of the peak stresses with the number of cycles..... 89

Figure 40: An illustration of the direction of axes in the FE model to calculate the *SWT* values at the fatigue hotspots (i.e. Crown and K_t point) based on the respective longitudinal and transversal directions of each hotspot.....93

Figure 41: Comparison between the crown and K_t point (a) damage parameters on different plane orientation angles, (b) damage parameters on the determined critical plane under a range of load amplitudes. 95

Figure 42: The fitted calibration curves based on the fatigue life of mooring chains for the Smith-Watson-Topper (SWT) using the stress/strain data at the crown fatigue hotspot for the different material models. 96

Figure 43: Mooring system arrangement in this simulation taken from Flexcom [183].....99

Figure 44: Comparison of the predicted fatigue damage accumulation using different approaches. 100

Figure 45: Mean load effects on the fatigue damage ratio in a range of mean load for Mono-Rampi (a) full range of MBLs 0-60% (b) change in behaviour due to amplitude at mean load of 20% MBL, and for Cyclic-Rampi (c) full range of MBLs 0-60% (d) change in behaviour due to amplitude at mean load of 20% MBL. 101

Figure 46: Fatigue simulation when the proof load is applied, released, and followed by cyclic loads with an amplitude of 20% MBL in an incremental mean load with an interval of 1% MBL for each progressive cycle, showing (a) the stress-strain responses, (b) the plastic strain accumulation. 103

Figure 47: Mean load distribution in the individual loading cycles of tension-spectrum for (a) sea-states 1-3 (b) sea-states 4-6 (c) sea-states 7-9, where the horizontal axis denotes ranges of load amplitudes in the percentage of the minimum breaking load (% MBL) and the green represents mean load below 20% MBL and the red represents mean load above 20% MBL. 106

Figure 48: The separation line between high-cycle and low-cycle fatigue predictions for the traditional SN approach and the critical plane approach.109

Figure 49: Summary plot for each sea-state in terms of the proportion of mean load above 20% MBL in the respective tension spectrum and the difference in fatigue damage accumulation predictions between the critical plane approach and the traditional SN approach. 111

Research Thesis: Declaration of Authorship

Print name:	Gilang Muhammad Gemilang
Title of thesis:	Low-cycle Fatigue Assessment of Mooring Chains based on the Critical Plane Approach

I declare that this thesis and the work presented in it are my own and has been generated by me as the result of my own original research.

I confirm that:

1. This work was done wholly or mainly while in candidature for a research degree at this University;
2. Where any part of this thesis has previously been submitted for a degree or any other qualification at this University or any other institution, this has been clearly stated;
3. Where I have consulted the published work of others, this is always clearly attributed;
4. Where I have quoted from the work of others, the source is always given. With the exception of such quotations, this thesis is entirely my own work;
5. I have acknowledged all main sources of help;
6. Where the thesis is based on work done by myself jointly with others, I have made clear exactly what was done by others and what I have contributed myself;
7. Parts of this work have been published as:

- G. M. Gemilang, P. A. S. Reed and A. J. Sobey, Selection of appropriate numerical models for modelling the stresses in mooring chains, Marine Structures, 2020. (Published).
- G. M. Gemilang, P. A. S. Reed and A. J. Sobey, Low-cycle Fatigue Assessment of Offshore Mooring Chains Under Service Loading, Marine Structures, 2020. (Published).
- G. M. Gemilang, P. A. S. Reed and A. J. Sobey, Fatigue approaches of mooring chains subjected to wear degradation, Proceedings of the ASME 38th International Conference on Ocean, Offshore and Arctic Engineering, OMAE2019-96386, 2019, Glasgow, UK. (Published)

- G. M. Gemilang, P. A. S. Reed and A. J. Sobey, Multiaxial fatigue analysis of mooring chains subjected to low-cycle fatigue load and variable mean load, Poster, FSI Away Day, Southampton, UK, 2020
- G. M. Gemilang, P. A. S. Reed and A. J. Sobey, Why mooring line often fail in offshore field?, Poster, FSI Showcase, Southampton, UK, 2017.

Signature: Date: 08/10/2020

Acknowledgements

I would like to thank my supervisors, Dr. Adam Sobey and Prof. Philippa Reed for their guidance, time and supports during all these years.

I would also like to thank God (Allah Subhanawata'ala) and my parents (Irianto Rab and Solvadiana), my wife (Herian Stiyani), my newborn baby (Starla Zikra Gemilang), my brother (Imam) and sister (Chairunnisa), colleagues and friends whose moral supports have been priceless.

Finally, the author would like to thank Indonesian Endowment Fund for Education (LPDP) for their sponsorship of this PhD study.

Definitions and Abbreviations

API	American Petroleum Institute
ABS	American Bureau of Shipping
ALS	Accidental Limit State
BC	Boundary Condition
DNV	Det Norske Veritas
FE	Finite element
FEA	Finite element Analysis
FEM	Finite element method
FLS	Fatigue Limit State
FPSO	Floating production, storage and offloading unit
HCF	High-cycle fatigue
IACS	International Association of Classification Societies
IBC	Initial Boundary Condition
IPB	In-plane bending
ISO	International Organization for Standardization
ISSC	International Ship and Offshore Structures Congress
JIP	Joint Industry Project
JONSWAP	Joint North Sea Wave Project
LCF	Low-cycle fatigue
LF	Low frequency
LEFM	Linear elastic fracture mechanics

MBL	Minimum breaking load
MODU	Mobile Drilling Unit
NDT	Non-destructive testing
OPB	Out-of-plane bending
PM	Pierson-Moskowitch
PL	Proof Load
PSB	Persistent Slip Band
RAO	Response amplitude operator
QTF	Quadratic transfer function
SCF	Stress concentration factor
SWT	Smith-Watson-Topper
WF	Wave frequency
VIM	Vortex Induced Motion

Nomenclatures

D	chain diameter
L	chain length
W	chain width
R	chain radius of curved section
ε_p	plastic strain
ν	poisson's ratio
ρ	density
E	modulus elasticity
φ	plane angle
$\sigma_{n,max}$	maximum normal stress on the plane
$\Delta\varepsilon_n$	normal strain range on the plane
σ_n	normal stress on the plane
ε_n	normal strain on the plane
SWT	Smith-Watson-Topper parameter
ε_f'	fatigue ductility coefficient
c	fatigue ductility exponent
σ_f'	fatigue strength coefficient
b	fatigue strength exponent
A_1	material constant
A_2	material constant
a_1	material constant

a_2	material constant
$\dot{\bar{\varepsilon}}^{\mathrm{pl}}$	equivalent plastic strain
$\dot{\varepsilon}^{\mathrm{pl}}$	plastic strain rate component
$\sigma\|_0$	yield stress at zero plastic strain
Q_∞	maximum change in yield strength
$\bar{\varepsilon}^{\mathrm{pl}}$	plastic strain accumulation
b_{T}	the rate at which the yield surface changes
A_{T}	total elongation
γ	changing rate of the kinematic hardening moduli
C_{T}	initial kinematic hardening moduli
N_f	total number of cycles to failure
σ_{nom}	nominal stress
S	nominal stress range
m	fitting parameter
a_D	fitting parameter
σ_{a}	stress amplitude
σ_{TS}	tensile strength
$\Delta\varepsilon_p$	plastic strain range
ε_e	elastic strain
ε_p	plastic strain
$\Delta\varepsilon$	strain range

R_ε	strain ratio
H_s	significant wave height
T_z	zero-crossing period of wave spectrum
T_p	peak period of wave spectrum
p	probability of occurrence
U_w	mean wind velocity
U_c	mean current velocity

Chapter 1: Introduction

1.1 Mooring chain fatigue failures

There are many natural energy resources offshore, including oil, gas, wind, and wave. As a result, floating offshore platforms are widely used for the exploitation of these energy sources [1] [2]. Continuous operation of floating offshore platforms relies on the integrity of mooring lines to keep these platforms in position against adverse environments. One of the floating offshore platforms used by the offshore oil and gas industry for the production, processing, and storage of hydrocarbons is FPSO (Floating Production Storage and Off-loading), accounting for 65% of oil and gas production floaters in operation [3]. FPSOs have large storage capacity and can be used in locations where pipeline infrastructure is inaccessible [3]. Figure 1 shows one of the operating FPSOs, known as Usan FPSO, which can store 2 million barrels of oil and process 180,000 barrels of oil and 5 million cubic metres of gas daily [3].

Figure 1: The Usan FPSO operating in the West African oil field [3].

FPSOs are held in place using mooring lines at a relatively fixed position within a specified offset tolerance during service life without regular dry-docking for inspection or repair. The mooring line is installed permanently for 20-year design life or longer, meaning that these systems are not moved to avoid adverse weather conditions, that is, disconnection is not a planned operation.

The integrity of mooring lines is essential to the safety of FPSOs. Concurrently, the mooring integrity is also of great importance to the safety of floating renewable energy structures, which are projected to rise five times by 2040 [4], indicating even greater importance of the mooring integrity for the exploitation of many energy resources in the future. A mooring line configuration consists of a combination of chain, wire rope, and chain sections. The chain sections are used in the upper section and the lower section of the mooring line configuration, connecting to the floating platform and the anchor, respectively, while the wire rope section is used in between of the two chain sections. Among the chain and wire rope, most of the mooring line failures are mostly attributed to the chain component failures (54%) [1] [5] [6]. In addition, among the chain and wire rope, the chain is most vulnerable to fatigue failures [7].

A failure of mooring chain component represents serious consequences in terms of environmental and financial implications, e.g. vessel drifting, hull penetration, riser ruptures, line replacement cost, field-shutdown and oil-spillage [5] [8]. A single-line replacement for a mooring line failure can cost $2 million [9]. In addition, the field shut-down of two days due to failure and replacement of a mooring line could lead to a loss of $3 million because of production delay for an FPSO with a capacity of producing 50,000 barrels per day, while this cost could rise to $15 million when the FPSO has a capacity of 250,000 barrels per day [8]. These costs are estimated without the possibility of riser rupture, oil-spillage or FPSO damage, which could reach $700 million [9]. For example, the Gryphon Alpha FPSO lost four of its ten mooring lines, and the insurance pay-outs hit nearly £440 million as the risers ruptured and the vessel drifted in a storm [10].

However, mooring line failures have been occurring earlier than they are designed for. For example, Kvitrud et al. [11] reported 16 early mooring line failure events that were happened in the Norwegian Continental Shelf during the 2010-2014 period. In addition to those failures, Ma et al. [5] reported more than 21 mooring line failures over 2000 and 2011, of which about half of the failures occurred in the first three years out of 20-year design lives. A single line breakage could consequently overload other adjacent lines, resulting in multiple line breakages due to a domino effect that could lead to catastrophic impacts,

e.g. vessel drift, riser rupture, oil spillage, hull penetration [5]. For example, there are eight incidents of multiple line breakages among those mooring failures reported by Ma et al. [5], which some of them leading to vessel drift. This illustrates how necessary it is to avoid any mooring lines from failing in a mooring system for the safety of operating floating platforms.

In another case, Fontaine et al. [1] also reported that over a third of 80 mooring line failures happened early in their design lives during the 1997-2013 period, with more than a third of the failure events occurring between the installation and the third year of operation. Among those 80 failures, 67% of which were fatigue-related, and seven multiple line breakages were reported. Of note is that 95% of failures occurred before 18 years, with 90% occurring before 13 years. The early mooring line failures were reported to occur when operating in harsh sea environments [1] [5] [6] [11]. In order to demonstrate a base failure frequency per mooring line year, Figure 2(a) plots both the cumulative number of mooring failures and exposed mooring line years based on the cumulative number of exposed mooring line years for the worldwide fleet, as reported by Fontaine et al. [1]. The cumulative number of failures is proportional to the number of exposed mooring line years, and the rise in the number of failures observed over the last decades can be explained by the increase in the fleet population [1]. This indicates the potential increase of mooring failure events with the increasing mooring line exposure years in the future. Further to this, Fontaine et al. [1] provided an annualised failure frequency (per mooring line per year) by counting the cumulative failures by a given year and the cumulative number of exposed mooring line leg years to the same point, as shown in Figure 2(b), which displays that it has been nearly constant over the last decades. This emphasises the importance to improve the current understanding in mooring lines to reduce the failure rate.

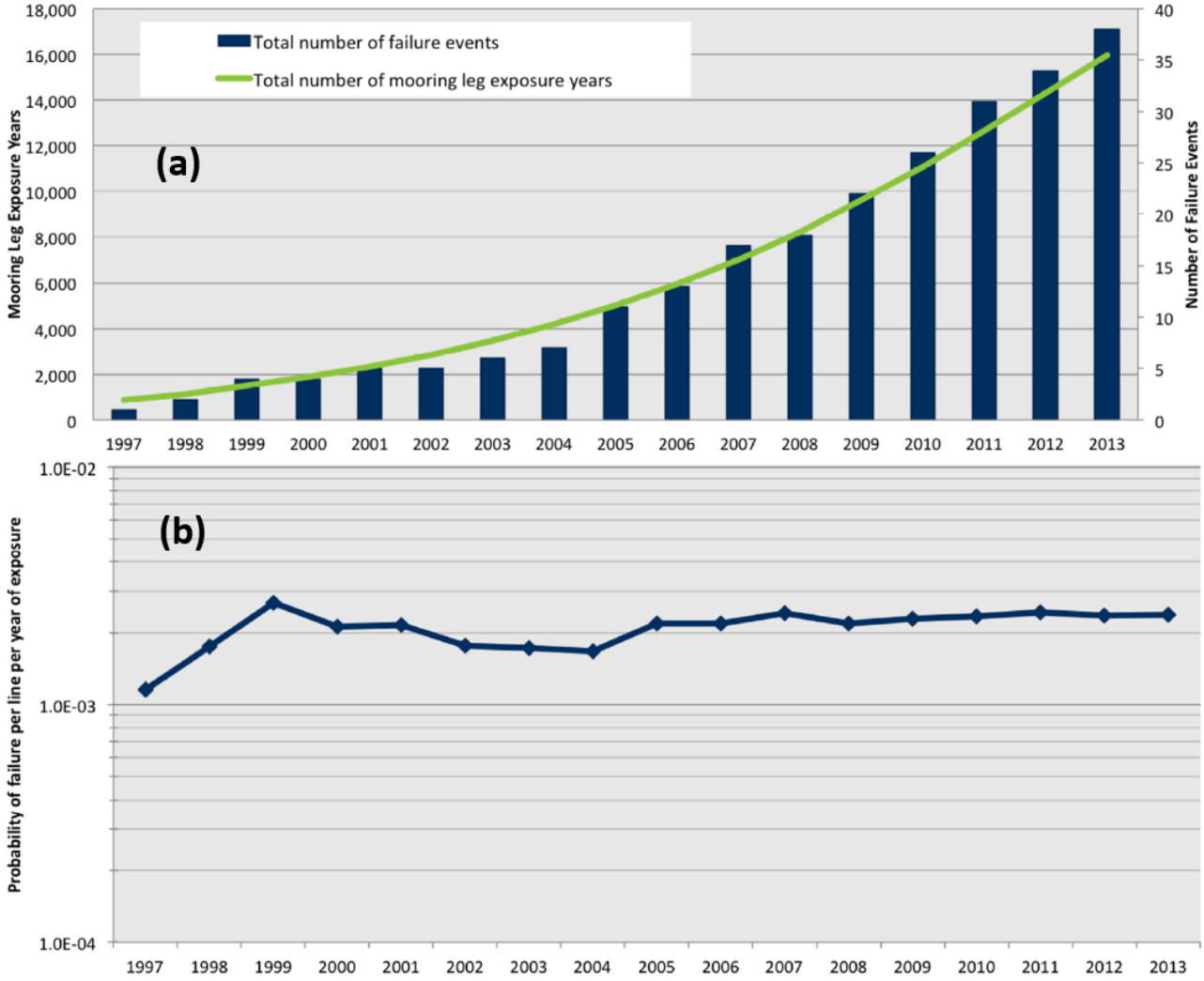

Figure 2: (a) cumulative failure events versus the number of mooring leg exposure years per year; (b) single line annual failure rate per line by each year [1].

Industry surveys [1] [12] have found various failure modes for mooring chains based on 107 reported mooring line failures from 73 assets in different regions, e.g. Brazil, Asia, North Sea, Gulf of Mexico, West Africa, as shown in Figure 3, of which fatigue failure is the most significant driver for these failures, showing that the reported mooring failures are 48 due to fatigue, 21 due to corrosion/wear, 8 due to mechanical wear, 8 due to improper installation, 8 mooring failures due to manufacturing defect, 6 mooring failures due to improper design and 8 due to unknown causes [1]. This finding that fatigue is the main cause of mooring failures is consistent with other industry surveys, where Ma et al. [5] documented 21 mooring failures of which 13 due to fatigue, 4 due to corrosion, 2 due to improper design and 2 due to manufacturing defect.

Further to this, Majhi et al. [6] also reported 42 mooring failures of which 18 due to fatigue, 6 due to corrosion/wear, 6 due to manufacturing defect, 5 due to improper installation and 7 due to unknown reasons.

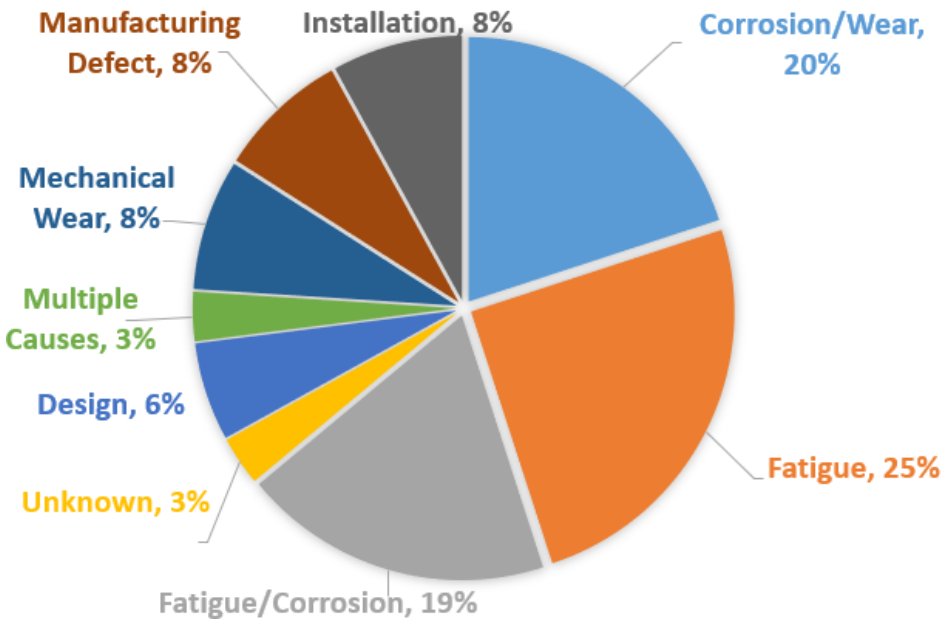

Figure 3: Types of failure modes for mooring chains by the proportion of occurrence [1].

Mooring chains are subjected to approximately 15×10^6 fatigue cycles over the first three years of operation, assuming a 6 s period of loading cycles on average. As the mooring fatigue failures occur early in their expected lives, this indicates that a high proportion of that damage within the fatigue cycles might occur under low-cycle fatigue conditions, and this is likely to be particularly significant when operating in harsh sea environments with high mean loads.

The low-cycle fatigue regime is commonly considered to be better described by strain-life approaches, applied to lives of less than 10^5 fatigue cycles, compared to the stress-life approaches for the high-cycle fatigue regime, $>10^5$ cycles [13]. Low-cycle fatigue is characterised by high mean loads, high-amplitude cyclic stresses, plastic strain accumulation with evolving multiaxial stress-strain responses leading to cyclic plastic degradation of the material properties, where the fatigue life is markedly shortened. In contrast, high-cycle fatigue is characterised by low mean loads and low-amplitude cyclic stresses.

However, the traditional SN approach, suggested by mooring standards [7], does not consider the mean load or cyclic plastic degradation effects for low-cycle fatigue. The lack of this consideration under low-cycle fatigue conditions is therefore proposed to be a contributing factor for the current non-conservative fatigue assessments of mooring chains. A more thorough approach, capable of considering these effects, need to be investigated for the accurate fatigue assessment of mooring chains.

1.2 Research aim and objectives

The research provides a better understanding of mooring chains through an investigation into the contribution of low-cycle fatigue to mooring line failures. This aim is achieved through a number of following objectives:

- Conduct a literature review of the different studies of mooring chains to demonstrate the novelty.
- Determine an appropriate FE model for predicting representative stresses and strains in mooring chains that are important to model low-cycle fatigue.
- Develop a fatigue approach, capable of modelling low-cycle fatigue for mooring chains.
- Perform a mooring line simulation of an FPSO to obtain the fatigue loading spectrum, and simulate fatigue experienced by the mooring chains in the FE model in order to demonstrate how important low-cycle fatigue to mooring line failures.

1.3 Research novelty

The novel contribution of this research is to develop a fatigue approach based on the critical plane multiaxial fatigue criteria, capable of considering the detrimental effects of mean load and cyclic plasticity on the fatigue damage, which governs the low-cycle fatigue of mooring chains under stochastic tension loading for intact mooring chains. This is achieved by incorporating all of the local stress-strain evolution at the fatigue hotspot into account when determining the fatigue response, including the proof load-induced effects (i.e.

strain hardening and residual stresses), mean load effects, and material constitutive responses in a mooring line fatigue simulation. This will contribute to determining the importance of low-cycle fatigue in mooring line failures.

1.4 Scope of work

Mooring systems can be classified into spread and turret single-point moorings. The spread mooring system that fixes the vessel heading is most widely used to moor non-ship-shaped floating structures, e.g. spars and semisubmersibles [14]. The turret single-point mooring system is usually used to moor ship-shaped floating structures for its weathervane capability to reduce vessel motions against environments [14]. As this study focused on the mooring system of an FPSO, which is ship-shaped, the turret single-point mooring system is selected. There are two types of the mooring chain geometry, i.e. studless chains and studded chains. This thesis focuses on studless chains since they are the most common type of mooring chains currently in use for their low weight, low cost, no risk of stud-looseness in comparison to studded chains [15]–[17]. The analysed mooring chains are in intact conditions to allow for the analysis of the low-cycle fatigue-induced effects without considering geometric adjustments due to other degradation mechanisms, e.g. corrosion, wear. This thesis focuses on the tension loading since this is the common loading mechanism between adjacent mooring chains, without considering other uncommon loading mechanisms, e.g. bending or torsion [18].

1.5 Thesis structure

The literature relating to issues of mooring chains is reviewed in chapter 2 to define the novelty, followed by the thesis methodology in chapter 3. Chapter 4 presents the determination of an appropriate finite element model for predicting representative stresses in mooring chains. The fatigue assessment based on the critical plane multiaxial fatigue criterion is developed and simulated in chapter 5. Chapter 6 sets out the discussion and limitations of the current study before being summarised in Chapter 7.

1.6 Publications

Journals:

G. M. Gemilang, P. A. S. Reed and A. J. Sobey, Selection of appropriate numerical models for modelling the stresses in mooring chains, Marine Structures, 2020. (Published).

G. M. Gemilang, P. A. S. Reed and A. J. Sobey, Low-cycle Fatigue Assessment of Offshore Mooring Chains Under Service Loading, Marine Structures, 2020. (Published).

Conference:

G. M. Gemilang, P. A. S. Reed and A. J. Sobey, Fatigue performance of mooring chains subjected to wear degradation, Proceedings of the ASME 38th International Conference on Ocean, Offshore and Arctic Engineering, OMAE2019-96386, 2019, Glasgow, UK. (Published).

Chapter 2: Literature review

2.1 Outline of the literature review

The structure of this literature review starts from how mooring chains are being manufactured including the proof load application in section 2.2, followed by the review of mooring chain failure scenarios based on previous incidents and experiences from industrial activities in section 2.3. Further, the literature relating to mooring line loading prediction is reviewed in section 2.4 to investigate the source of the fatigue loading. Then, the literature relating to chain models available in the literature relating to modelling the stresses and strains in mooring chains is reviewed in section 2.5. Afterwards, the literature relating to fatigue issues of mooring chains is reviewed in section 2.6, followed by section 2.7 which discusses fatigue approaches of relevance to this research objective in the literature. Finally, section 2.8 outlines the key gap in the current understanding of the literature, where the novelty and direction of this research are specified.

2.2 Manufacture of mooring chains

2.2.1 Manufacturing process

Chains are manufactured from steel bars, made from low-alloy steels with a carbon content of less than 0.30%, following the classification society, e.g. DNV-OS-E302 [19] and IACS [20]. The steel bars are heated before being bent into the shape of a chain link, where link dimensions and alignment are checked regularly. Afterwards, the two ends are subjected to a flash butt welding process at one of the straight parts [19]. Then, it is trimmed to remove excess material from the welded area. Afterwards, the heat treatment process starts by heating the chain, quenching it, and reheating it again to a temperature above 570°C, followed with water cooling [19]. By controlling the heating temperature or the quenching period, this process allows the material to meet the minimum mechanical properties for different steel grades, e.g. R3, R4, R5, with different yield and tensile strengths specified in standards [19] [20]. A non-destructive

examination is to be performed for each finished chain to ascertain that the surface is free of damage, e.g. cracks, notches and sharp edges [21].

2.2.2 Proof load test

After the heat treatment, mooring standards [20] [22] require mooring chains to be proof load tested before being installed offshore to assure the strength capability of mooring chains. The proof load test subject a chain up to 70% of the minimum breaking load and then back to zero. The minimum breaking load is the minimum tension required for the chain to break, as specified by standards, depending on the diameter and the steel grade. Table 1 presents the list of formulas for the minimum breaking load (MBL) as a function of the steel grade and the diameter, *D*, in mm, according to IACS [20] and ABS [22]. These formulas will be used to calculate the minimum breaking load and the proof load in this study.

Table 1: Formulas for the minimum breaking load (MBL) of studless link for different steel grades [20] [22].

Steel grade	MBL (kN)
R3	$0.0223D^2(44-0.08D)$
R3S	$0.0249D^2(44-0.08D)$
R4	$0.0274D^2(44-0.08D)$
R4S	$0.0304D^2(44-0.08D)$
R5	$0.0320D^2(44-0.08D)$

The proof load test causes residual stresses in mooring chains. The heat treatment process conducted before the proof load test also causes residual stresses in mooring chains; however, the residual stresses are later replaced by significantly greater residual stresses from the proof load test [23]. This is confirmed by Perez et al. [23] [24], who compared between a model with residual stresses from only the proof load and a model with residual stresses from both the proof load and heat treatment, showing no significant differences between them. Therefore, residual stresses from the heat treatment process have a negligible effect on the fatigue performance compared to residual stresses from the proof load test [23]. Thus, well-predicted residual stresses

from the proof load test are important for mooring chains' fatigue assessment; hence, many scholars worked on this topic to understand the effect of the proof load test on the fatigue performance of mooring chains.

Bastid and Smith [25] found that the magnitude of residual stresses depends on different regions on the chains' surfaces and the employed material model based on finite element studies. Pacheco et al. [26] found high residual stresses in elastoplastic finite element models when compared with elastic finite element chain models, suggesting that the elastoplastic material modelling is essential to capture the residual stresses. Subsequently, Pacheco et al. [27]–[29] showed the importance of appropriate interlink loading method in predicting the compressive residual stresses based on finite element studies. However, it was not clear how the residual stress might affect the fatigue capacity in the analysis as they did not compare the fatigue life of the model with the incorporation of the residual stress from the proof load and the one without it.

Further, Shoup et al. [30]–[32] compared the fatigue life of chains with different proof load levels (0%, 70%, 76% and 82% of the minimum breaking load) in fatigue tests, showing that the fatigue life improves with the increase of proof load levels because of the resulted compressive residual stresses from the proof load, as shown in Figure 4, where the vertical axis is the ratio between the load amplitude and the minimum breaking load, and the horizontal axis is the number of cycles to failure. This is in agreement with Bolt et al. [33] and Suzuki et al. [34], showing that the chains after the proof load test have fatigue lives well above the ones before the proof load test based on fatigue tests.

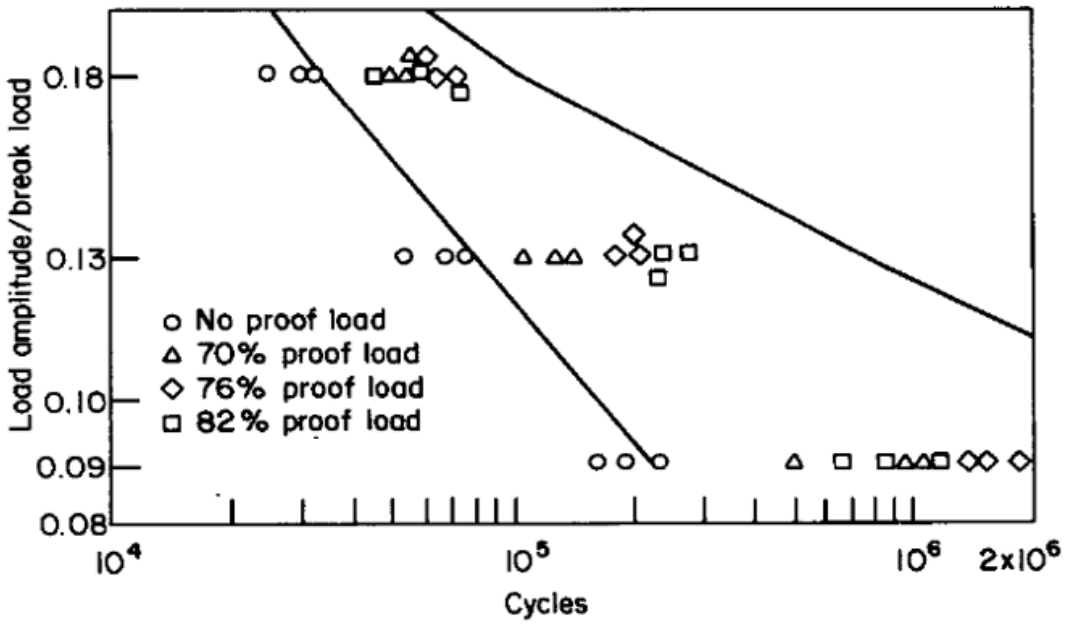

Figure 4: Logarithmic plot of load amplitude versus fatigue life for different proof load levels at a mean load of 20% of the minimum breaking load [30].

Recently, Ershad and Skallerud [35] measured the residual stresses of mooring chains in experiments, confirming the existence of high compressive residual stress due to the proof load test at the chain's crown, i.e. one of the fatigue hotspots. This explains the increase in fatigue capacity of proof loaded chains since the compressive residual stress reduces the mean stress at the fatigue hotspot [35]. In addition, the proof load test induces strain hardening that can cause significant yielding and prevent from a further line stretching in service [36]. In conclusion, the proof load test has been recognised in the literature to give beneficial effects on the fatigue capacity of mooring chains.

2.3 Mooring chain failure scenarios

As introduced in chapter 1, there is a consensus within the offshore oil & gas industry that there are many events of early mooring line failure in the past. As the key to improving the mooring integrity is learning from the past failures, this section reviews scenarios of the mooring line failures reported in the literature [1] [5] [6] [8] [11] [37] [38].

Figure 5 describes the common mooring chain failure locations, i.e. the upper chain section and lower chain section, where the wire rope section is positioned in between the upper and lower chain sections. The upper chain section is

connected to the FPSO, while the lower chain section is connected to the anchor point on the seabed. Fairlead is the point where the mooring line is connected to the FPSO. The chain failures commonly occur at the upper chain section near the fairlead and the lower chain section where it dynamically comes into contact with the seabed, whereas chain failures at connections between the chain and wire rope sections are unlikely to occur based on the literature [1] [5] [6] [11].

Table A-1 in Appendix A lists mooring line failure events with associated scenarios and causes taken from the literature, indicating that many mooring chain failures happened in their early lives. Table A-1 shows that the failures at the upper chain section have 77% proportion of the total occurrence in which the fatigue is the most common failure mode. This is supported by Fontaine et al. [1], which found that 57% proportion from 30 inspected chain failures were in the upper chain, 66% of which were fatigue-related accidents. The upper chain section as the most common fatigue failure location has also been highlighted in mooring standards. For example, API-RP-2SK [18] states, "fatigue damage of chain at the fairlead is typically higher than that away from the fairlead." ABS [22] also states that "fatigue evaluation is typically focused on the upper chain segment, which has the shortest fatigue life." This is because of the relatively greater loading tensions in the upper section than the lower section of the mooring line. This suggests that the fatigue performance in the upper chain section should be accurately evaluated during the design phase, especially in their early lives.

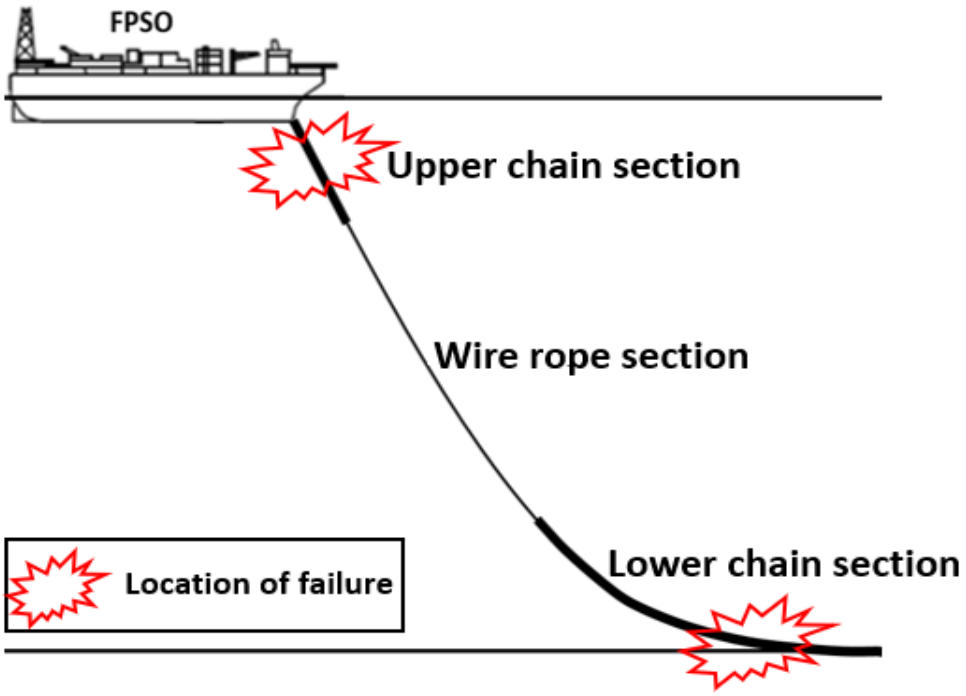

Figure 5: Schematic view of potential breaking locations of chains along a mooring line.

Another finding from the mooring chain failures listed in Table A-1 is that the early mooring chain failures commonly happened when operating in harsh sea environments or extreme storm situations. For example, Kvitrud [11] reported that Petrojarl Banff FPSO lost multiple mooring lines, triggered by overloading cycles due to a storm. Also, a mooring chain used in Petrojarl Varg FPSO failed in 2012 due to fatigue when operating in a storm [11]. In another case, Shoup [39] reported a case in which a failure occurred at the top of the upper chain section, as a result of highly loading cycles imposed by a typhoon. Suhara et al. [40] also reported that slack mooring lines are subjected to snap load when subjected to a sudden severe weather event, leading to an increase in tensions with high mean loads. This indicates that the failure mechanisms of mooring chains in the past could be attributed to low-cycle fatigue loading due to the harsh sea environments in service. The fatigue response of mooring chains against the mooring line loading in service needs to be accurately evaluated, such that any threats to mooring system integrity can be minimised across the entire life cycle of the facility.

2.4 Mooring line loading in service

Mooring line loading is the source of the fatigue loading determining the fatigue life of mooring chains. Mooring line loading is strongly dependent on motions of the moored platforms which are induced by the environmental actions due to waves, wind and current. Many studies [27] [30] [41]–[44] used deterministic cyclic loading at a constant amplitude and a constant mean load to study the fatigue behaviour of mooring chains. However, the mooring line loading is actually stochastic, i.e. with variable amplitudes and variable mean loads, and therefore should be determined from a combination of static and dynamic analyses in a mooring line simulation. According to API-RP-2SK [18], coupled interactions between a mooring system and a floating platform result in forces acting on the mooring lines that can be split into three components:

- a steady component that represents a combination of pretension and the mean forces of waves, wind and current acting on the vessel, known as mean wave drift forces;
- second-order motions that oscillate at the steady component, known as low-frequency (LF) tension variations;
- first-order motions that oscillate at the second-order motions, known as wave-frequency (WF) tension variations [18].

Figure 6 illustrates the tension time series with the three components [18]. In order to identify the loading regime on a mooring line, static and dynamic analyses are performed in a mooring line simulation. The steady component is determined in the static analysis, while the first-order and second-order motions are excited from the vessel motions against the wave actions calculated using RAO and QTF of vessel data, respectively, in the dynamic analysis.

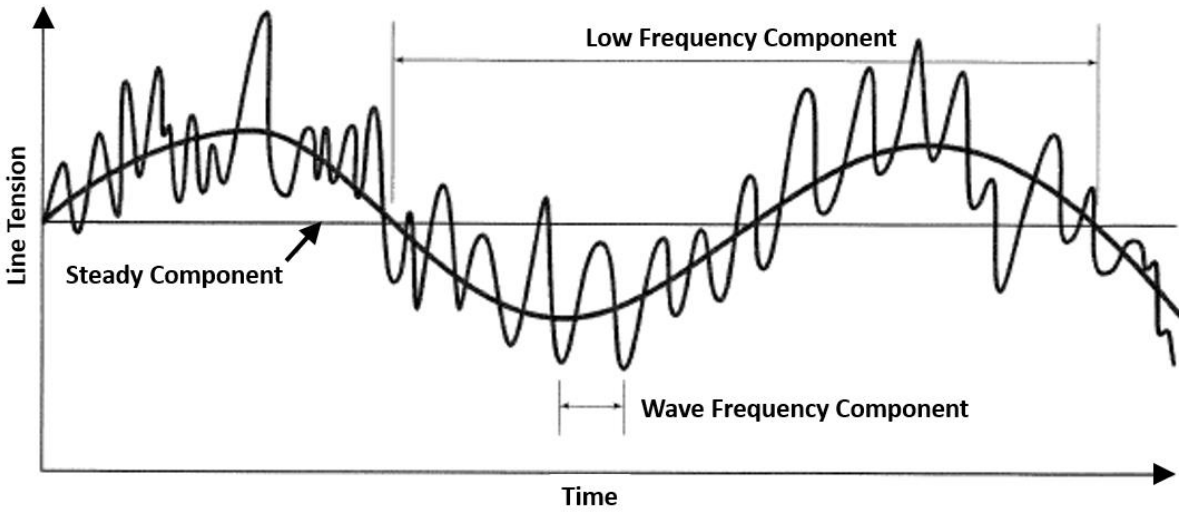

Figure 6: The components in tension time series of a mooring line [18].

The dynamics of a mooring line can be analysed in two different methods: frequency-domain (FD) and time-domain (TD). Brown et al. [45] found that the time-domain method is more accurate than the frequency-domain method based on experimental measurements. This is because the time-domain method can better consider the effect of the system's nonlinear interactions between moorings and vessels through a coupled dynamic analysis [46] [47]. In addition, many design practices recommend using the time-domain fatigue assessment method, which is widely considered to be a benchmark against the frequency-domain method [48] [49]. Hence, many mooring line literature investigates mooring line loading predictions to work out why mooring lines are failing in time-domain simulations. This is reflected in a high number of published studies [50], [51], [60]–[68], [52]–[59], attempting to look at fluid interactions of the mooring line with floating platforms, mooring configuration, various wave loads or vortex-induced motion to improve the prediction of mooring line loading, rather than the fatigue response at structural scale.

However, although the predictions of mooring line loading have been well investigated, the mooring line failures still occur early in their expected fatigue lives in the past. This indicates that the fatigue response of mooring chains against the mooring line loading needs further investigations to prevent those early mooring failures from occurring in addition to the investigation of mooring line loading estimations.

2.5 Chain models

An FE model is essential to predict the representative stresses and strains in mooring chains when being subjected to tension from the mooring line loading for failure analyses. However, there are many different types of FE model of a chain available in the literature; where these models use different software and different FE modelling parameters, i.e. interlink loading method, element type, and solution method, for different purposes of analysis. Table 2 summarises the available methodologies used for modelling mooring chains in the literature.

Table 2: Different numerical methods for modelling mooring chains in the open literature.

Ref.	Analysis	Software	Interlink loading method	Element type	Solution method
[69] [70] [71] [72]	Fracture mechanics	ANSYS	Contact interaction	SOLID95	Implicit
[26] [27] [29]	Residual stress	ANSYS	Pressure distribution	SOLID95	Implicit
[26] [27] [29] [28]	Residual stress	ANSYS	Contact interaction	SOLID95	Implicit
[23] [24] [25] [42] [43]	Fatigue and Residual stresses	ABAQUS	Contact interaction	C3D20R	Implicit
[73] [74] [75]	Bending effect	ABAQUS	Contact interaction	C3D8I	Implicit
[76]	Wear effect	ABAQUS	Contact interaction	C3D8R	Implicit
[77]	Ultimate strength	ABAQUS	Contact interaction	C3D8R	Explicit
[78]	Torsion effect	ABAQUS	Contact interaction	C3D8R	Implicit
[79]	Fracture mechanics	ABAQUS	Contact interaction	C3D8R	Implicit
[80]	Ultimate strength	ANSYS	Contact interaction	SOLID185	Implicit
[35] [81]	Fatigue of corroded chains	ABAQUS	Contact interaction	C3D8R	Implicit
[82] [83]	Fatigue of corroded chains	ABAQUS	Contact interaction	C3D10	Implicit
[84]	Stress concentration factor	ABAQUS	Contact interaction	C3D20R	Implicit

It is shown that the majority of numerical studies use an implicit solver, while there is only one numerical study using the explicit method for the solution method [77]. The solution method relates to how the finite element methods find a solution for the displacements in the element against the applied load. In the implicit approach, a solution to the set of finite element equations is unconditionally stable involving iteration until a convergence criterion is satisfied at each load increment [85]. In contrast, In the explicit approach, a solution is solved in a dynamic formulation and is conditionally stable, assuming the time increment selected is small enough.

Table 2 also shows that there are two different interlink loading methods, i.e. pressure distribution and contact interaction. These interlink loading methods relate to how chains are subjected to the contact force, transmitted across their common mating surface via interlink contact mechanisms. Figure 7 illustrates both types of the interlink loading method in the literature: (a) the pressure distribution method, which uses a pressure to replicate the contact force [27], and (b) the contact interaction method, which is more consistent with the real chain interaction than the pressure distribution [42]. This interlink loading method needs to be determined correctly so that the stress distribution in the chain is representative.

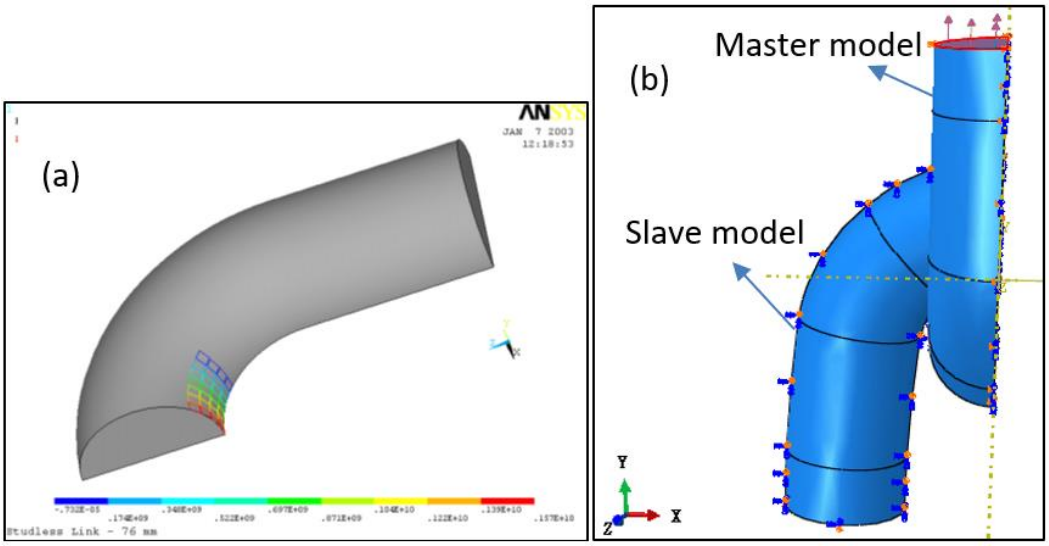

Figure 7: Interlink loading method in FEA: (a) a model with pressure distribution [27] and (b) a model with contact interaction [42].

In the pressure distribution method, the magnitude of the pressure is equivalent to the resultant load in the contact region and varies linearly from a maximum

value at the centre of the contact area to zero at the border, where a contact angle of 35^{o} is applied to represent the contact area from the axial direction [27]. In the contact interaction method, contact formulations are applied to connect the nodes on the mating surfaces. The upper chain is represented as the master model, and the lower chain is represented as the slave model. The bottom surface of the slave model is fixed, while the upper surface of the master model is loaded using a uniformly distributed surface traction acting at the top, as indicated in red in Figure 7(b).

There are a number of works modelling the whole chain in FEA [71] [72] [84]; while the majority of the literature modelling only a part of the chain by using symmetric boundary conditions as shown in Figure 7 [23], [24], [78], [81], [25]–[29], [35], [42], [43]. This is because a chain has three planes of symmetry, and so only a $1/8^{th}$ of a chain needs to be modelled to minimise the computational efforts for each chain, where the symmetry boundary condition is assigned at each symmetry plane. Modelling a part of the whole chain using the symmetric boundary conditions is more attractive than modelling the whole chain to ensure efficient computational effort when the chains are subjected to tension loading.

It has been demonstrated that the FE chain models available in the literature use different modelling parameters. However, there are no evaluations of how differently each FE model predicts stresses and strains in the literature. This makes it hard to make an appropriate choice from the literature when each of the different models is appropriate, indicating that there is a need for an investigation of comparison between these different FE models to select the most appropriate model in predicting the representative stresses and strains in mooring chains.

2.6 Fatigue of mooring chains

2.6.1 Fatigue in metallic materials

Before the main literature review on fatigue living methodologies of mooring chains, it is essential to introduce the main processes involved in the fatigue damage process. Fatigue is an important failure mode of metallic materials when

subjected to alternating loads. Suresh [13] defined fatigue as a term which is influenced by the material microstructure, material mechanical properties, the component geometry and loading conditions. Fatigue life is typically expressed in terms of number of cycles to failure, and the total fatigue life is the sum of the number of cycles in the initiation stage and the propagation stage.

In the fatigue initiation stage for defect-free materials (without initial cracks), fatigue cracks are usually found on the free surface, which has been postulated to be caused by the repetitive cyclic straining of the material resulting in varying amounts of net slipping on different slip bands (dislocations across the plane), also known as persistent slip bands (PSB) [13]. The resultant microscopic 'valleys' and 'hills' along the slip bands at the roughened surface are commonly referred to as intrusions and extrusions respectively, as illustrated in Figure 8. Fatigue cracks generally nucleate in this manner along those persistent slip bands where slip is particularly intense [86].

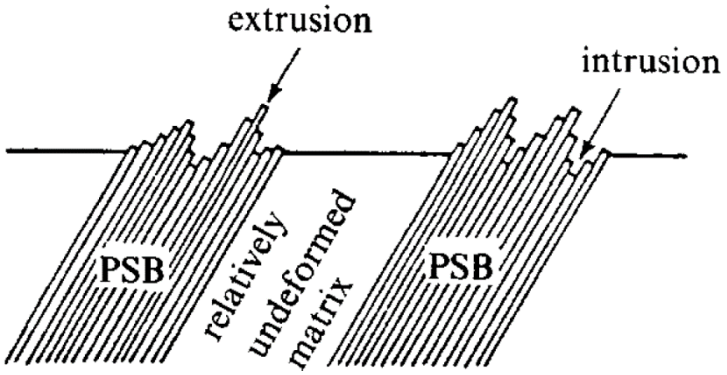

Figure 8: A rough surface consisting of hills and valleys in form of extrusion and intrusion, respectively [13].

In the fatigue propagation stage, the dominant crack develops slowly under steady fatigue loading, but begins to intensify when the reduction of the cross-section increases the local stress field near the crack tip. The crack has zone of plastic deformation surrounding the crack tip, which propagates within the dislocation movement of grains along the primary slip plane experiencing the maximum shear stress, resulting in a zigzag crack path [13] [87]. This mechanism leads to a crack growth path perpendicular to the applied stress, and final fracture occurs when the remaining cross-section area is too small to support the load [87].

The crack growth behaviour can be described using fracture mechanics as this method enables a quantification of the intrinsic resistance of the material to fatigue crack growth [13]. This method is also known as damage tolerant approaches since it is to estimate the crack growth of damage in structures containing initial cracks, as long as the pre-existing crack size is known [13]. The other life assessment method is total life approaches, which can be conveniently used to predict the number of total cycles, N_f, including both crack initiation and crack propagation stages for a structure to endure in terms of fatigue [13]. The total life approach pertains to defect-free assumption, meaning that the structures being analysed is assumed to have no pre-existing cracks. This assumption can be a reasonable approximation for mooring chains as the surface of mooring chains is inspected via non-destructive examination to ensure that there are no pre-existing surface defects (e.g. notches, sharp edges, pre-existing cracks) prior to deployment.

A sinusoidal loading history with a stress amplitude, σ_a, and a mean stress, σ_m, is the simplest representation of stress spectrum. Since the sinusoidal loading history is easily defined and simple to reproduce, it usually forms the basis for most experimental fatigue tests. Figure 9 shows a schematic demonstration of the sinusoidal cyclic stress used in fatigue test [86].

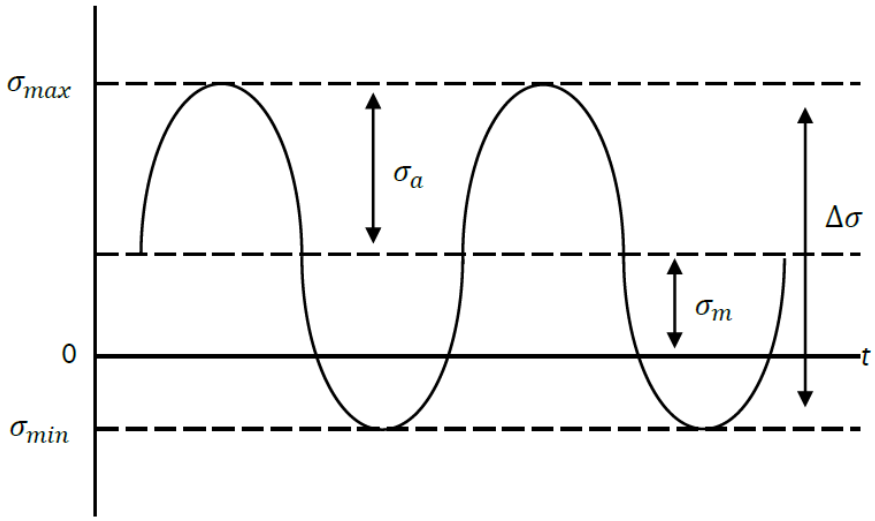

Figure 9: A schematic illustration of the sinusoidal waveform with nonzero mean stress [86].

The stress range, $\Delta\sigma$, the stress amplitude, σ_a, the mean stress, σ_m, and stress ratio, R_s, are commonly used to describe the cyclic stress, which can be defined

by Equations (1-4), respectively, where $\boldsymbol{\sigma_{max}}$ is the maximum stress and $\boldsymbol{\sigma_{min}}$ is the minimum stress,

$$\Delta\sigma = \sigma_{\max} - \sigma_{\min}, \qquad (1)$$

$$\sigma_{\mathrm{a}} = \frac{\sigma_{\max} - \sigma_{\min}}{2}, \qquad (2)$$

$$\sigma_{\mathrm{m}} = \frac{\sigma_{\max} + \sigma_{\min}}{2}, \qquad (3)$$

$$R_{\mathrm{s}} = \frac{\sigma_{\min}}{\sigma_{\max}}. \qquad (4)$$

Fatigue assessment methods separate into two broad categories based on the type of cyclic loading experienced by the structure, i.e. high-cycle fatigue and low-cycle fatigue [13]. Mooring chains subjected to degradation mechanisms and extreme loading conditions during their lifetime may experience a combination of the low-cycle fatigue and the high-cycle fatigue loading cycles, which needs to be properly addressed during the design in order to avoid the component failure. The high-cycle fatigue is characterised by low mean loads, low-amplitude cyclic stresses, and the stress-strain response is stabilised or under elastic shakedown, where stress is a good measure of strain because the elastic modulus applies so stress is proportional to strain. Thus, a stress-life approach has been widely used to characterise high-cycle fatigue [13]. However, low-cycle fatigue is characterised by high mean loads, high-amplitude cyclic stresses and elastoplastic material behaviour, where a low-cycle fatigue loading is commonly considered to be better described by strain-life approaches, applied to lives of less than 10^5 fatigue cycles, compared to the stress-life approaches for the high-cycle fatigue regime, $>10^5$ cycles [13].

In addition, McDowell and Dunne [88] state that microstructure-sensitive process of the high-cycle fatigue and low-cycle fatigue regimes can be based on the heterogeneity of cyclic plastic deformation at the scale of the microstructure. From a micromechanics perspective of the high-cycle fatigue regime, the cyclic plastic deformation is likely to be highly heterogeneous within the microstructure, corresponding to stress amplitudes below macroscopic yielding

under predominantly elastic shakedown [13] [88]. Transition to low-cycle fatigue regime occurs at higher applied stress amplitudes for which the mean stress increases and cyclic plasticity becomes widespread and more homogeneously distributed involving multisite cracking and coalescence of micro-voids under predominantly elastoplastic material behaviour [88]. The lifetime in the low-cycle fatigue regime is predominantly controlled by loading cycles below 10^5 number of cycles to failure, while the lifetime in the high-cycle fatigue regime is predominantly controlled by loading cycles above 10^5 number of cycles to failure [88].

Figure 10 demonstrates a schematically clear distinction between low cycle and high cycle fatigue loading cycles in terms of alternating stress versus the number of cycles to failure, taken from the literature [89].

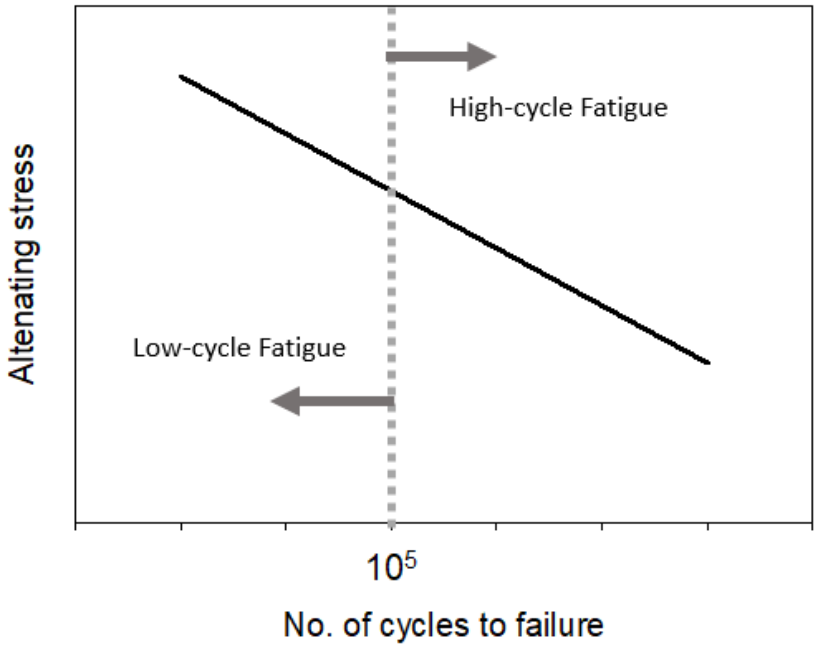

Figure 10: A schematic distinction between high-cycle fatigue loading cycles and low-cycle fatigue loading cycles [89].

2.6.2 Fatigue hotspots

It is important to identify the critical fatigue locations where the fatigue crack initiates to analyse the local stress and strain for fatigue analysis. Typical fatigue hotspots under tension loading have been identified in the literature based on

finite element studies and fatigue tests. Figure 11 shows the identified fatigue hotspots**,** i.e. crown and K_t point.

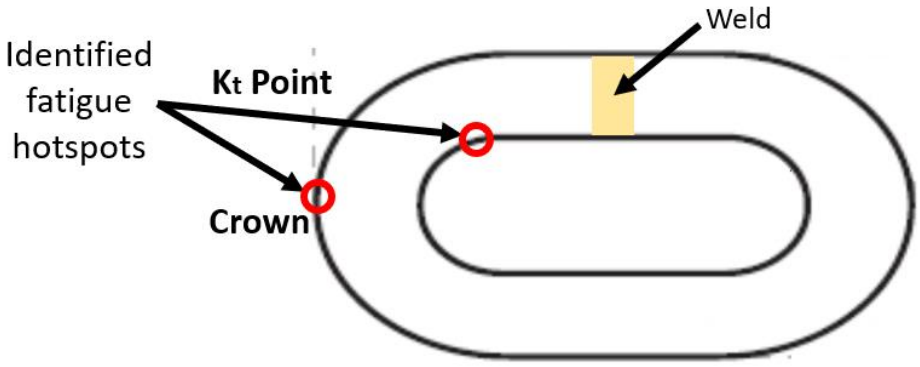

Figure 11: Identified fatigue hotspots in the literature.

From Figure 11, one might presume that the weld section is also one of the critical fatigue hotspots. However, many authors [44] [70] [81] [90] found that the weld section of mooring chains was not identified as one of the critical fatigue locations in the literature since the weld section is in a position which has no significant tensile stress ranges of loading cycles governing the fatigue of the component in comparison to the crown and K_t point based on fatigue tests and finite element studies. Therefore, many studies [24], [25], [31], [43], [84], [90]–[92] suggest that these two particular locations should be investigated for fatigue analysis. Figure 12 visualises the fatigue crack initiation points from failed mooring chains under tension loading retrieved from offshore fields [91]. The fatigue failure at the crown originates on the outside of the link and grows inwards, while the fatigue failure at the K_t point originates on the inside of the link and grows outwards [31].

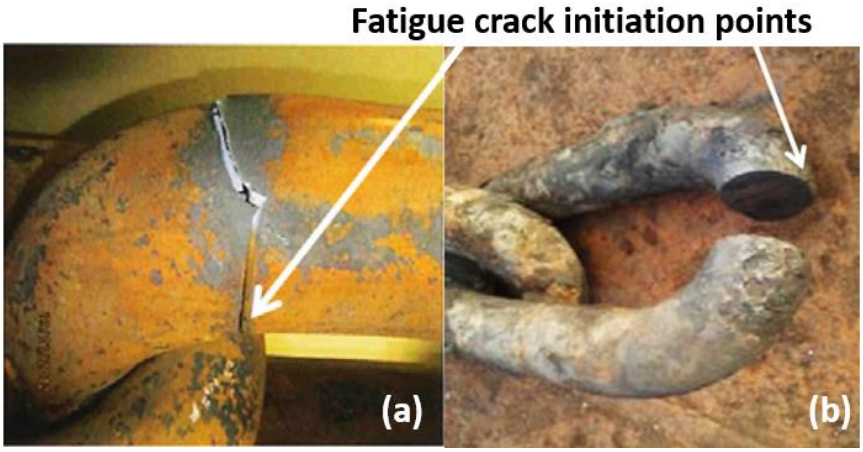

Figure 12: Illustrations of failed mooring chains in two distinct locations of fatigue hotspots: (a) the K_t point and (b) the crown point [91].

A number of studies compared the susceptibility to fatigue failure between the crown and the K_t point. Based on finite element studies, Vargas et al. [84] found that the stress concentration factor of the crown was higher by 15.7% than that of the K_t point, while Xue et al. [70] found that the stress concentration factor of the crown was 12.8% higher than that of the K_t point. In addition, Perez et al. [24] [43] and Zarandi [81] claimed that the crown was more prone to fatigue damage compared to the K_t point owing to the higher compressive residual stress at the K_t point than that at the crown based on their finite element studies. Further to this, Fernandez et al. [93] found that the stress concentration factor of the crown was 24% higher than that of the K_t point based on experiments with strain gauges, while Zhang et al. [94] found that the stress concentration factor of the crown was 32% higher than that of the K_t point based on experiments with strain gauges.

In agreement with [24] [43] [70] [81] [84] [93], many fatigue failures have been observed at the crown in full-scale fatigue tests. Zhang et al. [94] performed fatigue tests of mooring chains in seawater and found that 45 tests broke at the crown, while 17 tests broke at the K_t position. Ma et al. [95] performed six fatigue tests of corroded mooring chains retrieved from West African and North Sea fields in which all of the fatigue tests broke at the crown. Gabrielsen et al. [90] [94] [95] found that more than 80% of the fatigue breakages were at the crown, and only 15% of the fatigue breakages were at the K_t point based on fatigue tests of 47 used chains retrieved from offshore fields after several years of operation. In another study, Gabrielsen et al. [96]

[97] conducted fatigue tests on used chains recovered from fields in which nine out of ten tested chains broke at the crown. These experimental fatigue studies [90], [94]–[97] are in agreement that the crown is more critical than the K_t point in terms of fatigue failure. In contrast, Fernandez et al. [44] performed full-scale fatigue tests, resulting in nine tests broken at the K_t point and six tests broken at the crown.

In conclusion, it can be seen that there is still some debate as to which location (the crown or K_t point) is more susceptible to fatigue failure, with most studies indicating it is the crown. However, both locations have been confirmed to be critical in developing fatigue failure.

2.6.3 Fatigue design approach in the industry

The main fatigue design approach commonly used in offshore industries is the traditional SN approach to predict the fatigue life of mooring chains, according to DNV-OS-E301 [7]. This approach considers the nominal stress range as the fatigue damage parameter that controls the fatigue life of the mooring chain, represented as SN curves. Nominal stress is defined as the tension divided by the cross-sectional area of the two chain's round bars, as shown in Equation (5),

$$\sigma_{\mathrm{nom}} = \frac{T}{2\pi D^2/4}, \qquad (5)$$

where σ_{nom} is the nominal stress, T is the tension and D is the chain diameter. Figure 13 shows the SN curves derived from fatigue testing of the stud-link chain, open-link (studless chain), spiral-strand wire rope and six-strand wire rope [7]. A characteristic feature of fatigue testing is the large scatter in the test results, and this is particularly evident when a number of specimens of a specific material are tested at the same stress range level. The uncertainty that makes such large scatter in the test results is in the number of cycles during the crack initiation stage. Therefore, fatigue design of the SN curves uses the mean value of the large scatter fatigue testing data minus two times the

standard deviation for generating the SN curves in order to be on the safe side with lower band values based on the large scale fatigue testing results [98].

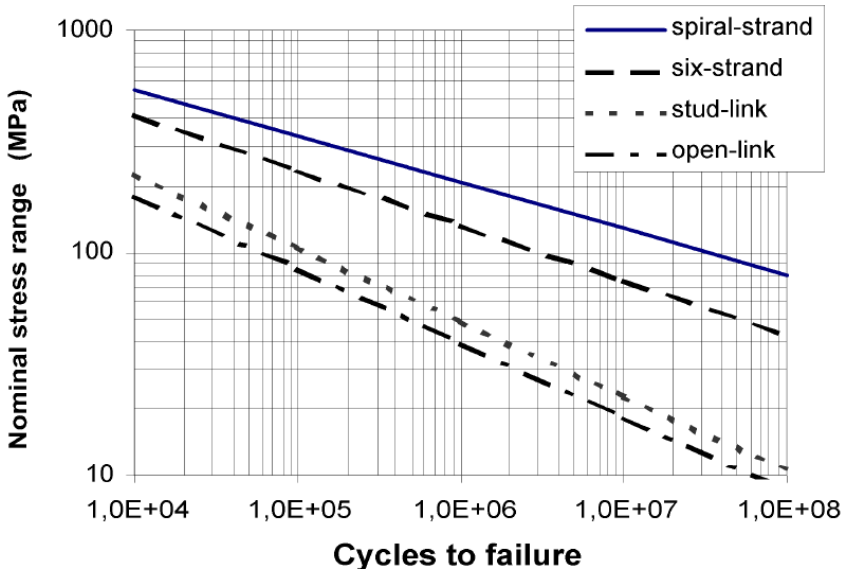

Figure 13: Mooring fatigue design SN curves, according to DNV-OS-E301 [7].

Equation (6) is used to assess the component capacity against tension fatigue in a general format,

$$N_{\mathrm{f}} \times S^{m} = a_{\mathrm{D}}, \tag{6}$$

where S is the nominal stress range, N_{f} is the number of cycles to failure, a_{D} and m are the fitting parameters derived from the fatigue testing. The other fatigue design approach is provided by API-RP-2SK [18], using TN curves derived from fatigue tests. This approach is similar to the traditional SN approach that this approach is exclusively based on the range of load applied to the chains, except that this approach takes the tension range as the fatigue driving parameter of what controls the fatigue life, instead of the nominal stress range.

When using the standard fatigue approaches, common industry practices suggest using a safety factor to cover the uncertainties of the fatigue damage prediction [7] [18]. Mooring standards [7] [18] suggest the use of a safety factor of 3.0 for regularly inspected components, and the safety factor can be increased up to 10.0 for non-inspected components. The expected fatigue life then is at least the safety factor times the design service life of the mooring

line. However, even with the use of the specified safety factors, early mooring chain failures have still occurred in the past, requiring further investigations for why these predictions are non-conservative, despite the large safety factors.

The traditional SN approach suggested by mooring standards, DNV-OS-E301 [7], is based on SN curves derived from full-scale fatigue tests on 76 mm chains of steel grades R3 and R4 under tensile loading at a constant mean load of 20% of the minimum breaking load in simulated seawater [7] [90] [94] [99]. These curves are used to compute the fatigue life regardless of the mean load experienced in service, thus the effect of mean loads above 20% of the minimum breaking load may not be anticipated by this approach. This approach assumes the overall load range applied to the chains controls the fatigue life, without considering the role of local stress-strain evolutions at the fatigue hotspot in determining the fatigue damage. This standard approach does not consider the effects of mean load or cyclic plastic degradation of the material on fatigue damage in low-cycle fatigue prediction. Albeit, previous fatigue studies for other structures [13], [100]–[104] have demonstrated that cyclic stress-strain evolution and mean load effects are the predominant factors controlling low-cycle fatigue behaviours of structural components during progressive loading cycles.

High-cycle fatigue is characterised by low mean loads, low-amplitude cyclic stresses, and the stress-strain response is stabilised or under elastic shakedown, where a stress-life based approach is appropriate because stress is proportional to strain, as the material can be assumed to behave elastically [13]. The traditional SN approach is stress-based and hence is suitable for the high-cycle fatigue regime where plastic deformation is small or negligible. However, low-cycle fatigue is characterised by high mean loads, high-amplitude cyclic stresses and plastic strain accumulation, where a strain-life based approach is more appropriate to consider the mean load effect and cyclic plastic degradation of the material in which the fatigue life is controlled by the multiaxial stress-strain evolutions at the fatigue hotspot [13]. The low-cycle fatigue regime is commonly considered to be better described by strain-life approaches, applied to lives of less than 10^5 fatigue cycles, compared to the stress-life approaches for the high-cycle fatigue regime, $>10^5$ cycles [13].

Mooring chains are subjected to approximately 5×10^6 fatigue cycles over three years of operation, assuming a 6s period of loading cycles on average. With many mooring chain fatigue failures occurring earlier in their expected lives, mooring chains are likely to experience a large proportion of low-cycle fatigue loading within the fatigue cycles experienced in the first three years of operation with high mean loads and large load amplitudes, when operating in harsh sea environments. The lack of consideration of mean load effects and cyclic plastic degradation of the material for low-cycle fatigue is therefore proposed to be a contributing factor for the current non-conservative fatigue assessments of mooring chains. Further work is therefore needed to capture the factors that have not been fully addressed in the standard fatigue approaches to improve the low-cycle fatigue assessment that can explain the early fatigue failures of mooring chains seen in the past.

2.6.4 Fracture mechanics analysis of mooring chains

There are a number of fracture mechanics analyses for fatigue analysis of mooring chains in the literature[70]–[72], [79], [105]–[110] based on both experiments and numerical studies. The studies show that the fracture mechanics approach is sensitive to the assumption of the initial crack size, and these studies do not investigate the effect of mean load and cyclic plasticity under low-cycle fatigue loading. Although the fracture mechanics approach can, in some cases, provide accurate fatigue life prediction, its accuracy is particularly sensitive to the assumption of the initial crack size, and requires non-destructive testing approaches of suitable sensitivity. Therefore, the fracture mechanics approach is not commonly used for fatigue design in the offshore industry, mainly because the initial crack size is often unknown for mooring chains working underwater, and the model test data of crack growth rate versus stress intensity factor range are relatively expensive to obtain compared with the standard total life approaches [91].

2.6.5 Fatigue tests of mooring chains

Many works used total life approaches to perform fatigue tests on used chains retrieved from offshore fields. Fredheim et al. [111] performed fatigue tests on used chains from two fields, i.e. Njord and Åsgard. The chain from Njord was

tested at a mean load of 13.5% MBL (Minimum Breaking Load, hereafter denoted as MBL) with significant interlink wear, while the chain from Åsgard was tested at a mean load of 16% MBL with pits and a rough surface due to corrosion. Prior to the tests, it was assumed that fatigue capacity of the used chains would be somewhat reduced due to the surface degradation. However, it was found that the fatigue lives of both chains were greater than predictions using the traditional SN approach. Gabrielsen et al. [90] [96] [97] also performed fatigue tests on 57 used chains at mean loads ranging from 6.4% to 18% of the minimum breaking load. The 57 used chains were retrieved from offshore fields after 5-20 years in operation and had surface degradation features due to interlink wear and corrosion. However, they found that the fatigue capacity of those used chains was also generally higher than predictions using the SN curve.

In other cases, Fernandez et al. [44] performed fatigue tests on 19 chains of R4 and R5 steel grade at mean loads ranging from 7% MBL to 15% MBL. The results also showed that the fatigue capacity of the tested chains was above the fatigue capacity predicted using the SN curve. These experimental fatigue studies [44] [90] [96] [97] [111] all agree that the used chains have an apparent fatigue capacity above the predictions using the standard SN curve. This may be due to the low mean loads used during the fatigue tests, which were generally less than the mean load of 20% MBL at which the SN curves were derived. This indicates that the mean load can have significant effects on fatigue life, more so than the surface degradation seen in those cases.

Wang et al. [82] and Ma et al. [95] performed fatigue tests at a mean load of 20% MBL on six used chain samples with evident surface degradation retrieved from six floating production facilities in the West Africa and the North Sea after 9-19 years in operation. The results of the fatigue tests showed that the six used chains failed after lifetimes in the ranges of 100,000 to 300,000, which was significantly less than lifetimes predicted (i.e. 600,000 to 1000,000) for new chains using the standard SN curve approach. The reduced fatigue life here, where the fatigue tests were run at a mean load of 20% MBL as used to derive the SN curves, clearly shows the detrimental effect of corrosion, when there is

no mean load effect. This serves to reinforce the importance of taking account of mean load effects in predicting mooring chain fatigue lives.

2.6.6 Quantification of mean load effects of mooring chains

Several studies have quantified the mean load effect at different load amplitudes in mooring chains, as summarised in Table 3. Gabrielsen et al. [99] found that fatigue life decreased by a factor of 5-10 due to an increase in mean load from 6.4% MBL to 20% MBL. Zhang et al. [94] found that fatigue life decreased by a factor of 4 due to an increase in mean load from 10% MBL to 20% MBL. Perez et al. [43] found a decrease in fatigue life by factors of 1.5-2.6 due to an increase in mean load from 10% MBL to 20% MBL based on the Dang Van fatigue criterion.

Table 3: The quantification of the mean load effect found in the literature

Ref.	Life Reduction Factor	Amplitude (% MBL)	Mean load range (% MBL)
[81]	2.3	8	16 – 20
[81]	1.44	10	16 – 20
[99]*	5-10	~5	6.4 – 20
[94]*	4	8	10 – 20
[43]	1.5-2.6	8	10 – 20

*Experimental study

Zarandi and Skallerud [81] found that the fatigue crack initiation life of a corroded mooring chain decreased by a factor of 2.3 and 1.44 due to an increase in mean load from 16% MBL to 20% MBL at load amplitudes of 8% MBL and 10% MBL, respectively, based on finite element studies. Zarandi and Skallerud [81] claimed that the mean load has a more significant effect than the load amplitude on the fatigue crack initiation life of chains; however, this was only based on limited studies, i.e. two mean loads (16% MBL and 20% MBL) and two load amplitudes (8% MBL and 10% MBL). In addition, they [81] assessed chains

with corrosion damage on the chain's surface, thus they did not consider the mean load effect in isolation, somewhat complicating the assessment.

It can be seen from the current literature [43] [81] [94] [99], that mean load effects have only been studied with mean loads equal to or below 20% MBL, while many mooring chains may have failed under harsh sea-environments or storms that might induce mean loads above 20% MBL. This indicates the need to investigate the detrimental effects of mean load levels over a broader range below and beyond 20% MBL. The range of mean load levels assessed should be based on what mooring chains experience in service to quantify the extent of the mean load's impact on the fatigue performance of mooring chains in the field.

2.7 Fatigue of steel structures

2.7.1 Critical plane based multiaxial fatigue criteria

In order to find a fatigue approach capable of considering the mean load and cyclic plasticity effects on the fatigue damage of mooring chains under low-cycle fatigue, this section reviews available fatigue methods in the literature that are relevant to the objectives of this research. The effect of mean stress depends on the state of stress whether it is tensile or compression. A compressive mean stress (σ_m<0) improves the fatigue performance, while a tensile mean stress (σ_m>0) decreases the fatigue performance [13].

In order to consider the mean stress effects from fatigue tests, mean stress corrections are commonly used to adjust fatigue test results with regards to mean tension. The well-known mean stress corrections are Gerber [112], Goodman [113] and Soderberg [114], where the mean stress effects depend on the ratio of the mean stress (σ_m) to the tensile strength (σ_{TS}) or to the yield strength (σ_y). It is presented in Equations (7)-(9) for Soderberg, modified Goodman and Gerber, respectively, where $\left.\frac{\Delta\sigma}{2}\right|_{\sigma_m=0}$ is the stress amplitude for fully reversed loading when mean stress is zero,

$$\frac{\Delta\sigma}{2} = \frac{\Delta\sigma}{2}\Big|_{\sigma_m=0}\left(1-\frac{\sigma_m}{\sigma_y}\right), \tag{7}$$

$$\frac{\Delta\sigma}{2} = \frac{\Delta\sigma}{2}\Big|_{\sigma_m=0}\left(1-\frac{\sigma_m}{\sigma_{TS}}\right), \tag{8}$$

$$\frac{\Delta\sigma}{2} = \frac{\Delta\sigma}{2}\Big|_{\sigma_m=0}\left(1-\left(\frac{\sigma_m}{\sigma_y}\right)^2\right). \tag{9}$$

However, these correction functions are issued from uniaxial fatigue tests. When the stress tensors are multiaxial and the mean stresses from mean load are superimposed with residual stresses, the quantification of the influence of mean stresses is not as straightforward as in the uniaxial case [43]. In addition, the correction functions are generally applicable to cases of long fatigue lives for high-cycle fatigue loading cycles as they are stress-based approaches.

For low-cycle fatigue approach, a strain-based approach based multiaxial fatigue criteria are more appropriate to give an accurate estimation of mean stress effect in both high-cycle fatigue and low cycle fatigue regimes [13] [115]. In engineering components, the stresses and strains at a fatigue hotspot are multiaxial, generated by complex loading conditions, residual stresses, material nonlinearities and geometric nonlinearities [86] [116]. During multiaxial fatigue cycling of a component, the critical plane, where fatigue damage and cracking occurs, is considered to be the plane on which the tensile normal stress or the shear stress is at maximum, and this remains fixed relative to the axis of the applied of loading cycles [13].

Multiaxial fatigue approaches based on the critical plane approach have proven successful in capturing both effects of mean load and material degradation due to cyclic plasticity in a wide range of applications and materials [117]–[121]. This is because the critical plane approaches can reflect the physical nature of the damage process on a particular plane, the most damaged plane due to fatigue [120]. This multiaxial fatigue approach pertains to the total fatigue life of a nominally smooth-surface under a defect-free assumption. This assumption can be a reasonable approximation as the surface of mooring chains is inspected

via non-destructive examination to ensure that there are no visible surface defects (e.g. notches, sharp edges, pre-existing cracks) prior to deployment.

Over the past few decades, several approaches based on the critical plane have been developed, e.g. Sines [122], Crossland [123], Dang Van [124], the Findley [125] and Matake [126]. Sines [122] proposed a criterion based on the Von Mises stress and the hydrostatic pressure. Afterwards, Crossland [123] modified the Sines criterion by taking into account the mean normal stress effect using the maximum hydrostatic stress. Further, the Dang Van approach [124] combines the largest allowable shearing and hydrostatic stresses, with an assumed elastic shakedown behaviour [127]. Findley [125] proposed a damage parameter based on the linear combination of the shear stress amplitude and maximum normal stress acting on the critical plane.

Matake [126] proposed a fatigue criterion based on the critical plane approach, which uses a damage parameter based on the linear combination of the shear stress amplitude and maximum normal stress acting on the critical plane. However, the above-mentioned multiaxial fatigue criteria (the Sines, the Crossland, the Dang Van, the Findley and the Matake) are simply stress-based. Therefore, they are only appropriate for the high-cycle fatigue regime where plastic deformation is relatively minor or negligible. Although the stress-based approaches can, in some cases, effectively predict the low-cycle fatigue behaviour [128]–[131], they cannot reflect the constitutive behaviour of the material when the fatigue response changes from the high-cycle to low-cycle fatigue regime [120] [130] [131]. Therefore, the stress-life approach may underestimate the proportion of low-cycle fatigue in mooring line loading.

The Smith-Watson-Topper critical plane criterion [132] is considered one of the most robust fatigue methods among these multiaxial fatigue criteria for accurately capturing the mean load and cyclic plasticity effects in both high-cycle and low-cycle fatigue regimes, where fatigue damage is assessed directly in terms of local strains and stresses at the fatigue hotspot [86] [117] [133]. The Smith-Watson-Topper critical plane criteria is derived from the combination of Basquin's relation and strain-life relation, as shown in Equation (10) and Equation (11), respectively,

$$\sigma_a = \sigma_f'(2N_f)^b, \qquad (10)$$

$$\frac{\Delta\varepsilon}{2} = \frac{\sigma_f'}{E}(2N_f)^b + \varepsilon_f'^{(2N_f)^c}, \qquad (11)$$

where E is Young's modulus, $2N_f$ is the number of stress reversals to failure, N_f is the number of cycles to failure, σ_a is the stress amplitude, $\Delta\varepsilon$ is strain amplitude, σ_f' is fatigue strength coefficient, b is the fatigue strength exponent, ε_f' is fatigue ductility coefficient, and c is the fatigue ductility exponent [13]. Smith et al. [132] and Socie et al. [134] used Basquin's relation for the maximum stress and multiplied it by the strain-life equation to obtain the *SWT* damage parameter, $\sigma_{n,max}\frac{\Delta\varepsilon_n}{2}$, for a critical plane multiaxial fatigue criterion to consider both cyclic plastic degradation and mean stress effects in high-cycle and low-cycle fatigue as defined by Equation (12),

$$\sigma_{n,max}\frac{\Delta\varepsilon_n}{2} = \frac{(\sigma_f')^2}{E}(2N_f)^{2b} + \sigma_f'\varepsilon_f'^{(2N_f)^{b+c}}, \qquad (12)$$

where $\sigma_{n,max}$ is the maximum normal stress on the critical plane and $\Delta\varepsilon_n$ is the normal strain range perpendicular to the critical plane during one stabilised cycle. The *SWT* damage parameter, $\sigma_{n,max}\frac{\Delta\varepsilon_n}{2}$, represents the real physical properties of the stress-strain function at the critical fatigue location, and has been demonstrated to govern the fatigue of metal structures [132] [134]. The Smith-Watson-Topper (SWT) critical plane criterion is best suited for mode I cracks that are developed by high tensile stresses [132]. This makes the method is suitable for predicting the fatigue life of mooring chains since the high tensile stresses on the chain surface at the fatigue hotspots under tension loading were observed in both experiments [94] and in FE models [26]–[29].

You et al. [117] found that the Smith-Watson-Topper criteria predicted fatigue lives accurately for low-cycle and high-cycle fatigue tests of notched and unnotched specimens subjected to multiaxial residual stresses due to shot peening. Further, several fatigue studies [117], [135]–[143] found that the Smith-Watson-Topper criteria successfully provides acceptable agreement with experiments for multiaxial fatigue problems in a broad range of loading conditions which consider both mean stress and cyclic plasticity effects. As the

application of multiaxial fatigue criteria relies on the prediction of representative stress-strain states in the structural components, an appropriate material model is required to obtain the representative stress-strain response under progressive fatigue loading in service. The following sections will review the material response and material models suitable for use in mooring chain analysis.

2.7.2 Material response under fatigue loading

When a material is subjected to cyclic stresses smaller than the elastic limit, the material is under elastic shakedown, where the stress-strain response is stabilised. However, when a material is subjected to cyclic stresses higher than the elastic limit, the material may harden or soften due to its cyclic plasticity response as plastic strains continue to accumulate until the stress-strain response becomes stabilised or a newly achieved elastic shakedown is reached, depending on the material mechanical properties and initial state [13]. Cyclic plasticity parameters are commonly used to describe the evolving stress-strain response, where they can be derived from a strain-controlled test with a constant strain amplitude [144]. Figure 14 illustrates typical cyclic hardening and softening behaviours influencing the stress range at a constant strain amplitude during a strain-controlled test [144].

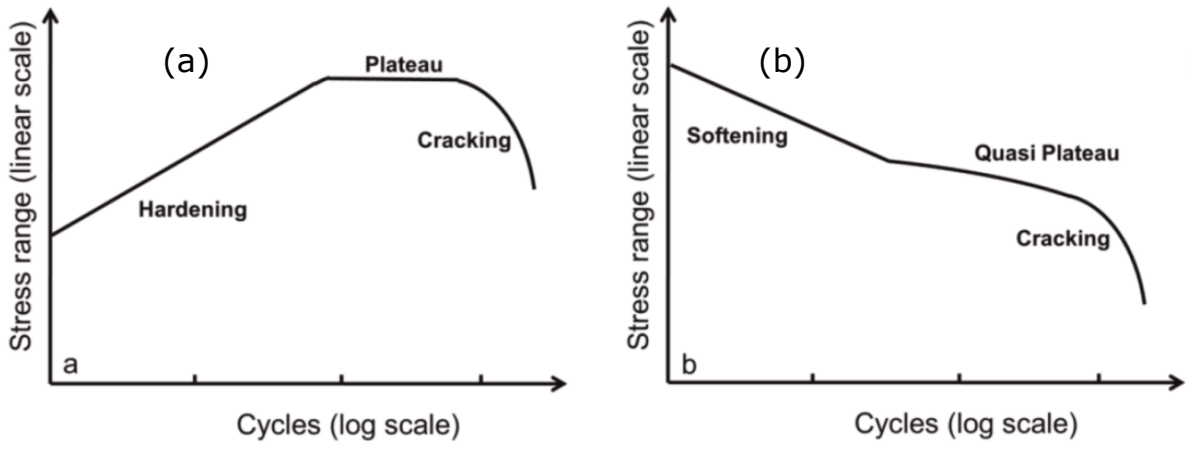

Figure 14: Illustrations of cyclic plasticity effect on a material: (a) a cyclically hardening material and (b) a cyclically softening material [144].

Cyclic hardening exhibits an increase in stress range with increasing number of cycles before reaching saturation in the plateau. In contrast, cyclic softening

induces a reduction of the stress range with increasing number of cycles; the reduction rate considerably slows down in the quasi-plateau.

An appropriate cyclic material model is required to simulate the hardening/softening behaviour under fatigue loading [145]. Several cyclic material models have been developed to predict the cyclic response of materials using the evolution of the yield surface with plastic increments, including isotropic and kinematic hardening components, as illustrated in Figure 15(a) and Figure 15(b) [146]. The isotropic component is a uniform expansion of the yield surface in stress space during plastic loading. It has been found that the use of an isotropic hardening model alone may lead to poor accuracy in terms of elastoplastic local response [146]. This is because the isotropic hardening models cannot include the Bauschinger effect. The Bauschinger effect refers to the experimental result that reverse yielding occurs at lower stress when the loading direction is reversed than for continuous forward deformation [117]. This means that there is a kinematic shift in the position of the yield surface, and so a kinematic hardening component is required to capture this effect [13] [86].

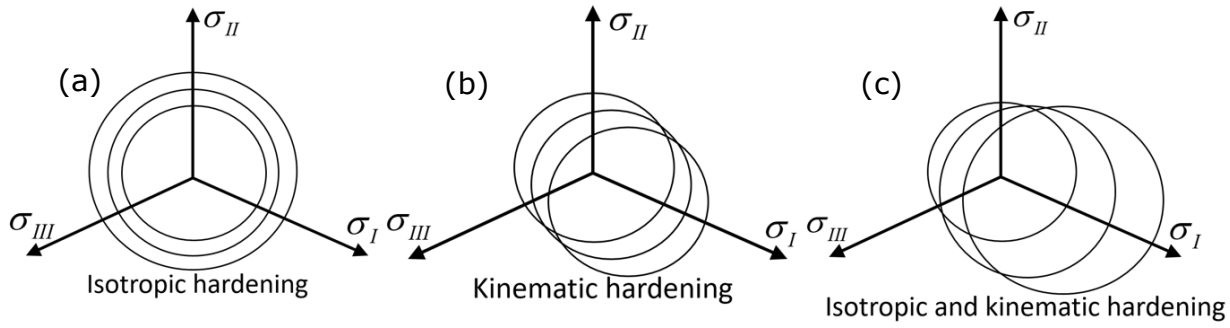

Figure 15: Evolution of yield surface in the principal stress space: (a) isotropic hardening (b) kinematic hardening (c) combination of both hardening [146].

To address this issue, Prager [147] proposed a linear kinematic hardening model, capable of capturing the Bauschinger effect. However, Prager's hardening rule [147] fails to consider the accumulation of plastic strain, also known as a ratcheting response, in the presence of a mean stress effect due to its constant plastic hardening modulus [148]. Further, an Armstrong-Frederic hardening rule was proposed by adding a nonlinear term to Prager's hardening rule, capable of considering the plastic strain path observed in experiments due

to the kinematic hardening for the forward and reverse parts in loading cycles [149].

Further, the idea of describing the evolution of kinematic hardening variables in terms of nonlinear differential equations from the initial work of Armstrong and Frederick has been developed by Chaboche et al. [150] with a combined nonlinear isotropic-kinematic hardening model to improve the ratcheting prediction. This combined constitutive material model is capable of considering the Bauschinger effect and the smooth elastic-plastic transition as well as the isotropic hardening effect, as illustrated in Figure 15(c) [150] [151]. Giovanni et al. [146] and You et al. [117] also confirmed that the use of the Chaboche material model in FE simulations was capable of providing a good agreement with low-cycle fatigue tests.

2.7.3 Material models

Table 4 outlines a number of different material models used for fatigue analysis of mooring chains in the literature: a bilinear material model, a Ramberg-Osgood material model and a Chaboche material model. In the bilinear material model, the work hardening is assumed to increase linearly with plastic strain (i.e. a plastic modulus is assumed) until the maximum stress is reached, when perfectly plastic behaviour is assumed, without considering any material cyclic softening under progressive loading cycles. The Ramberg-Osgood material model is basically similar to the bilinear material model, except that the work hardening response increases nonlinearly with plastic strain until the maximum stress is reached, when again perfectly plastic behaviour is assumed.

Table 4: Different material models used in the literature for fatigue analysis of mooring chains.

	Bilinear material model	**Ramberg-Osgood material model**	**Cyclic material model**
Ref.	[25] [27] [28] [29] [42] [69] [70] [71] [72]	[73] [74] [78] [82] [83] [152]	[24] [35] [43] [75] [81] [153]

The first two material models are derived from tensile test data, which are representative of the monotonic mechanical properties assuming isotropic hardening behaviour under elastic-plastic response, while the cyclic material model is derived from low-cycle fatigue tests, which is representative of cyclic mechanical properties. The cyclic material model is a Chaboche material model, capable of considering the evolution of the yield surface under plastic strain hardening/softening, including the isotropic and kinematic hardening components during reversed loading cycles, as discussed in the previous section.

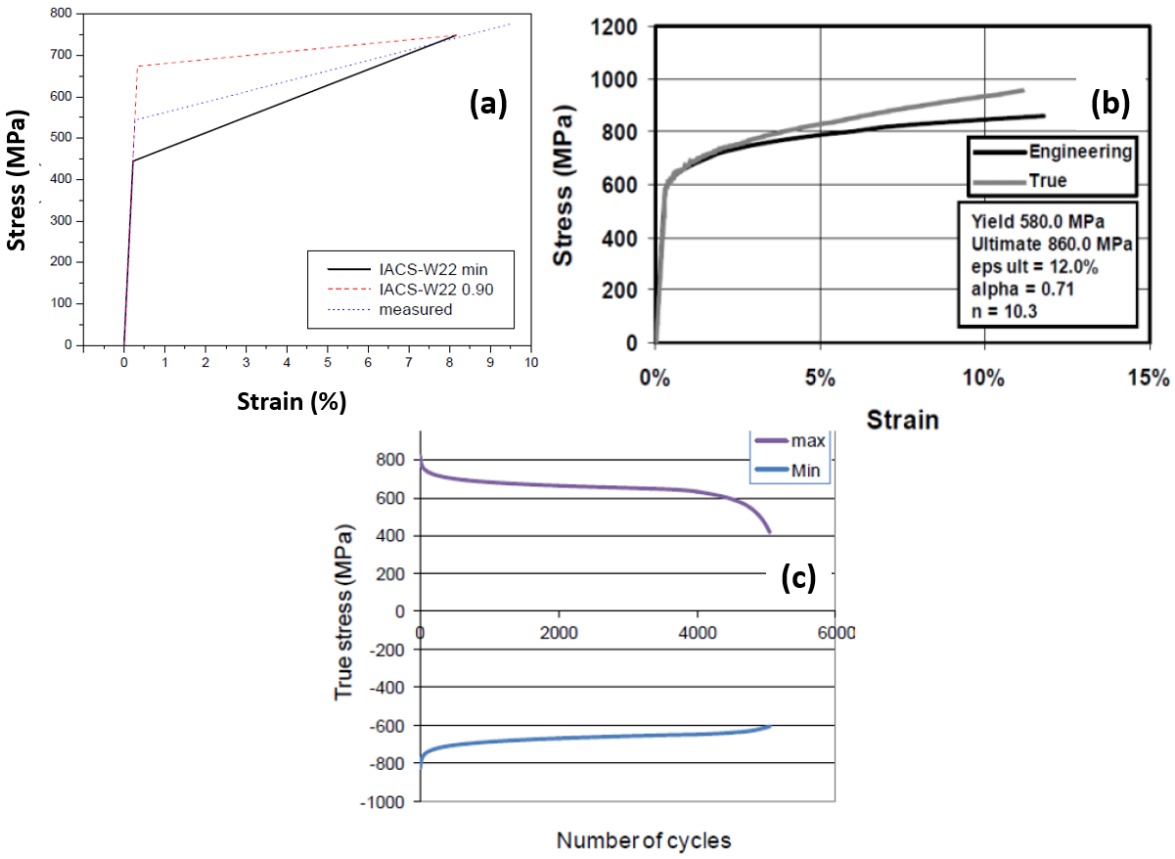

Figure 16: Illustrations of each material model: (a) the bilinear material model under monotonic loading, showing the bilinear stress-strain relationship [28] (b) the Ramberg-Osgood material model under monotonic loading, showing the stress-strain curves [73] (c) the cyclic material model under cyclic loading, showing the softening evolution of the maximum and minimum values of the peak stresses with the number of cycles [75].

Figure 16 illustrates the responses of each material model taken from the literature for a bilinear material model, a Ramberg-Osgood material model and

a cyclic material model. The traditional SN approach does not make use of these different material models, and it is still unclear how such materials response assumptions will affect the predicted fatigue of mooring chains. A parametric study reviewing the effect of different material models is required to determine their differences in modelling representative hotspot stresses and strains that will be important for an improved fatigue assessment of mooring chains.

2.8 Summary from the literature

Mooring chain failures are occurring significantly earlier than their design lives when operating in the harsh sea environment, as reviewed in section 2.3. Fatigue failure is the most significant cause of these premature failures. In the mooring line literature, many published papers [50], [51], [60]–[68], [52]–[59] have investigated the mooring line loading predictions to work out why mooring lines are failing, using the traditional SN approach to assess the fatigue life. However, many mooring chain failures are still occurring early in their expected fatigue lives in service, requiring further investigation as to why those fatigue predictions from the traditional SN approach are non-conservative.

The classification rules [7] [18] traditionally prescribe a simplified fatigue analysis (traditional SN approach) assuming the range of tension or nominal stress controls the fatigue life of mooring chains, which lacks an explicit consideration of the material's cyclic stress-strain evolutions at the fatigue hotspot when determining the fatigue response. The current fatigue design approach does not consider the mean load and the cyclic plasticity effects which govern the low-cycle fatigue behaviour in mooring line loading, as reviewed in section 2.6.3. The observed early fatigue failures of mooring chains indicate that the mooring chains are likely to be experiencing a higher proportion of low-cycle fatigue loading than currently assumed. This is because the traditional SN approach does not consider those effects when determining fatigue damage under low-cycle fatigue loading, and this is proposed to be a contributing factor for the current non-conservative fatigue assessments of mooring chains.

Table 5: Summary of fatigue studies for mooring chains in the literature.

Fatigue assessment methods		**Structure**		**Material**	
		Intact	**Damaged**	**Intact**	**Damaged**
Fracture mechanics approach	Pure tension	[70] [71] [72] [79] [107]* [108] [110]	[108]* [109]* [154]	[105]* [106]* [154]	[105]* [106]*
	Tension+ bending	[69]	[69]	N/A	N/A
	Tension+ torsion			N/A	N/A
Total life approach, stress-life based approach (High-cycle Fatigue prediction)	Pure Tension	[23] [24] [25] [26] [27] [28] [29] [30]* [31]* [32]* [33]* [34]* [42] [43] [44]* [84] [94]* [93]* [99]* [107]* [108]* [155]* [156] [157] [158]*	[44]* [81] [82] [83]* [90]* [94] [95]* [96]* [97]* [108]* [109] [111]* [155]* [159]* [160] [161]* [162] [163] [164]* [165]	[105]* [106]* [107]* [166]* [167]*	[105]* [106]* [108]* [159]* [166]* [168]*
	Tension+ bending	[8]* [37]* [69] [74] [75] [152] [169] [170]*[171] [172] [173]* [174]* [175]* [176]	[8]* [37]* [170]* [177]* [178]* [173]*	N/A	N/A
	Tension+ torsion	[41]* [78] [153] [179]* [180] [181]	[96]* [153]	N/A	N/A
Total life approach, strain-life based approach, (Low-cycle fatigue prediction)	Pure Tension		[35] [81]	[75]* [81]*	
	Tension+ bending			N/A	N/A
	Tension+ torsion			N/A	N/A

*: Experimental study

To summarise this literature review, Table 5 outlines the experimental and numerical studies for mooring chain fatigue assessment in different loading modes, i.e. tension, bending and torsion, from the literature, where "intact" refers to the new condition and "damaged" refers to the used condition with an

altered surface due to corrosion or wear. The "structure" term refers to the full-scale chain, while "material" term refers to the small specimens of a mooring chain's material. The shaded areas in Table 5 highlight the areas that remain uninvestigated. In terms of bending response, an improved understanding of the bending fatigue phenomena in mooring chains is now available in a significant number of studies [37], [69], [172], [173], [177], [178], [73]–[75], [152], [153], [169]–[171]. Based on these experimental and numerical studies, some measures to prevent bending occurring in chains are proposed. In terms of torsion response, several studies [41] [78] [153] [179]–[181] have been reported based on experimental studies and numerical models of fatigue, showing that torsion stress states have negligible effects on the fatigue capacity of mooring chains.

Generally, both fracture mechanics and total life approaches have been applied to predict the fatigue life of mooring chains. Most published studies of total life approaches are based on a stress-life based approach for high-cycle fatigue analysis. Although in some cases stress-life based approaches can predict low-cycle fatigue behaviour [128]–[131], they cannot reflect the constitutive behaviour of the material when the fatigue response changes from the high-cycle to low-cycle fatigue regime [120] [130] [131]. Therefore, the use of a stress-life based approach may underestimate the proportion of low-cycle fatigue in mooring line loading and its effects.

In terms of low-cycle fatigue analysis, low-cycle fatigue tests of small specimens cut from a mooring chain have been performed to derive relevant cyclic plasticity parameters in the literature [75] [81]. In structural applications of mooring chains, the number of studies investigating low-cycle fatigue behaviour in mooring lines is limited, with only Zarandi and Skallerud [35] [81] using strain-life based approaches to find the fatigue crack initiation life of corroded mooring chains. However, this was limited to deterministic cyclic loading, and assessing how fatigue damage accumulation changes from the high-cycle to low-cycle fatigue regime in terms of the stochastic mooring line loading in service was not investigated. Additionally, the addition of corrosion damage in these cases means it is difficult to isolate the effects of the low-cycle fatigue loading case on the mooring line failures.

The novel contribution of this research is then to develop a fatigue approach, capable of considering the effects of mean load and cyclic plasticity evolution on the accumulation of fatigue damage, which governs the low-cycle fatigue of mooring chains under stochastic tension loading. This will be achieved by assessing the local stress-strain evolution at the fatigue hotspot in the mooring chains, to determine the fatigue response, including the proof load-induced effects (i.e. strain hardening and residual stresses), mean load effects and material constitutive responses in a mooring line fatigue simulation. This will contribute to determining the importance of low-cycle fatigue in determining mooring line failures. The analysis excludes geometric adjustments due to other damage mechanisms (e.g. corrosion pitting, wear), allowing for the isolation of the low-cycle fatigue-induced effects on mooring chain analysis in intact conditions.

Among the total life approaches (as discussed in section 2.7.1), the stress-strain-based Smith-Watson-Topper approach using a critical plane multiaxial fatigue criterion is selected. This is because it has been demonstrated to accurately capture mean load and cyclic plasticity effects, where fatigue damage is assessed directly in terms of local strains and stresses at the critical fatigue location in both high-cycle and low-cycle fatigue regimes [117]–[121], [133] [182]. The critical plane approach will be developed for mooring chains based on the multiaxial stress-strain conditions at the hotspot and this will be correlated with the fatigue life derived from tests taken from the literature. The fatigue damage predictions of the critical plane approach will be compared with those of the traditional SN approach under stochastic tension loading to investigate how fatigue damage prediction changes with a more accurate representation of the low-cycle fatigue regime, using the critical plane approach.

As this study simulates fatigue in finite element analyses, an appropriate finite element model for predicting the representative stresses and strains required by the critical plane approach is essential. However, there are different finite element models available in the literature for predicting the stresses and strains in mooring chains, which adopted different modelling parameters (as discussed in section 2.5), and there are no evaluations of which model is appropriate. Therefore, this study will also benchmark the different types of finite element models available in the literature to understand how well each model works. The

most appropriate finite element model will be used to predict the multiaxial stress-strain response for the critical plane fatigue analysis proposed for this research.

Chapter 3: Methodology

This chapter describes the methodology, which is developed to study low-cycle fatigue of mooring chains and to evaluate if it could help to explain the short lives of mooring chains. The simulation of fatigue experienced by mooring chains in service is performed to predict the fatigue damage under low-cycle fatigue conditions. The relationship between sections in this thesis are illustrated in Figure 17.

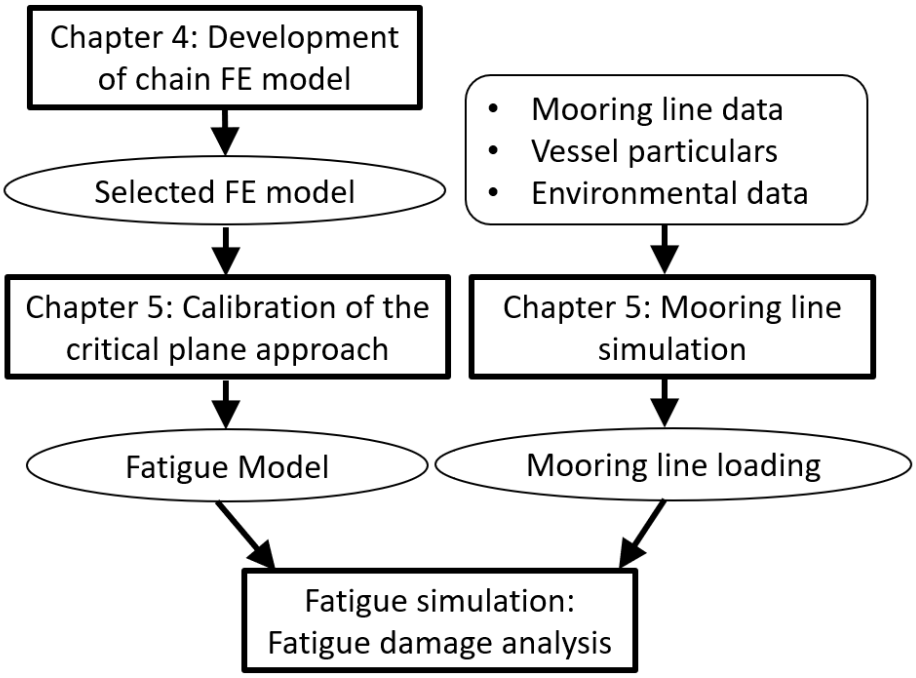

Figure 17: Flowchart of the model developed to study low-cycle fatigue behaviour of mooring chains in the present study.

3.1 Development of chain FE model

The FE simulation was performed using ABAQUS version 6.14 and automated using a Python script. As this study simulates fatigue in finite element analyses, an appropriate numerical model for predicting the representative stress-strain parameters that affect low-cycle fatigue is essential. However, there are a number of different finite element models of mooring chains reported in the literature, as shown in the literature review, chapter 2. Those FE models use different modelling details, e.g. element types, interlink loading methods, and finite element solvers (implicit/explicit), which could lead to different predictions

of stresses and strains in mooring chains. However, there are no assessments of which model is most appropriate to predict representative stresses and strains in the literature.

Therefore, chapter 4 provides a comparison between different types of FE models available in the literature to select the most appropriate FE model for modelling low-cycle fatigue in this research study. To allow this comparison, the different FE models from the literature are replicated using the most similar meshing and modelling techniques available in ABAQUS to match the published responses. One of the papers for each type of FE model is selected as the reference for the verification to provide the published response. The replicated FE models are then compared to experiments, provided by Tipton and Shoup [31], to determine their accuracy. Afterwards, the different FE models are then benchmarked to check their different performances in predicting the stresses and strains that will be important to low-cycle fatigue modelling.

3.2 Calibration of the critical plane approach

Chapter 5 provides the calibration of the Smith-Watson-Topper critical plane approach to develop its fatigue model for mooring chains. Figure 18 shows the methodology, where the critical plane approach is calibrated against fatigue life data obtained from fatigue tests in FE simulations. Material models extracted from experiments taken from the literature [75] [81] are adopted to the chain's structural model in ABAQUS. The calibration simulates the fatigue test which comprises the proof load application and then cyclic loads. During a stabilised cyclic load, the multiaxial stress-strain state at the fatigue hotspots in mooring chains for different planes are extracted to determine the critical plane, where the plane with the highest damage parameter of Smith-Watson-Topper (SWT) is defined as the critical plane.

Subsequently, the SWT damage parameters for the determined critical plane at the critical fatigue hotspot are correlated with the number of cycles to failure from the corresponding fatigue tests under different load amplitudes based on the mooring chain service lives. Further, a fitted curve is generated to interpolate SWT damage parameters across a range of the number of cycles to

failure during fatigue loading. This is performed for each considered material model, allowing the fatigue life to be predicted by a fitted curve for each particular material model.

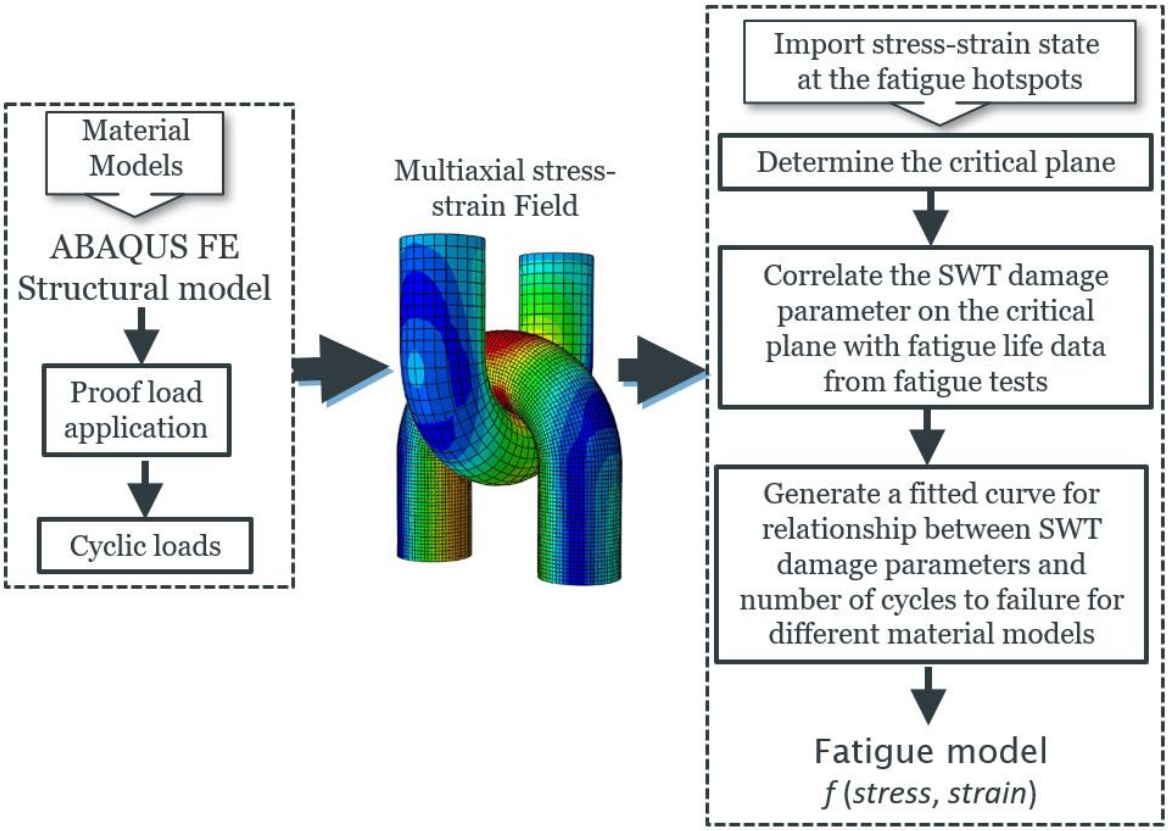

Figure 18: The calibration methodology of the critical plane approach.

The fatigue model of the critical plane approach is then developed by taking all of the local stress-strain evolution into account when determining the fatigue response, including the proof load-induced effects, i.e. strain hardening and residual stresses, mean load effects and material model nonlinearities. The developed fatigue model is then compared with the traditional SN approach to investigate how fatigue damage prediction changes with a more accurate representation of the low-cycle fatigue regime using the developed fatigue model. The comparison is performed under stochastic tension loading in order to simulate fatigue experienced by mooring chains in service, where the stochastic tension loading is obtained from a mooring line simulation of an FPSO, as discussed in the following section.

3.3 Mooring line simulation

Chapter 5 also provides the mooring line simulation, which is performed using FLEXCOM version 8.10 [183]. Figure 19 shows an illustration of the modelling work, showing the model of a mooring system with an FPSO in the FLEXCOM at a water depth of 810 m. The mooring line simulations subject a mooring system of an FPSO to offshore environmental forces in specific sea-states, which are adopted from Gao and Moan [184] and Song and Wang [48] as case studies. The mooring system is of an eight-line catenary system with chain-wire rope-chain components, connected to a turret of the FPSO with an angular spread of 45° between each mooring line. The anchor radius from the turret centreline is 700 m, with which the mooring line anchor points are constrained, and each fairlead is attached to the FPSO by means of a hinge at 8 m below the mean water level. The detailed parameters of the mooring line simulations are provided in Chapter 5.

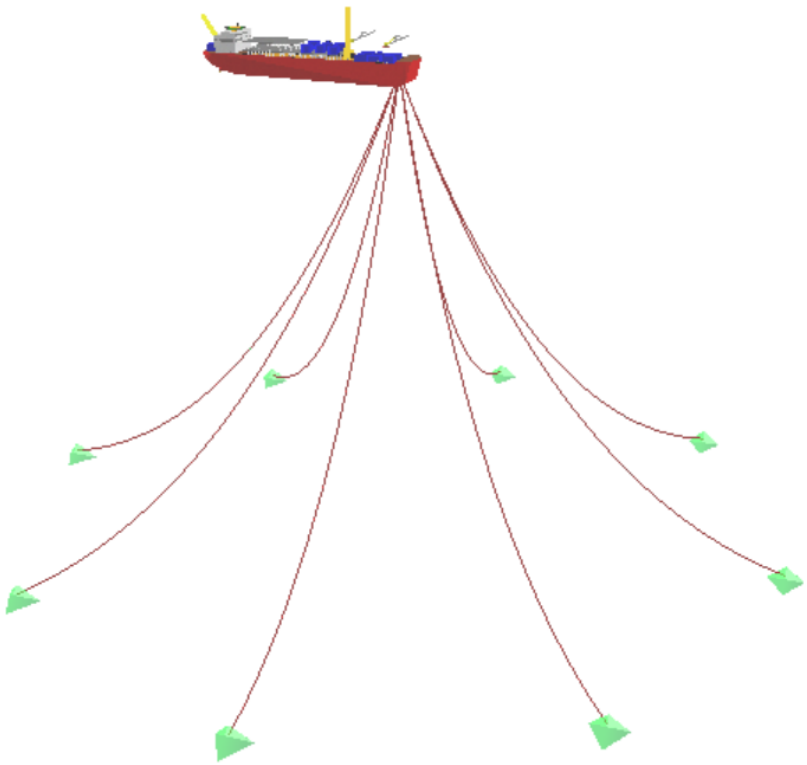

Figure 19: The model of the mooring system connecting an FPSO on the water level to anchor points on the seabed.

Figure 20 shows the methodology of the mooring line simulation, comprising static and dynamic analyses, where the mooring line data and the vessel particulars are adopted from the Flexcom package [183]. The static analysis is performed to establish a static equilibrium configuration of the mooring line at a specific water depth under functional loads, e.g. self-weight, buoyancy, wind, current and pretension. The converged results of the static analysis are used as an initial mooring configuration for the dynamic simulation to provide a gentle start from a static position to complete dynamic motions [7] [18]. The dynamic analysis subjects the mooring system of an FPSO to the wave loading in a time-domain simulation over a specific period. Both wave-frequency and low-frequency tension variations are included in the resultant tension spectrum through the coupled dynamic analysis between the mooring system and the FPSO motions.

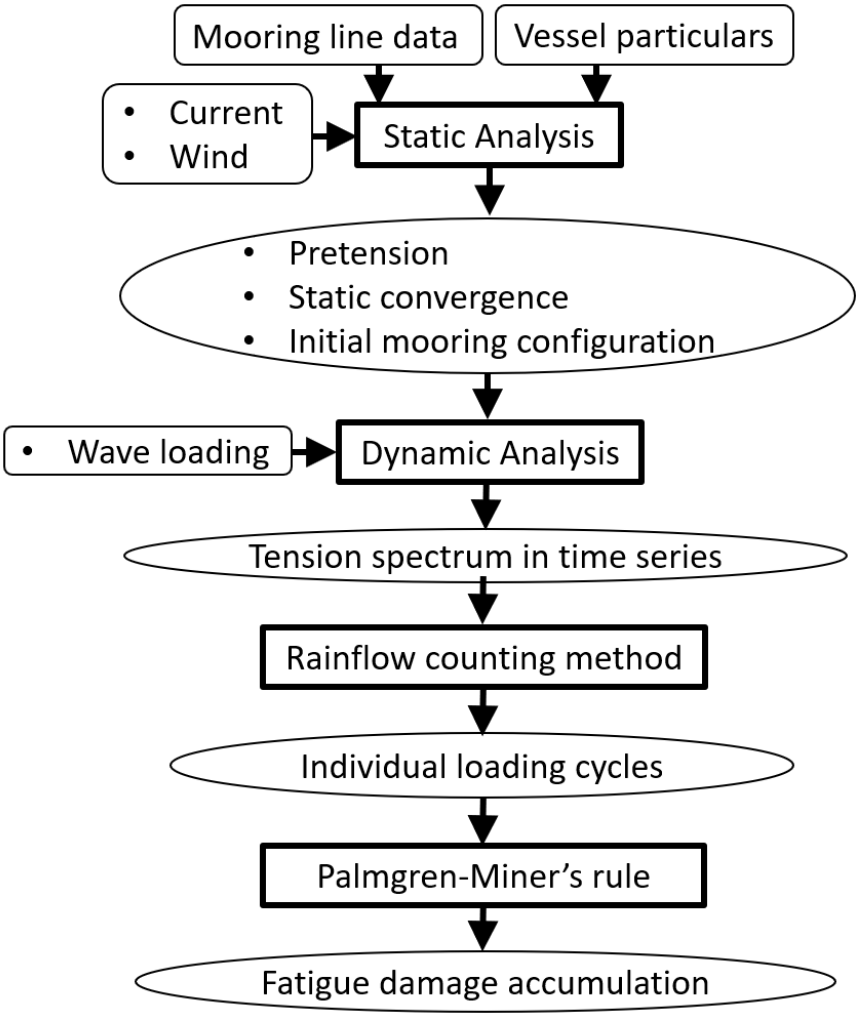

Figure 20: Mooring line simulation methodology.

To investigate the mean load and cyclic plasticity effects, the tension spectrum of the top chain in the line with the greatest load is analysed for fatigue analysis, as suggested by API-RP-2SK [18]. The rainflow counting method [47] is used to identify individual loading cycles with the associated mean loads, load amplitudes and the frequencies from the tension spectrum. The fatigue damage from each individual loading cycle is then accumulated using the Palmgren-Miner's rule [185]. This is then followed by a comparison between the critical plane approach and the traditional SN approach to investigate their differences in fatigue damage predictions.

Chapter 4: Selection of appropriate numerical models for modelling stresses in mooring chains

To simulate the fatigue response under low-cycle fatigue condition in finite element analyses, an appropriate finite element model of a chain is essential to obtain representative stresses and strains in mooring chains. Therefore, the finite element parameters for modelling mooring chains, e.g. interlink loading method, element types, finite element solvers, are compared. A comparison between finite element methods available in the literature are detailed and discussed in order to make an appropriate choice of the finite element model of a chain for this study.

Substantial parts of the work presented in this chapter have been published in the following paper:

G. M. Gemilang, P. A. S. Reed and A. J. Sobey, Selection of appropriate numerical models for modelling the stresses in mooring chains, Marine Structures, 2020. [186].

4.1 The criticality of accurate structural modelling in mooring chain failure analysis

Mooring chains are critical components used to maintain the stability and operating location of floating platforms. However, mooring failures have been regularly occurring earlier than their design lives. These failures represent critical accidents with economic and environmental impacts [9] [10]. Industry surveys [1] [5] [12] have found various failure modes reported for mooring chains, e.g. fatigue, corrosion, wear and ultimate strength failure. Each of these failure modes needs associated stresses and strains to be accurately predicted to reduce the number of these failures, especially fatigue failure which is the most significant failure mode. However, although the operating stresses play a major role in determining the failure mechanisms of mooring chains, there are many different finite element models to predict the operating stresses and

strains in mooring chains, varying in the available literature, as also discussed in section 2.5. Table 6 outlines a number of different FE models reported in the literature, showing that the majority of numerical studies use an implicit FE formulation, while there is only one numerical study using the explicit method for mooring chain modelling [77]; although this method obtains a good agreement with experiments. These FE models use different modelling parameters regarding finite element solvers (solution method), material modellings, element types and interlink loading methods.

Table 6: Summary of numerical analyses for mooring chains in the literature.

Solution Method	**Element Type**	**Material modelling**	**Interlink Loading method**	**Reference**
Implicit	Hexahedral-Reduced integration, 20 node brick element	Elastic	Pressure Distribution	[26] [27] [29]*
		Elastoplastic	Pressure Distribution	[26] [27] [28]* [29]
		Elastoplastic	Contact Interaction	[24] [25] [26] [27] [28] [29] [42]* [43] [70] [71] [84] [153] [163]
	Hexahedral-Incompatible Mode Integration, 8 node brick element	Elastoplastic	Contact Interaction	[73] [74]* [75]
Explicit	Hexahedral-Reduced integration, 8 node brick element	Elastoplastic	Contact Interaction	[77]

*: Selected verification papers for the replication

These different modelling parameters may lead to different predictions of stresses and strains in mooring chains. However, there are no evaluations of how each FE model works for predicting representative stresses and strains, making it hard to make an appropriate choice from the literature for this study. Therefore, this chapter benchmarks the different FE models in order to select

the most appropriate finite element model for predicting representative stresses in mooring chains, which will be used for the subsequent low-cycle fatigue assessment in this study.

To allow this comparison, a verification study is performed for each FE model, where the FE models from the literature are replicated, using the most similar meshing and modelling techniques available in ABAQUS. One FE model is selected to represent each distinct model, as indicated in Table 6. These models are then calibrated to match the published responses. These FE models are then compared to experiments [31], to assess their accuracy in a validation study. The chain models are then benchmarked, intact without considering geometric adjustments due to failure mechanisms, to consider the effect of the resultant stress/strain parameters that will be important to low-cycle fatigue analysis to allow a comparison between the different methods.

4.2 Finite element model definition

This section provides the standard finite element definitions that will be used in this chapter. The FE model was constructed in ABAQUS version 6.14 and automated using a Python script. Hexahedral elements were selected over tetrahedral elements since they give superior performance in terms of convergence rate and accuracy of the solution [187]–[189]. The standardised dimension for the chain geometry of a studless chain is used in this study based on IACS standard [20] with a diameter, D, where the total length, L, is equal to $6D$, the total width, W, is $3.35D$ and the radius of the curved section, R, is $0.675D$, as illustrated in Figure 21.

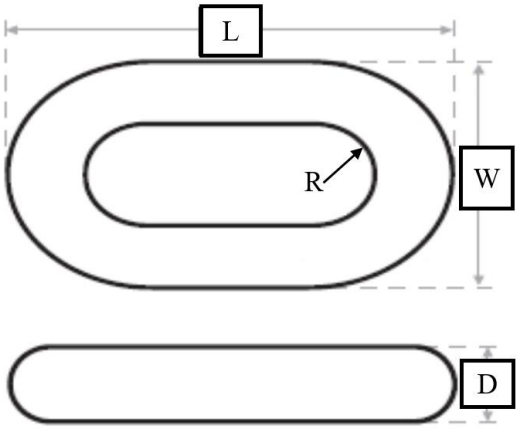

Figure 21: The IACS specification for the design of a studless chain link [20].

The DNV-OS-E302 standard [19] provides the minimum mechanical properties for mooring chain steel grades, depending on the nominal tensile strength of the steels used for manufacture. As this study aims to replicate the response from the published analyses, the same material models used in these analyses are employed for the current simulations. Grades R3 and R4S are used to replicate previous studies with properties specified in the standard, DNV-OS-E302 [19], as shown in Table 7.

Table 7: Minimum mechanical properties for chain materials [19].

Steel grade	**Yield stress (MPa)**	**Tensile strength (MPa)**	**Total elongation (%)**
R3	410	690	17
R4S	700	960	12

The grade R3 material model is used in sections 4.3.2, 4.3.3 and 4.4.2 and is taken from Pacheco et al. [28] [29] and Bjørnsen [42], which also incorporates bilinear isotropic hardening, with an elastic modulus (E) of 210 GPa and a Poisson ratio (v) of 0.29. The strain associated with the tensile strength is adopted as half the total elongation [28]. The grade R4S material model is used in section 4.3.4 and is based on Kim et al. [74], where a Ramberg-Osgood curve is used with an isotropic hardening exponent of 0.597, elastic modulus (E) of 209 GPa and Poisson ratio (v) of 0.3. The engineering material stresses and strains are converted into the true stress and logarithmic strain for input into ABAQUS. Figure 22 shows the true stress-strain diagrams for both grades of steel, R3 and R4S, which are used as the input for ABAQUS. The model also considers geometric nonlinearities to consider large deformation effects.

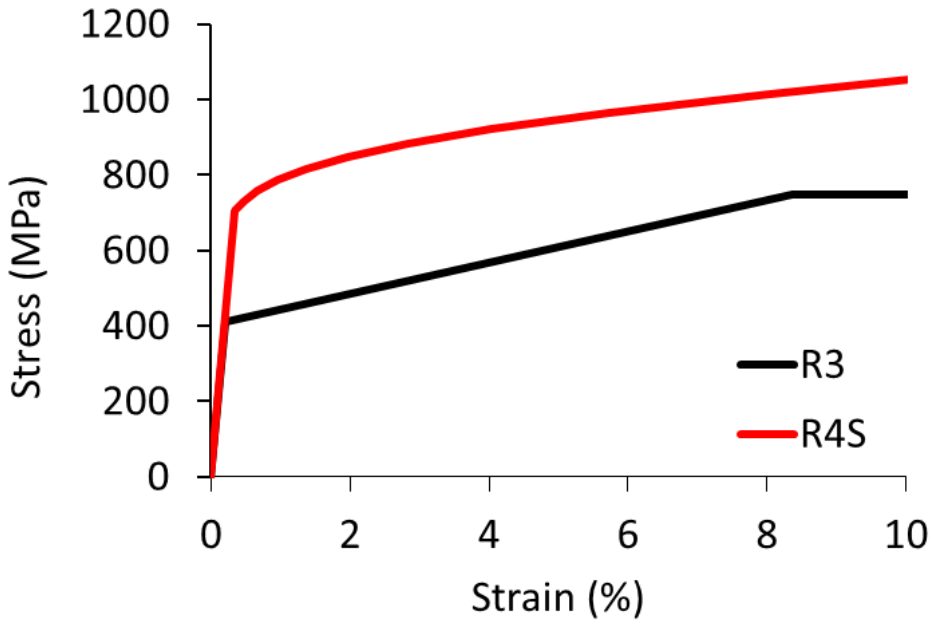

Figure 22: Stress-strain diagrams of R3 and R4S grade steel.

Two types of interlink loading method are investigated in the present study: (i) the pressure distribution method [28] [29], which uses a pressure to replicate the contact force between the mooring links, and (ii) the contact interaction method [42], which is more consistent with the real chain interaction than using the pressure distribution. The pressure distribution method is replicated from Pachecho et al. [28] [29], where the magnitude of the pressure is equivalent to the resultant load in the contact region. The pressure distribution varies linearly from a maximum value at the centre of the interlink contact area to zero at the border. The contact angle of 35° is used to represent the contact area from the axial direction, and the total area over which the pressure is applied is determined by a design parameter, H, as shown in Figure 23. The pressure distribution is found by applying Equation (13) to the ABAQUS analytical-fields,

$$f(x,y) = 0.610865 - \tan^{-1}\left(\frac{x}{y}\right), \tag{13}$$

where $f(x,y)$ is a function of the pressure distribution, 0.610865 is the 35° in radian, and the origin of x and y is located at the centre of the chain's curved part, as indicated in Figure 23.

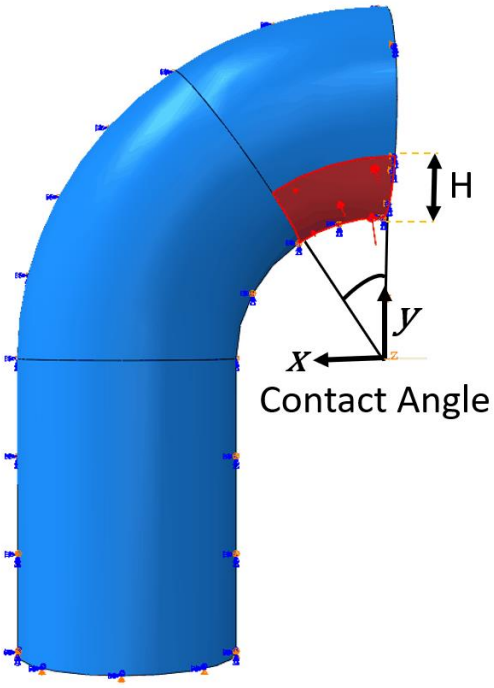

Figure 23: Finite element definition for a model with pressure distribution method.

In the contact interaction method, the contact discretisation is defined as surface-to-surface with a penalty contact constraint, as illustrated in Figure 24. The surface-to-surface discretisation is used, as this is suggested by ABAQUS [187], to provide more accurate stress and pressure results than node-to-surface discretisation. There are two tracking approaches in ABAQUS to consider the relative motion of two interacting surfaces in mechanical contact simulations, i.e. finite-sliding and small-sliding. Finite-sliding assumes no sliding between contacting surfaces, while small-sliding contact assumes that there will be relatively little sliding of one surface along with the other [187]. Finite sliding is considered in this study, as the tension-tension simulation assumes no sliding of one surface along with the other for two contacting chains, with a friction coefficient of 0.7 based on previous studies [28] [29] [42] [74].

The upper chain is represented as the master model, and the lower chain is represented as the slave model, which has a finer mesh as this is where the resultant stresses/strains are extracted for analysis. The bottom surface of the slave model is fixed, while the upper surface of the master model is loaded using a uniformly distributed surface traction acting at the top, as indicated in red in Figure 24.

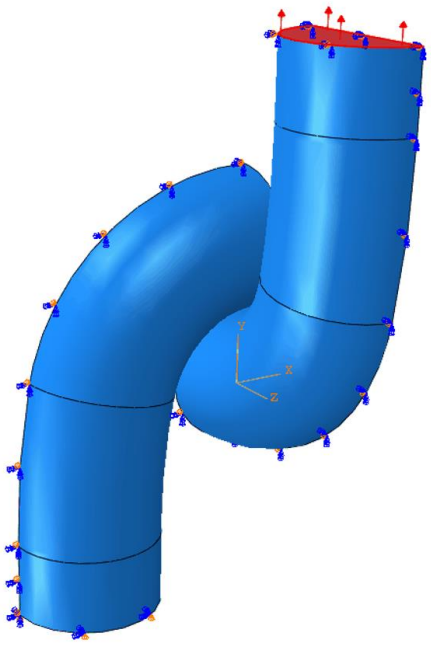

Figure 24: Finite element definition for a model with contact interaction method.

The chain model has three planes of symmetry, and so only an 1/8th of the chain needs to be modelled. The symmetry boundary condition is assigned at the symmetry planes indicated in red in Figure 25 for the models using the pressure distribution method. For the models with contact interaction, the loaded surface at the top of the master model does not have this boundary condition, to allow the load to be applied in the axial direction.

Six degrees of freedom are employed for each node, except for nodes on each of the symmetry planes, which have only three degrees of freedom, corresponding to the number used in the models taken from the literature. The symmetry boundary conditions constrain the displacement of nodes lying on each symmetry plane in the normal direction and the rotation in the other two directions. For example, the bottom surface of the slave model was constrained against displacement in the y-axis and against rotation in the x and z-axes.

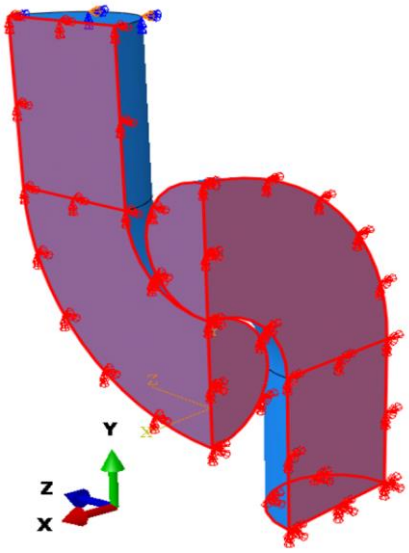

Figure 25: Finite element definition for symmetric boundary conditions in the chain model.

The most probable locations for cracks due to fatigue failure are documented as being at the outer crown and the inner bend, also known as the K_t point [25] [31] [90]. Paths 1, 2 and 3, shown in Figure 26, are selected to represent the key regions in the mooring line where the stresses and strains need to be accurately modelled for fatigue analysis and other failure modes of the mooring chains. The fatigue hotspots are the outer crown, located at the end of paths 1 and 2, and the inner bend (K_t point), located at the start of path-3 [25] [31] [90]. Path-1 represents the stress-strain field on the surface near the contact region. While paths 2 and 3 represent the stress-strain field along the cross-section of the fatigue hotspots.

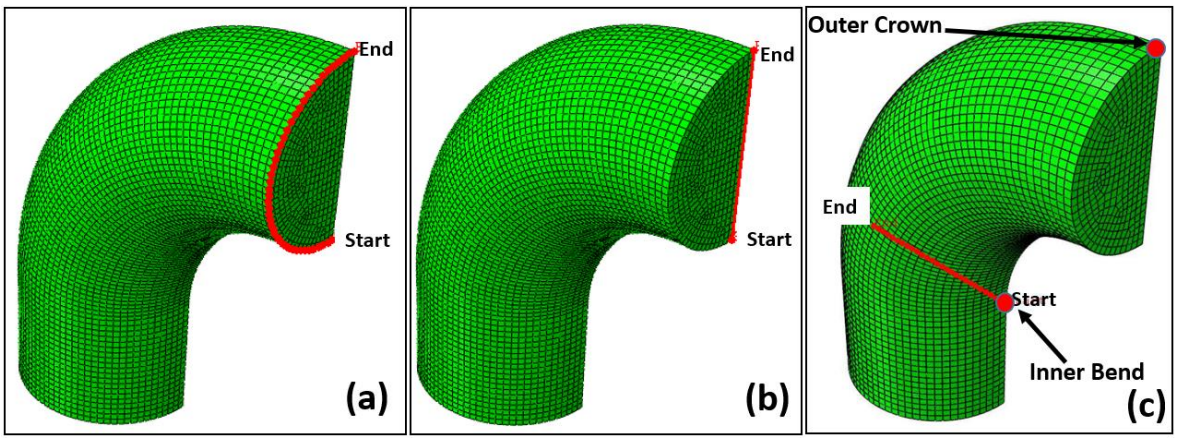

Figure 26: Key paths for stress-strain field prediction for a chain: (a) path-1, (b) path-2 and (c) path-3.

4.3 Definition and calibration of the numerical models

The prior numerical models available from the literature are calibrated and verified in this section. The analysis uses the same modelling inputs that are documented in the respective verification papers. During verification of the models, it is found that some utilise un-converged meshes, these meshes are used to compare to the original literature but are then converged using convergence mesh analyses before comparing to the experiments and the other numerical models.

4.3.1 Elastic model with pressure distribution, 20 node brick element with reduced integration (EP20R)

The elastic model with pressure distribution (EP20R) is calibrated and verified for a 76 mm studless chain with the grade R3 steel material properties, Pacheco et al. [29]. The R3 material model is used without any material plasticity as this is an elastic model. The model was originally analysed using the finite element code, ANSYS, and the input values are the same as used in the original analysis, shown in Table 8. The element type is changed from the SOLID95 elements to the equivalent brick structural solid 20-node second-order element in ABAQUS, C3D20R.

Table 8: Original inputs for the elastic model with pressure distribution (EP20R).

Design Parameter	**Pacheco et al.** [29]
Pressure distribution contact angle (°)	35
Elastic Modulus (GPa)	207
Poisson Ratio	0.29
Element Type	SOLID95
Mesh size (mm)	7.5
Load Magnitude (kN)	810.5

The results of the longitudinal stress are provided for a part of path-2, from a distance of 22 mm to 76 mm. The design parameter, H, shown in Figure 23, is not documented, and therefore, a calibration is performed to replicate the result

from the original paper shown in Figure 27. A value of 11.3 mm is selected for H as it gives the lowest absolute mean difference compared to the original results across the whole path with an absolute mean difference of 2%.

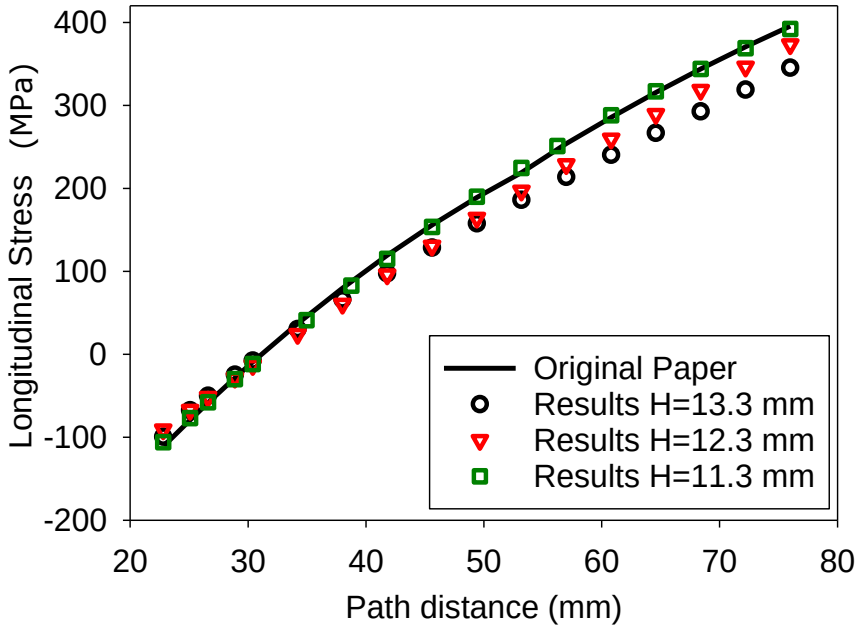

Figure 27: Calibration of H along a part of path-2 for the longitudinal stress.

4.3.2 Elastoplastic model with pressure distribution, 20 node brick element with reduced integration (P20R)

The elastoplastic model with pressure distribution (P20R) is calibrated and verified for a 76 mm studless chain with grade R3 steel material properties, and the input values are the same as used in the original analysis, presented in Table 9, Pacheco et al. [28]. The model was also originally analysed using the finite element code, ANSYS, and the SOLID95 is again changed to C3D20R.

Table 9: Original inputs for the elastoplastic model with pressure distribution (P20R).

Design Parameter	**Pacheco et al.** [28]
Pressure distribution contact angle (°)	35
Elastic Modulus (GPa)	207
Poisson Ratio	0.29
Element Type	SOLID95
Mesh (mm)	7.5
Load Magnitude (kN)	3242
True Yield Stress (MPa)	410
True Tensile Stress (MPa)	748.65
True Tensile Strength Strain	0.0816

The original paper [28] provides the results of the longitudinal stress along a part of path-2, from a distance of 19 mm to 76 mm. The design parameter H is again not documented, and therefore, the H value of 11.3 mm is chosen from the previous verification study. A comparison of the results using this value to the original results is shown in Figure 28 and gives an absolute mean difference of 3.5% across the whole path.

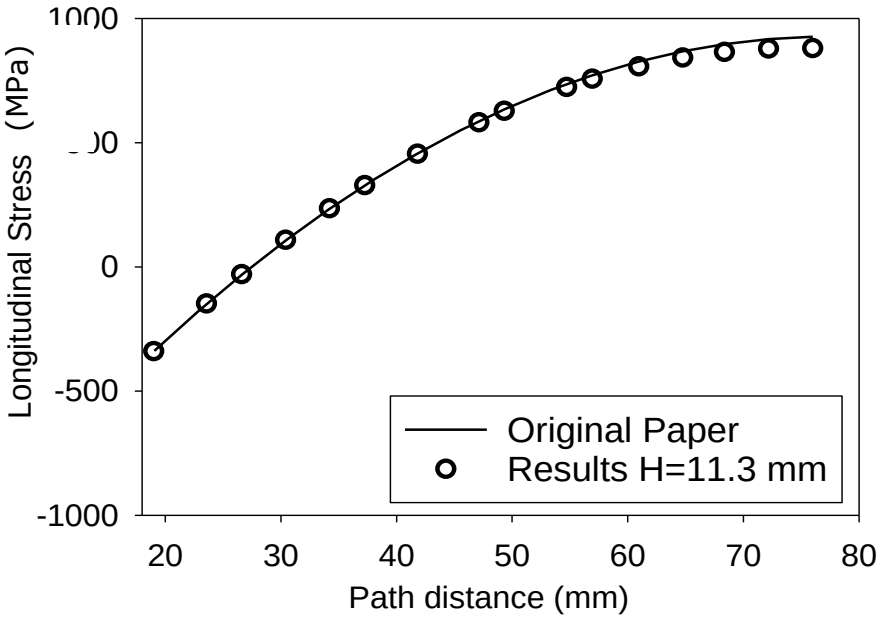

Figure 28: Verification of H=11.3mm for the P20R model along path-2 for the longitudinal stress.

4.3.3 Elastoplastic model with contact interaction, 20 node brick element with reduced integration (C20R)

An elastoplastic implicit model with contact interaction and reduced second-order elements (C3D20R) is calibrated and verified for a 76 mm studless chain using grade R3 steel material properties based on Bjørnsen [42]. The input values are the same as used in the original analysis, as shown in Table 10. However, the contact analysis in the implicit method has convergence problems as it tries to enforce the suddenly activated contact constraint, causing a severe discontinuous iteration. To resolve this issue, an initial boundary condition (IBC) is used to give initial contact conditions where the displacement acting towards the load direction is applied and then removed after the contacting surfaces are adequately constrained through contact with other components before applying the operational load as suggested by ABAQUS [190]. This initial boundary condition (IBC) is not documented in the original paper, and therefore, a parametric study is used to determine this value.

Table 10: Original inputs for the elastoplastic model with contact (C20R).

Design Parameter	**Bjørnsen** [42]
Elastic Modulus (GPa)	210
Poisson Ratio	0.29
Element Type	C3D20R
Slave Model Mesh (mm)	8
Master Model Mesh (mm)	10
True Yield Stress (MPa)	410
True Tensile Stress (MPa)	748.65
True Tensile Strength Strain	0.0816
Interaction – Tangential	Penalty - 0.7 Friction
Interaction – Normal	Normal – Hard
Load Magnitude (kN)	1221.075

The results of the parametric study are presented in Figure 29 for path-1 and show a difference from the original results in the first 5 mm. However, the initial

boundary condition value of 5×10^{-4} m is selected since it gives the lowest absolute mean difference of 4% compared to the original paper.

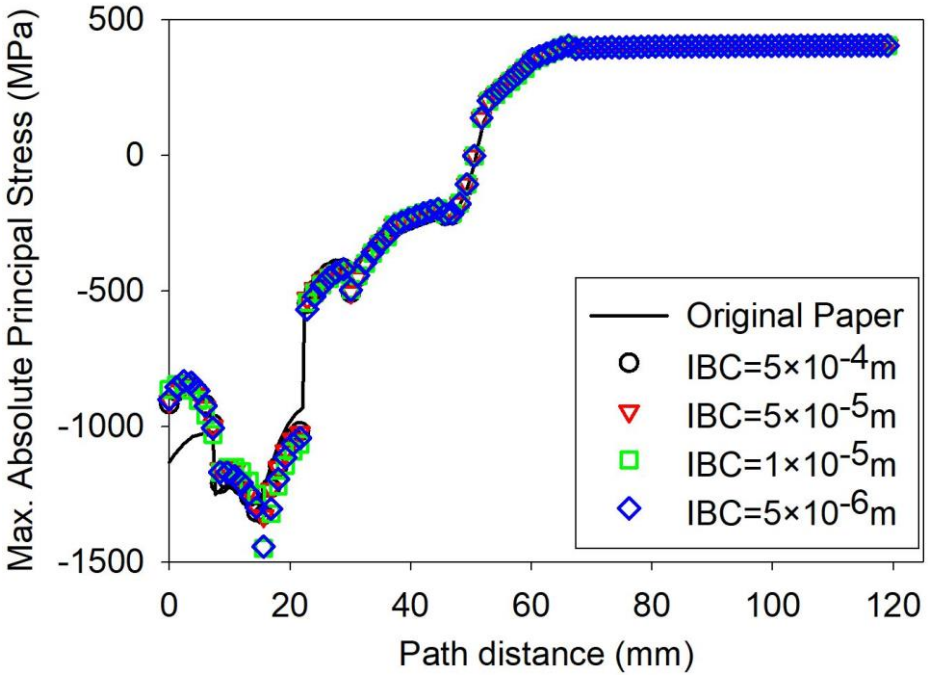

Figure 29: Calibration of the Initial Boundary Condition (IBC) for the maximum absolute principal stress along path-1.

4.3.4 Elastoplastic model with contact interaction, 8 node brick element with incompatible mode (C8I)

The elastoplastic implicit model with contact interaction and incompatible mode elements (C8I) is calibrated and verified for a 152 mm studless chain with the grade R4S steel material properties based on the Kim et al. [74]. The input values are the same as used in the original analysis, as shown in Table 11.

The model is verified using the maximum stress concentration factor, the ratio between the maximum absolute value of the principal stresses within the chain and the nominal tensile stress. The nominal tensile stress is defined as the tensile load divided by the cross-sectional area of the chain's round bars resulting in a stress of 74.535 MPa. The FE model uses the implicit method, requiring contact initialisation to start the interlink contact in the FE modelling; the initial boundary condition (IBC) of 5×10^{-4} m from the previous model is checked and is selected. The maximum absolute value of the principal stresses within the chain predicted by the current FE model is 288.34 MPa, giving a

maximum stress concentration factor of 3.87. This value is compared to the maximum stress concentration factor from the original paper [74], which is 3.9, which gives a 0.80% difference. The model is, therefore, considered to be correctly calibrated and verified.

Table 11: Original inputs for the elastoplastic model with contact interaction (C8I).

Design Parameter	**Kim et al.** [74]
Elastic Modulus (GPa)	209
Poisson Ratio	0.3
Element Type	C3D8I
Slave Model Mesh (mm)	10
Master Model Mesh (mm)	10
Yield Stress (MPa)	700
Tensile Stress (MPa)	960
Tangential interaction	Lagrange Multiplier - 0.7 Friction
Interaction – Normal	Normal – Hard
Load (kN)	2705

4.3.5 Elastoplastic model with contact interaction, explicit solver 8 node brick element with reduced integration (CEx8R)

The solution methods in the finite element formulation can be classified as either implicit or explicit. In the implicit approach, a solution to the set of finite element equations is unconditionally stable involving iteration until a convergence criterion is satisfied for each increment [85]. The unconditionally stable implicit method encounters some difficulties when a complicated three-dimensional model involving contact is considered [85] [135] [191] [192]. The reasons are as follows, taken from the literature:

- the implicit method is not suited to problems dominated by highly discontinuous nonlinearities, such as frequent change of contact and stick/slip frictional sliding [191];

- the unconditionally stable implicit method encounters some difficulties for contact problems where the excessive contact changes and numerical instabilities mean that force equilibrium is difficult to achieve which may then lead to more iterations per increment and reduced increment size [85] [135] [191] [192];
- as the reduction of the time increment continues, the computational cost in the tangent stiffness matrix is dramatically increased and can cause divergence in the solution [85] [135] [191];
- severe convergence problems caused by divergent results in the iterative computations might occur when solving contact problems in the implicit solutions [193].

However, recent research using the explicit method for studded chains shows good agreement with experiments [77], despite it not being documented for studless chains. This is in agreement with the literature [193]–[200] where the explicit solver is shown to provide accurate predictions to experiments, for solving different types of contact problems.

In the explicit approach, a solution is solved in a dynamic formulation and is conditionally stable, assuming the time increment selected is small enough to maintain the stability limit. The stability limit is that the time increment must be less than a critical value of the smallest transition time for a dilatational wave to cross any element in the mesh [85]. The time increment is automatically set by ABAQUS/Explicit depending on the element dimensions and material properties [191].

To allow quasi-static analysis in the explicit method, the loading amplitude uses a smooth step, and the kinetic energy is always checked so that it does not exceed 5% of its internal energy throughout the simulation [191]. For the contact pair algorithm, the contact surface weight is set to 1.0 to specify a pure master-slave relationship with the first surface as the master surface between links. The first-order hexahedral elements with reduced integration schemes (C3D8R) are used, and the final meshes are defined using a mesh convergence analysis. Since the explicit method takes into account the inertia of the component, the mass density of 7850 kg/m^3 is considered for metallic structures of a chain [19].

In addition, the explicit method enables the use of mass scaling to speed up the simulation. Mass scaling is the artificial increase of the mass of an element to increase the value of the time increment that reduces the running time [192]. However, as the user increases the factor of mass scaling, the kinetic energy of the moving material also increases [191]. There is, therefore, a limit to the amount by which the factor of mass scaling can be increased before the kinetic energy exceeds 5% of the internal energy to obtain a reliable solution as accurate as for the model without the mass-scaling. Successful implementation of mass scaling, therefore, requires a number of analyses to be carried out with different factors, in order to determine the mass scaling factor that gives the optimum results with reduced computational efforts, while maintaining the kinetic energy to remain below 5% of the strain energy.

Therefore, mass scaling factors of 10, 100 and 1000 are evaluated in comparison to the same model without mass scaling using a chain model of 76 mm diameter and grade R3 material under 25% minimum breaking load. A mass scaling factor of 100 gives the optimum effect with 8.5 times lower computational time and the same memory usage, and the resultant von Mises stresses along path-1 show a 0.1% mean absolute error with a maximum error of 0.9%. Therefore, the mass scaling factor of 100 is considered to improve computational efficiency for the explicit model, CEx8R.

4.4 Model selection

The differences between the FE models are documented in Table 12. An additional implicit method with C3D8R elements is included as C8R, Jones [78] and Zarandi [81], but it is assumed that only changing the element type from the C20R model will not reduce the accuracy of the model.

Table 12: Differences in modelling between the different FE models.

Model	EP20R	P20R	C20R	C8I	CEx8R	C8R
Solution Method	Implicit	Implicit	Implicit	Implicit	Explicit	Implicit
Interlink Loading Method	Pressure distribu-tion	Pressure distribu-tion	Contact interac-tion	Contact interac-tion	Contact interac-tion	Contact interac-tion
Element type	C3D20R	C3D20R	C3D20R	C3D8I	C3D8R	C3D8R
Contact Tangential behaviour	N/A	N/A	Penalty	Lagrange Multiplier	Penalty	Penalty
Contact Normal behaviour	N/A	N/A	Hard contact	Hard contact	Hard contact	Hard contact
Mass Scaling	-	-	-	-	100	-

4.4.1 Validation of the numerical models

To validate the accuracy of the different numerical models, they are used to simulate the experimental data from Tipton and Shoup [31]. The model geometry is defined to be the same where the chain diameter is 10 mm and the total length, L, is equal to $5D$, the total width, W, is $3.6D$ and the radius of the curved section, R, is $0.8D$. It should be noted that this geometry is different from the IACS [20] standard design. The final meshes for each model were defined using convergence analyses, where the details of mesh convergence results are given in Appendix B.

The chain for this experiment is manufactured according to the ANSI/ASTM A-391-86 standard specification for the alloy steel chain. The original paper documented the engineering stress-strain relationship for the material used in the tests, derived from the average of two tensile tests conducted at a constant stress rate of approximately 30 MPa per second [31]. The engineering stress-strain relationship is converted to true stress-strain relationship for input into

ABAQUS. Figure 30 shows the true stress-strain relationship, where the elastic modulus (E) is 213.745 GPa, and the Poisson ratio (v) is 0.29.

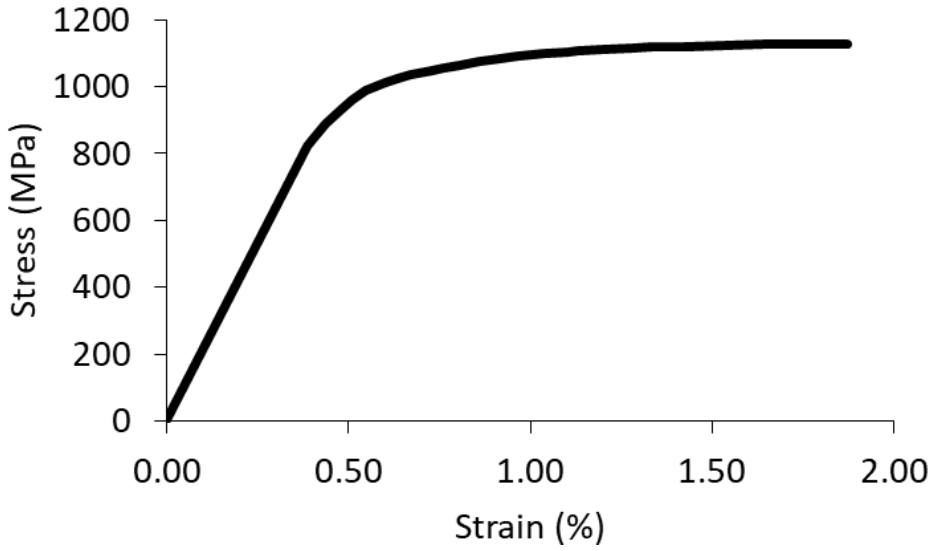

Figure 30: Stress-strain relationship used in the current simulation derived from the tensile tests [31].

In the experiments, the chains were initially heat-treated to relieve manufacturing residual stresses, and then proof loaded at 70%, 76% and 82% of the minimum breaking load. The minimum breaking load was obtained from five break strength tests as 106.8 kN [31]. The proof load is given then released, resulting in a permanent elongation and residual stress at the outer crown. In this experiment, the permanent elongations are obtained from measurements, and the residual stresses are calculated by using the measured strains from strain gauges compared to the monotonic tensile stress-strain curve where the unloading strain is assumed elastic, and the constraint of transverse strains is assumed negligible. The documented permanent elongations are 0.512 mm, 1.021 mm and 1.682 mm for proof loads of 70%, 76% and 82% of the minimum breaking load, respectively. The documented residual stresses are -855 MPa and -648 MPa, for proof loads of 70% and 50% of the minimum breaking load, respectively.

Figure 31 displays the comparisons of the normalised permanent elongations obtained by the FE analyses and experimental tests. The elastic model with pressure distribution (EP20R) is not included since it does not capture the material plasticity. The results of the predicted permanent elongations show a

good agreement between the FE models and the experiments, as shown in Figure 31. The measurement method of the permanent elongations is not documented in the original paper, but it is assumed that they used visual measurement with length meters.

In general, as the permanent elongations increase at higher levels of proof load, the FE model results predict the experimental results more closely. It is assumed that this is because it is difficult to measure relatively small permanent elongations in the experiment. However, in the elastoplastic model with pressure distribution (P20R), the error in predicted permanent elongation increases with larger load levels. This is ascribed to the usage of the pressure distribution method, which is less consistent with real interlink interactions than the contact interaction method. The explicit model (CEx8R) provides the closest agreement in the prediction of permanent elongation for all load levels with the lowest mean error of 13% over the three tests, while the implicit reduced second-order model (C20R) gives the maximum mean error of 47%.

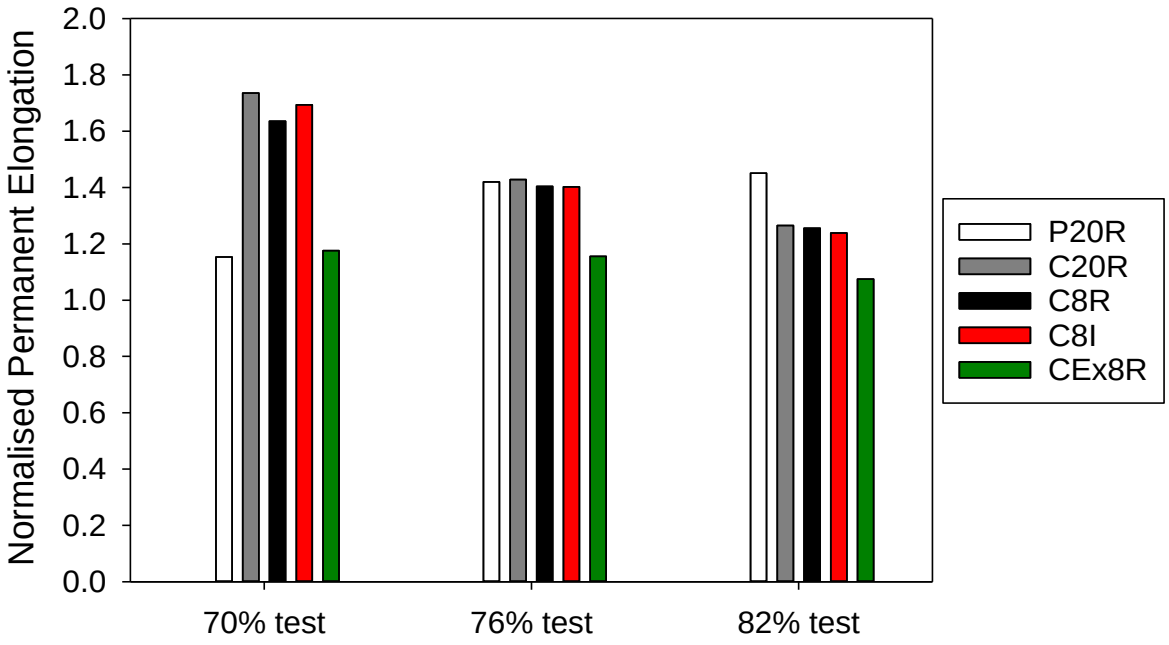

Figure 31: The predicted permanent elongations of the different FE models normalised against experimental tests.

In general, all of the FE models concordantly underestimate the residual stresses with a mean error of 44% for the 70% test, which reduces to 35% for the 50% test. This is except for the elastoplastic model with pressure

distribution (P20R) in the 70% test, which exhibits higher residual stresses that are closest to the experiments with normalised residual stress of 0.99. The residual stress levels are determined from the measured strains by the strain gauges and the monotonic tensile stress-strain curve, where the unloading strain is assumed to be elastic according to Tipton and Shoup [31]. During the experiment, the strain gauge application is documented as being difficult due to the curved surface at the crown region, so this curvature, coupled with the plastic strains imposed by proof loading, may result in erroneous strain gauge applications, with potential for errors in the residual stress estimation. Additionally, the residual stress estimation does not account for some of the physical factors such as Poisson's ratio effects and the constraint of the transverse strains, and strain gauge corrections were not documented. Therefore, the documented results for the residual stresses are considered to be inaccurate.

Overall, these results provide validation for the different FE models. In general, the explicit model (CEx8R) provides the most accurate predictions for the analysis of the permanent elongations and is therefore adopted as the reference for the remainder of the benchmarking studies, due to a lack of further validation material in the open literature.

4.4.2 Benchmarking of the numerical models

The accuracy of the stress-strain field within the chain model is explored to further demonstrate the comparison between the numerical models in predicting important parameters of stresses and strains in mooring chains that will be important to low-cycle fatigue modelling, e.g. the peak stress, stress range, mean stress, plastic strain. The predictions of peak stress along the critical path on the chain surface are firstly compared between the different numerical models. In addition to low-cycle fatigue modelling, an accurate peak stress prediction is also required for strength failure analysis. The prediction of peak stress is also essential for an analysis of mechano-electrochemical induced corrosion as the corrosion is influenced by many factors, one of which is the surface stress, which influences the corrosion rate [201].

The stress along path-1 under the 50% minimum breaking load is shown in Figure 32 based on the prior validation study, where region A signifies the contact region.

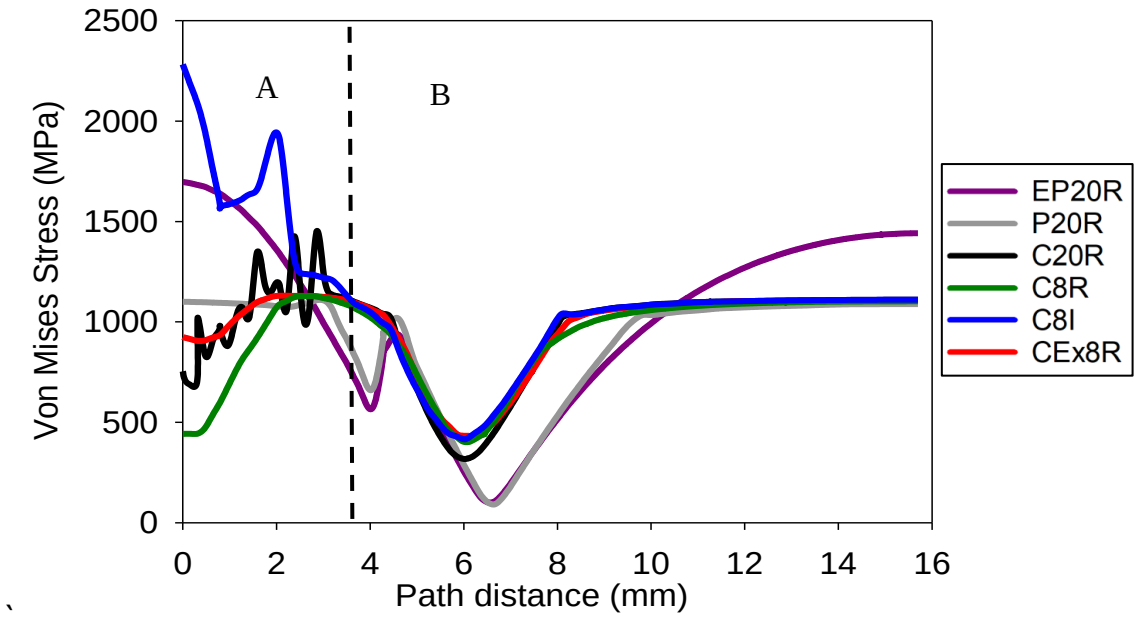

Figure 32: Comparison of the von Mises stresses for the different FE models in the validation study under 50% of the minimum breaking load along path-1.

In general, the results for all of the models with contact interaction, i.e. C20R, C8R, C8I, CEx8R, provide inconsistent results in region A, either through sharp changes in gradient or extreme stress values, and then the stress for all of the models converges at the end of path-1, apart from the elastic model, EP20R. The difference in results in region A is because of the local instabilities and convergence difficulties of the implicit solutions that make force equilibrium difficult to achieve over the contact area. The oscillating stresses exhibited by the implicit models may pick up erroneous peak stresses, since these exhibited peak stresses may not exist. This may mislead the prediction of the peak stress in mooring chains for low-cycle fatigue modelling. However, the explicit model (CEx8R) predicts a smoother stress profile, which results in better predictions based on the prior validation study.

In comparison to the explicit model (CEx8R), the implicit reduced first-order model (C8R) and the elastoplastic model with pressure distribution (P20R) predict similar peak stresses within 0.7 mm. However, the implicit incompatible first-order model (C8I) overestimates the peak stress by 69% at the same

location compared with the explicit model (CEx8R), while the implicit reduced second-order model (C20R) overestimates the peak stress by 28% at a location 0.8 mm from the explicit model, CEx8R.

The different numerical models are then compared using the standardised geometry (L=6D, W=3.35D), 76 mm diameter and of grade R3 with an elastic modulus (E) of 210 GPa and a Poisson ratio (v) of 0.29, in order to be consistent with the current practice of offshore industries. The minimum breaking load for the standardised dimension is 4884 kN based on the IACS standard [20]. The final meshes were determined through a convergence analysis for each model, as detailed in Appendix B. The simulation is a one-step analysis up to the maximum load. The analysis does not consider the effect of proof loading tests or residual stresses, to allow a comparison of the stress/strain modelling in the chain from the same initial condition. The comparison of the von Mises stress profile using the standardised geometry shows similar behaviour with the prior comparison of the von Mises stress profile. However, a difference is found for the results of the elastoplastic model with pressure distribution (P20R) in which it overestimates the peak stress by 12% and the stress at the end of path-1 by 19% compared to the explicit model (CEx8R) under 50% of the minimum breaking load in the standardised dimension.

To further investigate the stress state which is necessary for low-cycle fatigue modelling, the predictions of the stress range and the mean stress at the fatigue hotspots are compared for these different numerical models. The two fatigue hotspots are the outer crown, located at the end of paths 1 and 2, and the inner bend, located at the start of path-3. The comparison of the stresses at these locations are presented in Figure 33, where the load levels of 25% and 50% minimum breaking load are set as the minimum and maximum loading to simulate fatigue loading conditions. The models with contact interaction (i.e. C20R, C8R, C8I, CEx8R) have similar predictions for all of the comparisons with the largest difference, 5%, for the implicit reduced second-order model (C20R) at the outer crown. In comparison to the models with contact interaction, the elastoplastic model with pressure distribution (P20R) gives a mean difference of 46% for the stress range, which reduces to 8% for the mean stress at both locations; while the elastic model with pressure distribution (EP20R) predicts

the stress range by more than 2.5 times, which reduces to 1.6 times for the mean stress at both locations in comparison to the other models with contact interaction, which could lead to inaccurate estimations of the fatigue life.

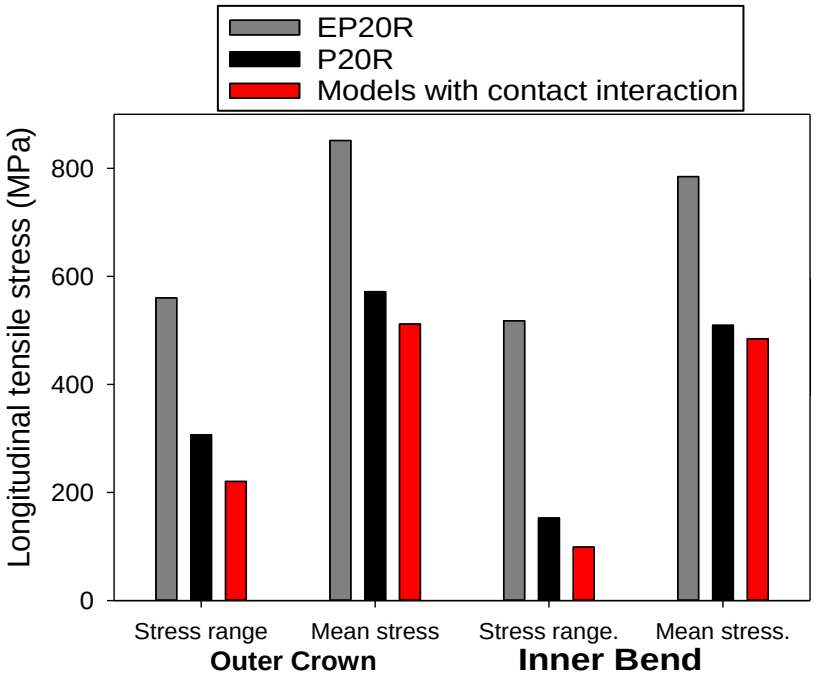

Figure 33: Comparison of the stress range and mean stress for the different FE models at both fatigue hotspots.

The nominal stress is commonly used as a fatigue driving parameter by the traditional SN approach, offshore standards [7], to calculate the fatigue life of mooring chains based on SN curves. The nominal stress is analytically calculated based on the corresponding tension divided by the total cross-sectional area of the chain's round bars. The nominal stress predicted by the FE models is calculated by averaging the longitudinal stress in the mid-cross-section of the straight part of the chain. The models with contact interaction (C20R, C8R, C8I and CEx8R) result in less than a 1% difference to the analytical calculation, while the models with pressure distribution (EP20R and P20R) result in 5.5% difference since they do not capture the contact interactions.

For further comparison between these different numerical models, the local tensile stress field along path-2 and path-3 are examined since they are critical cross-section paths of the fatigue hotspots for low-cycle fatigue modelling [25] [31] [90]. In addition, this prediction is also particularly useful for a fracture of crack propagation analysis. As shown in Figure 34(a), the models with contact

interaction (C20R, C8R, C8I and CEx8R) have considerable dissimilarities in the first 7 mm of path-2 due to their different performances in the contact area. The implicit incompatible first-order model (C8I) gives the largest value of -32 MPa; while the implicit reduced first-order model (C8R) gives the lowest value of -593 MPa. However, the stresses converge along most of path-2, especially at the important location at the end of path-2, where the fatigue crack initiates when subjected to low-cycle fatigue loading.

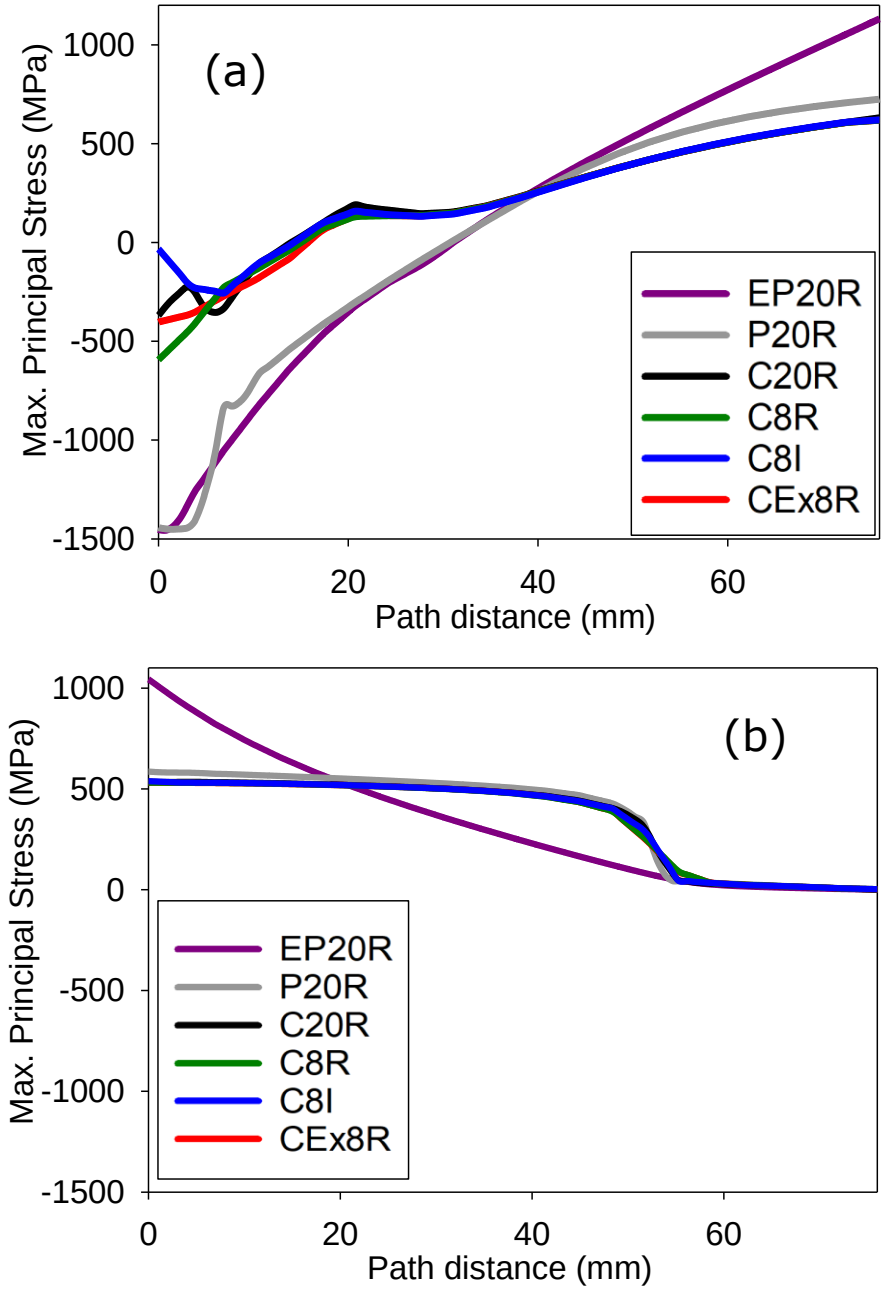

Figure 34: Comparison of the maximum principal stress for the different FE models under 50% of the minimum breaking load along (a) path-2 and (b) path-3.

The models with contact interaction also give the same results along the whole of path-3, as shown in Figure 34(b), indicating similar performances in predicting stresses in these paths 2 and 3 for low-cycle fatigue modelling. However, the elastic and elastoplastic models with pressure distribution (EP20R and P20R) give absolute mean differences of 80% and 63% along path-2, which reduce to 43% and 11% along path-3, respectively, indicating their lack of ability to predict the stress field over the cross-sectional paths. The results found in this comparison are for the stresses, but similar results were also found for the strains.

For further comparison between these different numerical models, the prediction of plastic strain along the chain surface is investigated since this prediction is important to low-cycle fatigue when modelling cyclic plasticity effects. In addition, this prediction will also be particularly useful for an analysis of contact problems, where ratcheting wear may cause interlink wear on the contact surface. This is because the ratcheting wear is the accumulation of plastic strain due to significant contact forces [202].

Figure 35 shows the equivalent plastic strains (PEEQ) over path-1 under 50% of the minimum breaking load. The elastic model with pressure distribution (EP20R) is not included since it does not capture the material plasticity. In general, the results for all of the models with contact interaction, i.e. C20R, C8R, C8I, CEx8R, again provide inconsistent results in region A, but then they converge in region B. In region A, the implicit incompatible first-order model (C8I) overestimates the peak plastic strain by 2.4 times more than the explicit model (CEx8R) at the same location, while the implicit reduced second-order model (C20R) underestimate it by 10% at a location 3.6 mm away from the explicit model. The implicit reduced first-order model (C8R) gives a similar peak plastic strain to the explicit model, but it shifts to the peak location by 3.8 mm. However, the elastoplastic model with pressure distribution (P20R) fails to capture the peak plastic strain in region A and overestimates the plastic strain by 58% at the end of path-1, indicating it is not appropriate for predicting plastic strains for low-cycle fatigue modelling.

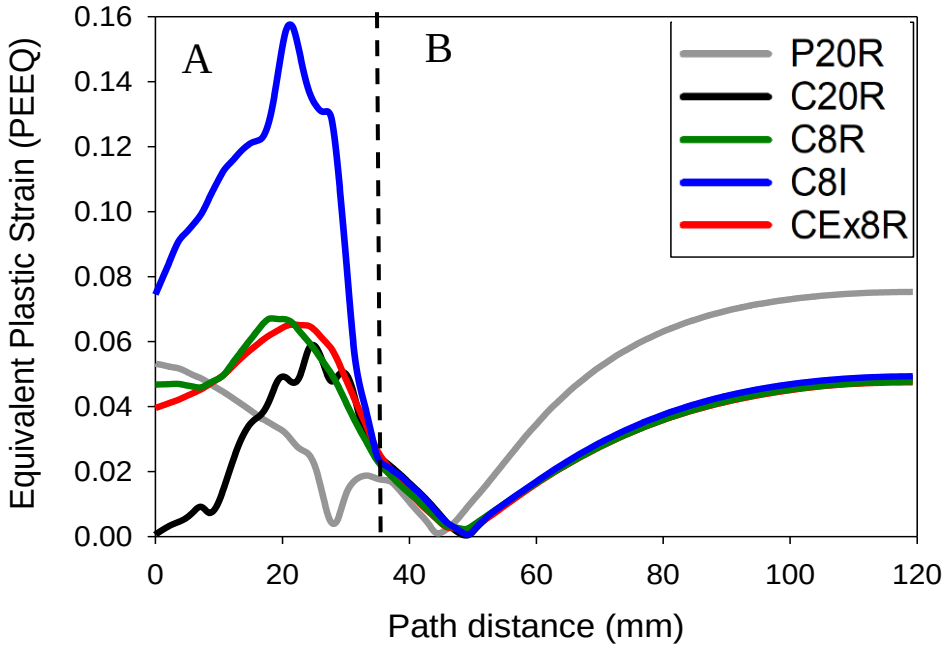

Figure 35: Comparison of the equivalent plastic strains (PEEQ) for the different FE models under 50% of the minimum breaking load along path-1.

4.5 Discussion

This chapter investigates the different performances in predicting stress-strain parameters between different numerical models in order to select the most appropriate one for low-cycle fatigue modelling. Table 13 is compiled to show when a numerical model is appropriate to predict stress-strain parameters, where a circle indicates the results are within 10% of the explicit model (CEx8R) in predicting important parameters for those particular failure analyses and a cross indicates they are not. Here the explicit model is deemed appropriate based on the match to the available experimental data.

Low-cycle fatigue modelling requires the key elements in terms of stress and strain, e.g. peak stress, mean stress, plastic strain, permanent elongation, to be accurately modelled. Table 13 demonstrates that the explicit model (CEx8R) is the most appropriate model for modelling those stress-strain parameters for low-cycle fatigue modelling based on this study, and therefore the bottom line is added accordingly. In addition, these predictions are found not only important to low-cycle fatigue modelling, but also important to analyses of other failure modes of mooring chains, e.g. fracture of crack propagation, ratcheting wear,

ultimate strength, mechano-electrochemical corrosion; and these other failure modes are also indicated in the relevant lines.

Table 13: Summary of appropriate models for predicting stress-strain parameters in mooring chains.

Stress-strain parameters	**EP20R**	**P20R**	**C8I**	**C20R**	**C8R**	**CEx8R**
Nominal stress for SN approach	O	O	O	O	O	O
Residual stress	X	X	O	O	O	O
Stress range and mean stress	X	X	O	O	O	O
Stress along critical path for fracture of crack propagation analysis	X	X	O	O	O	O
Plastic strain for ratcheting wear analysis	X	X	x	O	O	O
Peak stress for ultimate strength	X	X	x	X	O	O
Peak stress for mechano-electrochemical corrosion	x	X	x	X	O	O
Permanent elongation	x	X	X	X	x	O
Low-cycle fatigue modelling	x	X	X	X	x	O

The elastic model with pressure distribution (EP20R) has been demonstrated to be inaccurate at predicting any failure modes since it lacks material plasticity. The elastoplastic model with pressure distribution (P20R) can give similar results with other models with contact interaction under low load levels, e.g. under 25% of the minimum breaking load in the standardised dimensions. However, it is found that at higher load levels, e.g. 50% of the minimum breaking load, there is a larger difference to the models with contact interaction (C20R, C8R, C8I and CEx8R), which is ascribed to its different method in contact application, indicating that the pressure distribution method is not accurate to be used for low-cycle fatigue modelling of mooring chains.

In general, all of the models with contact interaction (C20R, C8R, C8I and CEx8R) can accurately model most of the failure modes. However, convergence problems are a critical issue in the implicit models (C20R, C8R and C8I), where

severe discontinuity iterations occur during simulation, requiring the user to apply unrealistic simplifications to the initial boundary condition to adjust the slave nodes to be in contact with the master nodes in the first step to provide the initial contact conditions [190].

The implicit incompatible first-order model (C8I) exhibits a much higher stress-strain field in the areas of contact, although it manages to capture a similar stress-strain field to the other models (C20R, C8R and CEx8R) in regions far from the contact area, region B. This is because the incompatible mode elements are sensitive to mesh distortions due to significant contact forces in the contact area. The element distortions mean that the finite element interpolation functions have convergence problems, making the elements too stiff and reducing the accuracy [203]. Therefore, care must be taken to ensure that the element distortions are minimal in the areas of interests. Cases, where the incompatible mode elements can be used more appropriately, are bending/buckling analyses of thin members, for example, plate or pipe structures, where the element distortions are low, and this is supported in previous studies into these structures [204]–[206].

The implicit reduced second-order model (C20R) exhibits oscillating stresses in the contact area; this is an issue when using second-order elements in the contact region, even when the mesh size is reduced. This is due to the contact algorithm's difficulties in determining if the force distribution represents constant contact pressure or an actual variation across the surface of the second-order elements, composed of curved edges. The directions of the consistent nodal forces resulting from the pressure load are not uniform in the two-contact surfaces of the second-order elements, making it difficult for the equivalent nodal forces to converge because they do not have the same sign for constant pressure. The convergence problems cause a severe discontinuity iteration until sufficiently small tolerances are satisfied, which is a complicated process involving large memory usage, especially if both the contacting bodies are deformable [192].

The implicit first-order model (C8R) shows superior performance among the other implicit models because the equivalent nodal forces for the applied pressures on the surfaces of the first-order elements always have a consistent

sign and magnitude; therefore, there is no ambiguity regarding the contact state represented by a given distribution of nodal forces [192]. However, obtaining convergence for the initial contact condition remains an issue for all elements in the implicit solver.

The results of this study show that the model that is the most accurate for all scenarios is the explicit model (CEx8R), which predicts a smooth gradient of the stress-strain in the contact area. The explicit model (CEx8R) runs the contact interaction without any convergence problems. When contact occurs, the resisting forces and masses of all contacting nodes on the slave surface are distributed to the nodes on the master surface and add to the total inertial mass of the contacting interfaces. To maintain the stability of the contact enforcement, the explicit solver uses these distributed forces and masses to calculate an acceleration correction to obtain a corrected contact configuration [187]. The small-time increments used by the explicit solver ensure that the highly nonlinear material behaviour and contact changes in the contact area can be captured by adjusting the displacements and velocities of surface nodes involved in contact to remove small initial overclosures to be kinematically correct.

To compare the computational costs, the simulation time and memory usage for each model are shown in a normalised scale against the explicit model in Table 14, using the standardised dimensions with a diameter of 76 mm under 50% of the minimum breaking loading.

Table 14: The computational costs and memory for the different FE models normalised against the explicit model.

Model	Simulation time	Memory usage
Elastic model with pressure distribution (EP20R)	0.13	0.26
Elastoplastic model with pressure distribution (P20R)	0.38	0.37
Implicit reduced second-order model (C20R)	113.84	41.33
Implicit incompatible first-order model (C8I)	15.32	52.67
Implicit reduced first-order model (C8R)	5.88	4.75

Table 14 shows that the explicit model (CEx8R) has a lower computational cost compared to the implicit models with contact interaction (C20R, C8R and C8I). This is because the implicit models experience a number of discontinuity iterations. In addition, the mass-scaling is used in the explicit model to increase the time increment and consequently decrease the computational costs for running the simulation. However, the models with pressure distribution (EP20R and P20R) have much lower computational costs since they do not have interlink contact interactions and half of the models are used. This indicates some benefits in carefully selected simulations in order to model low-cycle fatigue modelling efficiently, where the results for the stress-strain analysis are shown to be of acceptable accuracy.

4.6 Summary

Low-cycle fatigue modelling requires key elements in terms of stress and strain, e.g. peak stress, mean stress, plastic strain, permanent elongation, to be accurately modelled. However, a number of different types of finite element models for predicting the stresses in mooring chains vary in the literature, and there are no comparisons of these models to help determine when they are appropriate and how differently they model the stresses in mooring chains. Therefore, this chapter provides a comparison of the different numerical models

for modelling mooring chains under tension to select the most appropriate finite element model to model low-cycle fatigue.

The predictions of the different finite element models are checked against experimental tests, and this is followed by benchmarking the different finite element models in terms of their performances in modelling the stresses along critical paths of mooring chains. The explicit model developed in the current study has been demonstrated to be both the most accurate and most efficient in predicting the key elements in terms of stresses and strains in mooring chains. The explicit model is, therefore, selected to model the representative stresses and strains for low-cycle fatigue analysis using the critical plane fatigue approach in this stud

Chapter 5: Low-cycle Fatigue Assessment of Mooring Chains Under Service Loading

This chapter aims to develop a fatigue approach capable of accurately predicting low-cycle fatigue behaviour of mooring chains, considering the mean load and cyclic plasticity effects on the fatigue damage, which govern low-cycle fatigue. The fatigue approach is based on a critical plane multiaxial fatigue criterion of Smith-Watson-Topper. The developed finite element model introduced in chapter 4 is used in this chapter to develop the critical plane approach.

Substantial parts of the work presented in this chapter have been published in the following paper:

G. M. Gemilang, P. A. S. Reed and A. J. Sobey, Low-cycle Fatigue Assessment of Offshore Mooring Chains under Service Loading, Marine Structures, 2020. (Published) [207].

5.1 Introduction

This chapter aims to develop a fatigue approach capable of considering the mean load and cyclic plasticity effects on the fatigue damage which governs low-cycle fatigue of mooring chains, to determine the importance of low-cycle fatigue in early failures currently observed in operating mooring lines. The analysis excludes geometric adjustments due to other damage mechanisms (e.g. wear, corrosion pitting), allowing for the isolation of the low-cycle fatigue-induced effects. The Smith-Watson-Topper approach using critical plane multiaxial fatigue criteria is selected since this approach has been demonstrated to accurately capture the mean load and cyclic plasticity effects in both high-cycle and low-cycle fatigue regimes, where fatigue damage is assessed directly in terms of local strains and stresses at the fatigue hotspot [117], [135]–[143], [208].

The application of this approach has also been extended to different material models in the present study to understand how the material selection process

affects the fatigue damage prediction. The fatigue damage accumulation predicted by this approach and that predicted by the traditional SN approach are compared in a mooring line simulation of an FPSO, using the rainflow counting method and Palmgren-Miner's rule.

5.2 Development of a representative chain model

A model of a mooring chain is developed using the IACS [20], standardised dimensions for an offshore studless chain with a diameter, *D*, of 76 mm. The total length, *L*, is equal to 6*D*; the total width, *W*, is 3.35*D* and the curved section radius, *R*, is 0.675*D,* as illustrated in Figure 36. The analysis is performed at two local hotspots, determined at the critical fatigue locations where the majority of fatigue failures have been found in experiments when working under tension loading [44] [90] [94]. The two local fatigue hotspots are indicated in Figure 36 as the Crown and K_t points.

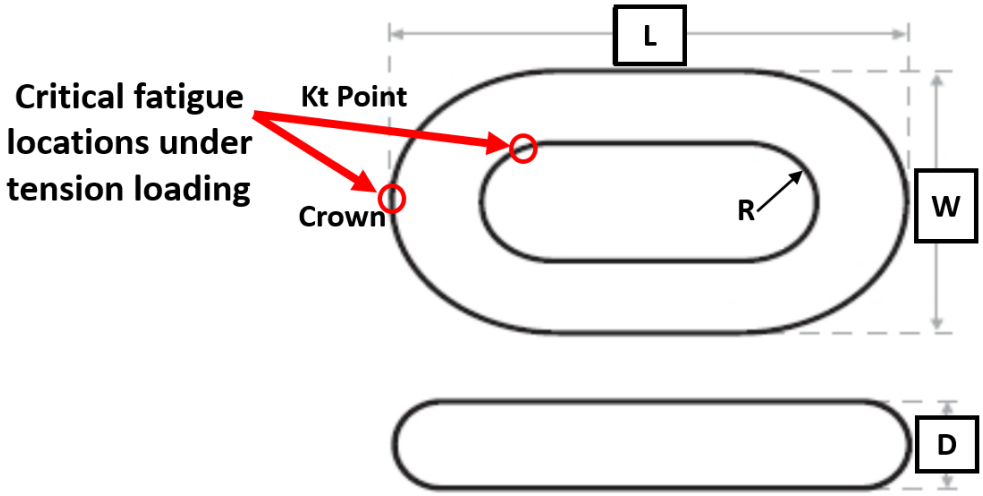

Figure 36: The standardised dimensions for a studless chain, taken from IACS, and the critical fatigue locations.

The FE model is developed in ABAQUS 6.14 and automated using a Python script, considering both material and geometric nonlinearities using the explicit solver with C3D8R elements and a mass-scaling factor of 100, based on the previously developed method, CEx8R, as introduced in chapter 4.

A 1/8th portion of the chain is modelled that takes advantage of the three symmetry planes and minimises the computational cost, as shown in Figure 37, where the slave model has a finer mesh as the resultant stresses and strains

are extracted from these locations. The final mesh is defined using a convergence analysis which has a corresponding size of 3.5 mm for the slave model and 10 mm for the master model, where the mesh convergence analysis is detailed in Appendix B.

Symmetric boundary conditions are applied to the symmetry planes shown in red in Figure 37. The loaded surface at the top of the master model does not have this boundary condition, to allow the load to be applied in the axial direction. The symmetry boundary conditions constrain the displacement of nodes on each symmetry plane in the normal direction and the rotation in the other two directions. For example, the bottom surface of the slave model is constrained against displacement in the y-axis and against rotation in the x and z-axes. The contact discretisation is defined as surface-to-surface with a finite sliding formulation, as the tension-tension simulation assumes no sliding of one surface along with the other [187]. A friction coefficient of 0.7 is used for the tangential interaction behaviour [29].

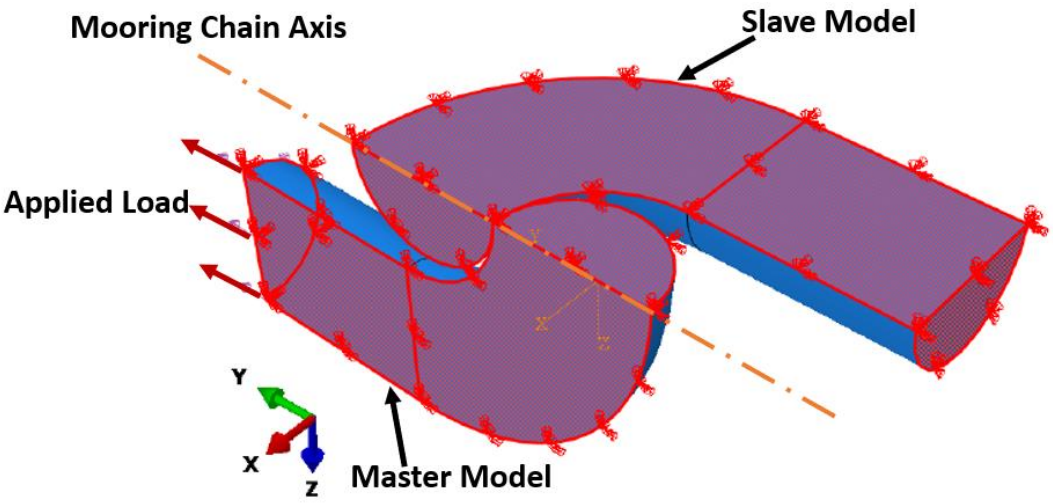

Figure 37: The finite element model of the chain-link used in this analysis, where the left part is the master and the right part is the slave.

5.3 Material Models

In order to determine how the material selection affects the fatigue predictions, material models representative of the monotonic and cyclic mechanical properties are considered, and a comparison is made between them. The R4 steel grade, which complies with DNVGL-OS-E302 [19], is considered, as it is

the most prevalent material grade currently in use for mooring chains [90]. A monotonic material model is developed from mechanical properties derived from tensile tests conducted by Rampi et al. [75], in which a bilinear isotropic hardening is used, and the strain associated with the tensile strength is adopted as half the total elongation specified in the standards [19] [28], this is designated Mono-Rampi.

Two models are developed to describe the cyclic material responses, which are derived from low-cycle fatigue tests conducted by Rampi et al. [75], designated Cyclic-Rampi, and Zarandi and Skallerud [81], designated Cyclic-Zarandi, using the constitutive model of the combined nonlinear isotropic-kinematic hardening proposed by Chaboche [150]. This constitutive model has been widely used in modelling fatigue and has been shown to be robust in describing the mechanical properties of a material under cyclic loading [150] [151], and the cyclic material models have been shown to exhibit an accurate stress-strain response when compared to material testing data under low-cycle fatigue tests in the literature [75] [81].

Table 15 outlines the material properties with a Young's modulus, *E*, of 206.6 GPa and a Poisson's ratio, ν, of 0.3 for each model, where σ_{y} is the monotonic yield strength, σ_{T} is the monotonic tensile strength, A_{T} is total elongation, $\sigma|_0$ is the yield strength at zero plastic strain, Q_∞ is the maximum change in yield strength, b_{T} is the rate at which the yield surface changes with the development of plastic strain accumulation, C_{T} is the initial kinematic hardening moduli, and γ determines the decreasing rate of the kinematic hardening moduli with increasing plastic strain accumulation.

Table 15: Parameters for the monotonic and cyclic material models.

Monotonic material model	**Ref.**	**Yield strength**	**Tensile strength**		**Total elongation**	
		σ_y **(MPa)**	σ_T **(MPa)**		A_T **(%)**	
Mono-Rampi	[75]	903	1039		12	
Cyclic material model	**Ref.**	**Initial yield strength**	**Isotropic component**		**Kinematic component**	
		$\sigma\|_0$ **(MPa)**	Q_∞ **(MPa)**	b_T	C_T	γ
Cyclic-Rampi	[75]	723.6	-141.6	1.42	244100	1379
Cyclic-Zarandi	[81]	546	-227	3.1	536565	1500

These material models are scrutinised in ABAQUS using a single element model under displacement control to show their differences in describing the material response for predicting the stresses and strains under monotonic loading and cyclic loading conditions.

Figure 38 shows the materials' stress-strain curves under monotonic loading, where Cyclic-Rampi and Cyclic-Zarandi exhibit similar plastic responses. For these models, the stresses decrease with increases in plastic strain due to the materials' cyclic softening response. However, the curve of the Mono-Rampi increases linearly from the yield stress to the tensile stress but remains constant when the plastic strain is above the tensile strength, without any cyclic softening. The Mono-Rampi properties were selected to determine the difference in life predictions between monotonic or cyclic material models as the amount of plastic strain will be underestimated, in comparison to the cyclic material models, when subjected to monotonic loading. These differences will lead to variations in the initial elastic shakedown for the first cycle, the state where the stress-strain relationship is stabilised in elastic behaviour [13].

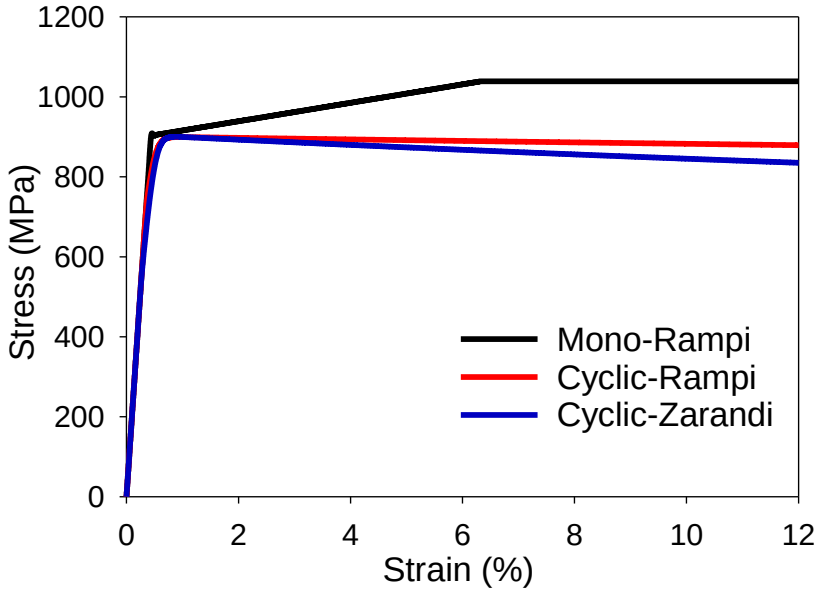

Figure 38: Comparison between each model under monotonic loading, showing the stress-strain curves.

Figure 39 shows the material responses under cyclic loading, where cyclic loading at a strain range, $\Delta\varepsilon$, of 0.0155 and a strain ratio, R_ε, of -1 is selected to show the evolution of the maximum and minimum values of the peak stresses over the progressive number of cycles experienced by the material models. Figure 39(a) shows the material response in the hysteresis loop, and Figure 39(b) shows the evolutions of maximum and minimum values of the peak stresses from the hysteresis loop for each progressive number of cycles.

Under this cyclic loading, the Cyclic-Rampi and Cyclic-Zarandi models exhibit cyclic softening behaviour in the early cycles, which then develops more slowly during the subsequent cycles until stabilisation of the elastic shakedown is achieved. Cyclic-Zarandi has a more significant cyclic softening behaviour, leading to a higher amount of plastic strain than Cyclic-Rampi. This is because the Cyclic-Zarandi is derived from low-cycle fatigue tests at a higher strain range than the one used to obtain Cyclic-Rampi, resulting in a more significant cyclic softening response [75] [81].

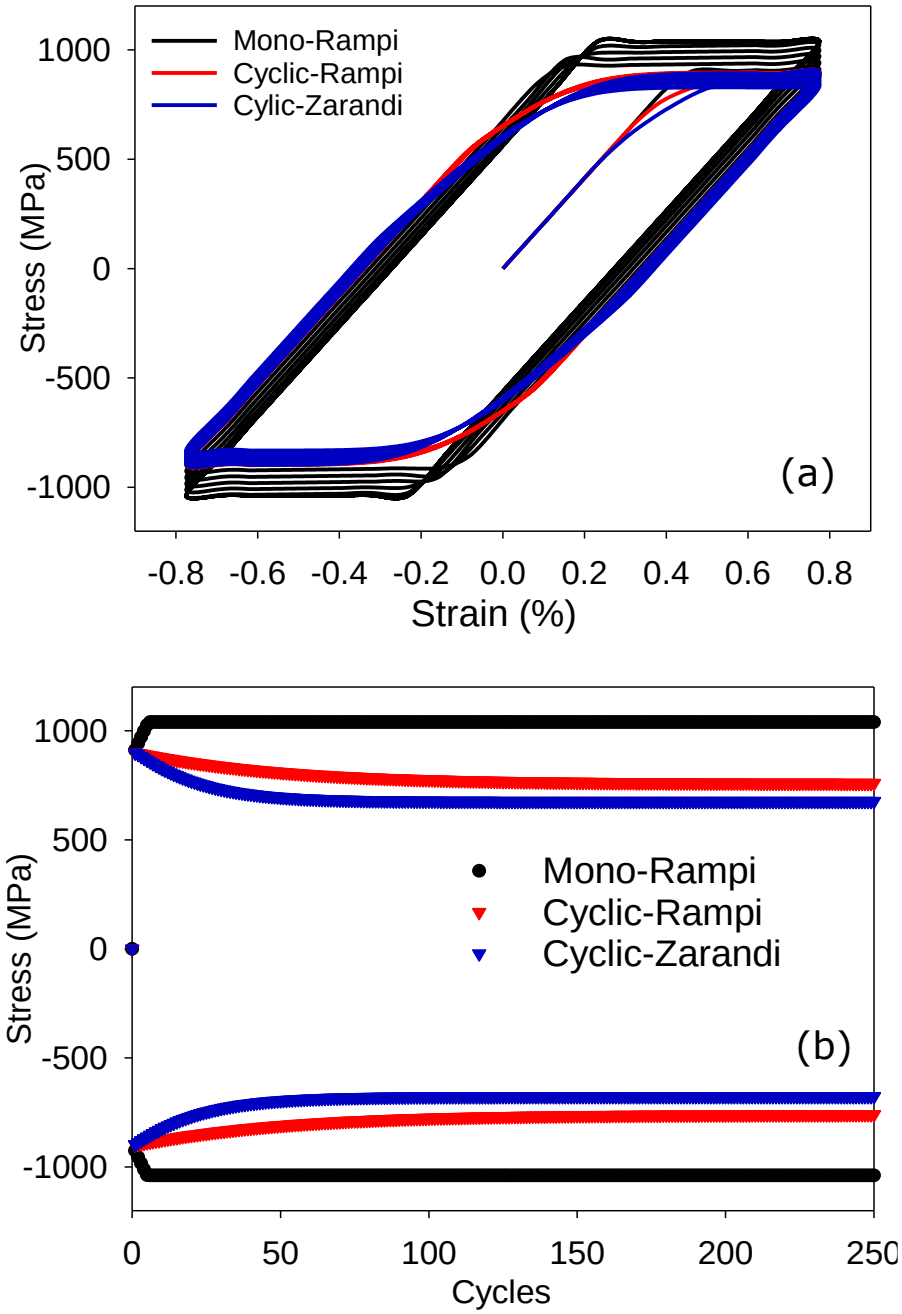

Figure 39: Comparison between each model under cyclic loading, (a) showing the stress-strain relationship in the hysteresis loop, (b) showing the evolution of the maximum and minimum values of the peak stresses with the number of cycles.

However, the Mono-Rampi is unable to simulate the cyclic softening behaviour, instead exhibiting hardening behaviour in the first five cycles, and develops elastic shakedown before the cyclic material models. Therefore, the Mono-Rampi will develop the highest values of peak stresses throughout the cycles. This implies that the use of the monotonic material models will significantly

underestimate the amount of plastic strain and the cyclic plasticity effects in applications where the components are experiencing cyclic stress-strain evolution under progressive loading cycles, which may lead to inaccurate fatigue life estimations.

5.4 Development of the critical plane fatigue assessment for mooring chains

5.4.1 The Smith Watson Topper Critical Plane Approach

Smith et al. [132] and Socie [134] developed a critical plane multiaxial fatigue method, where fatigue damage is assessed directly in terms of local strains and stresses at the critical fatigue location under progressive loading cycles. This critical plane multiaxial fatigue criterion is described by Equation (14),

$$SWT = \sigma_{\mathrm{n,max}} \frac{\Delta\varepsilon_{\mathrm{n}}}{2}, \qquad (14)$$

where *SWT* is the damage parameter, $\sigma_{\mathrm{n,max}}$ and $\Delta\varepsilon_{\mathrm{n}}$ are respectively the maximum normal stress and the normal strain range perpendicular to the plane during one stabilised cycle. This critical plane multiaxial fatigue model has been shown to accurately capture the mean load and cyclic plasticity effects and provides accurate life prediction results for a range of different structures, materials and loading conditions [117], [135]–[143], [208]. This is because the *SWT* damage parameter represents the real physical properties of the stress-strain function at the critical fatigue location based on the most severely damaged plane due to fatigue (the critical plane), that has been demonstrated governing the fatigue of metal structures in both high-cycle and low-cycle fatigue regimes [120] [132] [134]. The critical plane is, therefore, determined by checking the value of *SWT* on different planes at the fatigue hotspot during a stabilised cyclic load, where the plane with the highest *SWT* is defined as the critical plane.

The *SWT* damage parameter is related to fatigue life using Equation (15),

$$\sigma_{\mathrm{n,max}}\frac{\Delta\varepsilon_{\mathrm{n}}}{2}=\frac{\left(\sigma_{\mathrm{f}}^{'}\right)^{2}}{E}(2N_{\mathrm{f}})^{2b}+\sigma_{\mathrm{f}}^{'}\varepsilon_{f}^{'(2N_{\mathrm{f}})^{b+c}}, \quad (15)$$

where E is Young's modulus, N_f is the number of cycles to failure, σ_f' is fatigue strength coefficient, b is the fatigue strength exponent, ε_f' is fatigue ductility coefficient, and c is the fatigue ductility exponent [13]. Equation (15) is the product of the combination of the Basquin's relation and the strain-life equation from which this critical plane multiaxial fatigue criterion is derived [132] [134], as reviewed in section 2.7.1. By combining the constants in the right-hand side in Equation (15), a general formula is obtained as shown in Equation (16),

$$SWT = A_1 N_{\mathrm{f}}^{a_1} + A_2 N_{\mathrm{f}}^{a_2}, \quad (16)$$

where N_f is the number of cycles to failure, $A1$, A_2, a_1 and a_2 are material constants and can be determined by calibration tests from experimental data. This general formula is used to generate a fitted curve for *SWT* damage parameters across a range of number of cycles to failure.

5.4.2 Calibration of the critical plane approach

DNVGL-OS-E301 [7] provides the number of cycles to failure of mooring chains under different loading conditions providing fatigue design data based on SN curves derived from full-scale fatigue tests. The full-scale fatigue tests are simulated in the FE model to establish the *SWT* damage parameters correlated to the fatigue life data based on the conventional design data adopted from DNVGL-OS-E301 [7] at different load amplitudes. The tests subject a chain with a diameter of 76 mm, and made from R4 steel grade, to a first proof load cycle up to 70% of the minimum breaking load and then back to zero. This is followed by cyclic loads with a constant mean load equal to 20% of the minimum breaking load, but under a different load amplitude for each test [7] [90] [94] [99].

The minimum breaking load is 6001 kN for this chain type according to the standard, IACS-W22 [20]. The proof load results in significant plastic deformation and compressive residual stresses developed at both the fatigue hotspots, the crown and K_t point. The stabilised stress-strain response better describes the subsequent fatigue behaviour [117] [129], and therefore the cyclic loads are run until the stress-strain response is stabilised under elastic

shakedown, where the maximum normal stress, $\sigma_{n,max}$, and the normal strain range, $\Delta\varepsilon_n$, on the critical plane are extracted from the FE results to calculate the *SWT* damage parameters, according to Equation (14).

To determine the critical plane, the *SWT* value is checked in the stabilised cyclic load state for all plane orientations between -90° < φ < 90° with an interval of 1°, where the plane with the highest *SWT* value is taken as the critical plane. The plane angle, φ, is measured counter-clockwise from the longitudinal direction to the normal vector on an inclined plane. The normal stress, σ_n, and normal strain, ε_n, on the plane were calculated using the multiaxial stress-strain results at the node of element, according to Equations (17)-(18) for crown and Equations (19)-(20) for K_t point based on the respective longitudinal and transversal directions in the FE model based on the literature of SWT method [117] [134], where the direction of axes is shown in Figure 40,

$$\sigma_n = \frac{\sigma_{xx} + \sigma_{zz}}{2} + \frac{\sigma_{xx} - \sigma_{zz}}{2}\cos 2\varphi + \sigma_{xz}\sin 2\varphi\,, \tag{17}$$

where σ_{xx} is the longitudinal stress, σ_{zz} is the transversal stress, σ_{xz} is the shear stress at the crown,

$$\varepsilon_n = \frac{\varepsilon_{xx} + \varepsilon_{zz}}{2} + \frac{\varepsilon_{xx} - \varepsilon_{zz}}{2}\cos 2\varphi + \varepsilon_{xz}\sin 2\varphi\,, \tag{18}$$

where ε_{xx} is the longitudinal strain, ε_{zz} is the transversal strain, ε_{xz} is the shear strain at the crown,

$$\sigma_n = \frac{\sigma_{yy} + \sigma_{zz}}{2} + \frac{\sigma_{yy} - \sigma_{zz}}{2}\cos 2\varphi + \sigma_{yz}\sin 2\varphi\,, \tag{19}$$

where σ_{yy} is the longitudinal stress, σ_{zz} is the transversal stress, σ_{yz} is the shear stress at the K_t point,

$$\varepsilon_n = \frac{\varepsilon_{yy} + \varepsilon_{zz}}{2} + \frac{\varepsilon_{yy} - \varepsilon_{zz}}{2}\cos 2\varphi + \varepsilon_{yz}\sin 2\varphi\,, \tag{20}$$

where ε_{yy} is the longitudinal strain, ε_{zz} is the transversal strain, ε_{yz} is the shear strain at the K_t point.

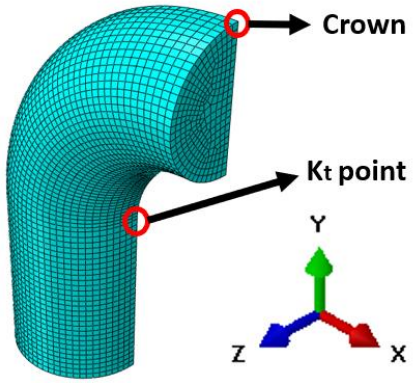

Figure 40: An illustration of the direction of axes in the FE model to calculate the *SWT* values at the fatigue hotspots (i.e. Crown and K_t point) based on the respective longitudinal and transversal directions of each hotspot.

It was found that the *SWT* damage parameter is at the maximum when φ=0° for both crown and K_t point under various load amplitudes, i.e. from 1% to 19% MBL. Figure 41(a) shows an example where the resultant *SWT* damage parameters on different planes for both crown and K_t point under a load amplitude of 11% MBL are shown, indicating that the maximum damage parameter is reached when φ=0°; this is then defined as the critical plane and is used to calculate the *SWT* damage parameter.

Figure 41(b) shows the damage parameters on the critical plane of the K_t point are lower than those of the crown with a mean absolute difference of 0.0352 and a maximum absolute difference of 0.049, across the range of selected load amplitudes. The result is in line with full-scale experimental fatigue results [90] [94] [95], where the crown is found to be more susceptible to fatigue damage than the K_t point. This is because the residual compressive stress at the K_t point, which is 489 MPa, is greater than that at the crown, which is 358 MPa, upon release of the proof load. Subsequent analyses, therefore, concentrate on the crown for the fatigue assessments. The results presented in Figure 41 use the Cyclic-Rampi material model, but similar results were found using the other material models. Figure 41(b) also shows that the *SWT* damage parameter is near zero when the load amplitude is relatively low. This is because the critical plane approach assumes no fatigue damage occurs when the maximum normal stress perpendicular to the critical plane is compressive, and the compressive stresses have been induced by previous proof load applications.

The maximum normal stress, $\sigma_{\mathrm{n,max}}$, and the normal strain range, $\Delta\varepsilon_{\mathrm{n}}$, on the critical plane at the crown hotspot during the stabilised cyclic load are therefore used to calculate the *SWT* damage parameters, according to Equation (14). The *SWT* damage parameters are correlated with the respective number of cycles to failure from the fatigue life predictions of DNVGL-OS-E301 [7] by simulating the fatigue tests under different loading conditions of cyclic load, which are a constant mean load of 20% MBL and various load amplitudes, i.e. from 1% to 19% MBL, based on mooring chains service lives. The number of cycles to failure for each load amplitude is calculated according to Equation (6) based on DNVGL-OS-E301 [7], as reviewed in section 2.6.3.

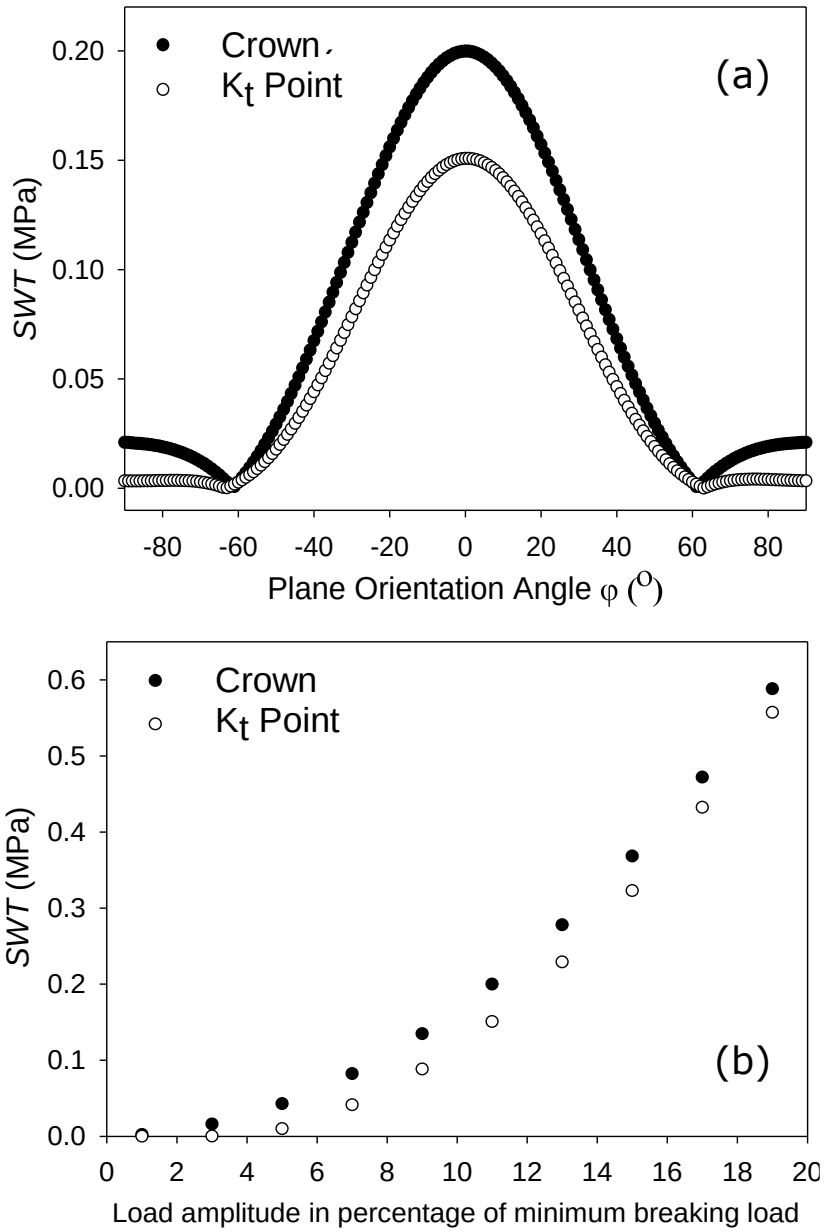

Figure 41: Comparison between the crown and K_t point (a) damage parameters on different plane orientation angles, (b) damage parameters on the determined critical plane under a range of load amplitudes.

The resultant *SWT* damage parameters, under different load amplitudes, are used to calibrate the parameters of the fitted curves based on the general formula of Equation (16) in order to interpolate the number of cycles to failure from the corresponding *SWT* damage parameters during fatigue loading. Figure 42 shows the generated fitted curves, using the resultant *SWT* damage parameters, across a range of the number of cycles to failure. Appendix C provides the details of *SWT* damage parameters under different load amplitudes and the calibration of the fitted curves.

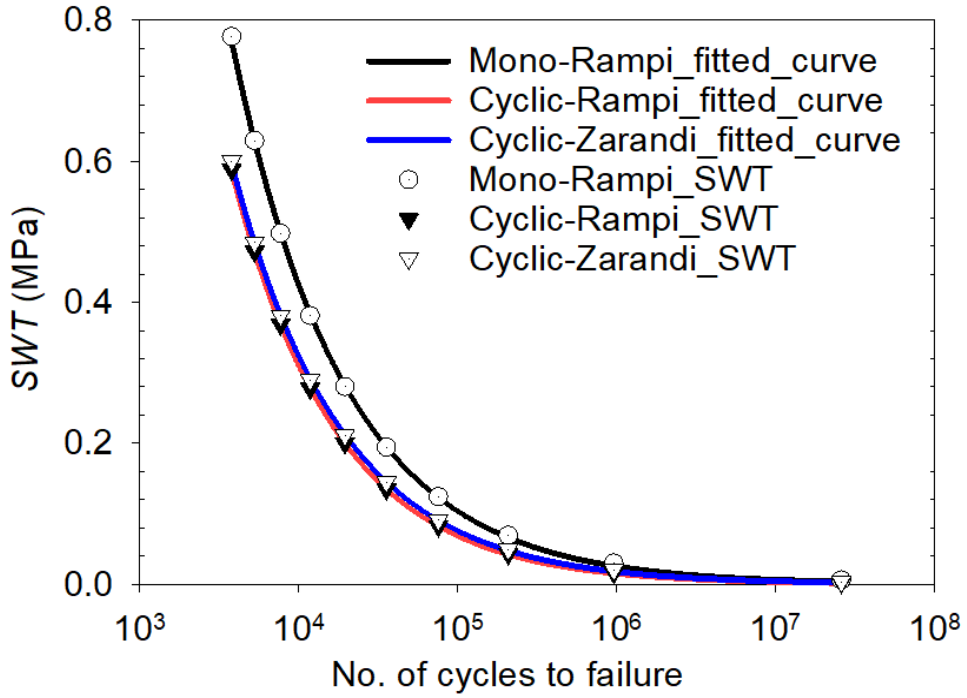

Figure 42: The fitted calibration curves based on the fatigue life of mooring chains for the Smith-Watson-Topper (SWT) using the stress/strain data at the crown fatigue hotspot for the different material models.

Cyclic-Rampi and Cyclic-Zarandi have similar curves as both exhibit cyclic softening during the first cycle, while the curve of the Mono-Rampi increases to a higher value than the others. This is because the significant hardening behaviour of Mono-Rampi during the first cycle results in a high maximum normal stress, $\sigma_{n,max}$. Unlike the traditional SN approach, the critical plane approach takes all of the local stress-strain evolution into account when determining the fatigue response, including the proof load-induced effects i.e. strain hardening and residual stresses, mean load effects, material model nonlinearities and geometric nonlinearities. The FE-based critical plane approach has been correlated with the fatigue design data adopted from DNVGL-OS-E301 [7], allowing the fatigue life to be predicted by a fitted curve for a particular material model.

5.5 Fatigue Simulations

5.5.1 Mooring Chain loading

In order to simulate the fatigue experienced by the mooring chains in service, the tension-spectrum, representing the fatigue loading, is simulated in a mooring line simulation of an FPSO as a case study using the Flexcom package [183]. The case study simulates a mooring system of an FPSO at a water depth of 810 m in a specific sea-state adopted from Gao and Moan [184] for short-term analysis. The sea-state is characterised by the significant wave height, H_s=6.25 m, a spectral peak period, T_p=12.5 s, a 1-hour mean wind velocity, U_w=7.5 m/s, and a mean current velocity, U_c=0.5 m/s, where the Pierson-Moskowitz wave spectrum is applied, and all environmental loads are assumed to act from the head sea. The main particulars of the FPSO are adopted from the Flexcom package [183], which are listed in Table 16. The RAO and QTF are taken from the Flexcom package [183] to include the first-order and second-order motions of the FPSO to give the combined vessel response.

Table 16: Main particulars of the FPSO taken from Flexcom [183].

Parameter	**Value**
Vessel mass	382,734 t
Vessel draft	21.2 m
Vessel beam	58.2 m
Length from COG to forward perpendicular	162.5 m
Length from COG to aft perpendicular	176.7 m
Length from COG to turret point	150 m

The mooring system is an eight-line catenary system with chain-wire rope-chain components connected to a turret of the FPSO with a pretension of 1037 kN (17% MBL) for each line.

Table 17 shows the mooring component principals, which are adopted from the Flexcom package [183].

Table 17: Mooring component principals [183].

Parameter	Length (m)	Size (mm)	Mass per meter (kg/m)	Axial stiffness (kN)	Normal drag coeff.	Longitudinal drag coeff.
Lower chain	500	76	115	4.935×10^5	2.4	1.15
Wire rope	400	89	62	7.03×10^5	1.2	0.1
Upper chain	200	76	115	4.935×10^5	2.4	1.15

Figure 43 shows the horizontal projection of the mooring system with an angular spread of 45^o between the lines. The anchor radius from the turret centreline is 700 m, with which the mooring line anchor points are constrained, and each fairlead is attached to the FPSO via hinges at 8 m below the mean water level. A time-domain simulation of 3 hours is used, as suggested by the mooring standard DNV-OS-E301 [7], to provide adequate statistics with a time step of 0.1 s. The effect of the system's nonlinear characteristics is included through both the wave-frequency and the low-frequency tension spectra through coupled dynamic analysis. Line 1 is selected for low-cycle fatigue analysis to investigate the effects of mean load and cyclic plasticity, as it experiences the greatest tension. The tension-spectrum of the top chain is used for fatigue analysis, as suggested by the mooring standard, API-RP-2SK [18].

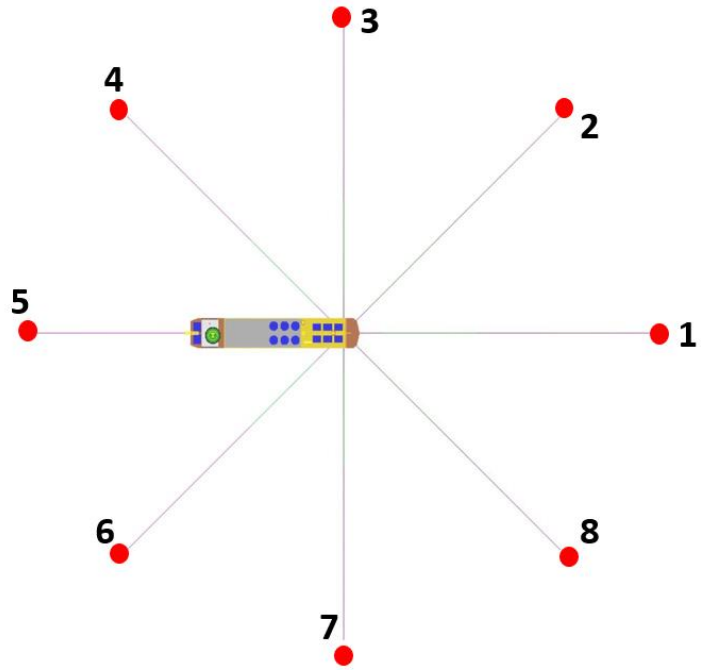

Figure 43: Mooring system arrangement in this simulation taken from Flexcom [183].

5.5.2 Fatigue Damage Comparison

The tension-spectrum from the mooring line simulation consists of combined high-cycle and low-cycle fatigue loading with a maximum tension of 2595 kN, a mean of 1272 kN and a minimum of 617 kN. The rainflow counting method [47] is used to identify individual loading cycles within the tension-spectrum because it has been shown to give reasonable fatigue estimates [209]. The total fatigue damage is calculated using the Palmgren-Miner's rule [185], assuming that the total fatigue damage caused by a number of stress cycles equals the summation of damages caused by the individual loading cycles. The individual loading cycles from the tension-spectrum are simulated in the FE chain model after which the proof load, and its release, are applied to simulate the mooring chains' loading history. The fatigue damage accumulation is predicted using the Smith-Watson-Topper critical plane approach and the traditional SN approach to allow a comparison between these two approaches.

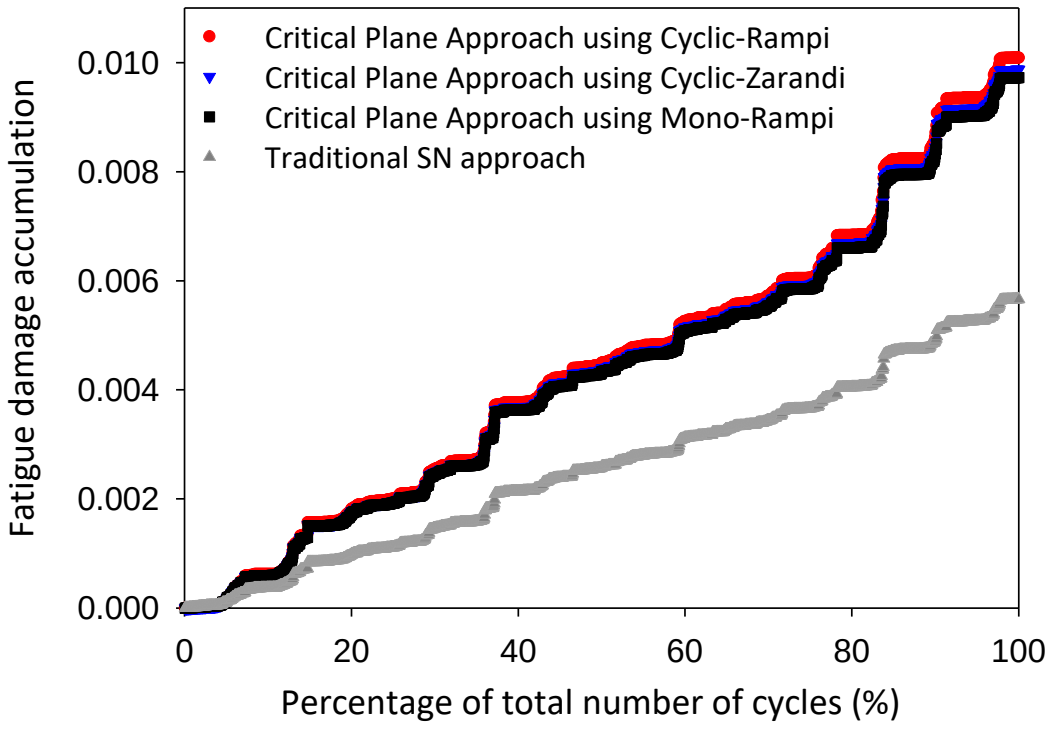

Figure 44: Comparison of the predicted fatigue damage accumulation using different approaches.

Figure 44 shows that the predicted fatigue damage accumulation of the critical plane approach is significantly higher than that of the traditional SN approach. The different material models used in the critical plane approach all predict a significantly higher fatigue damage accumulation relative to the traditional SN approach, by 78.1% using Cyclic-Rampi, 74.3% using Cyclic-Zarandi and 71.74% using Mono-Rampi. On average, the traditional SN approach predicts 7.2% of all the individual loading cycles will contribute to low-cycle fatigue, while the critical plane approach predicts 12.9% will, across all the material models considered. This indicates that the critical plane approach captures a greater number of important low-cycle fatigue events in the mooring line loading because it accounts for the effects of the mean load and cyclic plasticity in the fatigue life assessment.

Figure 45 shows the ratio between the fatigue damage predicted by the critical plane approach and that predicted by the traditional SN approach over a range of mean loads and load amplitudes, using Cyclic-Rampi and Mono-Rampi material models as these represent the maximum and minimum predictions from the critical plane approach in the case study. The mean load effect changes

at 20% MBL, showing that the lower the load amplitude, the higher the fatigue damage ratio when the mean load level is above 20% MBL, while the opposite happens when the mean load level is below 20% MBL. The fatigue damage ratio is one at the mean load of 20% MBL, since the critical plane approach is calibrated based on the same fatigue design data as the traditional approach at this mean load level, obtained from DNVGL-OS-E301 [7]. At higher mean loads, the fatigue damage prediction is higher for the critical plane approach than the traditional SN approach, resulting in the difference between the two methods being more significant even if the stresses at the hotspot are smaller than the elastic limit, and this becomes more significant with lower load amplitudes.

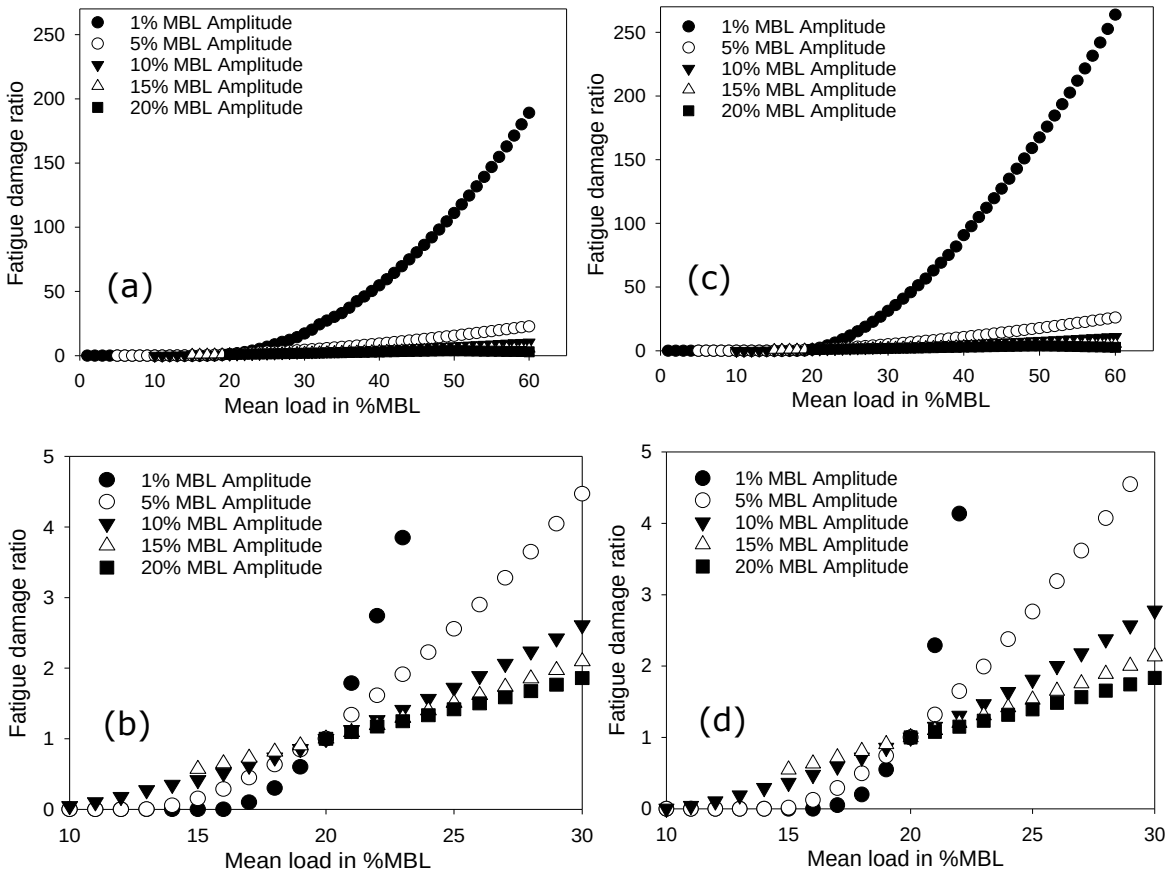

Figure 45: Mean load effects on the fatigue damage ratio in a range of mean load for Mono-Rampi (a) full range of MBLs 0-60% (b) change in behaviour due to amplitude at mean load of 20% MBL, and for Cyclic-Rampi (c) full range of MBLs 0-60% (d) change in behaviour due to amplitude at mean load of 20% MBL.

These mean load effects are reflected in the accumulated fatigue damage comparison shown in Figure 44, where about half of all the individual load cycles in the tension-spectrum have mean loads above 20% MBL and load amplitudes mostly ranged from 0% to 5% MBL. The fatigue damage ratios of the Cyclic-Rampi are higher than the fatigue damage ratios of the Mono-Rampi, explaining the increase in fatigue damage accumulation for the Cyclic-Rampi model compared to that for the Mono-Rampi. Although the Mono-Rampi cannot predict the cyclic softening behaviour, the strain hardening effect due to the proof load during the first cycle maintains the stress-strain response in the elastic shakedown with no clear plastic deformation beyond the first cycle, meaning that the cyclic plasticity effects are not evident during fatigue loading in the case study. Therefore, the results of Mono-Rampi and Cyclic-Rampi are similar.

In order to investigate the cyclic plasticity effect, Figure 46(a) and Figure 46(b) show the stress-strain responses and equivalent plastic strain, respectively, when the proof load is applied, released, and followed by cyclic loads with an amplitude of 20% MBL in an incremental mean load with an interval of 1% MBL for each progressive cycle. The cyclic stress-strain evolution and the plastic strain accumulation starts to occur at a mean load of 50% MBL, meaning that cyclic plasticity starts to take effect when the cyclic load reaches the proof load level. In contrast, the cyclic plasticity does not take effect when the cyclic load is below 70% MBL. This is because strain hardening, due to the proof load on the first cycle, has a significant effect on maintaining the stress-strain response in elastic shakedown throughout all cycles that are below 70% MBL. Therefore, the cyclic plasticity effect is minor in the case study for all material models since the individual loading cycles within the tension-spectrum are below 70% MBL. The Mono-Rampi model underestimates the amount of cumulative plastic straining with a mean difference of 28% relative to the Cyclic-Rampi model since the monotonic material model cannot predict the cyclic-softening behaviour, leading to an inaccurate estimation of the fatigue life when cyclic plasticity is involved during fatigue loading in service.

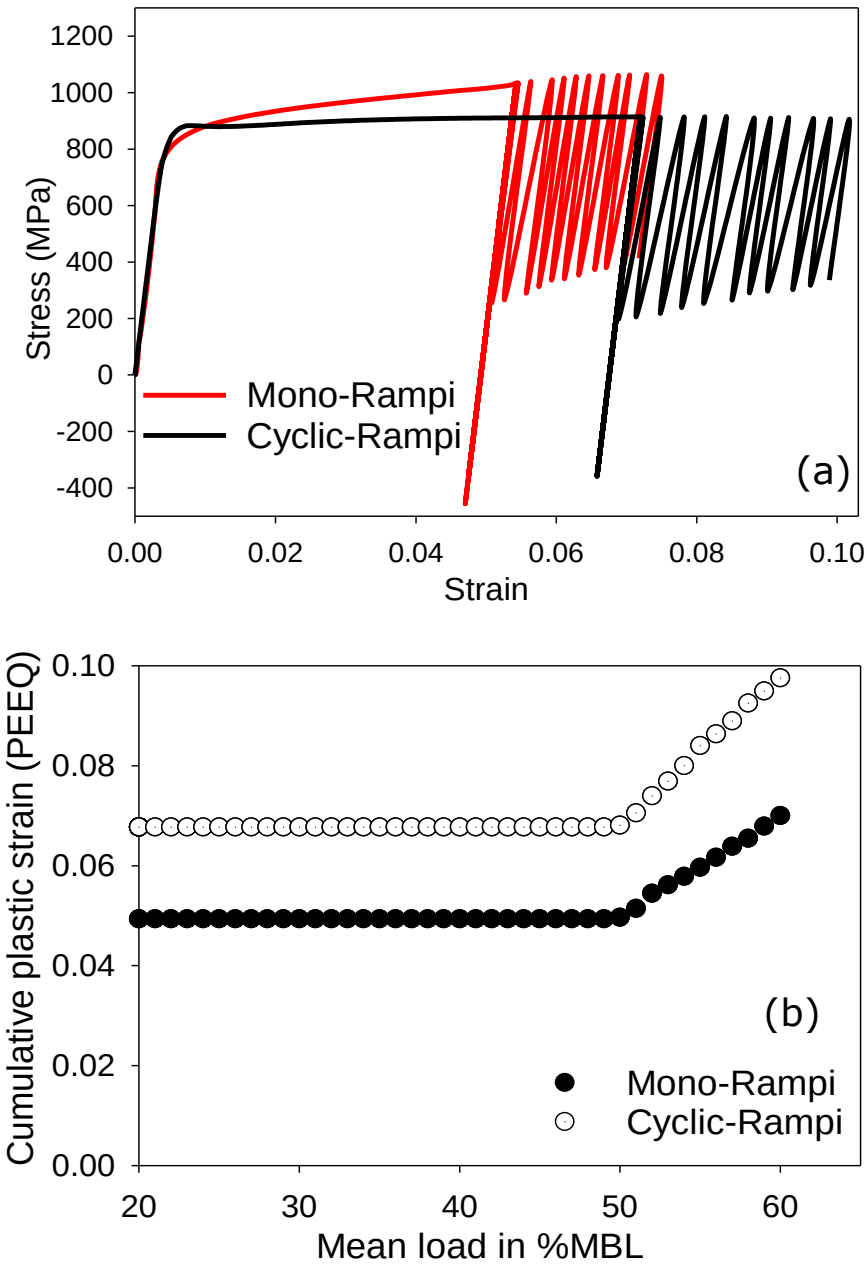

Figure 46: Fatigue simulation when the proof load is applied, released, and followed by cyclic loads with an amplitude of 20% MBL in an incremental mean load with an interval of 1% MBL for each progressive cycle, showing (a) the stress-strain responses, (b) the plastic strain accumulation.

5.5.3 Parametric study for fatigue in different sea-states

Since the mean load is shown to have a significant effect, a parametric study for fatigue in different sea-states is used to assess how often the mean load is above 20% MBL, to identify when the critical plane approach is of significance and to understand the importance of the mean load on fatigue life. The variation of waves over the long-term environment can be described by several representative sea-states, against which the fatigue damage is weighted using the lumped occurrence probability, the proportion of occurrences of a representative sea-state out of the total probability for all sea-states. A typical scatter diagram in the North Sea, consisting of 197 original sea-states, is adopted from Song and Wang [48] which uses the JONSWAP wave spectrum to define the significant wave height, H_s, and up-crossing wave period, T_z.

The scatter diagram is partitioned into nine representative sea-state blocks at which the time-domain dynamic analysis is simulated for this parametric study, as presented in Appendix D. Only the wave loads are changed in the representative sea-states, while the other assumptions and parameters remain the same as the previous case study described in section 5.5.1. Table 18 shows the selected representative sea-state blocks based on the highest occurrence rate within each block, with the respective lumped occurrence probability, p.

Table 18: The wave parameters for the nine representative partitions of the North Sea.

No.	H_s (m)	T_z (s)	p (%)
1	1.5	7.5	47.976
2	2.5	10.5	20.588
3	5.5	8.5	15.356
4	4.5	11.5	11.067
5	7.5	9.5	2.643
6	8.5	12.5	1.878
7	11.5	10.5	0.167
8	10.5	12.5	0.292
9	13.5	11.5	0.032

Figure 47 shows the mean load distribution in the individual loading cycles of tension-spectrum for each sea-state, separating mean loads at greater than 20% MBL. Sea-states 1, 2, and 3 in Figure 47(a) are benign, having respectively 0%, 0.3% and 5.3% of the mean load proportion above 20% MBL; therefore, the traditional SN approach can be used. However, sea-states 4, 5 and 6 in Figure 47(b) have respectively 21.4%, 33.5% and 36.3% of the mean load proportion above 20% MBL, and sea-states 7, 8 and 9 in Figure 47(c) have respectively 42.4%, 44% and 46.3% of the mean load proportion above 20% MBL.

At these higher sea-states, it is important to consider the detrimental effect of the mean load on the fatigue life by using the critical plane approach. Similarly, the first case study also has about half of the mean load proportion above 20% MBL. However, the load-amplitude proportions above 5% MBL, that can cause the number of cycles to failure below 10^5 in the low-cycle fatigue regime, are 15.8%, 19.4%, 34.7% for the sea-states 7-9, respectively, while this is 12.9% for the first case study. This shows that in conditions with higher proportions of severe sea-states, the higher the proportion of time the mean load is above 20% MBL and the more important the critical plane approach becomes.

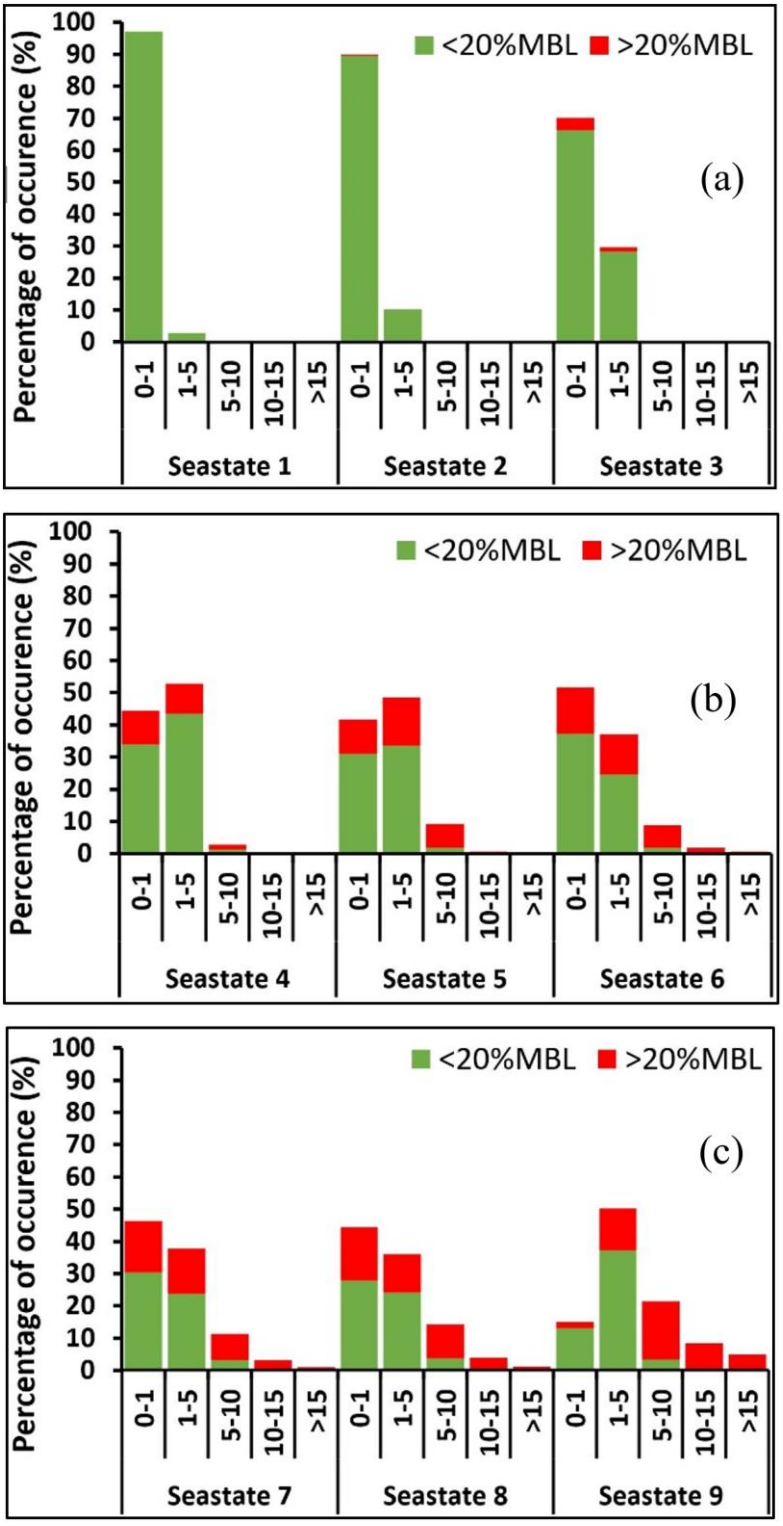

Figure 47: Mean load distribution in the individual loading cycles of tension-spectrum for (a) sea-states 1-3 (b) sea-states 4-6 (c) sea-states 7-9, where the horizontal axis denotes ranges of load amplitudes in the percentage of the minimum breaking load (% MBL) and the green represents mean load below 20% MBL and the red represents mean load above 20% MBL.

5.6 Discussion

The fatigue damage accumulation of the critical plane approach is significantly higher relative to the traditional SN approach, 75% on average for all of the material models used in the case study. This is mainly because the mean load effects are incorporated in the critical plane approach.

The 70% MBL is the load level for proof load to be applied in the first cycle prior to offshore installation; this 70% MBL proof load level is the same for every mooring chain required by the mooring standards [7] [18]. The Palmgren-Miner's rule can only be applied if the cycles are comparable where there is no material evolutionary effects or cyclic plasticity, as it doesn't account for the load sequence effects [185]. It was found that the 70% MBL is the limit for cyclic plasticity; if the tension load exceeds 70% MBL, the cyclic plasticity might induce ratcheting where plastic strain accumulates after yielding in which the loading sequence could give a detrimental effect and the Palmgren-Miner's rule could therefore no longer be applicable in that scenario [210] [211]. However, no cyclic plasticity was observed in the case study as the mechanisms are only applied when the tension load exceeds 70% MBL due to the strain hardening effect from the proof load during the first cycle, and therefore the assumption of the Palmgren-Miner's rule can be applied, although the Palmgren-Miner's rule does not account for any load sequence effects [185]. In addition, in order to keep the Palmgren-Miner's rule applicable, API-RP-2SK [18] requires using a tension limit to be below 70% MBL for the intact condition in dynamic analysis, meaning that an extreme line tension exceeding 70% MBL in a given sea-state should be anticipated for not exceeding the proof load level in design.

The mean load effect of the critical plane approach shows that fatigue life decreases with an increase in mean load. This is in agreement with full-scale tests in the recent literature [94] [99], which found that the fatigue life decreases by a factor of 5-10 as the mean load increases from 6.4% MBL to 20% MBL and found that the fatigue life decreases by a factor of 4 as the mean load increases from 10% MBL to 20% MBL.

When using the standard SN approach, common industry practices suggest using a safety factor of 3 for regularly inspected components and that this safety factor can be increased up to 10 for non-inspected components [7] [18].

However, the critical plane approach suggests that these suggested safety factors may be insufficient, indicating that the fatigue life in mooring chain failures can be overpredicted when using the traditional SN approach by factors higher than the suggested safety factors in some cases. The factors are quantified in terms of the fatigue damage ratio in Figure 45, showing that the higher the mean load, the larger the separation in fatigue damage prediction between the critical plane approach and the traditional SN approach; this can be many times larger when the mean load is above 20% MBL, depending on the mean load and the load amplitude levels.

A feature of this critical plane approach is that it predicts lower fatigue damage than the traditional SN approach when the mean load is below 20% MBL, and the difference depends on the load amplitude and the mean load as demonstrated in Figure 45. This is because the critical plane approach accounts for the compressive residual stress from the proof load during the first cycle.

To show the difference in low-cycle fatigue prediction between both approaches, Figure 48 shows the demarcation between low-cycle and high-cycle fatigue loading, at the lifetime of 10^5 cycles, predicted by using the different approaches, where the region above each line represents the low-cycle fatigue regime and the region below it indicates the high-cycle fatigue regime. The lines are generated by calculating at which load amplitude level the respective fatigue approach predicts the lifetime of 10^5 cycles across different mean load levels. The traditional SN approach shows this demarcation as a straight line at a load amplitude of just over 6% MBL since it does not consider the mean load effects, while the critical plane approach shows this demarcation as a curve where the higher the mean load, the lower load amplitude to reach the low-cycle fatigue regime.

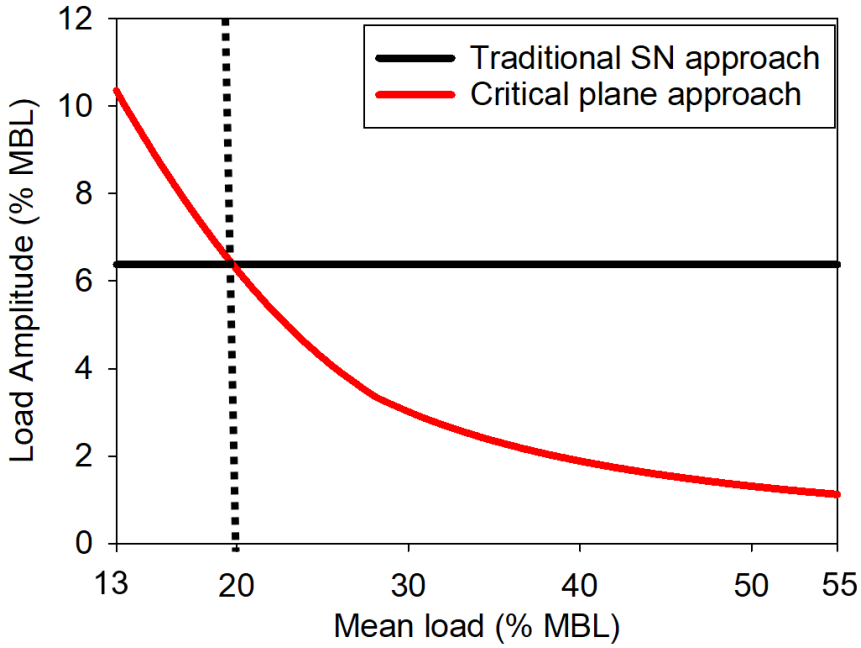

Figure 48: The separation line between high-cycle and low-cycle fatigue predictions for the traditional SN approach and the critical plane approach.

The region on the left-hand side is where the mean load is below 20% MBL and illustrates the conservativeness of the traditional SN approach as it predicts low-cycle fatigue at lower amplitude. However, on the right-hand side, the critical plane approach is more conservative from the mean load level of 20% MBL onwards, predicting low-cycle fatigue at increasingly lower amplitudes and showing a larger proportion of low-cycle fatigue for a given sea-state. The more conservative prediction of the critical plane approach is reflected in the previous case study since about half of the individual loading cycles have mean load levels above 20% MBL, where the critical plane approach predicts 12.9% in the low-cycle fatigue regime, while the traditional SN approach predicts only 7.2%. The result shows that the critical plane approach predicts almost twice the proportion of low-cycle fatigue than the traditional SN approach predicts.

The results of the case studies here show the importance of considering low-cycle fatigue contributions in mooring failures. For example, mooring chains are subjected to approximately 15×10^6 total loading cycles over three years of operation, assuming total individual loading cycles of 1828 for every 3 hours of operation based on the case study. The critical plane approach comes closer to explaining why some mooring chain failures are reported as occurring in the first three years [1] [5]. This is because it predicts a higher proportion of low-cycle

fatigue loading cycles within the total loading cycles during this period than the traditional SN approach, as demonstrated in Figure 45 and Figure 48.

The pretension affects the mean loads as the higher the pretension, the higher the mean loads, and mooring systems in the field normally have a pretension between 10% and 20% MBL [95], where the pretension in the case study is 17% MBL. As the mooring chain failures occurred in harsh sea environments [1] [5], it is hypothesised that the pretension of the greatest loaded line increases with the mean loads, which leads to an increase in the proportion of low-cycle fatigue causing the reported early failures in the first three years of operation. This is also reflected in the sea-states parametric study in section 5.5.3, where the more severe the sea-states, the higher the proportion of time the mean load is above 20% MBL and the more accurate the critical plane approach becomes. This implies that in calm sea regions, the traditional SN approach is conservative, but in harsh sea regions, the traditional SN approach can be non-conservative which is where the most early failures have occurred [1] [5].

It was found that the critical plane approach is helpful for high sea states, but not for low sea states; hence, the analysis of what approximate proportion of the mean load above 20% MBL for a sea-state needs to be performed to determine when a sea-state is high to use the critical plane approach beneficially over the traditional SN approach. Therefore, rough estimations regarding how much the fatigue damage for different metocean exposure scenarios, i.e. sea-states 1-9, are performed in comparison between the fatigue damage accumulation predictions of the critical plane approach and the traditional SN approach. This is done by using and interpolating the data of fatigue damage ratios demonstrated in Figure 45 by means of the Cyclic-Rampi model for this analysis and the tension spectrums resulted from the mooring simulations for the sea-states 1-9. The results are plotted in Figure 49. On one hand, it was found that the critical plane approach predicts lower fatigue damage accumulation for sea-states 1-4, 59.5%, 40.4%, 22.5%, 4.6%, respectively, relative to the traditional SN approach, where the mean load proportions above 20% MBL are below 25% under these low sea-states, as outlined in section 5.5.3. On the other hand, the critical plane approach predicts higher fatigue damage accumulation for sea-states 5-9, 21.9%, 46.4%, 52.9%, 51.7%, 78%,

respectively, than the traditional SN approach, where the mean load proportions above 20% MBL are above 25% under these high sea-states. This shows that, when the mean load proportion above 20% MBL is above 25% in the tension spectrum, the critical plane approach has a tangible benefit to the mooring fatigue problems in overcoming the current lack of the traditional SN approach for high sea-states; however, when the opposite happens, the traditional SN approach can still be used in mooring fatigue analysis for low sea-states. This reinforces the finding of this research that in calm sea regions, the traditional SN approach is conservative; but in harsh sea regions, the traditional SN approach is non-conservative because it doesn't take into account for the detrimental mean load effect in fatigue assessment, and the critical plane approach has a tangible benefit to the analysis outcome of mooring problems that can overcome the shortcoming.

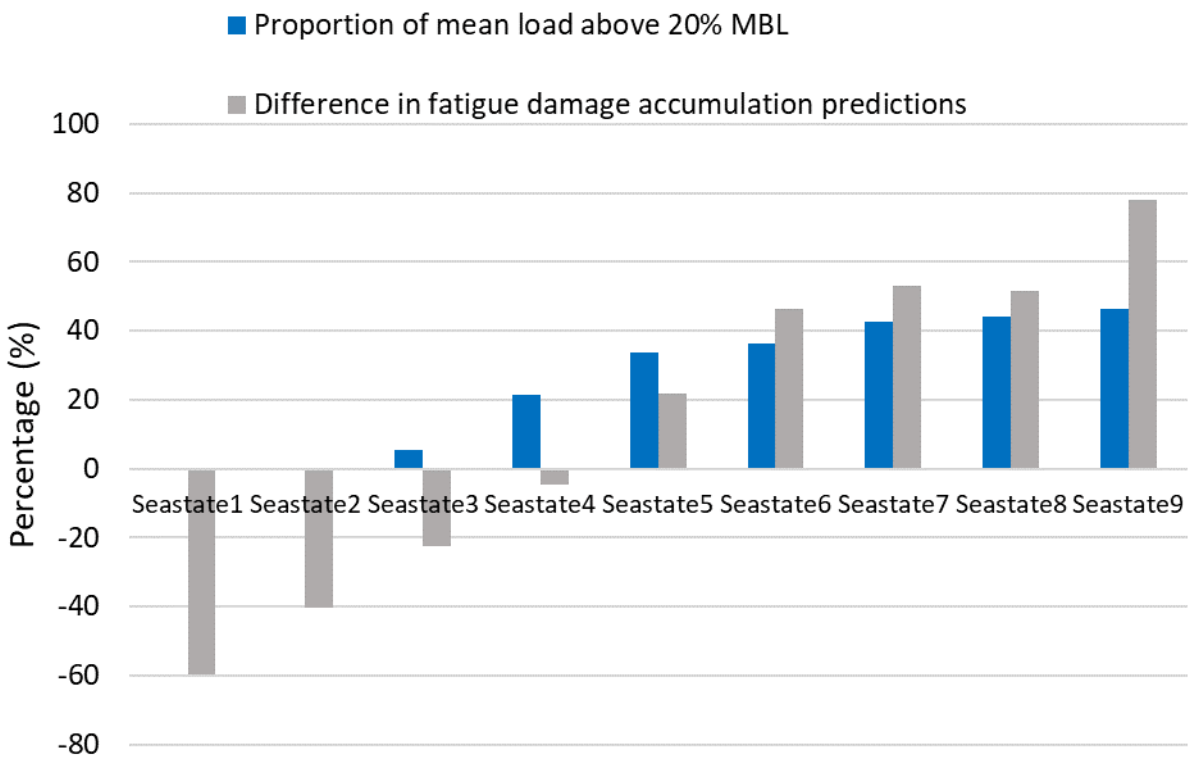

Figure 49: Summary plot for each sea-state in terms of the proportion of mean load above 20% MBL in the respective tension spectrum and the difference in fatigue damage accumulation predictions between the critical plane approach and the traditional SN approach.

5.7 Summary

This chapter explores how fatigue damage estimation changes under stochastic tension loading in operation for intact mooring chains with a more accurate representation of the low-cycle fatigue regime, using a stress-strain-based critical plane approach. The critical plane approach has been established for mooring chains based on the multiaxial stress-strain conditions at the fatigue hotspot and this is correlated with the fatigue life derived from experiments taken from the mooring standards.

The main conclusions from the findings in this chapter are summarised as follows:

- The fatigue damage accumulation predicted by the critical plane approach is significantly higher than the traditional SN approach, 75% on average for all of the material models considered here. The low-cycle fatigue assessment for mooring lines using the developed Smith-Watson-Topper critical plane approach is more sensitive to the mean load effects than to the cyclic plasticity effect. The mean load effect is detrimental when it is above 20% of the minimum breaking load. However, the effect of the cyclic plasticity is limited as the mechanisms are only applied when the tension load exceeds 70% of the minimum breaking load due to the strain hardening from the proof load application during the first cycle.

- The different material models show no significant differences in the prediction of fatigue damage accumulation since both monotonic and cyclic material models maintain the stress-strain response in the elastic shakedown with no cyclic plasticity effects involved during fatigue cycles.

- The result in the case study shows that the critical plane approach predicts approximately twice the proportion of low-cycle fatigue than the traditional SN approach predicts. The case studies of sea-states show that the proportion of mean loads above 20% of the minimum breaking load increase with higher sea-states, indicating that the more severe the environment, the more important the critical plane approach becomes to

capture the detrimental effects of the mean load, and the more different proportion of low-cycle fatigue predicted between the critical plane approach and the traditional SN approach.

- In terms of the different sea-states exposure scenarios, it was also found that the traditional SN approach is conservative when the mean load proportion above 20% MBL is below 25% in the tension spectrum which was shown in low sea-states 1-4; however, when the opposite happens which was shown in high sea-states 5-9, the traditional SN approach can be non-conservative because it doesn't take into account for the detrimental mean load effect in fatigue assessment, and the critical plane approach can overcome the shortcoming.

- The traditional SN approach is conservative when the mean load is below 20% of the minimum breaking load, but after this, it is non-conservative, which is observed in harsh environments where the majority of mooring chain failures have been found.

Chapter 6: Discussion and limitations

This thesis investigates how much fatigue damage prediction improves with a more accurate representation of the low-cycle fatigue regime, using the stress-strain based critical plane approach, Smith-Watson-Topper. The critical plane approach requires stress-strain states in mooring chains to be accurately predicted. However, there are different types of finite element models for mooring chains available in the literature which had adopted different modelling parameters, as demonstrated in chapter 4, indicating that the structural modelling work in the literature is not fully established. Therefore, this study firstly replicated these different numerical models to allow a reasonable comparison to provide the basis for choosing the most appropriate finite element model for the low-cycle fatigue analysis in this study.

These different finite element models were shown to have different performance in predicting the key elements in terms of stresses and strains along the critical paths in mooring chains. Chapter 4 demonstrates that the FE model with explicit solver, CEx8R, has no convergence problems with the least computational cost while providing the most accurate predictions of stresses and strains when compared with other models. Therefore, by using the determined finite element model (CEx8R), chapter 5 developed a Smith-Watson-Topper critical plane approach by evaluating local stresses and strains at the fatigue hotspots based on experimental fatigue test data available in the literature for mooring chains.

The developed critical plane approach demonstrates that the effects of mean load are critical in increasing fatigue damage accumulation, while the cyclic plasticity has limited effect as the mechanism is only applied when the tension load exceeds 70%. This is ascribed to the proof load application before the service fatigue cycles, as the strain hardening experienced maintains the stress-strain states in elastic shakedown throughout progressive fatigue cycles. This finding also supports the fact that the proof load application gives beneficial effects on fatigue capacity of mooring chains which agrees with results from experimental studies in the literature [30]–[35]. This mechanism also results in the material model selection having little significant impact on the estimations of fatigue damage accumulation, as shown in the case study, since both

monotonic and cyclic material models maintain the stress-strain response in the elastic shakedown with no cyclic plasticity effects involved during subsequent fatigue cycles.

The mean load effect accounted for in the critical plane approach indicates that the fatigue damage increases with an increase in mean load. The critical plane approach captures approximately twice the proportion of low-cycle fatigue events than the traditional SN approach captures in the case study used. This mean load effect is well-known in fatigue studies for other metallic engineering structures [13], [100]–[104]. However, it is not considered in the current fatigue design of mooring chains which use the traditional SN approach. Figure 45 and Figure 48 in chapter 5 indicate that the safety factor used in mooring standards may indeed not be sufficient to cover the uncertainty in their fatigue predictions. This is due to their lack of consideration of the mean load effect when the mean load is above 20% MBL, and this is likely to be of high proportion in harsh sea-states, as demonstrated in sea-states 5-9.

6.1 Potential increase in proportion of low-cycle fatigue events in the mooring line loading

The parametric study, presented in section 5.5.3, found that the higher the sea-state the more proportion of mean loads above 20% MBL within the fatigue cycles, where the highest sea-state gives 46.3% proportion of mean loads above 20% MBL within the fatigue cycles at the significant wave height of 13.5 m. However, Reistad et al. [212] highlighted how the significant wave height, H_s, in Northern North Sea could be worsened to values in the excess of 19 m in extreme weather conditions which are more than the maximum significant wave height (13.5 m) used in the parametric study. The wave height of 19 m may give above 55% proportion of mean loads above 20% MBL within the fatigue cycles, assuming a logarithmic extrapolation based on the data of mean load proportions of the sea-states in the parametric study, section 5.5.3. Such extreme weather conditions will lead to more low cycle fatigue events and lower fatigue lives predicted by the critical plane approach compared to the traditional SN approach than were witnessed in the current case study; and use of the

critical plane approach will be even more critical to capture the effect of mean loads in such extreme weather conditions.

In terms of the loading components, this case study includes a combination of wave-frequency and low-frequency tension spectrum without considering the influence of vortex-induced motion (VIM) since the moored platform used in this study is a ship-shaped, FPSO, which is not subject to the VIM according to API-RP-2SK [18]. However, other types of moored platforms with large circular cylinders, e.g. semi-submersibles, spars may experience the VIM, which causes oscillations and drag in the mooring line tension [7]. The VIM will occur if the natural frequency of the platform in the transverse direction lies in the vicinity of the vortex shedding frequency of the cylindrical structure when exposed to a steady current [7] [18]. Oscillations in the line tensions caused by the VIM could be significant, adding to the wave-frequency and low-frequency tension spectrum, especially when the oscillations coincide with one another in superpositions, resulting in increased proportion of load amplitudes above 5% MBL within the fatigue cycles. In addition, the occurrence of VIM also increases the mean drag force in the current direction [7], implying increased mooring line tension and increased proportion of mean loads above 20% MBL within the fatigue cycles.

The magnitude of the oscillations and the drag depends on how close the natural frequency with the vortex shedding frequency, where the natural frequency is dependent on the inertia of the platform, and vortex shedding frequency is dependent on the current speed and diameter; DNV-OS-E301 [7] suggest to check for occurrence of VIM using the current speed with 100-years return period, indicating a potential frequency of VIM for every 100 years. Hence, the proportion of low-cycle fatigue contributions will increase particularly for mooring lines of moored platforms with columns or pontoons, e.g. spars and semi-submersible that experience the VIM. In addition, as an area of interest for offshore wind turbines gets larger and further away from the onshore in the future, this will also increasingly be important to moored offshore wind turbines which mainly use columns as their platforms on the sea-surface.

The potential increase in the proportion of low-cycle fatigue events, discussed here, would lead to a greater difference in the accumulated fatigue damage predictions between the critical plane approach and traditional SN approach,

and the use of the critical plane approach will be even more critical to capture the low-cycle fatigue contribution in the mooring line loading.

6.2 Potential increase in low-cycle fatigue proportion from the critical plane approach

The Smith-Watson-Topper critical plane approach has been demonstrated by previous studies in the literature [117], [135]–[143], [208] to provide satisfactory results when compared to experiments by accurately capturing the effects of mean load and cyclic plasticity. This is because it takes the stress-strain function at the fatigue hotspot as the *SWT* damage parameter on the most severely damaged plane due to fatigue. This is a better physical representation of what controls fatigue life than just simple stress range as it considers the mean load and any cyclic plasticity effects on the evolution of fatigue damage, which will govern low-cycle fatigue [132] [134].

However, Chao et al. [117] found that using the averaged stress-strain gradients over a reasonably defined distance into the hotspot depth (approximately 5% of diameter), known as the critical distance method [213], could increase the accuracy of the Smith-Watson-Topper critical plane approach, rather than simply using the surface stress-strain parameters at the hotspot for shot-peening effects study. It might be beneficial to compare the current results presented in this study with the results using the critical distance method to determine their differences in low-cycle fatigue estimations for further development of this method for mooring chains.

In order to ensure accurate life prediction, it has been suggested that the applied critical plane criterion should be chosen according to a specific cracking mode that is commonly observed [134]. The Smith-Watson-Topper critical plane approach is most suitable for Mode I cracks that are developed by high tensile stresses, and this is selected since high tensile stresses have been observed at the fatigue hotspots of mooring chains under tension loading [26]–[29], [94]. However, this cracking mode can be difficult to determine since it depends on the internal defects and the manufacture of the material which may vary in the field [120] [133]. Therefore, comparing the result of Smith-Watson-Topper

criterion with other stress-strain-based critical plane criteria might be useful to describe all the possible failure situations to determine their differences in successfully predicting the low-cycle fatigue. The Fatemi-Socie criterion [214] is one of the other well-known stress-strain-based critical plane approaches, which assumes cracks developed by high shear stresses in mode II, and this criterion can be used for comparison to assess if this provides a better description of the governing fatigue processes.

The critical plane approaches described here are total life approaches which can conveniently be used to predict the total fatigue life in mooring chains. However, this is based on the assumption that the surface of the component is intact without considering the effects of varying surface roughness, or any pre-existing defects. This assumption is reasonable as the chain is inspected to ensure that there are no visible surface defects prior to deployment. However, it is difficult to directly apply this method in predicting the remaining life of a component containing initial surface-defects because of the inherent limitation of this defect-free assumption. Hence, prior to deployment, the surface of mooring chains must be carefully checked to make sure that there are no visible surface defects, e.g. initial surface cracks, to allow confidence that a reasonable fatigue life estimation is provided using the critical plane approach proposed here. In conditions where pre-existing defects, e.g. initial cracks, on the surface significantly accelerate the crack initiation life, a more advanced life assessment approach which can consider the detrimental effects of pre-existing defects and model their growth under the applied loading conditions (e.g using as fracture mechanics) might be applied instead to better capture the fatigue behaviour in mooring chains rather than the total life, critical plane approach proposed here.

6.3 Recommendations for application

This study found that the traditional SN approach is conservative when the mean load is below 20% MBL, but after this, it is non-conservative. Significant numbers of loading events above 20% MBL can be observed in harsh environments, where the majority of premature mooring chain failures have been found. This is because the critical plane approach predicts higher fatigue damage than the traditional SN approach, for the case study considered here,

since it allows for the consideration of mean load effects when the mean load is above 20% MBL. The case studies of sea-states also show that the proportion of mean loads above 20% MBL increase with higher sea-states, indicating that the more severe the environment, the more important the critical plane approach becomes to capture the detrimental effects of the mean load. In terms of the different sea-states exposure scenarios, it was also found that the traditional SN approach is conservative when the mean load proportion above 20% MBL is below 25% in the tension spectrum which was shown in low sea-states 1-4; however, when the opposite happens which was shown in high sea-states 5-9, the traditional SN approach can be non-conservative because it doesn't take into account for the detrimental mean load effect in fatigue assessment, and the critical plane approach can overcome the shortcoming. Therefore, it is suggested to use the critical plane approach for analysing fatigue of mooring lines, particularly when operating in harsh sea-environments where there are high sea states.

Fatigue tests of intact mooring chains should also be performed with mean load levels above 20% MBL across a range of load amplitudes to further validate the findings in this study to ensure this method is reliable to be adopted into classification rules and for industrial use.

It is useful to revisit early failure incidents in the past to explore where the developed approach would have been helpful. One example is Petrojarl Banff FPSO whose five of its ten mooring lines parted at its position at Canadian Natural Resources' Banff field in the North Sea, resulting vessel drifted as well as a lengthy shutdown period for repairs [5]. An investigation found that the initiating cause on Banff was a chain failure near the fairlead was during stormy conditions, making the mooring lines to withstand a much larger force than originally design for [11]. It was reported that the storm in the location may reach a significant wave height, H_s, of 19 m [212]. Such high sea-state conditions during the storm and the large force tensions may have caused high proportions of the mean load above 20% MBL in the five broken mooring lines; hence, the critical plane approach could have been helpful to anticipate the failures from happening by providing a more accurate low-cycle fatigue

assessment and suggesting a more appropriate means to avoid the failures from happening.

Another example is Gryphon Alpha FPSO which lost four of its eight mooring lines [5], and the insurance pay-outs hit nearly £440 million as the vessel drifted to a certain distance pulling their risers to rupture in a storm [10]. The accident was reportedly due to top chain failures in the harsh environment of North Sea, where an investigation indicates the wave height may reach 26.5 m [215], which is the 100-year North Sea storm condition, and a maximum wind speed reaching 110 km/h [216]. Such stormy condition could impose strong drag forces to mooring lines and significantly increase the proportions of mean loads above 20% MBL in the four broken mooring lines; in such situation, the critical plane approach could have been helpful by predicting a more accurate low-cycle fatigue lives and providing a more conservative design for the mooring lines in order to prevent the failures from happening.

A mooring system has many design parameters, and these parameters can be designed to minimise the low-cycle fatigue problems found in this study. In order to comply with the standard, e.g. DNV-OS-E301, this study uses the 20% MBL mean load to develop the critical plane approach based on the fatigue tests and this 20% MBL mean load is the same for every offshore mooring chain used in the fatigue tests for different material grades (i.e. R3 and R4) across different load ranges which derived the SN curve for the traditional SN approach in the standard DNV-OS-E301. The reference to this has been documented in many mooring chain literatures [7] [90] [94] [99].

The critical plane approach was correlated with fatigue life predictions based on the fatigue tests deriving the SN curve using material grade R4. If a different material grade is used, then the mean load level used in the fatigue tests will be adjusted to 20% MBL of the corresponding material grade being used to as the higher the steel strength the greater the minimum breaking load, and the effects of low-cycle fatigue contribution for the critical plane approach will be proportional to the corresponding minimum breaking load. This is supported by Zhang et al. [94] who also confirmed that fatigue performance of material grade R4 is proportional to the fatigue performance of material grade R5 based on fatigue tests which were performed at a constant mean load of 20% MBL, as

long as the used mean load level is adjusted to the respective 20% MBL of the corresponding material grade being used in the fatigue tests when the load is expressed in the respective % MBL of each chain.

In regard to chain diameter, this study analyses the mooring line loading in terms of % MBL experienced with a diameter of 76 mm; if larger diameters are used, the effects of low-cycle fatigue contribution found in this study (the critical plane approach) will be proportional to the minimum breaking load that the chains have, as the larger diameter the greater the minimum breaking load of the chain. This is supported by the fatigue test results found by Zhang et al. [94] that there was proportionality in fatigue performance between two different chain diameters (76 mm and 127 mm) when the load is expressed in the respective % MBL of each chain. However, if the traditional SN approach is developed based on fatigue tests at a different mean load (other than 20% MBL mean load), then the threshold of 20% MBL will shift to the different mean load particularly, and the critical plane approach will need to be recalibrated to the relevant fatigue test data.

In order to put the developed method in mooring design and analysis context, some design aspects are discussed. One common recommendation in the industry is to increase the minimum breaking load by increasing the chain diameter, which will decrease the cyclic load magnitude in terms of % MBL experienced; however, this can increase the applied pretension to above 20% MBL because the larger the diameter, the heavier the mooring line will be. Another recommendation is to lower the pretension by making the mooring line longer; however, this may reduce the mooring line damping, increasing the motions and decreasing the fatigue life [46] [67]. Another recommendation to reduce the mooring line weight for lowering the pretension is by shortening the chain section and extending the wire rope section, as the wire rope section is lighter than the chain section. However, this will decrease the stiffness and increase flexibility in areas with large movements, leading to an increase in the mooring line motions and a decrease in the fatigue life [42] [46]. For another recommendation, increasing the steel grade to achieve a greater minimum breaking load could be a viable solution to reduce the cyclic load magnitude in terms of % MBL; however, this is not a simple substitution and should be

adopted with caution since the higher the strength of steels, the more prone to hydrogen-assisted cracking they may be, bringing in additional failure modes, not accounted for in the fatigue evaluation [11] [217] [218].

In the design process, FLS (Fatigue Limit State) is commonly assessed on which all mooring lines are in intact conditions, where the configuration of mooring lines is optimised for application in a particular project; the case study in this study was performed the analysis with intact mooring lines. However, another design analysis of ALS (Accidental Limit State) requires a mooring system to still be capable of serving its station-keeping function when one mooring line is assumed to have failed, according to mooring standards, e.g. DNV-OS-E301 [7] and Norsok N-003 [219]. A significant increase in the proportion of mean loads above 20% MBL in the greatest loaded mooring line loading is therefore expected when one mooring line is removed from the mooring system against the load in service, and again this accident will lead to more low-cycle fatigue events and lower fatigue lives predicted by the critical plane approach compared to the traditional SN approach than were observed in the current case study. Therefore, increasing the number of mooring lines could be a viable solution in order to reduce the tensions of mooring lines, although this method will increase the financial cost. It can be seen from the discussion above that some alternatives in the mooring design can be applied to address the implications of findings in this study in order to reduce the mooring line fatigue failures in the future.

It should also be noted that the chain can also be corroded or subject to wear, which may reduce the chain fatigue capacity by promoting local stress concentration leading to locally more detrimental mean load effects, leading to a decrease in the 20% MBL apparent (global) mean load threshold and an increase in the proportion of low-cycle fatigue events experienced. The addition of corrosion effects in the fatigue prediction may also become more complicated because, in addition to the expected morphology change, many physical interactions (e.g. corrosion-fatigue interactions [220], mechano-electrochemical induced corrosion [201]) could also be considered, above and beyond the effect of local stress raisers due to pitting in the chain geometry. The critical plane approach could however be modified further to consider the effects of pits on local stress state evolution. This is an important failure

mechanism and the combination of low-cycle fatigue and corrosion are likely to form a vicious cycle, with each exacerbating the other, and requires further in-depth analysis.

6.4 Future work

Based on the discussion above, a number of recommendations for future work to provide more understanding on this topic are derived, as follows:

- Provide fatigue testing data of intact mooring chains at mean load levels above 20% MBL across a range of load amplitudes to further validate the findings in this study;
- Perform low-cycle fatigue assessment on a moored platform consisting of cylindrical structures subjected to the vortex-induced motion (VIM) to assess how much the influence of the VIM might increase the proportion of low-cycle fatigue events;
- Compare the results presented in this study with the results using the critical distance method to determine their differences in low-cycle fatigue estimations for further development of this method for mooring chains;
- Compare the results of Smith-Watson-Topper criterion with other stress-strain-based critical plane criteria to assess if this provides a better description of the governing fatigue processes for mooring chains;
- Modify further the critical plane approach to consider the effects of pits on local stress state evolution for mooring chains with geometric changes due to wear or corrosion.

Chapter 7: Conclusion

The safety and continuous operation of a range of offshore floating platforms rely on the integrity of mooring chains to keep these platforms in position against adverse environments over design lives of 20-years, or longer. However, mooring chain failures have occurred at a critically high rate in recent decades below this design life. Fatigue failure is the most significant cause of these premature failures, and this is likely to be particularly significant when operating in harsh sea environments. Since failure in service occurs earlier than the design lives, it is proposed that the mooring chains are likely to have experienced a high proportion of low-cycle fatigue loading with high mean loads, and the lack of consideration of mean load effects and cyclic plasticity effects during low-cycle fatigue in the current design is therefore proposed to be a contributing factor for the current non-conservative fatigue assessments of mooring chains.

Therefore, this thesis performs a fatigue analysis incorporating a more accurate representation of the low-cycle fatigue regime, using a stress-strain-based critical plane approach. The fatigue analysis also considers stochastic tension loading in service for intact mooring chains to determine the importance of low-cycle fatigue in some of the early failures currently observed in operating mooring lines. This approach allows the consideration of mean load and cyclic plasticity effects on the fatigue damage which governs the low-cycle fatigue, where fatigue damage is assessed directly in terms of local strains and stresses at the fatigue hotspot.

As this study simulates fatigue in finite element analyses, an appropriate finite element model for predicting the representative stress-strain parameters required by the critical plane approach is essential. However, there are different finite element models available in the literature for predicting the stresses and strains in mooring chains, and no direct evaluations of which model is appropriate for this purpose in the literature. Therefore this study firstly benchmarks different types of FE models, and found that they model the stresses and strains differently along the critical paths in mooring chains. The results of the comparison show that the explicit model (CEx8R) has no

convergence problems with the least computational cost while providing the most accurate predictions of the stresses and strains in mooring chains.

The explicit model has then been used to develop the stress-strain-based critical plane approach based on the multiaxial stress-strain conditions at the hotspot, and this is correlated with the fatigue life derived from tests taken from the mooring standards. The fatigue damage accumulation predicted by the critical plane approach is significantly higher than for the traditional SN approach, 75% higher on average for all of the material models considered here, using a mooring line simulation of an FPSO as a case study. It is found that the mean load effect is detrimental compared to SN predictions when it is above 20% of the minimum breaking load, which was shown to be a high proportion of sea-states 5-9. However, the effect of the cyclic plasticity assumptions in the materials models is limited as the mechanism was only applied when the tension load exceeds 70% of the minimum breaking load, leading to elastic shakedown for further cycles due to the strain hardening provided by the proof load application during the first cycle.

The critical plane approach predicts higher proportions of low-cycle fatigue than the traditional SN approach in the mooring line loading when the mean load is above 20% of the minimum breaking load, with the difference being dependent on the mean loads and the load amplitudes witnessed in operation. This is reflected in the case study, showing that the critical plane approach predicts about twice the proportion of low-cycle fatigue than the traditional SN approach predicts. The traditional SN approach is conservative when the mean load is below 20% of the minimum breaking load, but after this, it is non-conservative, which is likely to be observed in harsh environments where the majority of mooring chain failures were witnessed. The low-cycle fatigue analysis presented in this study comes closer to explaining why current fatigue assessment in mooring chain applications is non-conservative and demonstrates that the critical plane approach should be accounted for in mooring line design as it accounts for mean load effects.

It was also found that the traditional SN approach is conservative when the mean load proportion above 20% MBL is below 25% in the tension spectrum which was shown in low sea-states 1-4; however, when the opposite happens

which was shown in high sea-states 5-9, the traditional SN approach can be non-conservative because it doesn't take into account for the detrimental mean load effect in fatigue assessment, and the critical plane approach can overcome the shortcoming. Therefore, in terms of the implications of this research, the stakeholders of moorings can take technical advice based on the finding of this thesis, and this requires the owners, vendors and designers to work together in improving the mooring integrity accordingly. A suggested practice to achieve this is to rigorously check the proportion of mean load above 20% MBL within the tension spectrums for different representative sea-states during the design phase. If the proportion of mean load above 20% MBL within the tension spectrum is more than 25% for a sea-state, then the critical plane approach needs to be used to consider the detrimental mean load effect to obtain a more accurate low-cycle fatigue assessment and a safer design more conservatively than the traditional SN approach; otherwise, the traditional SN approach could still be used in fatigue assessment. In addition, increasing the chain diameter or changing other parameters of chain design may exacerbate this problem, indicating that more explicitly tailored chain design is needed to reduce this issue. Therefore, a suggested practice is to carefully select and evaluate the mooring design parameters, e.g. chain diameter, mooring line length, number of mooring lines, material grade, during the design phase in order to ensure that the majority of tension spectrums have less than 25% of the proportion of mean load above 20% MBL for the representative sea-states. Such engineering design system shall improve the mooring integrity to prevent short lives of mooring chains from happening due to low-cycle fatigue problems in the future.

Appendix A List of Early Mooring Chain Failure Scenarios

Table A-1: Early mooring chain failure scenarios in the past found in the literature.

Year of accident	Vessel Name	Age at failure	Failure scenarios and attributed root causes	Failure location	Ref.
1981	Argyl Transworld	6 years	Fatigue: three mooring chains failed near the fairlead after the rig had been hit by an unusually large wave. Multiple mooring line failure resulting vessel drifted away and risers being ripped out.	Upper	[8]
1982	CALM 1	2 months	Fatigue: failure due to bending-induced fatigue occurred during typhoon 2 months after installation. The chains failed at the top of a mooring line.	Upper	[8]
1986	CALM 2	4 years	Abrasion-corrosion: excessive corrosion and abrasion are the main attributed causes at touch down	Lower	[6]
1994	Petrojarl 1	8 years	Fatigue: four of eight lines failed simultaneously after being hit by a 20 to 25m high wave. The chains parted in an area close to the top of a mooring line.	Upper	[8]
2002	Girassol	8 Months	Fatigue: five of nine lines broke due to out-of-plane bending induced fatigue at the top chain of a mooring line in 3 events during 2002 and 2003.	Upper	[37]

2005	Foinaven	9 years	Fatigue-corrosion: a total of five lines broken initiated at corrosion pitting due to SRB enhanced corrosion.	Upper	[5]
2006	Schiehalion	8 years	Fatigue: one of 14 lines parted in chain inside chain hawse pipe due to bending-induced fatigue	Upper	[5]
2006	Varg	7 years	Abrasion-corrosion: one of ten lines parted in the corroded chain due to sulphate reducing bacteria.	Lower	[5]
2006	Nanhai Shengli	9 years	Fatigue: A typhoon damaged six of ten mooring lines at the fairlead and three flexible risers completely broke away.	Upper	[38]
2007	Kikeh	2 months	Material defects: one line parted in shackle on anchor due to cracks on the material.	Lower	[5]
2008	Dalia	2 years	Abrasion-fatigue: one of twelve lines broken near the anchor pile. The chains might have been knotted in the mud.	Lower	[5]
2008	Balder	9 months	Fatigue: one of ten lines parted in the chain due to fatigue failure near the fairlead when operating in harsh sea-environments.	Upper	[5]
2008	North Sea FPSO	4 years	Fatigue-wear: excessive wear occurred in the fairlead chain.	Upper	[6]
2010	Transocean Winner	4 years	Abrasion-fatigue: The sudden fracture caused by long-term fatigue loading and interaction with the seabed. They broke about 175m from the fairlead in a 195m long section.	Lower	[11]

2010	Jubarte	2 years	Fatigue-Corrosion: 3 lines broken likely due to microbiological induced corrosion leading to increased stress and failure by fatigue.	Lower	[5]
2011	Songa Dee	5 years	Fatigue: the chain broke at the fairlead and fell to the seabed. All observations corresponded with overloading of the chain-link due to a storm.	Upper	[11]
2011	Transocean Leader	3 years	Fatigue-corrosion: the chain broke inside chain hawse at the top end of the mooring line. The reduced cross-section due to corrosion would have resulted in lower strength and lower fatigue performance.	Upper	[11]
2011	Gryphon Alpha	17 years	Fatigue: the vessel broke four of its 10 mooring chains in a storm, causing the vessel drifted and risers broken.	Upper	[10]
2011	Banff	12 years	Fatigue: 5 of 10 lines failed in a storm, causing the vessels drifted 250 metres off location.	Upper	[5]
2011	Fluminese	8 years	Fatigue: one of nine lines parted in a top chain during extreme loading situations.	Upper	[5]
2012	Transocean Spitsbergen	3 years	Fatigue-corrosion: the chain failed about 10m from the fairlead with corrosion pits acting as stress concentrations to initiate fatigue crack.	Upper	[11]

2012	Deepsea Atlantic	3 years	Fatigue: the chain failed approximately 10 m from the fairlead due to a storm.	Upper	[11]
2012	Norne FPSO	5 years	Fatigue-wear: the chains failed in the fairlead. The failure was attributed to fatigue caused by bending of the chain.	Upper	[11]
2013	Petrojarl Varg	8 years	Fatigue-wear: the chains failed due to bending-induced fatigue in the fairlead. Wear on the chain's surface acted as stress intensifiers.	Upper	[11]
2013	Leiv Eiriksson	1 year	Fatigue: the chain failed at the fairlead. fatigue overloading occurred in combination with stress concentrations in the region of failure.	Upper	[11]
2014	Deepsea Bergen	1 year	Fatigue: a chain-link failed due to a storm near the fairlead.	Upper	[11]

Appendix B Mesh convergence analysis

The fundamental concept of FEA is based on the concept that structures are approximated by a number of discrete elements. The size of the mesh elements of a structure has an effect on the results when the mesh size is considerably large. A mesh convergence analysis should therefore be performed to evaluate the converging mesh size where the effect of the mesh element size becomes negligible in order to ensure the efficiency and the accuracy of the FE model. The mesh convergence analyses are used to define the final mesh size for the slave model since the results are extracted from these locations, while the mesh size for the master model is relatively coarse. The effect of the mesh element size on the longitudinal stress at the crown, i.e. the critical fatigue hotspot, of mooring chains was examined by gradually refining the mesh size from a coarse mesh size to a fine mesh size.

ABAQUS simulations were run at each mesh size until the convergence is achieved when the mesh size no longer influences the results more than a 0.3% difference between the finest mesh size and the second finest mesh size. The difference is considered to be negligible and provide confidence in the FE model, fulfilling the convergence criteria according to ABAQUS [192]. Thus, the second finest mesh size is determined to be the final mesh size for the slave model since it fulfils the convergence criteria and satisfactorily balances accuracy and computational efforts. The mesh convergence analysis is performed for each section that have been referred to this Appendix.

Appendix B.1 Mesh convergence analysis referred in section 4.4.1

This mesh convergence analysis is performed for different numerical models at a tension load of 53.4 kN with a chain diameter of 10 mm. For each numerical model, the second finest mesh size is selected for the slave model since it has been checked to have less than a 0.3% difference compared to the finest mesh size to fulfill the mesh convergence criteria and to ensure the efficiency and the accuracy of the FE model. The results of the convergence analysis are shown in a table, where the resulted stress and the element number are plotted in the following figure for the different numerical models, i.e. EP20R, P20R, C20R, C8R,

C8I and CEx8R. The convergence analyses found that the final meshes for each model have a corresponding size of 0.4 mm for the slave model and 1 mm for the master model.

EP20R

Table B-1 Different mesh sizes and the resulted longitudinal stress for EP20R.

No.	Element Number	Mesh density level in size (mm)	Longitudinal stress (MPa)
1	792	1.2	1470.23
2	1300	1	1467.99
3	3060	0.8	1466.74
4	6660	0.6	1465.8
5	21186	0.4	1465.14
6	32175	0.35	1465

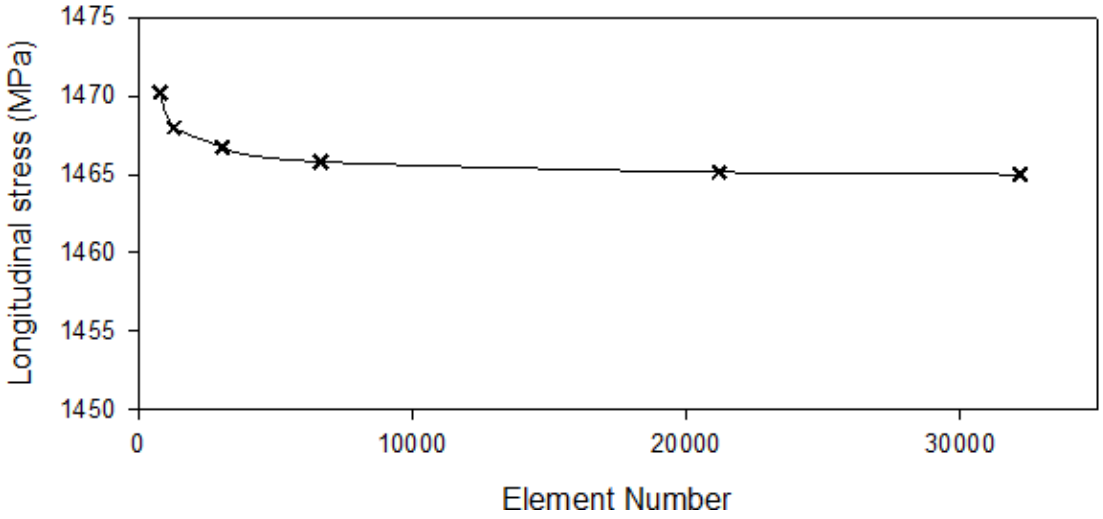

Figure B-1 Mesh convergence study at the crown for EP20R model.

P20R

Table B-2 Different mesh sizes and the resulted longitudinal stress for P20R.

No.	Element Number	Mesh density level in size (mm)	Longitudinal stress (MPa)
1	792	1.2	1086.92
2	1300	1	1085.11
3	3060	0.8	1083.4
4	6660	0.6	1082.66
5	21186	0.4	1082.09
6	32175	0.35	1081.99

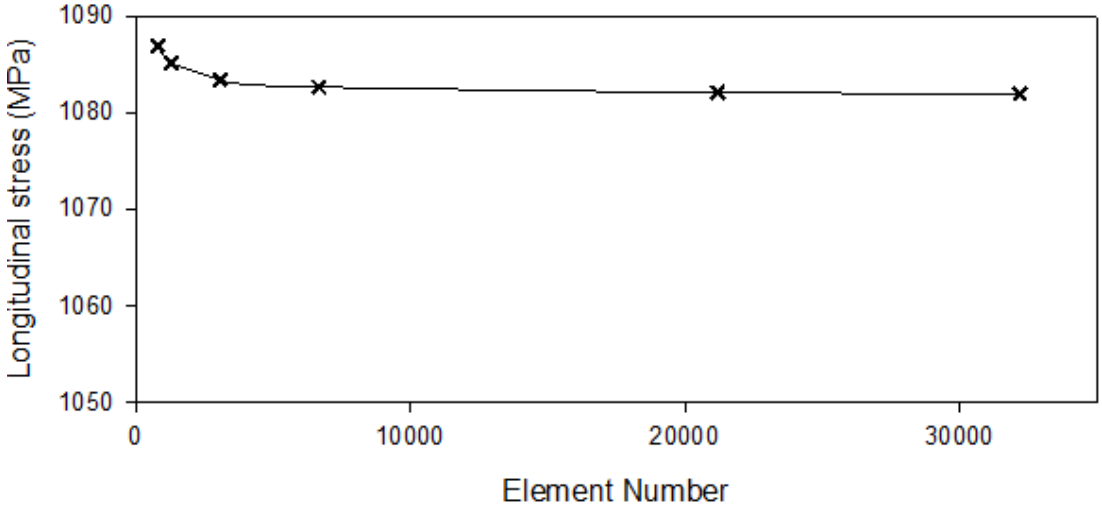

Figure B-2 Mesh convergence study at the crown for P20R model.

C20R

Table B-3 Different mesh sizes and the resulted longitudinal stress for C20R.

No.	Element Number	Mesh density level in size (mm)	Longitudinal stress (MPa)
1	943	1.2	1086.47
2	1431	1	1086.51
3	2890	0.8	1083.86
4	7682	0.6	1082.89
5	21828	0.4	1082.51
6	33228	0.35	1082.38

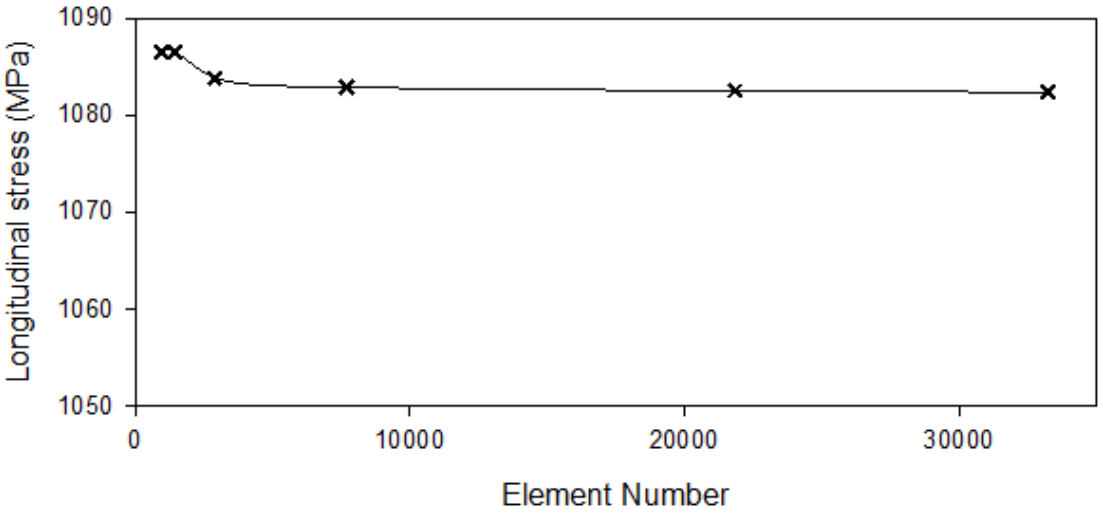

Figure B-3 Mesh convergence study at the crown for C20R model.

C8R

Table B-4 Different mesh sizes and the resulted longitudinal stress for C8R.

No.	Element Number	Mesh density level in size (mm)	Longitudinal stress (MPa)
1	943	1.2	1079.64
2	1431	1	1082.3
3	2890	0.8	1083.2
4	7682	0.6	1083.22
5	21828	0.4	1084.11
6	33228	0.35	1083.96

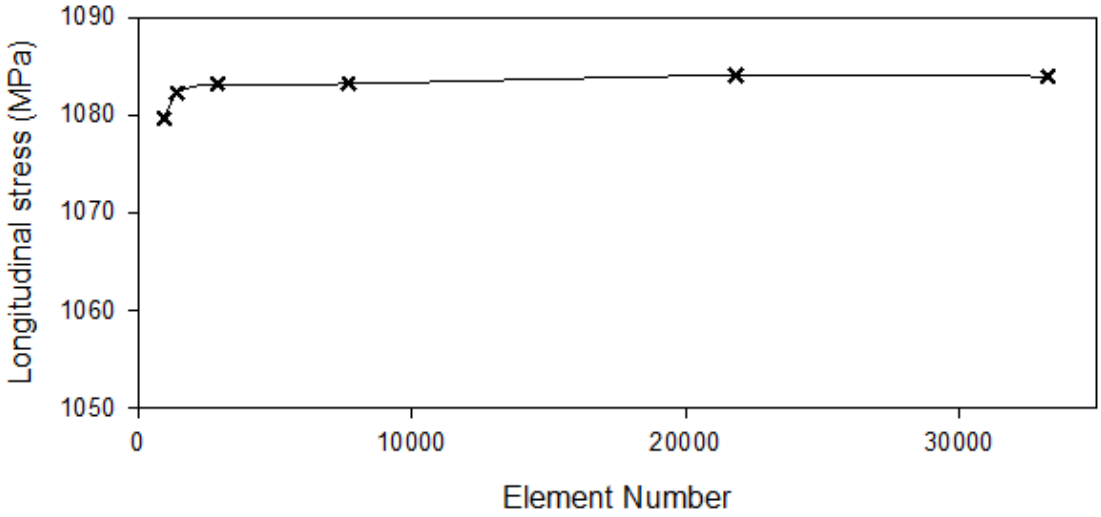

Figure B-4 Mesh convergence study at the crown for C8R model.

C8I

Table B-5 Different mesh sizes and the resulted longitudinal stress for C8I.

No.	Element Number	Mesh density level in size (mm)	Longitudinal stress (MPa)
1	828	1.2	1060.72
2	1485	1	1058.25
3	2754	0.8	1061.17
4	6440	0.6	1066.6
5	23046	0.4	1071.38
6	33228	0.35	1072.45

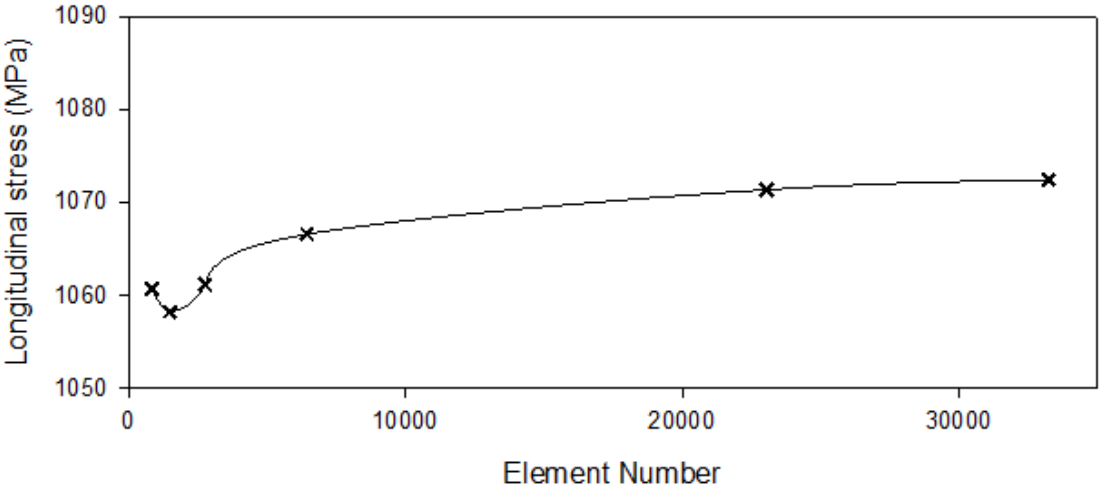

Figure B-5 Mesh convergence study at the crown for C8I model.

CEx8R

Table B-6 Different mesh sizes and the resulted longitudinal stress for CEx8R.

No.	Element Number	Mesh density level in size (mm)	Longitudinal stress (MPa)
1	851	1.2	1060.72
2	1404	1	1058.25
3	2618	0.8	1061.17
4	6532	0.6	1066.6
5	23046	0.4	1071.38
6	32760	0.35	1071.96

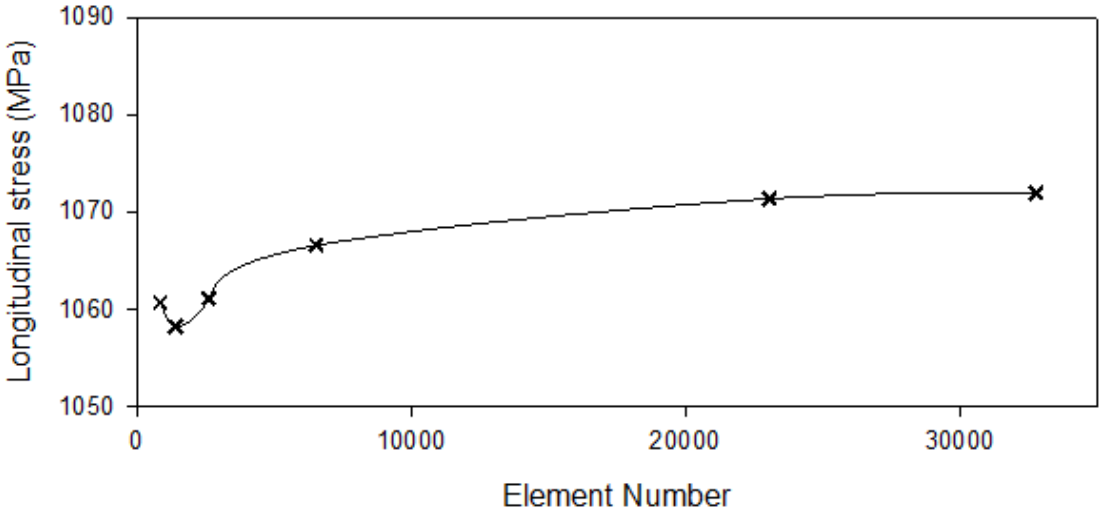

Figure B-6 Mesh convergence study at the crown for CEx8R model.

Appendix B.2 Mesh convergence analysis referred in section 4.4.2

This mesh convergence analysis is performed for different numerical models at a tension load of 2442 kN with a chain diameter of 76 mm. For each numerical model, the second finest mesh size is selected for the slave model since it has been checked to have less than a 0.3% difference compared to the finest mesh size to fulfill the mesh convergence criteria and to ensure the efficiency and the accuracy of the FE model. The results of the convergence analysis are shown in a table, where the resulted stress and the element number are plotted in the following figure for the different numerical models, i.e. EP20R, P20R, C20R, C8R, C8I and CEx8R. The convergence analyses found that the final meshes for each model have a corresponding size of 3.5 mm for the slave model and 10 mm for the master model.

EP20R

Table B-7 Different mesh sizes and the resulted longitudinal stress for EP20R.

No.	Element Number	Mesh density level in size (mm)	Longitudinal stress (MPa)
1	500	12	1137.7
2	690	10	1135.4
3	1650	8	1133.9
4	3560	6	1132.8
5	11328	4	1132
6	17204	3.5	1131.8
7	27360	3	1131.7

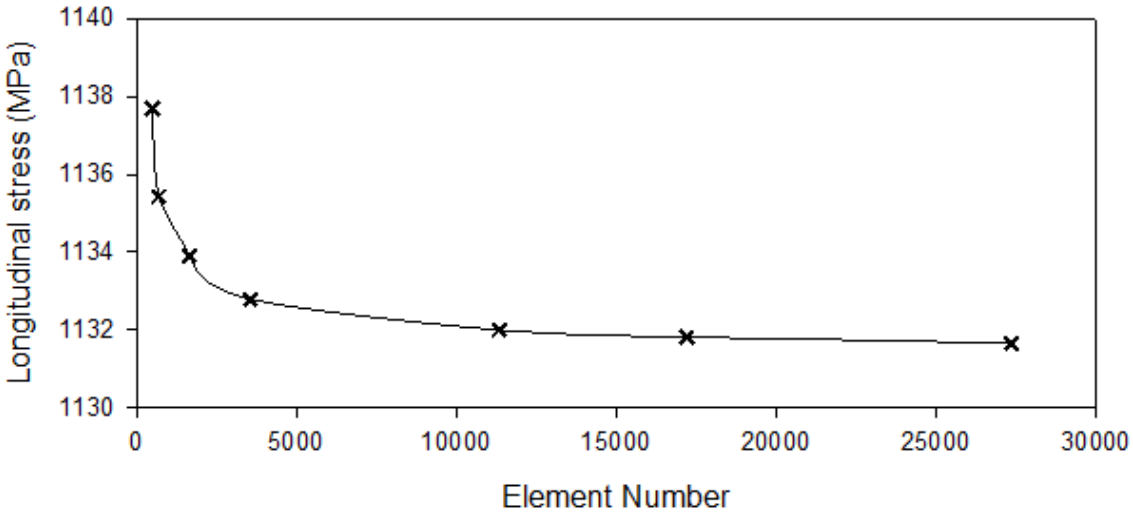

Figure B-7 Mesh convergence study at the crown for EP20R model.

P20R

Table B-8 Different mesh sizes and the resulted longitudinal stress for P20R.

No.	Element Number	Mesh density level in size (mm)	Longitudinal stress (MPa)
1	500	12	732.26
2	690	10	722.15
3	1650	8	726.12
4	3560	6	725.63
5	11328	4	725.05
6	17204	3.5	725.27
7	27360	3	724.86

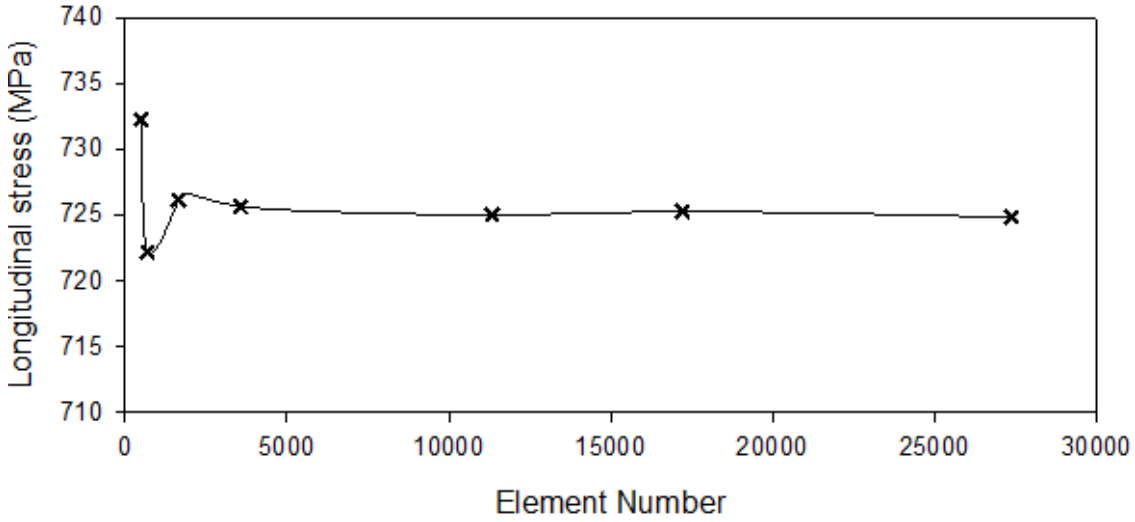

Figure B-8 Mesh convergence study at the crown for P20R model.

C20R

Table B-9 Different mesh sizes and the resulted longitudinal stress for C20R.

No.	Element Number	Mesh density level in size (mm)	Longitudinal stress (MPa)
1	400	12	638.04
2	768	10	633.02
3	1710	8	631.72
4	3640	6	630.64
5	11820	4	628.93
6	16767	3.5	629.46
7	27783	3	629.27

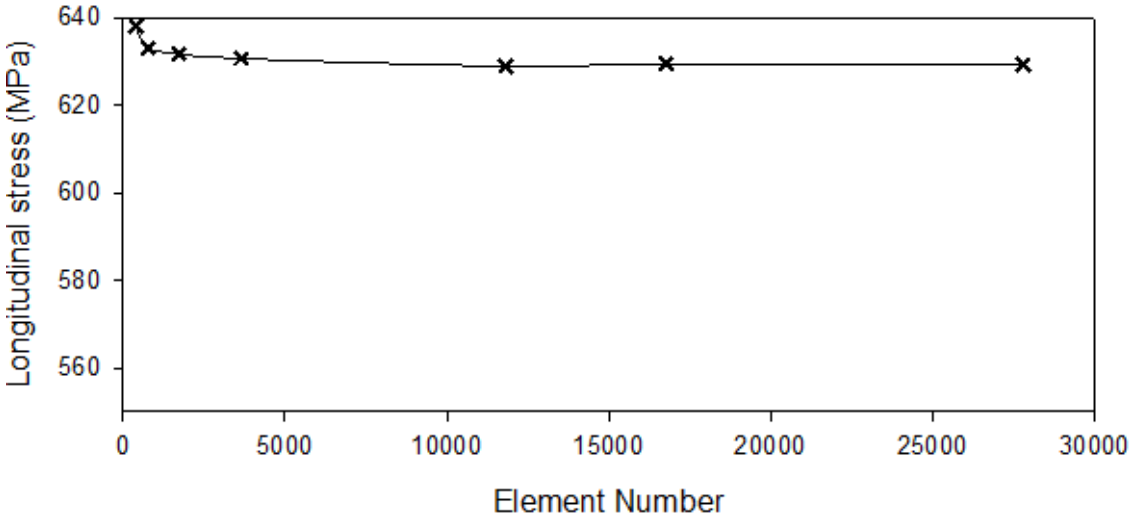

Figure B-9 Mesh convergence study at the crown for C20R model.

C8R

Table B-10 Different mesh sizes and the resulted longitudinal stress for C8R.

No.	Element Number	Mesh density level in size (mm)	Longitudinal stress (MPa)
1	400	12	590.08
2	768	10	599.2
3	1710	8	609.45
4	3640	6	612.33
5	11820	4	617.67
6	16767	3.5	618.71
7	27783	3	619.63

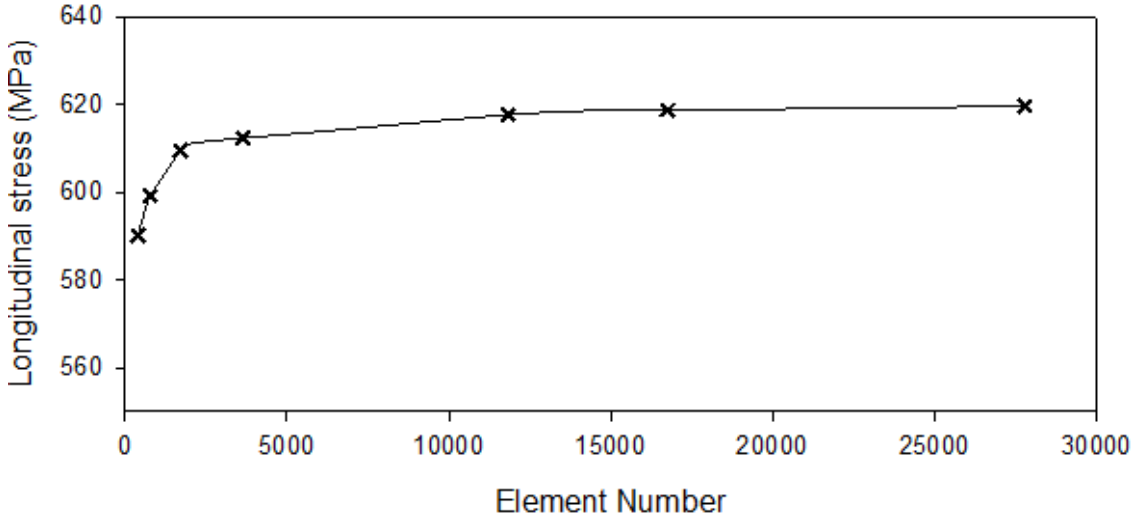

Figure B-10 Mesh convergence study at the crown for C8R model.

C8I

Table B-11 Different mesh sizes and the resulted longitudinal stress for C8I.

No.	Element Number	Mesh density level in size (mm)	Longitudinal stress (MPa)
1	400	12	600.46
2	768	10	600.99
3	1710	8	610.55
4	3640	6	613.19
5	11820	4	618.66
6	16767	3.5	620.21
7	27783	3	621.94

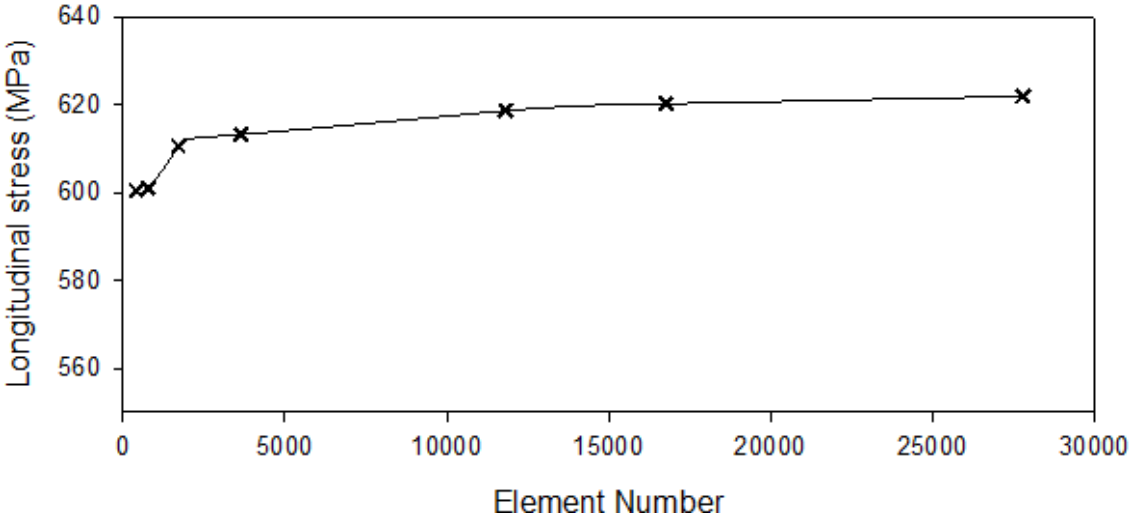

Figure B-11 Mesh convergence study at the crown for C8I model.

CEx8R

Table B-12 Different mesh sizes and the resulted longitudinal stress for CEx8R.

No.	Element Number	Mesh density level in size (mm)	Longitudinal stress (MPa)
1	440	12	562.24
2	648	10	597.43
3	1680	8	606.46
4	3720	6	610.24
5	11940	4	618.29
6	16974	3.5	618.72
7	27378	3	620.18

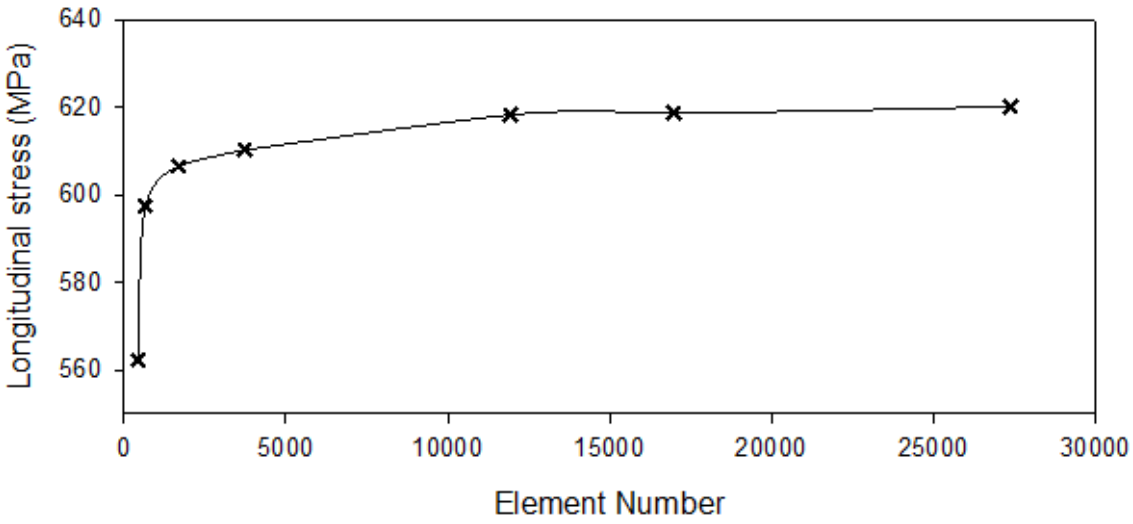

Figure B-12 Mesh convergence study at the crown for CEx8R model.

Appendix B.3 Mesh convergence analysis referred in section 5.2

This mesh convergence analysis is performed for different material models at a tension load of 4200 kN with a chain diameter of 76 mm. For each material model, the second finest mesh size is selected for the slave model since it has been checked to have less than a 0.3% difference compared to the finest mesh size to fulfill the mesh convergence criteria and to ensure the efficiency and the accuracy of the FE model. The results of the convergence analysis are shown in a table, where the resulted stress and the element number are plotted in the following figure for the different material models, i.e. Mono-Rampi, Cyclic-Rampi and Cyclic-Zarandi. The convergence analyses found that the final meshes for each model have a corresponding size of 3.5 mm for the slave model and 10 mm for the master model.

Material model of Mono-Rampi

Table B-13 Different mesh sizes and the resulted longitudinal stress for the model with Mono-Rampi Material model.

No.	Element Number	Mesh density level in size (mm)	Longitudinal stress (MPa)
1	380	12	983.377
2	720	10	1007.78
3	1470	8	1024.4
4	3400	6	1026.73
5	11460	4	1031.71
6	17871	3.5	1034.25
7	26973	3	1032.69

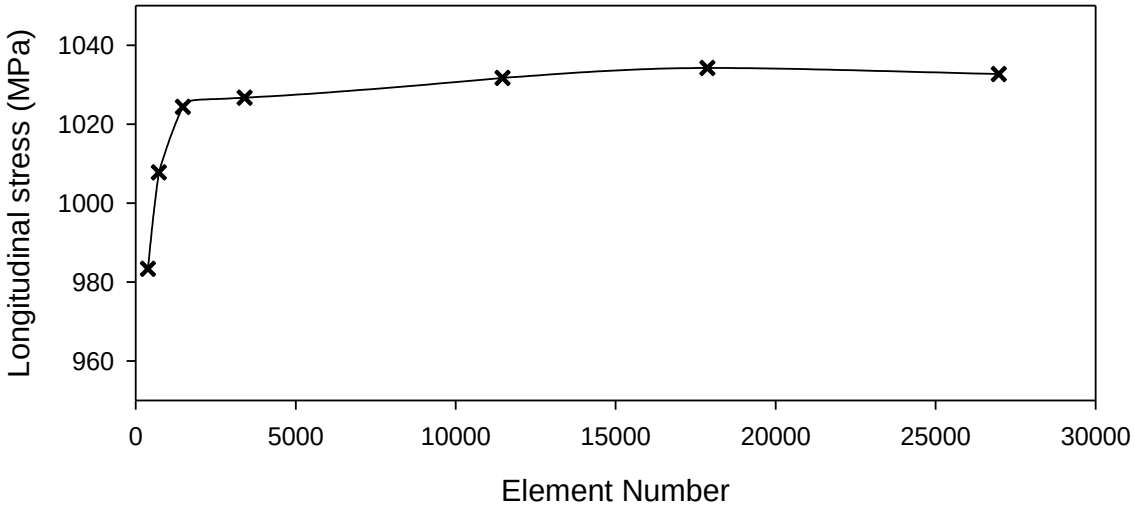

Figure B-13 Mesh convergence study at the crown for the model with Mono-Rampi material model.

Material model of Cyclic-Rampi

Table B-14 Different mesh sizes and the resulted longitudinal stress for the model with Cyclic-Rampi material model.

No.	Element Number	Mesh density level in size (mm)	Longitudinal stress (MPa)
1	380	12	978.896
2	720	10	967.033
3	1470	8	951.124
4	3400	6	931.376
5	11460	4	918.714
6	17871	3.5	913.253
7	26973	3	915.192

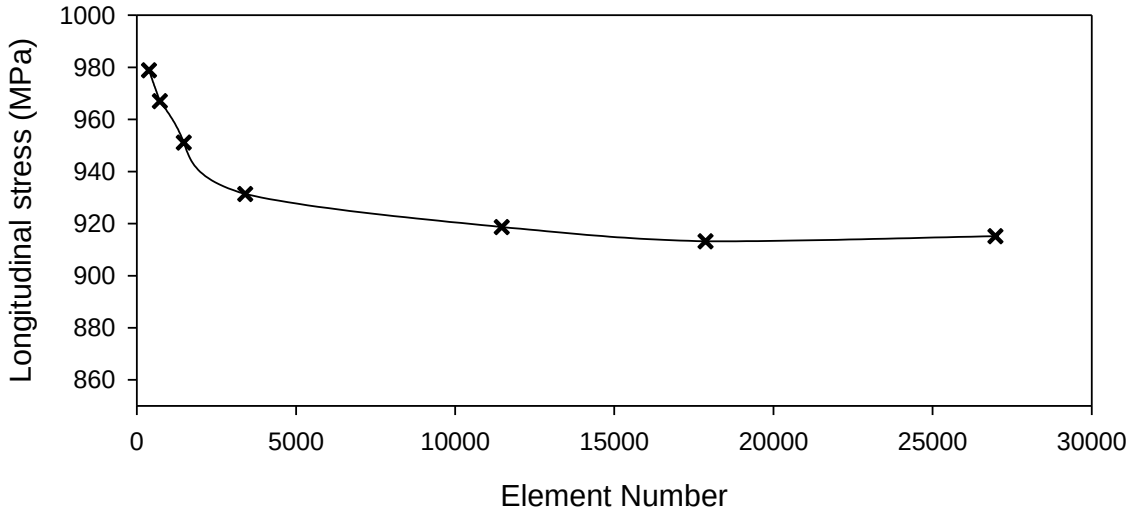

Figure B-14 Mesh convergence study at the crown for the model with Cyclic-Rampi material model.

Material model of Cyclic-Zarandi

Table B-15 Different mesh sizes and the resulted longitudinal stress for the model with Cyclic-Zarandi material model.

No.	Element Number	Mesh density level in size (mm)	Longitudinal stress (MPa)
1	380	12	959.849
2	720	10	953.232
3	1470	8	926.384
4	3400	6	907.02
5	11460	4	884.641
6	17871	3.5	883.667
7	26973	3	883.914

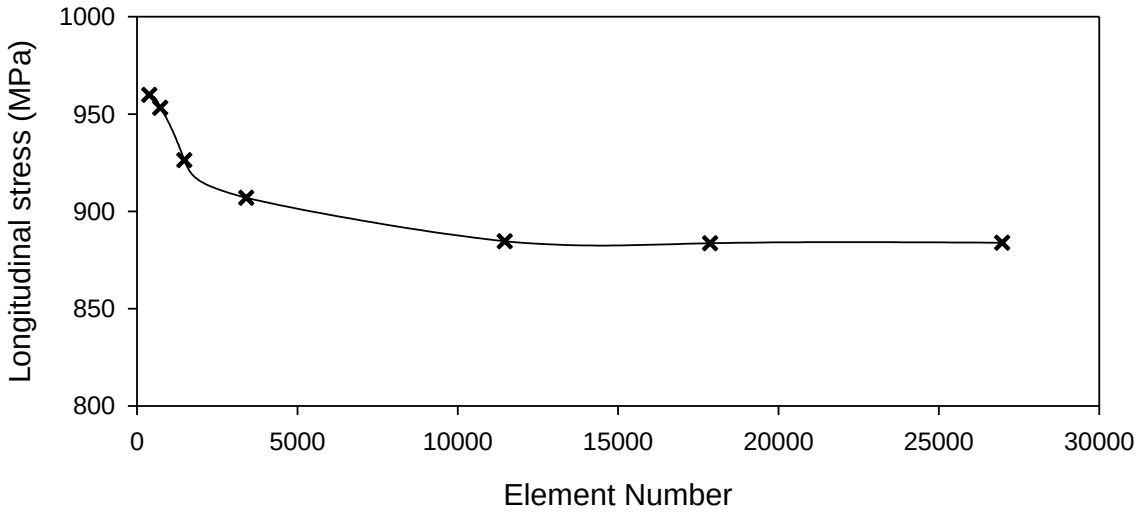

Figure B-15 Mesh convergence study at the crown for the model with Cyclic-Zarandi material model.

Appendix

Appendix C Calibration results of *SWT* damage parameters

Table C-1 presents the resultant *SWT* damage parameters, according to Equation (14), and the correlated number of cycles to failure from the fatigue life predictions based on SN curve of DNVGL-OS-E301 [7] under different load amplitudes, from 1% to 19% MBL.

Appendix

Table C-1 Resultant *SWT* fatigue damage parameters for different amplitudes and the correlated number of cycles to failure.

Amplitude (% MBL)	No. of cycles to failure	Mono-Rampi			Cyclic-Rampi			Cyclic-Zarandi		
		$\sigma_{n,max}$ (MPa)	$\Delta\varepsilon_n$	*SWT* (MPa)	$\sigma_{n,max}$ (MPa)	$\Delta\varepsilon_n$	*SWT* (MPa)	$\sigma_{n,max}$ (MPa)	$\Delta\varepsilon_n$	*SWT* (MPa)
19	3778	420.826	0.003694	0.77716	350.278	0.003359	0.58822	362.488	0.003313	0.60048
17	5275	381.147	0.003304	0.62959	314.186	0.003005	0.47205	327.542	0.002962	0.48516
15	7679	341.579	0.002915	0.49791	277.977	0.002651	0.36851	291.943	0.002613	0.38149
13	11796	301.763	0.002526	0.38116	241.775	0.002298	0.27776	256.228	0.002265	0.29014
11	19471	262.004	0.002139	0.28024	205.567	0.001944	0.19983	220.473	0.001916	0.21125
9	35550	222.164	0.001749	0.19427	169.330	0.001591	0.13467	184.743	0.001568	0.14483
7	75556	182.396	0.001361	0.12411	133.120	0.001237	0.08234	149.016	0.001219	0.09085
5	207326	142.544	0.000972	0.06924	96.827	0.000884	0.04278	113.244	0.000871	0.04931
3	959844	102.589	0.000583	0.02992	60.522	0.000530	0.01605	77.445	0.000523	0.02023
1	25915776	62.673	0.000194	0.00609	24.188	0.000177	0.00229	41.600	0.000174	0.00362

The resultant *SWT* damage parameters under different load amplitudes, shown in Table C-1, are used to calibrate the parameters of the fitted curves based on the general formula of Equation (16) in order to interpolate the number of cycles to failure from the corresponding *SWT* damage parameters during service fatigue loading. Table C-2 provides details regarding the calibration of parameters of the fitted curves. Good-match fitting is needed to give an accurate fitted curve between the predicted *SWT* damage parameters across a range of the number of cycles to failure. Therefore, in order to generate a good fit to the data, the fitting curves are separated into lower and upper fitting curves, where the lower fitting curves are used when the number of cycles to failure is below 75556, and the upper fitting curves are used when the number of cycles to failure above 75556. It is seen that using the upper and lower fitting curves, good fits are obtained with R-squared, R^2, above 99.9%.

Table C-2 Parameters of fitted curves for predicted *SWT* fatigue damage parameters.

Material		Material constants based on Equation (16)				R^2
		$A1$	$a1$	$A2$	$a2$	
Mono-Rampi	Upper fittings	60.05743	-0.612928	60.05743	-0.612928	99.989%
	Lower fittings	15.32255	-0.500088	15.32255	-0.500088	99.904%
Cyclic-Rampi	Upper fittings	65.53905	-0.656548	65.53905	-0.656548	99.999%
	Lower fittings	33.80939	-0.60351	33.80939	-0.60351	99.961%
Cyclic-Zarandi	Upper fittings	54.05119	-0.631039	54.05119	-0.631039	99.995%
	Lower fittings	17.35095	-0.537771	17.35095	-0.537771	99.930%

Appendix D Wave scatter diagram in the North Sea

Tabel D-1 presents the scatter diagram in the North Sea where the joint occurrence probabilities of significant wave height, H_s, and up-crossing wave period, T_z, are presented in the wave scatter diagram. The scatter diagram, consisting of 197 original sea-states, is partitioned into nine representative sea-state blocks at which the mooring line simulation is performed.

Appendix

Tabel D-1 The wave scatter diagram in the North Sea [48], and the selected nine blocks of representative sea-states for this present study.

H_s (m)	T_z (s)																	
	1.5	2.5	3.5	4.5	5.5	6.5	7.5	8.5	9.5	10.5	11.5	12.5	13.5	14.5	15.5	16.5	17.5	18.5
0.5	0	0	13	1337	8656	11860	6342	1863	369	56	7	1	0	0	0	0	0	0
1.5	0	0	0	293	9860	49760	77380	55697	23757	7035	1607	305	51	8	1	0	0	0
2.5	0	0	0	22	1975	21588	62300	74495	48604	20660	6445	1602	337	63	11	2	0	0
3.5	0	0	0	2	349	6955	32265	56750	50991	28380	11141	3377	843	182	35	6	1	0
4.5	0	0	0	0	60	1961	13543	32885	38575	26855	12752	4551	1309	319	69	13	2	0
5.5	0	0	0	0	10	510	4984	16029	23727	20083	11260	4636	1509	410	97	21	4	1
6.5	0	0	0	0	2	126	1670	6903	12579	12686	8259	3868	1408	422	109	25	5	1
7.5	0	0	0	0	0	30	521	2701	5944	7032	5249	2767	1117	367	102	25	6	1
8.5	0	0	0	0	0	7	154	979	2559	3506	2969	1746	776	277	84	22	5	1
9.5	0	0	0	0	0	2	43	332	1019	1599	1522	992	483	187	61	17	4	1
10.5	0	0	0	0	0	0	12	107	379	675	717	515	273	114	40	12	3	1
11.5	0	0	0	0	0	0	3	33	133	266	314	247	142	64	24	7	2	1
12.5	0	0	0	0	0	0	1	10	44	99	128	110	68	33	13	4	1	0
13.5	0	0	0	0	0	0	0	3	14	35	50	46	31	16	7	2	1	0
14.5	0	0	0	0	0	0	0	1	4	12	18	18	13	7	3	1	0	0
15.5	0	0	0	0	0	0	0	0	1	4	6	7	5	3	1	1	0	0
16.5	0	0	0	0	0	0	0	0	0	1	2	2	2	1	1	0	0	0

Appendix

Appendix E Gemilang et al. [186] **(Published)**

Appendix

Marine Structures 75 (2021) 102864

Contents lists available at ScienceDirect

Marine Structures

journal homepage: http://www.elsevier.com/locate/marstruc

Selection of appropriate numerical models for modelling the stresses in mooring chains

G.M. Gemilang [a,b,*], P.A.S. Reed [c], A.J. Sobey [a,d]

[a] Maritime Engineering Group, University of Southampton, Boldrewood Innovation Campus, Southampton, SO16 7QF, UK
[b] Faculty of Infrastructure Planning, Department of Civil Engineering, Universitas Pertamina, Terusan Simprug, Jakarta, 12220, Indonesia
[c] Engineering Materials Group, University of Southampton, Highfield, Southampton, SO17 1BJ, UK
[d] Marine and Maritime Group, Data-centric Engineering, The Alan Turing Institute, The British Library, London, NW1 2DB, UK

ARTICLE INFO

Keywords:
Mooring line failures
Finite element method (FEM)
Contact stresses
Benchmarking

ABSTRACT

Mooring chains are key components for floating platforms. The failure of these components can be catastrophic in terms of the economic and environmental impacts, especially when dealing with the potential failure of FPSOs. However, mooring failures have been regularly occurring much earlier in their service lives than expected, with almost 50% of the reported failures happening in the first 3 years of 20-year design lives. Although the operating stresses play a major role in determining the failure mechanisms of mooring chains, the methods of predicting the operating stresses in mooring chains vary in the openly available literature, and the accuracy of these different numerical methods for predicting types of mooring failures is unknown. There is currently little evidence provided for when one model is appropriate for a particular scenario. Therefore, this paper benchmarks the different available methods for modelling mooring chains under tension, including FE models found in the literature. These models are calibrated and verified against previous studies and compared with experiments and a developed FE explicit model. There is a significant difference in the way that the numerical models behave, which are discussed in terms of their applicability and limitations in modelling mooring chains. The results of this study show that the explicit modelling approach should be utilised for accurate assessment of mooring lines, as it provides the most realistic response, with a substantial reduction in the computational cost and without any convergence problems.

1. Introduction

Mooring chains are critical components used to maintain vessel stability and operating location. However, in the past decades, mooring failures have occurred at a critically high rate. There were more than 23 mooring failures between 2000 and 2011, with roughly half of these occurring in the first three years of a 20-year design life [1,2]. Among these, there were eight cases of multiple lines being damaged, leading to vessel drifting. In addition to those failures, 16 mooring failures occurred in the period 2010–2014 on the Norwegian Continental Shelf [3]. These failures could be catastrophic in terms of both financial and environmental impacts. Single-line replacement costs can reach $2 million [4], and single-line breakage can cause neighbouring lines to fail, resulting in multiple mooring line replacements which can cost $15-$20 million [4]. The field shut down of two days due to failure and

* Corresponding author. Maritime Engineering Group, University of Southampton, Boldrewood Innovation Campus, Southampton, SO16 7QF, UK.
E-mail address: gmg1g16@soton.ac.uk (G.M. Gemilang).

https://doi.org/10.1016/j.marstruc.2020.102864
Received 8 March 2020; Received in revised form 16 June 2020; Accepted 8 September 2020

replacement of a mooring line could result in lost production costs of $3 million for an FPSO with a capacity of producing 50,000 barrels per day, while this cost could rise to $15 million when the FPSO has a capacity of 250,000 barrels per day [5]. These costs are calculated without the possibility of riser rupture, oil spill and FPSO damage, which can exceed $700 million [4]. For instance, an FPSO, Gryphon Alpha, broke four of its ten mooring chains and the insurance pay-outs reached nearly $570 million as the risers ruptured and the vessel drifted in a storm [6]. Industry surveys [1,7,8] have found various failure modes reported for mooring lines, as shown in Fig. 1, based on 107 reported failures from 72 assets [7]. Each of these failure modes needs to be accurately modelled to reduce the number of failures, and a better understanding of the stresses and strains exhibited in operation are required.

There are several methods available in the literature to predict the operating stresses and strains in the chains. Table 1 outlines a number of different FE models reported in the literature, showing that the majority of numerical studies use an implicit FE formulation, while there is only one numerical study using the explicit method for mooring chain modelling [9]; although this method obtains a good agreement with experiments. These FE models use different element types, contact models and solvers (implicit/explicit). However, no evaluation of which model is appropriate for a particular failure mode has been made, and it is hard to determine from the literature when each of different models is appropriate.

The novelty of this paper is therefore to compare these different methods to understand how accurately each one models different types of failure modes. To allow this comparison, the different FE models from the literature are replicated, using the most similar meshing and modelling techniques available in ABAQUS. These models are then calibrated to match the published responses and are then compared with experiments [10], to determine their accuracy. The chain models are then benchmarked, intact without considering geometric changes due to failure mechanisms, to consider the effect of the resultant stress/strain relationships that would be important to different failure mechanisms to allow a comparison between the different methods.

2. Finite element model definition

The FE model was constructed in the ABAQUS 6.14 package and automated using a Python script. Hexahedral elements were selected over tetrahedral elements since they give superior performance in terms of convergence rate and accuracy of the solution [23–25]. The standardised dimensions for the chain geometry of a studless chain with diameter, D, are provided by IACS [26] where the total length, L, is equal to $6D$, the total width, W, is $3.35D$ and the radius of the curved section, R, is $0.675D$, as illustrated in Fig. 2.

DNV-OS-E302 standard [27] provides minimum mechanical properties for mooring chain steel grades, depending on the nominal tensile strength of the steels used for manufacture. Grades R3 and R4S are used to replicate previous studies with properties specified in the standard, DNV-OS-E302 [27], as shown in Table 2. The engineering material stresses and strains are converted into the true stress and logarithmic strain for input into ABAQUS. There are many nonlinear hardening models, e.g. Armstrong-Frederick, that can be used to reflect more complex cyclic material properties. However, as this study aims to replicate the response from the published analyses, the same material models used in these analyses are employed for the current simulations. The grade R3 material modelling is based on Pacheco et al. [11,14] and Bjørnsen [15] in which a bilinear isotropic hardening is used, where an elastic modulus (E) of 210 GPa and Poisson ratio (ν) of 0.29 are used. The strain associated with the tensile strength is adopted as half the total elongation [14]. Grade R3 is used in sections 3.2, 3.3 and 4.2. The grade R4S material modelling is based on Kim et al. [20], where a Ramberg-Osgood curve is used with an isotropic hardening exponent of 0.597. An elastic modulus (E) of 209 GPa and Poisson ratio (ν) of 0.3 are used. This grade R4S is used in section 3.4. Fig. 3 shows the stress-strain diagrams for both grades of steel, R3 and R4S, which are used as an input for ABAQUS. The model also considers geometric nonlinearities to consider large deformation effects.

Two types of contact loading method are investigated in the present study: (i) the pressure distribution method [11,14], which uses a pressure to replicate the contact force between the mooring links, and (ii) the contact interaction method [15], which is more consistent with the real chain interaction than using the pressure distribution. The pressure distribution method is replicated from Pacheco et al. [11,14], where the magnitude of the pressure is equivalent to the resultant load in the contact region. The pressure

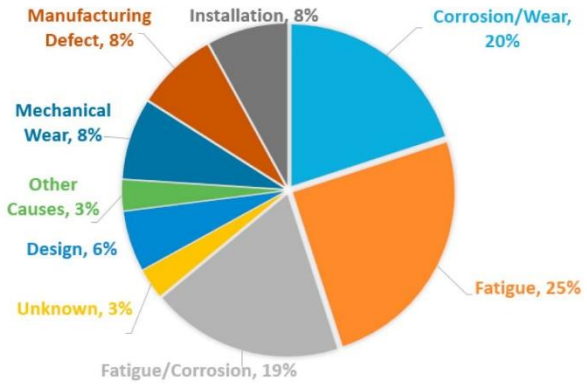

Fig. 1. Types of failure modes for mooring chains by the proportion of occurrence [7].

Appendix

Table 1
Summary of numerical analyses for mooring chains in the open literature.

Solution Method	Element Type	Material modelling	Loading Methods	Reference
Implicit	Hexahedral-Reduced integration	Elastic	Pressure Distribution	[11],[a] [12,13]
		Elastoplastic	Pressure Distribution	[11–14],[a]
		Elastoplastic	Contact Interaction	[11–15],[a] [16–19]
	Hexahedral-Incompatible Mode Integration	Elastoplastic	Contact Interaction	[20],[a] [21,22]
Explicit	Hexahedral-Reduced integration	Elastoplastic	Contact Interaction	[9]

[a] Selected verification papers.

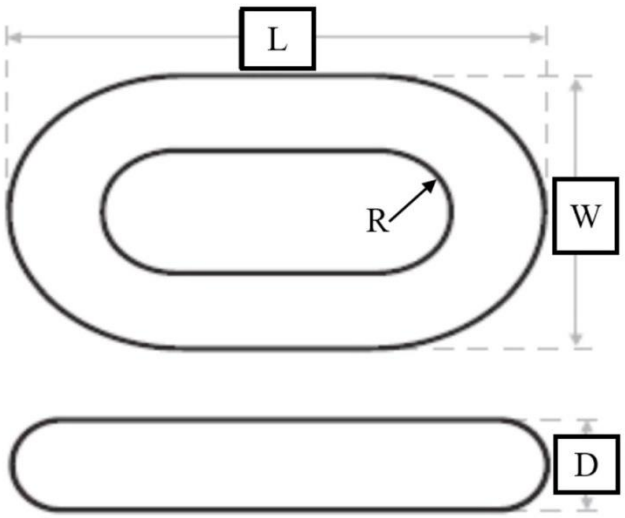

Fig. 2. The IACS specification for the design of a studless chain link [26].

Table 2
Minimum mechanical properties for chain materials [27].

Steel grade	Yield stress (MPa)	Tensile strength (MPa)	Total elongation (%)
R3	410	690	17
R4S	700	960	12

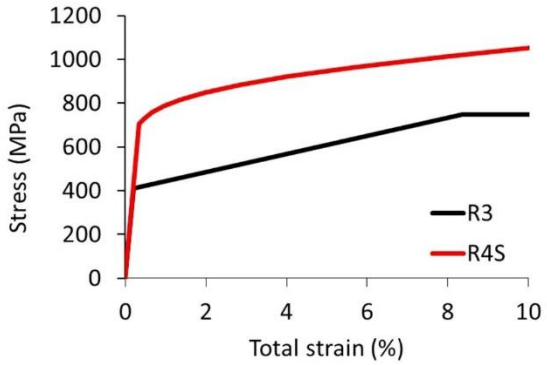

Fig. 3. Stress-strain diagrams of R3 and R4S grade steel.

distribution varies linearly from a maximum value at the centre of the interlink contact area to zero at the border. The contact angle of 35° is used to represent the contact area from the axial direction, and the total area over which the pressure is applied is determined by a design parameter, H, as shown in Fig. 4(b). The pressure distribution is found by applying Eq. (1) to the ABAQUS analytical-fields,

$$f(x,y) = 0.610865 - \tan^{-1}\left(\frac{x}{y}\right), \tag{1}$$

where $f(x,y)$ is the function of pressure distribution, 0.610865 is the 35° in radian, and the origin of x and y is located at the centre of chain's curved part, as indicated in Fig. 4(b).

In the contact interaction method, the contact discretisation is defined as surface-to-surface with a penalty contact constraint, as illustrated in Fig. 4(c). The surface-to-surface discretisation is used as this is suggested by ABAQUS [28] to provide more accurate stress and pressure results than node-to-surface discretisation. Finite sliding is considered, as the tension-tension simulation assumes no sliding of one surface along with the other, with a friction coefficient of 0.7 based on previous studies [11,14,15,20]. The upper chain is represented as the master model, and the lower chain is represented as the slave model, which has a finer mesh as this is where the resultant stresses/strains are extracted for analysis. The bottom surface of the slave model is fixed, while the upper surface of the master model is loaded using a uniformly distributed surface traction acting at the top, as indicated in red in Fig. 4(c).

The chain model has three planes of symmetry and so only an $1/8^{th}$ of the chain model needs to be modelled. The symmetry boundary condition is assigned at the symmetry planes indicated in red in Fig. 4(a) for the models using the pressure distribution method. For the models with contact interaction, the loaded surface at the top of the master model does not have this boundary condition, to allow the load to be applied in the axial direction. Six degrees of freedom are employed for each node, except for nodes on each of the symmetry planes, which have only three degrees of freedom, corresponding to the number used in the models taken from the literature. The symmetry boundary conditions constrain the displacement of nodes lying on each symmetry plane in the normal direction and the rotation in the other two directions. For example, the bottom surface of the slave model was constrained against displacement in the y-axis and against rotation in the x, z-axes.

The most probable locations for cracks are documented as being at the outer crown and the inner bend, also known as the K_t point [10,16,29]. Paths 1, 2 and 3, shown in Fig. 5 are selected to represent the key regions in the mooring line where the stresses and strains must be accurately modelled to predict the various failure mechanisms of the mooring chains: ultimate strength, corrosion, fatigue, fracture and permanent deformations. Path-1 is used to study the stress-strain field on the surface near the contact region. While paths 2 and 3 are used to study crack propagation; the cracks at the outer crown originate on the outside of the link and grow inwards along path-2, shown in Fig. 5(b), while the cracks at the inner bend hotspot originate on the inside of the link and grow outwards along path-3, Fig. 5(c) [10].

3. Definition and calibration of the numerical models

The prior numerical models available from the literature are calibrated and verified based on the selected models. The analysis uses the same modelling inputs that are documented in the respective verification papers. During verification of the models, it is found that some utilise unconverged meshes, these meshes are used to compare to the original literature but are then converged before comparing to the experiments and the other numerical models.

3.1. *Elastic model with pressure distribution, 20 node brick element with reduced integration (EP20R)*

The elastic model with pressure distribution (EP20R) is calibrated and verified for a 76 mm studless chain with grade R3 steel

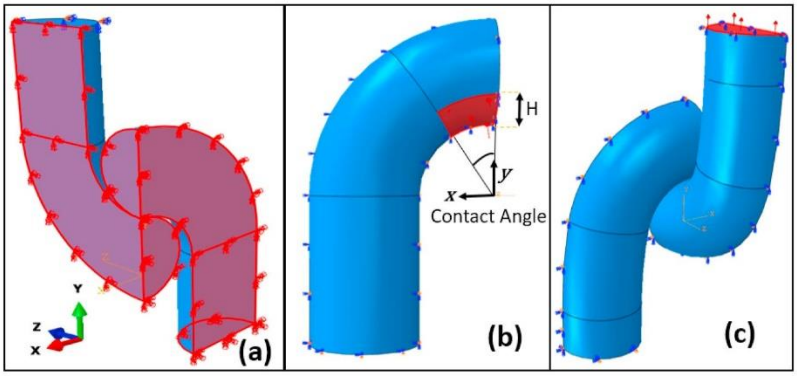

Fig. 4. Finite element definition: (a) symmetric boundary condition for chain modelling, (b) a model with pressure distribution, (c) a model with contact interaction.

Appendix

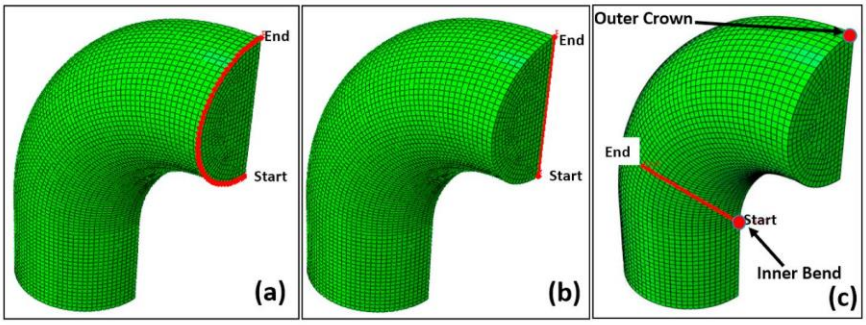

Fig. 5. Key paths for mooring line failure prediction: (a) path-1, (b) path-2 and (c) path-3.

material properties, Pacheco et al. [11]. The model was originally analysed using the finite element code, ANSYS, and the inputs are shown in Table 3. The element type is changed from the SOLID95 elements to the equivalent brick structural solid 20-node second-order element in ABAQUS, C3D20R.

The results of the longitudinal stress are provided for a part of path-2, from a distance of 22 mm–76 mm. The design parameter, H, shown in Fig. 4(b), is not documented, and therefore, a calibration is performed to replicate the result from the original paper shown in Fig. 6. A value of 11.3 mm is selected for H as it gives the lowest absolute mean difference compared to the original results across the whole path with an absolute mean difference of 2%.

3.2. *Elastoplastic model with pressure distribution, 20 node brick element with reduced integration (P20R)*

The elastoplastic model with pressure distribution (P20R) is calibrated and verified for a 76 mm studless chain with grade R3 steel material properties, and the inputs are presented in Table 4, Pacheco et al. [14]. The model was also originally analysed using the finite element code, ANSYS, and the SOLID95 is again changed to C3D20R. The original paper [14] provides the results of the longitudinal stress along a part of path-2, from a distance of 19 mm–76 mm.

The design parameter H is again not documented, and therefore, the H value of 11.3 mm is chosen from the previous verification study. A comparison of the results using this value to the original results are shown in Fig. 7 and give an absolute mean difference of 3.5% across the whole path.

3.3. *Elastoplastic model with contact interaction, 20 node brick element with reduced integration (C20R)*

An elastoplastic implicit model with contact interaction and reduced second-order elements (C3D20R) is calibrated and verified for a 76 mm studless chain using grade R3 steel material properties based on Bjørnsen [15]. The input values are the same as used in the original analysis, shown in Table 5. However, the contact analysis in the implicit method has convergence problems as it tries to enforce the suddenly activated contact constraint, causing a severe discontinuous iteration. To resolve this issue, an initial boundary condition (IBC) is used where the displacement acting towards the load direction is applied and then removed after the surfaces are adequately constrained through contact with other components before applying the operational load as suggested by ABAQUS [30]. This initial boundary condition (IBC) is not documented and therefore, a parametric study is used to determine this value.

The results of the parametric study are presented in Fig. 8 for path-1 and show a considerable difference from the original results in the first 5 mm. However, the initial boundary condition value of 5×10^{-4} m is selected since it gives the lowest absolute mean difference of 4% compared to the original paper.

3.4. *Elastoplastic model with contact interaction, 8 node brick element with incompatible mode (C8I)*

The elastoplastic implicit model with contact interaction and incompatible mode elements (C8I) is calibrated and verified for a 152

Table 3
Original inputs for the elastic model with pressure distribution (EP20R).

Design Parameter	Pacheco et al. [11]
Contact angle (°)	35
Elastic Modulus (GPa)	207
Poisson Ratio	0.29
Element Type	SOLID95
Mesh size (mm)	7.5
Load Magnitude (kN)	810.5

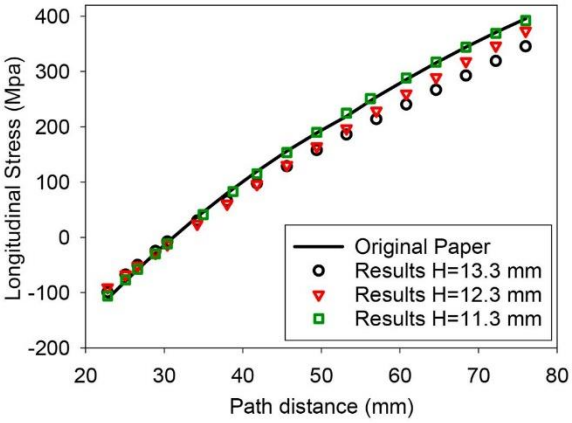

Fig. 6. Calibration of H along path-2 for the longitudinal stress.

Table 4
Original inputs for P20R.

Design Parameter	Pacheco et al. [14]
Contact angle (°)	35
Elastic Modulus (GPa)	207
Poisson Ratio	0.29
Element Type	SOLID95
Mesh (mm)	7.5
Load Magnitude (kN)	3242
True Yield Stress (MPa)	410
True Tensile Stress (MPa)	748.65
True Tensile Strength Strain	0.0816

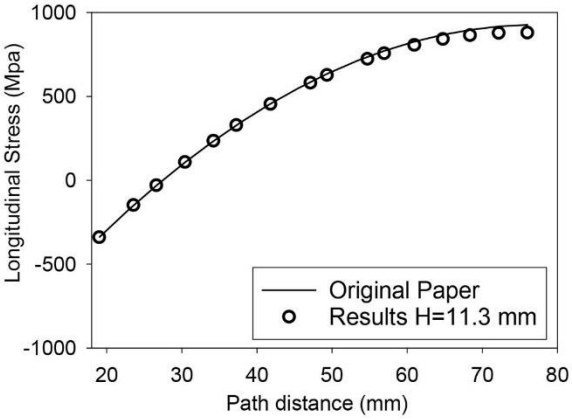

Fig. 7. Verification of H = 11.3 mm for the P20R model along path-2 for the longitudinal stress.

mm studless chain based on grade R4S steel material properties based on the Kim et al. [20]. The input values are the same as used in the original analysis, shown in Table 6.

The model is verified using the maximum stress concentration factor, the ratio between the maximum absolute value of the principal stresses within the chain and the nominal tensile stress. The nominal tensile stress is defined as the tensile load divided by the cross-sectional area of the chain's round bars resulting in stress of 74.535 MPa. The FE model uses the implicit method, requiring contact initialisation to start the interlink contact in the FE modelling; the initial boundary condition (IBC) of 5×10^{-4} m from the

Table 5
Original inputs for C20R.

Design Parameter	Bjørnsen [15]
Elastic Modulus (GPa)	210
Poisson Ratio	0.29
Element Type	C3D20R
Slave Model Mesh (mm)	8
Master Model Mesh (mm)	10
True Yield Stress (MPa)	410
True Tensile Stress (MPa)	748.65
True Tensile Strength Strain	0.0816
Interaction – Tangential	Penalty - 0.7 Friction
Interaction – Normal	Normal – Hard
Load Magnitude (kN)	1221.075

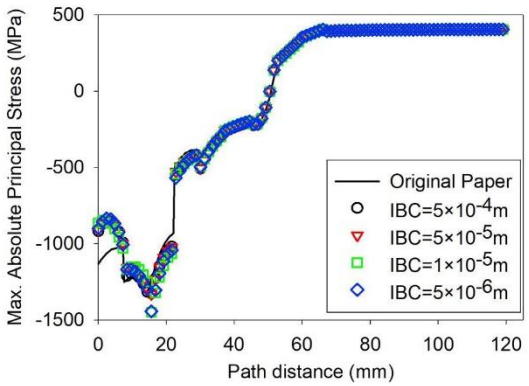

Fig. 8. Calibration of the Initial Boundary Condition (IBC) for the maximum absolute principal stress along path-1.

Table 6
Original inputs for C8I.

Design Parameter	Kim et al. [20]
Elastic Modulus (GPa)	209
Poisson Ratio	0.3
Element Type	C3D8I
Slave Model Mesh (mm)	10
Master Model Mesh (mm)	10
Yield Stress (MPa)	700
Tensile Stress (MPa)	960
Tangential interaction	Lagrange Multiplier - 0.7 Friction
Interaction – Normal	Normal – Hard
Load (kN)	2705

previous model is checked and is selected. The maximum absolute value of the principal stresses within the chain predicted by the current FE model is 288.34 MPa, giving a maximum stress concentration factor of 3.87. This value is compared to the maximum stress concentration factor from the original paper [20], which is 3.9, which gives a 0.80% difference. The model is therefore considered to be correctly calibrated and verified.

3.5. *Elastoplastic model with contact interaction, explicit solver 8 node brick element with reduced integration (CEx8R)*

Recent research using the explicit method for studded chains shows good agreement with experiments [9], despite it not being documented for studless chains. This is in agreement with the literature [31–38] where the explicit solver is shown to provide accurate prediction to experiments, for solving different types of contact problems. In the explicit approach, a solution is solved in a dynamic formulation and is conditionally stable, assuming the time increment selected is small enough to maintain the stability limit. The stability limit is that the time increment must be less than a critical value of the smallest transition time for a dilatational wave to cross any element in the mesh [39]. The time increment is automatically set by ABAQUS/Explicit depending on the element dimensions and material properties [40]. In the implicit approach, a solution to the set of finite element equations is unconditionally stable involving

iteration until a convergence criterion is satisfied for each increment. The unconditionally stable implicit method encounters some difficulties when a complicated three-dimensional model involving contact is considered [23,39–41].

To allow quasi-static analysis in the explicit method, the loading amplitude uses a smooth step, and the kinetic energy is checked so that it does not exceed 5% of its internal energy throughout the simulation. For the contact pair algorithm, the contact surface weighting is set to 1.0 to specify a pure master-slave relationship with the first surface as the master surface between links. The first-order hexahedral elements with reduced integration schemes (C3D8R) are used, and the final meshes are defined using a mesh convergence analysis. Mass scaling factors of 10, 100 and 1000 are evaluated in comparison to the same model without mass scaling using a chain model of 76 mm diameter and grade R3 material under 25% minimum breaking load. A mass scaling factor of 100 gives the optimum effect with 8.5 times lower computational time and the same memory usage. The resulting von Mises stresses along path-1 show a 0.1% mean absolute error with a maximum error of 0.9%.

4. Model selection

The differences between the FE models are documented in Table 7. An additional implicit method with C3D8R elements is included as C8R, Jones [42] and Zarandi [43], but there is no verification to determine its accuracy, but it is assumed that only changing the element type from the C20R model will not reduce the accuracy of the model. The final meshes for each model are defined using a mesh convergence analysis.

4.1. Validation of the numerical models

To validate the accuracy of the different numerical models, they are used to simulate the experimental data from Tipton and Shoup [10]. The model geometry is defined to be the same where the chain diameter is 10 mm and the total length, L, is equal to $5D$, the total width, W, is $3.6D$ and the radius of the curved section, R, is $0.8D$. It should be noted that this geometry is different from the IACS [26] standard design. The chain for this experiment is manufactured according to the ANSI/ASTM A-391-86 standard specification for the alloy steel chain. The engineering stress-strain relationship, derived from the average of two tensile tests conducted at a constant stress rate of approximately 30 MPa per second [10], is converted to true stress-strain relationship for input into ABAQUS. Fig. 9 shows the true stress-strain relationship, where the elastic modulus (E) is 213745 MPa and Poisson ratio (ν) is 0.29.

In the experiments, the chains were initially heat-treated to relieve manufacturing residual stresses, and then proof loaded at 70%, 76% and 82% of the minimum breaking load, which is obtained from five break strength tests as 106.8 kN [10]. The proof load is given then released, resulting in a permanent elongation and residual stress at the outer crown. In this experiment, the permanent elongations are obtained from measurements, and the residual stresses are calculated by using the measured strains from strain gauges compared to the monotonic tensile stress-strain curve where the unloading strain is assumed elastic, and the constraint of transverse strains is assumed negligible. The documented permanent elongations are 0.512 mm, 1.021 mm and 1.682 mm for proof loads of 70%, 76% and 82% of the minimum breaking load, respectively. The documented residual stresses are −855 MPa and −648 MPa, for proof loads of 70% and 50% of the minimum breaking load, respectively.

Fig. 10 displays the comparisons of the normalised permanent elongations obtained by the FE analyses and experimental tests. The elastic model with pressure distribution (EP20R) is not included since it does not capture the material plasticity to model both normalised permanent elongation and normalised residual stress. The results of the predicted permanent elongations show a good agreement between the FE models and the experiments, as shown in Fig. 10. In general, as the permanent elongations increase at higher levels of proof load, the FE model results predict the experimental results more closely. It is assumed that this is because it is difficult to measure relatively small permanent elongations in the experiment. However, in the elastoplastic model with pressure distribution (P20R), the error in predicted permanent elongation increases with larger load levels. This is ascribed to the usage of the pressure distribution method, which is less consistent with real interlink interactions than the contact interaction method. The explicit model (CEx8R) provides the closest agreement in the prediction of permanent elongation for all load levels with the lowest mean error of 13% over the three tests, while the implicit reduced second-order model (C20R) gives the maximum mean error of 47%.

In general, the FE models underestimate the residual stresses with a mean error of 44% for the 70% test, which reduces to 35% for the 50% test. This is except for the elastoplastic model with pressure distribution (P20R) in the 70% test, which exhibits higher residual stresses that are closest to the experiments with normalised residual stress of 0.99. Therefore, the documented results for the residual stresses are considered to be inaccurate. The residual stress levels are determined from the measured strains by the strain gauges and

Table 7
Differences in modelling between the different FE models.

Model	EP20R	P20R	C20R	C8I	CEx8R	C8R
Solution Method	Implicit	Implicit	Implicit	Implicit	Explicit	Implicit
Contact Loading Method	Pressure distribution	Pressure distribution	Contact interaction	Contact interaction	Contact interaction	Contact interaction
Element type	C3D20R	C3D20R	C3D20R	C3D8I	C3D8R	C3D8R
Contact Tangential behaviour	N/A	N/A	Penalty	Lagrange Multiplier	Penalty	Penalty
Contact Normal behaviour	N/A	N/A	Hard contact	Hard contact	Hard contact	Hard contact
Mass Scaling	–	–	–	–	100	–

Appendix

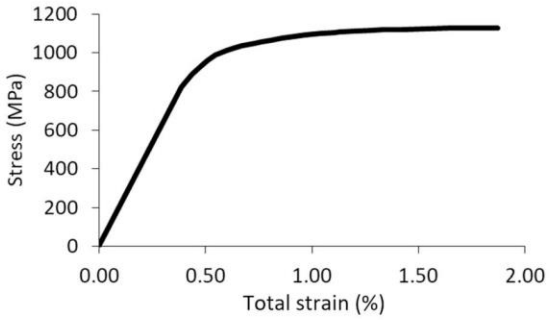

Fig. 9. Stress-strain relationship used in the current simulation derived from tensile tests [10].

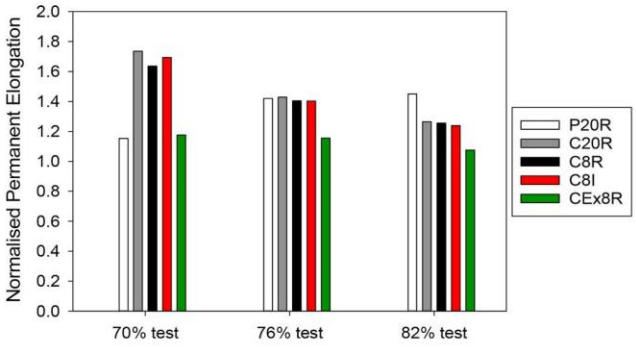

Fig. 10. The predicted permanent elongations of the different FE models normalised against experimental tests.

the monotonic tensile stress-strain curve, where the unloading strain is assumed to be elastic according to Tipton and Shoup [10]. During the experiment, the strain gauge application is documented as being difficult due to the curved surface at the crown region, so this curvature, coupled with the plastic strains imposed by proof loading, may result in erroneous strain gauge applications, with potential for errors in the residual stress estimation. Additionally, the residual stress estimation does not account for some of the physical factors such as Poisson's ratio effects and the constraint of the transverse strains, and strain gauge corrections were not used. The measurement method of the permanent elongations is not documented in the original paper, but it is assumed that they use visual measurement with length meters. Overall, these results provide validation for the different FE models. In general, the explicit model (CEx8R) provides the best predictions for the analysis of the permanent elongations and is therefore adopted as the reference for the remainder of the benchmarking studies, due to a lack of further validation material in the open literature.

4.2. Benchmarking of the numerical models

The accuracy of the stress within the chain model is explored to further demonstrate the comparison between the numerical models in the validation study. The stress along path-1 under the 50% minimum breaking load is shown in Fig. 11, where the region A signifies the contact area.

In general, the results for all of the models with contact interaction (i.e. C20R, C8R, C8I, CEx8R) provide inconsistent results in region A, either through sharp changes in gradient or extreme stress values. The difference in results in this region is because of the local instabilities and convergence difficulties of the implicit solutions that make force equilibrium difficult to achieve over the contact area. However, the stress for all of the models converges at the end of path-1 under 50% of the minimum breaking load, apart from the elastic model (EP20R).

The oscillating stresses exhibited by the implicit models may pick up erroneous peak stresses, since these exhibited peak stresses may not exist. This may mislead any failure analyses of the mooring chain. However, the explicit model (CEx8R) predicts a smoother stress profile, which results in better predictions based on the prior validation study. For a strength failure analysis, the prediction of peak stress requires good accuracy. The prediction of peak stress is also essential for an analysis of mechano-electrochemical induced corrosion as the corrosion is influenced by many factors, one of which is the surface stress, which influences the corrosion rate [44]. In comparison to the explicit model (CEx8R), the implicit reduced first-order model (C8R) and the elastoplastic model with pressure distribution (P20R) predict similar peak stress within 0.7 mm. However, the implicit incompatible first-order model (C8I) over-estimates the peak stress by 69% at the same location compared with the explicit model (CEx8R), while the implicit reduced second-order model (C20R) overestimates the peak stress by 28% at a location 0.8 mm from the explicit model (CEx8R).

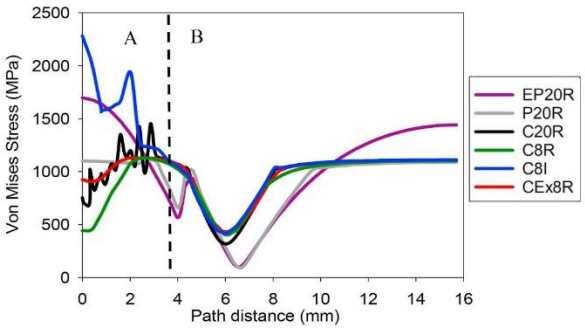

Fig. 11. Comparison of the von Mises stresses for the different FE models under 50% minimum breaking load along path-1.

The different numerical models are then compared using the standardised geometry (L = 6D, W = 3.35D), 76 mm diameter and of grade R3 in order to be consistent with the current practice of offshore industries. The minimum breaking load for the standardised dimension is 4884 kN based on the IACS standard [26]. The simulation is a one-step analysis up to the maximum load. The analysis does not consider the effect of proof loading tests or residual stresses, to allow a comparison of the stress/strain modelling in the chain from the same initial condition. The comparison of the von Mises stress profile using the standardised geometry shows similar behaviour with the prior comparison of the von Mises stress profile. However, a difference is found for the results of the elastoplastic model with pressure distribution (P20R) in which it overestimates the peak stress by 12% and the stress at the end of path-1 by 19% compared to the explicit model (CEx8R) under 50% minimum breaking load in the standardised dimension.

For a fatigue failure analysis, the predictions of the stress range and the mean stress at the fatigue location must be accurate. The two locations susceptible to fatigue damage are the outer crown, the end of path-2, and the inner bend, the start of path-3. The comparison of the stresses at these locations are presented in Fig. 12, where the load levels of 25% and 50% minimum breaking load are defined as the minimum and maximum loading to simulate fatigue loading conditions. The models with contact interaction (i.e. C20R, C8R, C8I, CEx8R) have similar predictions for all of the comparisons with the largest difference, 5%, for the implicit reduced second-order model (C20R) at the outer crown. In comparison to the models with contact interaction, the elastoplastic model with pressure distribution (P20R) gives a mean difference of 46% for the stress range, which reduces to 8% for the mean stress at both locations; while the elastic model with pressure distribution (EP20R) predicts the stress range by more than 2.5 times, which reduces to 1.6 times of the other models with contact interaction, which could lead to inaccurate estimations of the fatigue life.

The nominal stress is commonly used as a fatigue design parameter by offshore standards [45] to calculate the fatigue life of mooring chains based on S–N curves. The nominal stress is analytically calculated based on the corresponding tension divided by the total cross-sectional area of the chain's round bars. The nominal stress predicted by the FE models is calculated by averaging the longitudinal stress in the mid-cross-section of the straight part of the chain. The models with contact interaction (C20R, C8R, C8I and CEx8R) result in less than a 1% difference to the analytical calculation, while the models with pressure distribution (EP20R and P20R) result in 5.5% difference since they do not capture the contact interactions.

In a crack propagation analysis, the local tensile stress field development over the crack path needs to be accurately modelled. The comparisons of the maximum principal stress under 50% minimum breaking load along path-2 and path-3 are examined since they are critical paths for fracture in mooring chains [10,16,29]. As shown in Fig. 13, the models with contact interaction (C20R, C8R, C8I and

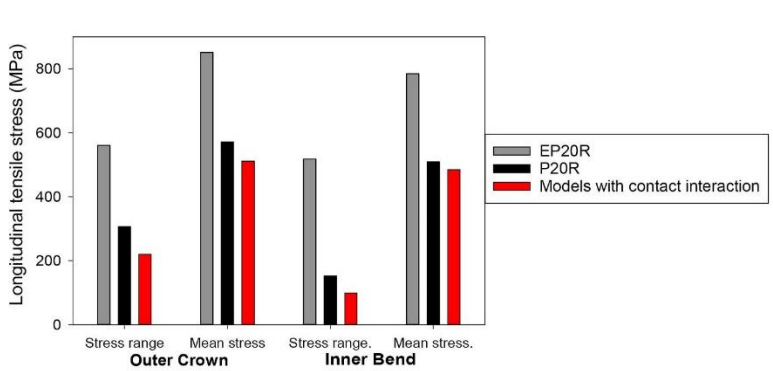

Fig. 12. Comparison of the stress range and mean stress for the different FE models at both critical locations for fatigue analysis.

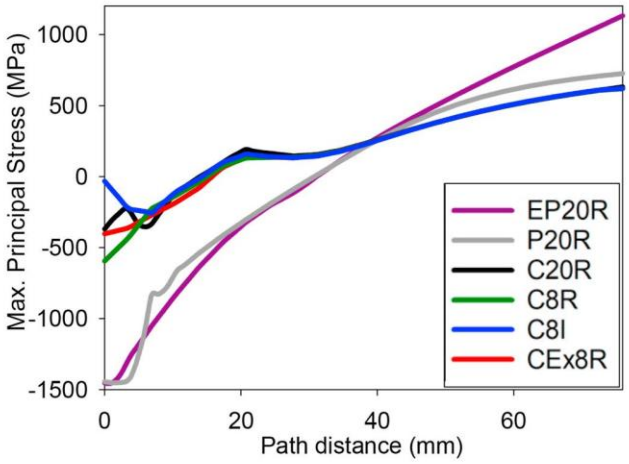

Fig. 13. Comparison of the maximum principal stress for the different FE models under 50% minimum breaking load along path-2.

CEx8R) have considerable dissimilarities in the first 7 mm of path-2 due to their different performances in the contact area. The implicit incompatible first-order model (C8I) gives the largest value of −32 MPa; while the implicit reduced first-order model (C8R) gives the lowest value of −593 MPa. However, the stresses converge along most of path-2, especially at the important location at the end of path-2, where the crack initiates. The models with contact interaction also give the same results along the whole of path-3, indicating similar performances in fracture analysis simulations. However, the elastic and elastoplastic models with pressure distribution (EP20R and P20R) give absolute mean differences of 80% and 63% along path-2, which reduce to 43% and 11% along path-3, respectively, indicating their lack of ability to predict the stress field over the cross-sectional paths for fracture analysis.

For the contact problem, ratcheting wear may cause interlink wear on the contact surface. The ratcheting wear is the accumulation of repeated plastic strain due to significant contact forces [46]. To investigate the plastic strain along the chain surface, the equivalent plastic strains (PEEQ) over path-1 under 50% minimum breaking load are shown in Fig. 14. The elastic model with pressure distribution (EP20R) is not included since it does not capture the material plasticity. In region A, the implicit incompatible first-order model (C8I) overestimates the peak plastic strain by 2.4 times more than the explicit model (CEx8R) at the same location, while the implicit reduced second-order model (C20R) underestimate it by 10% at a location 3.6 mm away from the explicit model. The implicit reduced first-order model (C8R) gives a similar peak plastic strain to the explicit model, but it shifts to the peak location by 3.8 mm. However, all of the models with contact interaction (C20R, C8R, C8I and CEx8R) converge in region B. The elastoplastic model with pressure distribution (P20R) fails to capture the peak plastic strain in region A and overestimates the plastic strain by 58% at the end of path-1, indicating it is not appropriate for ratcheting wear problems.

5. Discussion

A number of parametric studies are performed to allow a comparison of the numerical models for different failure modes. Table 8 is

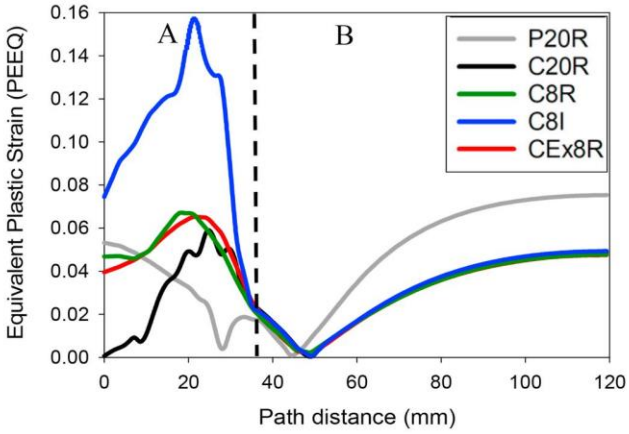

Fig. 14. Comparison of the equivalent plastic strains (PEEQ) for the different FE models under 50% minimum breaking load along path-1.

Table 8
Summary of appropriate models for different failure modes[].

	EP20R	P20R	C8I	C20R	C8R	CEx8R
Nominal stress for S-N approach	O	O	O	O	O	O
Residual stress	x	x	O	O	O	O
Fatigue damage	x	x	O	O	O	O
Fracture of crack propagation	x	x	O	O	O	O
Ratcheting wear in contact area	x	x	x	O	O	O
Ultimate strength	x	x	x	x	O	O
Mechano-Electrochemical corrosion	x	x	x	x	O	O
Permanent elongation	x	x	x	x	x	O

compiled to show when a numerical model is appropriate, where a circle indicates the results are within 10% of the explicit model (CEx8R) in predicting important parameters for that particular failure analyses and a cross indicates they are not. Here the explicit model is deemed appropriate based on the match to the available experimental data. Zarandi and Skallerud [47] measure the residual stresses in a mooring chain experimentally, which shows good agreement with a prediction from an FE model employing the implicit reduced eight-order model (C8R), supporting the fact that the FE models with contact interaction (C20R, C8R, C8I, CEx8R) are good for the residual stress prediction.

The elastic model with pressure distribution (EP20R) has been demonstrated to be poor at predicting any failure modes since it lacks material plasticity. The elastoplastic model with pressure distribution (P20R) can give similar results with other models with contact interaction under low load levels, e.g. under 25% minimum breaking load in the standardised dimensions. However, it is found that at higher load levels, 70% minimum breaking load, there is a larger difference to the models with contact interaction (C20R, C8R, C8I and CEx8R).

In general, all of the models with contact interaction (C20R, C8R, C8I and CEx8R) can accurately model most of the failure modes. However, convergence problems are a critical issue in the implicit models (C20R, C8R and C8I), requiring the user to apply unrealistic simplifications to the initial boundary condition to adjust the slave nodes be in contact with the master nodes in the first step [30]. The implicit incompatible first-order model (C8I) exhibits a much higher stress-strain field in the area of contact, although it manages to capture a similar stress-strain field to the other models (C20R, C8R and CEx8R) in regions far from the contact area, region B. This is because the incompatible mode elements are sensitive to mesh distortions due to significant contact forces in the contact area. The element distortions mean that the finite element interpolation functions cannot converge, making the elements too stiff and reducing the accuracy [48]. Therefore, care must be taken to ensure that the element distortions are minimal in the area of interests. Cases, where the incompatible mode elements can be used more appropriately, are bending/buckling analyses of thin members, for example, plate or pipe structures, where the element distortions are low, and this is supported in previous studies into these structures [49–51].

The implicit reduced second-order model (C20R) exhibits oscillating stresses in the contact area; even when the mesh size is reduced. This is due to the contact algorithm's difficulties in determining if the force distribution represents constant contact pressure or an actual variation across the surface of the second-order elements, composed of curved edges. The directions of the consistent nodal forces resulting from the pressure load are not uniform in the two-contact surfaces of the second-order elements, making it difficult for the equivalent nodal forces to converge because they do not have the same sign for constant pressure. The convergence problems cause a severe discontinuity iteration until sufficiently small tolerances are satisfied, which is a complicated process, especially if both the contacting bodies are deformable [23]. The implicit first-order model (C8R) shows superior performance among the other implicit models because the equivalent nodal forces for the applied pressures on the surfaces of the first-order elements always have a consistent sign and magnitude; therefore, there is no ambiguity regarding the contact state represented by a given distribution of nodal forces [23]. However, obtaining convergence remains an issue for all elements in the implicit solver.

The results of this study show that the model that is the best for all scenarios is the explicit model (CEx8R), which predicts a smooth gradient of the stress-strain in the contact area. The explicit model (CEx8R) runs the contact interaction without any convergence problems. When contact occurs, the resisting forces and masses of all contacting nodes on the slave surface are distributed to the nodes

Table 9
The computational costs and memory for the different FE models normalised against the explicit model.

Model	Simulation time	Memory usage
Elastic model with pressure distribution (EP20R)	0.13	0.26
Elastoplastic model with pressure distribution (P20R)	0.38	0.37
Implicit reduced second-order model (C20R)	113.84	41.33
Implicit incompatible first-order model (C8I)	15.32	52.67
Implicit reduced first-order model (C8R)	5.88	4.75

Appendix

on the master surface and add to the total inertial mass of the contacting interfaces. To maintain the stability of the contact enforcement, the explicit solver uses these distributed forces and masses to calculate an acceleration correction to obtain a corrected contact configuration [28]. The small-time increments used by the explicit solver ensure that the highly non-linear material behaviour in the contact area can be captured by adjusting the displacements and velocities of surface nodes involved in contact to remove small initial overclosures.

Table 9 shows that the explicit model (CEx8R) has a lower computational cost compared to the implicit models with contact interaction (C20R, C8R and C8I). This is because the implicit models experience a number of discontinuity iterations. In addition, the mass-scaling is used in the explicit model to increase the time increment and consequently decrease the computational costs for running the simulation. However, the models with pressure distribution (EP20R and P20R) have much lower computational costs since they do not have interlink contact interactions and half of the models are used. This indicates some benefits in carefully selected simulations, such as reliability analysis with Monte Carlo simulations or numerical optimisation methods, where the results for the stress-strain analysis are shown to be of acceptable accuracy.

6. Conclusion

Mooring lines regularly fail much earlier in their service life than predicted. The methods for predicting the stresses in mooring chains vary, but currently, there are no comparisons of these methods to help determine when they are appropriate. A comparison of the different methods for mooring chain modelling under tension is investigated. The predictions of the different models are checked against experimental tests. The convergence rate is found essential for accurate predictions of the mooring chain. The explicit model has no convergence problems with the least computational cost while providing the strongest performance across all of the failure modes.

Declaration of competing interest

The authors declare that they have no known competing financial interests or personal relationships that could have appeared to influence the work reported in this paper.

Acknowledgement

The authors gratefully acknowledge the funding by the Indonesia Endowment Fund for Education (LPDP) and the support of the Lloyd's Register Foundation (LRF). The authors also acknowledge the support of the University of Southampton for access to its IRIDIS5 High-Performance Computing Facility.

References

[1] Ma K, Duggal A, Smedley P, L'Hostis D, Shu H. A historical review on integrity issues of permanent mooring systems. In: Offshore technology conference OTC-24025, Houston, Texas, USA; 2013. p. 14.
[2] Majhi S, Souza RD. Application of lessons learned from field experience to design, installation and maintenance of FPS moorings. In: Offshore technology conference OTC-24181, Houston, Texas, USA; 2013. p. 15.
[3] Kvitrud A. Lessons learned from Norwegian mooring line failures 2010–2013. In: ASME 2014 33rd International conference on ocean, offshore and arctic engineering OMAE2014-23095. California, USA: San Fransisco; 2014. p. 10.
[4] Ryu A. Samsangsoo; heyl, caspar; duggal, "mooring cost sensitivity study based on cost-optimum mooring design. In: Proceedings of conference 2008 Korean society of ocean engineers; 2008. p. 5.
[5] Noble Denton Europe Limited. "RR444 - floating production system: JIP FPS mooring integrity," *Health and Safety Executive* [Online]. Available:. 2006. http://www.hse.gov.uk/research/rrpdf/rr444.pdf. [Accessed 19 July 2018].
[6] Crighton R. Gryphon insurance payouts close to £440m [Online]. Available: *Energy Voice*; 2013 [Accessed: 04-Feb-2019]. https://www.energyvoice.com/oilandgas/45369/gryphon-insurance-payouts-close-440m/.
[7] Fontaine E, Kilner A, Carra C, Washington D, Ma K, Phadke A. Industry survey of past failures, pre-emptive replacements and reported degradation for mooring systems of floating production units. In: Offshore technology conference OTC-25273, Houston, Texas, USA; 2014. p. 14.
[8] Gordon RB, Brown MG, Allen EM. Mooring integrity management: a state-of-the-art review. In: Offshore technology conference OTC-25134-MS, Houston, Texas, USA; 2014. p. 19. https://doi.org/10.4043/25134-MS.
[9] Sachan A, Choo YS. Mooring chain strength tests and ductile failure modeling using micromechanics and phenomenology based failure models. Ocean Eng 2020; 195:106663. November 2019.
[10] Tipton SM, Shoup GJ. The effect of proof loading on the fatigue behavior of open link chain. J Eng Mater Technol Jan. 1992;114(1):27–33.
[11] Pacheco P, Kenedi P, Jorge J, Savi M, Santos H. Finite element residual stress analysis applied to offshore studless chain links. In: ASME 2004 23rd International conference on offshore mechanics and arctic engineering OMAE2004-51508, Vancouver. Canada: British Columbia; 2004. p. 10.
[12] Pacheco P, Kenedi P, Jorge J, Santos H, Savi M, Paiva A. Modeling residual stresses in offshore chain links using finite element method. In: 17th International congress of mechanical engineering COBEM2003-0320. Brazil: Sao Paulo; 2003. p. 10.
[13] Pacheco P, Kenedi P, Jorge J. Elastoplastic analysis of the residual stress in chain links. In: 21st International Conference on offshore mechanics and arctic engineering, vol. 3. Oslo: Norway; 2002. p. 8. OMAE2002-28083.
[14] Pacheco P, Kenedi P, Jorge J, Paiva A. Analysis of the influence of mechanical properties on the residual stress in offshore chain links using the finite element method. In: ASME 2003 22nd International conference on offshore mechanics and arctic engineering OMAE2003-37205. Mexico: Cancun; 2003. p. 10.
[15] Bjørnsen E. Chains in mooring systems. M. S. Thesis. Trondheim, Norway: NTNU, Dept. Civil Engineering; 2014.
[16] Bastid P, Smith SD. Numerical analysis of contact stresses between mooring chain links and potential consequences for fatigue damage. In: ASME 2013 32nd International conference on ocean, offshore and arctic engineering OMAE2013-11360. France: Nantes; 2013. p. 8.
[17] Vargas PM, Hsu TM, Lee WK. Stress concentration factors for stud-less mooring chain links in fairleads. In: 23rd International conference on offshore mechanics and arctic engineering OMAE2004-51376, Vancouver. Canda: British Columbia; 2004. p. 9.
[18] Xue X, Chen NZ, Wu Y, Xiong Y, Guo Y. Mooring system fatigue analysis for a semi-submersible. Ocean Eng 2018;156:550–63.
[19] Xue X, Chen N. Fracture mechanics analysis for a mooring system subjected to Gaussian load processes. Eng Struct 2018;162(February):188–97.

[20] Kim Y, Kim MS, Park MJ. Fatigue analysis on the mooring chain of a spread moored FPSO considering the OPB and IPB. Int. J. Nav. Archit. Ocean Eng. 2018;11 (1):24.
[21] Rampi L, Bignonnet A, Le Cunff C, Bourgin F, Vargas P. Chain out of plane bending (OPB) fatigue joint industry project (JIP) FEA results and multiaxiality study results. In: ASME 2016 35th International conference on ocean, offshore and arctic engineering OMAE2016-54198. South Korea: Busan; 2016. p. 15.
[22] Edward C, Dev AK. Numerical methods for interlink stiffness formulations and parameters sensitivity of out-of-plane bending in mooring chains. In: ASME 2019 38th International conference on ocean, offshore and arctic engineering OMAE2019-96042, Glasgow, scotland, UK; 2019. p. 11.
[23] Dassault Systèmes Simulia Corp. Abaqus/CAE user's manual, theory guide. Version 6.12. Pawtucket, USA: ABAQUS, Inc.; 2012.
[24] Tian R, Yagawa G. "Generalized nodes and high-performance elements. Int J Numer Methods Eng Dec. 2005;64:2039–71. https://doi.org/10.1002/nme.1436.
[25] Tadepalli SC, Erdemir A, Cavanagh PR. Comparison of hexahedral and tetrahedral elements in finite element analysis of the foot and footwear. J Biomech 2011; 44(12):2337–43.
[26] IACS (International Association of Classification Societies). W22 offshore mooring chain [Online]. Available:. In: International association of classification societies; 2016. http://www.iacs.org.uk/publications/unified-requirements/ur-w/ur-w22-rev6-cln/. [Accessed 4 February 2019].
[27] Det Norske Veritas. "DNV-OS-E302 offshore mooring chain," DNV, Høvik, Norway [Online]. Available:. 2015. Accessed, https://rules.dnvgl.com/docs/pdf/DNV/codes/docs/2009-10/OS-E302.pdf. [Accessed 19 July 2018].
[28] Dassault Systèmes Simulia Corp. "Abaqus analysis user's guide 6.13 [Online]. Available: *ABAQUS, Inc.*; 2013. http://dsk.ippt.pan.pl/docs/abaqus/v6.13/books/usb/default.htm?startat=pt09ch36s03aus145.html. [Accessed 19 February 2020].
[29] Gabrielsen Ø, Larsen K, Reinholdtsen SA. "Fatigue testing of used mooring chain," in *ASME 2017 36th International Conference on ocean, Offshore and arctic engineering OMAE2017-61382*. Norway: Trondheim; 2017. p. 11.
[30] Dassault Systèmes Simulia Corp. ABAQUS documentation version 6.6 [Online]. Available: *ABAQUS, Inc.*; 2006. https://classes.engineering.wustl.edu/2009/spring/mase5513/abaqus/docs/v6.6/books/usb/default.htm?startat=pt09ch29s02aus124.html. [Accessed 7 March 2020].
[31] Ye J, Yan Y, Li J, Hong Y, Tian Z. 3D explicit finite element analysis of tensile failure behavior in adhesive-bonded composite single-lap joints. Compos Struct 2018;201:261–75.
[32] Harewood FJ, McHugh PE. Comparison of the implicit and explicit finite element methods using crystal plasticity. Comput Mater Sci 2007;39(2):481–94.
[33] Vulliet F, Ben Ftima M, Léger P. Stability of cracked concrete hydraulic structures by nonlinear quasi-static explicit finite element and 3D limit equilibrium methods. Comput Struct 2017;184:25–35.
[34] Liu P, Cheng X, Wang S, Liu S, Cheng Y. Numerical analysis of bearing failure in countersunk composite joints using 3D explicit simulation method. Compos Struct 2016;138:30–9.
[35] Li F, Hu W, Meng Q, Zhan Z, Shen F. A new damage-mechanics-based model for rolling contact fatigue analysis of cylindrical roller bearing. Tribol Int 2017;120 (September):105–14. 2018.
[36] Li HW, Yang H, Sun ZC. A robust integration algorithm for implementing rate dependent crystal plasticity into explicit finite element method. Int J Plast 2008;24 (2):267–88. https://doi.org/10.1016/j.ijplas.2007.03.014.
[37] Yang Z, Deng X, Li Z. Numerical modeling of dynamic frictional rolling contact with an explicit finite element method. Tribol Int 2019;129:214–31. https://doi.org/10.1016/j.triboint.2018.08.028.
[38] Yu H, Burgess IW, Davison JB, Plank RJ. Numerical simulation of bolted steel connections in fire using explicit dynamic analysis. J Constr Steel Res 2008;64(5): 515–25.
[39] Sun JS, Lee KH, Lee HP. Comparison of implicit and explicit finite element methods for dynamic problems. J Mater Process Technol 2000;105(1):110–8.
[40] Prior AM. Applications of implicit and explicit finite element techniques to metal forming. J Mater Process Technol 1994;45(1):649–56.
[41] Qin WJ, Guan CY. An investigation of contact stresses and crack initiation in spur gears based on finite element dynamics analysis. Int J Mech Sci 2014;83: 96–103.
[42] Jones J. Finite element analysis of the effect of twist on chain fatigue performance. In: ASME 2019 38th International conference on ocean. Glasgow, Scotland, UK: Offshore and Arctic Engineering OMAE2019-95276; 2019. p. 10.
[43] Zarandi EP, Skallerud BH. Cyclic behavior and strain energy-based fatigue damage analysis of mooring chains high strength steel. Mar Struct 2020;70:18.
[44] Gutman EM. Mechanochemistry of solid surfaces. Singapore: World Scientific Publishing Co., Pte. Ltd.; 1994.
[45] Det Norske Veritas. "Offshore standard DNV-OS-E301 position mooring," *DNV, Høvik, Norway* [Online]. Available:. 2013. Accessed, https://rules.dnvgl.com/docs/pdf/DNV/codes/docs/2013-10/OS-E301.pdf. [Accessed 19 July 2018].
[46] Widiyarta IM, Franklin FJ, Kapoor A. Modelling thermal effects in ratcheting-led wear and rolling contact fatigue. Wear 2008;265(9):1325–31.
[47] Zarandi EP, Skallerud BH. Experimental and numerical study of mooring chain residual stresses and implications for fatigue life. Int J Fatig 2019;135 (September):105530.
[48] Dassault Systèmes Simulia Corp. ABAQUS documentation version 6.5 [Online]. Available: *ABAQUS, Inc.*; 2004. https://classes.engineering.wustl.edu/2009/spring/mase5513/abaqus/docs/v6.5/books/gss/default.htm?startat=ch04s01.html. [Accessed 9 February 2020].
[49] Gong S, Sun B, Bao S, Bai Y. Buckle propagation of offshore pipelines under external pressure. Mar Struct 2012;29(1):115–30.
[50] Santos CCP, Pesce CP. An alternative strategy for offshore flexible pipes finite element analysis. Mar Struct 2019;65:376–416.
[51] Rabelo MA, Pesce CP, Santos CCP, Ramos R, Franzini GR, Gay Neto A. An investigation on flexible pipes birdcaging triggering. Mar Struct 2015;40:159–82.

Appendix F Gemilang et al. [207] (Published)

Appendix

Marine Structures 76 (2021) 102892

Contents lists available at ScienceDirect

Marine Structures

journal homepage: http://www.elsevier.com/locate/marstruc

Low-cycle fatigue assessment of offshore mooring chains under service loading

G.M. Gemilang [a,b,*], P.A.S. Reed [c], A.J. Sobey [a,d]

[a] Maritime Engineering Group, University of Southampton, Boldrewood Innovation Campus, Southampton, SO16 7QF, UK
[b] Faculty of Infrastructure Planning, Department of Civil Engineering, Universitas Pertamina, Terusan Simprug, Jakarta, 12220, Indonesia
[c] Engineering Materials Group, University of Southampton, Highfield, Southampton, SO16 7QF, UK
[d] Marine and Maritime Group, Data-centric Engineering, The Alan Turing Institute, The British Library, London, NW1 2DB, UK

ARTICLE INFO

Keywords:
FPSO
Finite element method
Cyclic plasticity
Mean load effect
Fatigue damage
Low-cycle fatigue

ABSTRACT

The integrity of mooring chains is essential to the safety of a range of offshore platforms. However, mooring line failures are occurring earlier than their design lives, with a high number of these failures occurring due to fatigue. Early in the fatigue life of the component fatigue initiation processes occur, where the fatigue hotspot is sensitive to the mean load and there is plastic strain accumulation from the multiaxial stress-strain responses of the material, leading to cyclic plastic damage accumulation. The traditional SN approach suggested by mooring standards does not consider these effects, and it is proposed that this lack of consideration under low-cycle fatigue conditions is the reason for the current non-conservative fatigue assessments of mooring chains. This paper aims to develop a fatigue approach based on a critical plane multiaxial fatigue criterion for mooring chains that can consider the damage-induced by the cyclic plasticity and the mean load effect, to investigate the importance of incorporating low-cycle fatigue into the mooring chain life prediction. To develop the critical plane approach, the multiaxial stress-strain states are extracted for the critical plane at the fatigue hotspot from a finite element model of a mooring chain. This is then correlated with a fatigue life prediction provided by conventional fatigue design data. It uses a simulation of an FPSO as a case study to demonstrate the importance of low cycle fatigue, which shows that the mean load effect is significant in reducing the fatigue life for mooring chain applications, while the effect of fatigue damage-induced cyclic plasticity is limited. The fatigue damage accumulation predicted by the critical plane approach is significantly higher than that of the traditional SN approach and should be accounted for in mooring line design.

1. Current design of mooring chains against fatigue

There are many natural energy resources offshore, including oil, gas, wind and wave. As a result, floating offshore platforms are widely used for the exploitation of these energy sources [1,2]. Continuous operation of floating offshore platforms relies on the integrity of mooring chains to keep these platforms in position against adverse environments over design lives of 20-years, or longer. However, mooring failures have occurred at a critically high rate in recent decades, with the potential for catastrophic financial and environmental impacts. Between 2000 and 2011, over 21 mooring failures occurred, of which about half occurred during the first three

* Corresponding author. Maritime Engineering Group, University of Southampton, Boldrewood Innovation Campus, Southampton, SO16 7QF, UK.
E-mail address: gmg1g16@soton.ac.uk (G.M. Gemilang).

https://doi.org/10.1016/j.marstruc.2020.102892
Received 25 August 2020; Received in revised form 22 October 2020; Accepted 4 November 2020

years [3,4]; there were a further 16 failures on the Norwegian Continental Shelf between 2010 and 2014 [5], where these failures occurred in harsh sea environments. Several industry surveys [1,3,4] have identified multiple failure modes for the mooring lines of which fatigue failure is the most significant, requiring further investigations into why these predictions are non-conservative.

The traditional SN approach suggested by mooring standards, DNVGL-OS-E301 [6], is based on SN curves derived from full-scale fatigue tests on 76 mm chains of steel grades R3 and R4 under tensile loading at a constant mean load of 20% of the minimum breaking load in simulated seawater [6–9]. This approach is stress-based, which is suitable for the high-cycle fatigue regime where plastic deformation is small or negligible but lacks an explicit consideration of the material's stress-strain evolution at the fatigue hotspot when determining the fatigue response. This approach does not consider the effects of mean load or cyclic plastic degradation of the material on the fatigue damage when subjected to low-cycle fatigue loading. However, since failure in service occurs earlier in their expected lives, it is proposed that the mooring chains are likely to have experienced a high proportion of low-cycle fatigue loading with high mean loads. The low-cycle fatigue regime is commonly considered to be better described by strain-life approaches, applied to lives of less than 10^5 fatigue cycles, compared to the stress-life approaches for the high-cycle fatigue regime, $>10^5$ cycles [10]. Mooring chains are subjected to approximately 15×10^6 fatigue cycles over three years of operation, assuming a 6 s period of loading cycles on average, showing that a high proportion of that damage occurs under low-cycle fatigue and this is likely be particularly significant when operating in harsh sea environments with high mean loads. The lack of consideration of mean load effects and cyclic plasticity effects for low-cycle fatigue is therefore proposed to be a contributing factor for the current non-conservative fatigue assessments of mooring chains.

In the mooring line literature, most published studies are limited to the stress-life approach which is suitable for the high-cycle fatigue regime, where plastic deformation is small or negligible [11–16]. Although in some cases the stress-life approaches can predict the low-cycle fatigue behaviour [17–20], they cannot reflect the constitutive behaviour of the material when the fatigue response changes from the high-cycle to low-cycle fatigue regime [19–21]. Therefore, the stress-life approach may underestimate the proportion of low-cycle fatigue in mooring line loading. The number of studies investigating low-cycle fatigue behaviour in mooring lines is limited, with only Zarandi and Skallerud [22,23] using a strain-life approach to find the fatigue crack initiation life of corroded mooring chains. However, this is limited to deterministic cyclic loading, without considering the stochastic mooring line loading, and the addition of corrosion means it is difficult to isolate the effects of low-cycle fatigue on the mooring line failure.

Therefore, this paper aims to develop a fatigue approach capable of considering the mean load and cyclic plasticity effects on the fatigue damage which governs the low-cycle fatigue of mooring chains, to determine the importance of low-cycle fatigue in early failures currently observed in operating mooring lines. The analysis excludes other damage mechanisms (e.g. corrosion pitting), allowing for the isolation of the low-cycle fatigue-induced effects. The Smith-Watson-Topper approach using critical plane multiaxial fatigue criteria is selected since this approach has been demonstrated to accurately capture the mean load and cyclic plasticity effects in both high-cycle and low-cycle fatigue regimes, where fatigue damage is assessed directly in terms of local strains and stresses at the fatigue hotspot [24–29]. The fatigue damage accumulation predicted by this approach and that predicted by the traditional SN approach, are compared in a mooring line simulation of an FPSO, using the rainflow counting method and the Palmgren-Miner's rule.

2. Development of a representative chain model

A model of a mooring line is developed using the IACS [30] standardised dimensions for an offshore studless chain with a diameter, D, of 76 mm. The total length, L, is equal to $6D$; the total width, W, is $3.35D$ and the curved section radius, R, is $0.675D$, as illustrated in Fig. 1. The analysis is performed at two local hotspots, determined at the critical fatigue locations where the majority of fatigue failures have been found when under tension loading and are indicated in Fig. 1 as the Crown and K_t points [8,9,31].

The FE model is developed in ABAQUS 6.14 and automated using a Python script, considering both material and geometric nonlinearities using the explicit solver with C3D8R elements and a mass-scaling factor of 100, based on a previously developed method [32]. A $1/8^{th}$ portion of the chain is modelled that takes advantage of the three symmetry planes and minimises the computational cost, as shown in Fig. 2, where the slave model has a finer mesh as the resultant stresses and strains are extracted from these locations. A mesh convergence analysis was performed to examine the sensitivity of local stress and strain at the critical fatigue locations; the final

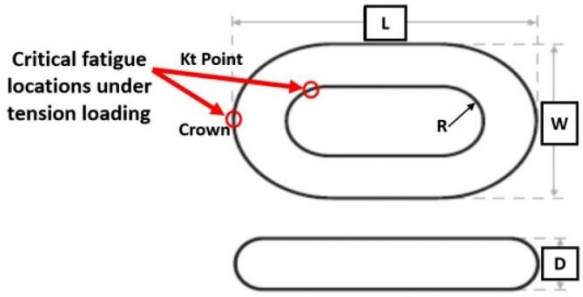

Fig. 1. The standardised dimensions for a studless chain, taken from IACS, and the critical fatigue locations.

Appendix

mesh has a corresponding size of 3.5 mm for the slave model and 10 mm for the master model. Symmetric boundary conditions are applied to the symmetry planes shown in red in Fig. 2. The loaded surface at the top of the master model does not have this boundary condition, to allow the load to be applied in the axial direction. The symmetric boundary conditions constrain the displacement of nodes on each symmetry plane in the normal direction and the rotation in the other two directions. For example, the bottom surface of the slave model is constrained against displacement in the y-axis and against rotation in the x and z-axes. The contact discretisation is defined as surface-to-surface with a finite sliding formulation, as the tension-tension simulation assumes no sliding of one surface along with the other [33]. A friction coefficient of 0.7 is used for the tangential interaction behaviour [12].

3. Material models

In order to determine how the material selection affects the fatigue predictions, material models representative of the monotonic and cyclic mechanical properties are considered, and a comparison is made between them. The R4 steel grade, which complies with DNVGL-OS-E302 [34], is considered, as it is the most prevalent material grade currently in use for mooring chains [8]. A monotonic material model is developed from mechanical properties derived from tensile tests conducted by Rampi et al. [35], in which a bilinear isotropic hardening is used, and the strain associated with the tensile strength is adopted as half the total elongation specified in the standards [14,34], this is designated Mono-Rampi. Two models are developed to describe the cyclic material responses, which were derived from low-cycle fatigue tests conducted by Rampi et al. [35], designated Cyclic-Rampi, and Zarandi and Skallerud [22], designated Cyclic-Zarandi, using the constitutive model of the combined nonlinear isotropic-kinematic hardening proposed by Chaboche [36]. This constitutive model has been widely used in modelling fatigue and has been shown to be robust in describing the mechanical properties of a material under cyclic loading [36,37], and the cyclic material models have been shown to exhibit an accurate stress-strain response when compared to material testing data under low-cycle fatigue tests in the literature [22,35]. Table 1 outlines the material properties with a Young's modulus, E, of 206.6 GPa and a Poisson's ratio, ν, of 0.3 for each model, where σ_y is the monotonic yield strength, σ_T is the monotonic tensile strength, A_T is total elongation, $\sigma|_0$ is the yield strength at zero plastic strain, Q_∞ is the maximum change in yield strength, b is the rate at which the yield surface changes with the development of plastic strain accumulation, C is the initial kinematic hardening moduli, and γ determines the decreasing rate of the kinematic hardening moduli with increasing plastic strain accumulation.

Fig. 3 demonstrates the material models in ABAQUS using a single element model under displacement control to show their differences in describing the material response under monotonic loading and cyclic loading conditions. Fig. 3(a) shows the materials' stress-strain curves under monotonic loading, where Cyclic-Rampi and Cyclic-Zarandi exhibit similar plastic responses. For these models, the stresses decrease with increases in plastic strain due to the materials' cyclic softening response. However, the curve of the Mono-Rampi increases linearly from the yield stress to the tensile stress but remains constant when the plastic strain is above the tensile strength, without any cyclic softening. The Mono-Rampi properties were selected to determine the difference in life predictions between monotonic or cyclic material models as the amount of plastic strain will be underestimated, in comparison to the cyclic material models, when subjected to monotonic loading. These differences will lead to variations in the initial elastic shakedown for the first cycle, the state where the stress-strain relationship is stabilised in elastic behaviour [10].

Fig. 3(b) shows the material responses under cyclic loading, where cyclic loading is selected to show the evolution of the maximum and minimum values of the peak stresses using the number of cycles experienced by the material models at a strain range, $\Delta\epsilon$, of 0.0155 and a strain ratio, R_ϵ, of -1. Under this cyclic loading, the Cyclic-Rampi and Cyclic-Zarandi models exhibit cyclic softening behaviour in the early cycles, which then develops more slowly during the subsequent cycles until stabilisation of the elastic shakedown is achieved. Cyclic-Zarandi has a more significant cyclic softening behaviour, leading to a higher amount of plastic strain than Cyclic-Rampi. This is because the Cyclic-Zarandi is derived from low-cycle fatigue tests at a higher strain range than the one used to obtain Cyclic-Rampi, resulting in a more significant cyclic softening response [22,35]. However, the Mono-Rampi is unable to simulate the cyclic softening behaviour, instead exhibiting hardening behaviour in the first five cycles, and develops elastic shakedown before the cyclic material models. Therefore, the Mono-Rampi will develop the highest values of peak stress throughout the cycles. This implies that the use of the monotonic material models will significantly underestimate the amount of plastic strain and the cyclic plasticity effects in applications where the components are experiencing cyclic stress-strain evolution under progressive loading cycles,

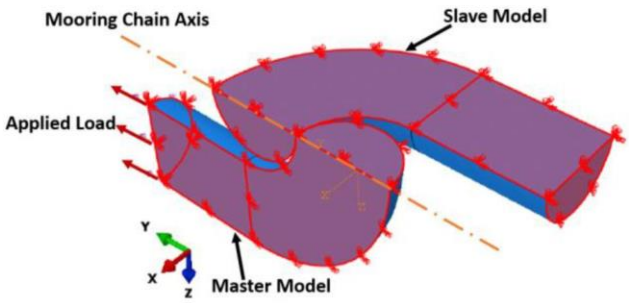

Fig. 2. The finite element model of the chain-link where the left part is the master and the right part is the slave.

Table 1
Parameters for the monotonic and cyclic material models.

Monotonic material model	Ref.	Yield strength	Tensile strength		Total elongation	
		σ_y (MPa)	σ_T (MPa)		A_T (%)	
Mono-Rampi	[35]	903	1039		12	
Cyclic material model	Ref.	Initial yield strength	Isotropic component		Kinematic component	
		$\sigma\|_0$ (MPa)	Q_∞ (MPa)	b	C	γ
Cyclic-Rampi	[35]	723.6	−141.6	1.42	244100	1379
Cyclic-Zarandi	[22]	546	−227	3.1	536565	1500

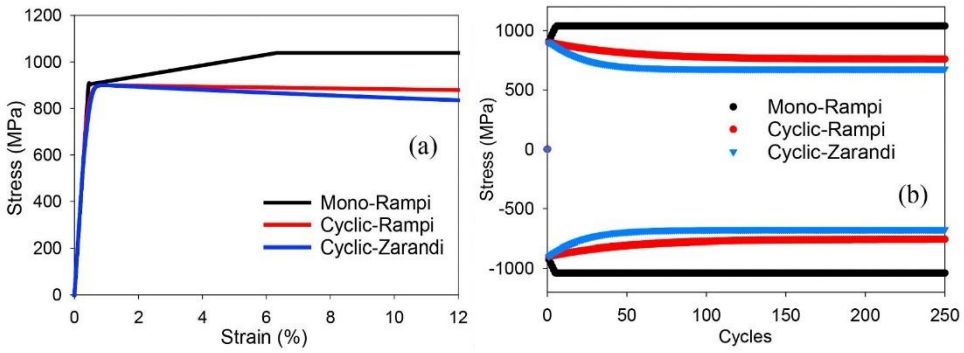

Fig. 3. Comparison between the bilinear monotonic material model and the Chaboche cyclic material models (a) under monotonic loading, showing the stress-strain curves (b) under cyclic loading, showing the evolution of the maximum and minimum values of the peak stresses with the number of cycles.

which may lead to inaccurate fatigue life estimations.

4. Calibration of the critical plane fatigue assessment

Smith et al. [38,39] proposed a critical plane multiaxial fatigue method, where fatigue damage is assessed directly in terms of local strains and stresses under progressive loading cycles. The method is described by Eq. (1),

$$SWT = \sigma_{n,max}\frac{\Delta\varepsilon_n}{2}, \tag{1}$$

where SWT is the damage parameter, $\sigma_{n,max}$ is the maximum normal stress and $\Delta\varepsilon_n$ is the normal strain range perpendicular to the critical plane during one cycle. The SWT damage parameter represents the real physical properties of the stress-strain function at the critical fatigue location, that has been demonstrated governing the fatigue of metal structures [38,39]. The critical plane is determined by checking the value of SWT on different planes in a stabilised cyclic load, where the plane with the highest SWT is defined as the critical plane. The SWT damage parameter can be related to fatigue life using a general formula given in Eq. (2),

$$SWT = A_1 {N_f}^{a_1} + A_2 {N_f}^{a_2}, \tag{2}$$

where N_f is the number of cycles to failure, $A1$, A_2, a_1 and a_2 are material constants and can be determined by calibration tests from experimental data. This general formula is used to generate a fitted curve for SWT damage parameters across a range of the number of cycles to failure. This method is based on the assumption that the surface of the part is intact without considering the effects of varying surface roughness, or pre-existing defects. This assumption can be considered to be reasonable as the chain is inspected to ensure that there are no visible surface defects prior to deployment. Therefore, in conditions where pre-existing defects do not significantly accelerate crack initiation and early propagation stages, acceptable life prediction results can be expected using this fatigue method as long as the macroscopic stress/strain evolutions at critical regions during fatigue loading are accurately determined so that the overall damage accumulation in the component is reasonably predicted.

DNVGL-OS-E301 [6] provides the number of cycles to failure of mooring chains under different loading conditions providing fatigue design data based on SN curves derived from full-scale fatigue tests. The full-scale fatigue tests are simulated in the FE model to establish the SWT damage parameters correlated to the fatigue life data based on the conventional design data adopted from DNVGL-OS-E301 [6] at different load amplitudes. The tests subject a chain with a diameter of 76 mm, and made from R4 steel grade, to

Appendix

a first proof load cycle up to 70% of the minimum breaking load and then back to zero. This is followed by cyclic loads with a constant mean load equal to 20% of the minimum breaking load, but under a different load amplitude for each test [6–9]. The minimum breaking load is 6001 kN for this chain type according to the standard, IACS-W22 [30]. The proof load results in significant plastic deformation and compressive residual stresses developed at both the fatigue hotspots, the crown and K_t point. The stabilised stress-strain response better describes the subsequent fatigue behaviour [18,24], and therefore the cyclic loads are run until the stress-strain response is stabilised under elastic shakedown, where the maximum normal stress, $\sigma_{n,max}$, and the normal strain range, $\Delta\varepsilon_n$, on the critical plane are extracted from the FE results to calculate the *SWT* damage parameters, according to Eq. (1).

To determine the critical plane, the *SWT* value is checked in the stabilised cyclic load state for all planes between $-90° < \phi < 90°$ measured counter-clockwise from the longitudinal direction to the normal vector with an interval of 1°, where the plane with the highest *SWT* value is taken as the critical plane. The normal stress, σ_n, and normal strain, ε_n, on the plane were calculated using the multiaxial stress-strain results at the node of the element for the crown, while the multiaxial stress-strain results are averaged at the node of the common elements for the K_t point. It was found that the *SWT* damage parameter is at the maximum when $\phi = 0°$ for both crown and K_t point under various load amplitudes, i.e. from 1% to 19% MBL. Fig. 4(a) shows an example where the resultant *SWT* damage parameters on different planes for both crown and K_t point under a load amplitude of 11% MBL are shown, indicating that the maximum damage parameter is reached when $\phi = 0°$; this is then defined as the critical plane and is used to calculate the *SWT* damage parameter. Fig. 4(b) shows the damage parameters on the critical plane of the K_t point are lower than those of the crown with a mean absolute difference of 0.0352 and a maximum absolute difference of 0.049, across the range of selected load amplitudes. The result is in line with full-scale experimental fatigue results [8,9,40], where the crown is found to be more susceptible to fatigue damage than the K_t point. This is because the residual compressive stress at the K_t point, 489 MPa, is greater than that at the crown, 358 MPa, upon release of the proof load. Subsequent analyses, therefore, concentrate on the crown for the fatigue assessments. The results presented in Fig. 4 use the Cyclic-Rampi material model, but similar results were found using the other material models. Fig. 4(b) also shows that the *SWT* damage parameter is near zero when the load amplitude is relatively low. This is because the critical plane approach assumes no fatigue damage occurs when the maximum normal stress perpendicular to the critical plane is compressive, and the compressive stresses have been induced by previous proof load applications.

The maximum normal stress, $\sigma_{n,max}$, and the normal strain range, $\Delta\varepsilon_n$, on the critical plane at the crown hotspot during the stabilised cyclic load are therefore used to calculate the *SWT* damage parameters, according to Eq. (1). The *SWT* damage parameters are correlated with the respective number of cycles to failure from the fatigue life predictions of DNVGL-OS-E301 [6] by simulating the fatigue tests under different loading conditions, which are a constant mean load of 20% MBL and various load amplitudes, i.e. from 1% to 19% MBL, based on mooring chains service lives. The resultant *SWT* damage parameters, under different load amplitudes, are used to calibrate the parameters of the fitted curves based on the general formula of Eq. (2) in order to interpolate the number of cycles to failure from the corresponding *SWT* damage parameters during fatigue loading. Fig. 5 shows the generated fitted curves, using the resultant *SWT* damage parameters, across a range of the number of cycles to failure. Appendix A provides the details of *SWT* damage parameters under different load amplitudes and the calibration of the fitted curves. Cyclic-Rampi and Cyclic-Zarandi have similar curves as both exhibit cyclic softening during the first cycle, while the curve of the Mono-Rampi increases to a higher value than the others. This is because the significant hardening behaviour of Mono-Rampi during the first cycle results in a high maximum normal stress, $\sigma_{n,max}$. Unlike the traditional SN approach, the critical plane approach takes all of the local stress-strain evolution into account when determining the fatigue response, including the proof load-induced effects i.e. strain hardening and residual stresses, mean load effects, material model nonlinearities and geometric nonlinearities. The FE-based critical plane approach has been correlated with the fatigue design data adopted from DNVGL-OS-E301 [6], allowing the fatigue life to be predicted by a fitted curve for a particular material model.

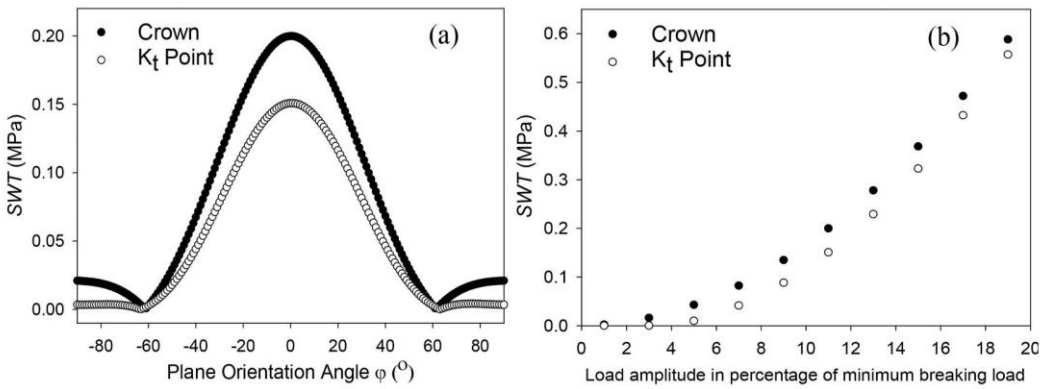

Fig. 4. Comparison between the crown and K_t point (a) damage parameters on different plane orientation angles, (b) damage parameters on the critical plane under a range of load amplitudes.

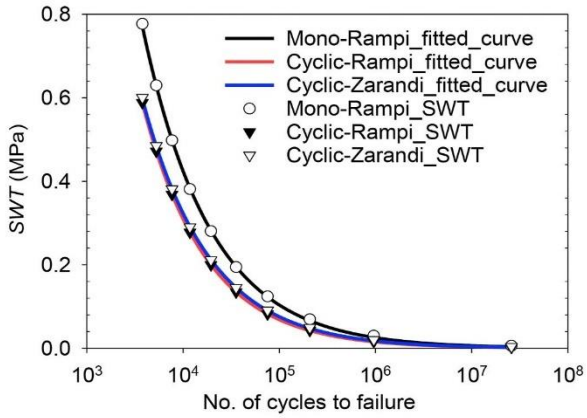

Fig. 5. The fitted calibration curves based on the fatigue life of mooring chains for the Smith-Watson-Topper (SWT) using the stress/strain data at the crown fatigue hotspot for the different material models.

5. Fatigue simulations

5.1. Mooring chain loading

In order to simulate the fatigue experienced by the mooring chains in service, the tension-spectrum, representing the fatigue loading, is simulated in a mooring line simulation of an FPSO as a case study using the Flexcom package [41]. The case study simulates a mooring system of an FPSO at a water depth of 810 m in a specific sea-state adopted from Gao and Moan [42] for short-term analysis. The sea-state is characterised by the significant wave height, $H_s = 6.25$ m, a spectral peak period, $T_p = 12.5$ s, a 1-h mean wind velocity, $U_w = 7.5$ m/s, and a mean current velocity, $U_c = 0.5$ m/s, where the Pierson-Moskowitz wave spectrum is applied, and all environmental loads are assumed to act from the head sea. The main particulars of the FPSO are adopted from the Flexcom package [41], which are listed in Table 2. The RAO and QTF are taken from the Flexcom package [41] to include the first-order and second-order motions of the FPSO to give the combined vessel response.

The mooring system is an eight-line catenary system with chain-wire rope-chain components connected to a turret of the FPSO with a pre-tension of 1037 kN (17% MBL) for each line. Table 3 shows the mooring component principals, which are adopted from the Flexcom package [41].

Fig. 6 shows the horizontal projection of the mooring system with an angular spread of 45° between the lines. The anchor radius from the turret centreline is 700 m, with which the mooring line anchor points are constrained, and each fairlead is attached to the FPSO via hinges at 8 m below the mean water level. A time-domain simulation of 3 h is used, as suggested by the mooring standard DNVGL-OS-E301 [6], to provide adequate statistics with a time step of 0.1 s. The effect of the system's nonlinear characteristics is included through both the wave-frequency and the low-frequency tension spectra through coupled dynamic analysis. Line 1 is selected for low-cycle fatigue analysis to investigate the effects of mean load and cyclic plasticity, as it experiences the greatest tension. The tension-spectrum of the top chain is used for fatigue analysis, as suggested by the mooring standard, API-RP-2SK [43].

5.2. Fatigue damage comparison

The tension-spectrum from the mooring line simulation consists of combined high-cycle and low-cycle fatigue loading with a maximum tension of 2595 kN, a mean of 1272 kN and a minimum of 617 kN. The rainflow counting method [44] is used to identify individual loading cycles within the tension-spectrum because it has been shown to give reasonable fatigue estimates [45]. The total fatigue damage is calculated using the Palmgren-Miner's rule [46], assuming that the total fatigue damage caused by a number of stress cycles equals the summation of damages caused by the individual loading cycles. The individual loading cycles from the

Table 2
Main particulars of the FPSO taken from Flexcom.

Parameter	Value
Vessel mass	382,734 t
Vessel draft	21.2 m
Vessel beam	58.2 m
Length from COG to forward perpendicular	162.5 m
Length from COG to aft perpendicular	176.7 m
Length from COG to turret point	150 m

Appendix

Table 3
Mooring component principals.

Parameter	Length (m)	Size (mm)	Mass per meter (kg/m)	Axial stiffness (kN)	Normal drag coeff.	Longitudinal drag coeff.
tableAnchor chain	500	76	115	4.935×10^5	2.4	1.15
Wire rope	400	89	62	7.03×10^5	1.2	0.1
Top chain	200	76	115	4.935×10^5	2.4	1.15

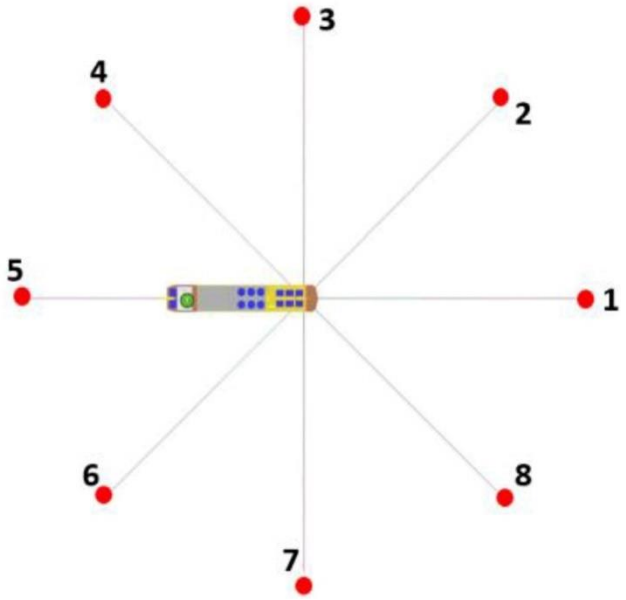

Fig. 6. Mooring system arrangement in this simulation taken from Flexcom [41].

tension-spectrum is simulated in the FE chain model after which the proof load, and its release, are applied to simulate the mooring chains' loading history. The fatigue damage accumulation is predicted using the Smith-Watson-Topper critical plane approach and the traditional SN approach to allow a comparison between these two approaches.

Fig. 7 shows that the predicted fatigue damage accumulation of the critical plane approach is significantly higher than that of the traditional SN approach. The different material models used in the critical plane approach all predict a significantly higher fatigue damage accumulation relative to the traditional SN approach, by 78.1% using Cyclic-Rampi, 74.3% using Cyclic-Zarandi and 71.74% using Mono-Rampi. On average, the traditional SN approach predicts 7.2% of all the individual loading cycles will contribute to low-

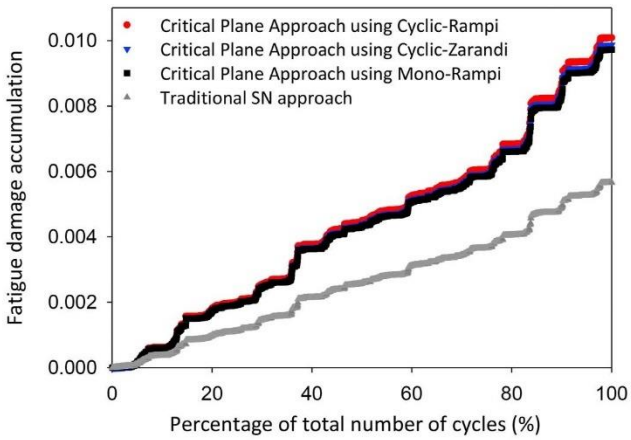

Fig. 7. Comparison of the predicted fatigue damage accumulation using different approaches.

cycle fatigue, while the critical plane approach predicts 12.9% will, across all the material models considered. This indicates that the critical plane approach captures a greater number of important low-cycle fatigue events in the mooring line loading because it accounts for the effects of the mean load and cyclic plasticity in the fatigue life assessment.

Fig. 8 shows the ratio between the fatigue damage predicted by the critical plane approach and that predicted by the traditional SN approach over a range of mean loads and load amplitudes, using Cyclic-Rampi and Mono-Rampi material models as these represent the maximum and minimum predictions from the critical plane approach in the case study. The mean load effect changes at 20% MBL, showing that the lower the load amplitude, the higher the fatigue damage ratio when the mean load level is above 20% MBL, while the opposite happens when the mean load level is below 20% MBL. The fatigue damage ratio is one at the mean load of 20% MBL, since the critical plane approach is calibrated based on the same fatigue design data as the traditional approach at this mean load level, obtained from DNVGL-OS-E301 [6]. At higher mean loads, the fatigue damage prediction is higher for the critical plane approach than the traditional SN approach, resulting in the difference between the two methods being more significant even if the stresses at the hotspot are smaller than the elastic limit, and this becomes more significant with lower load amplitudes.

These mean load effects are reflected in the accumulated fatigue damage comparison shown in Fig. 7, where about half of all the individual load cycles in the tension-spectrum have mean loads above 20% MBL and load amplitudes mostly ranged from 0% to 5% MBL. The fatigue damage ratios of the Cyclic-Rampi are higher than the fatigue damage ratios of the Mono-Rampi, explaining the increase in fatigue damage accumulation for the Cyclic-Rampi model compared to that for the Mono-Rampi. Although the Mono-Rampi cannot predict the cyclic softening behaviour, the strain hardening effect due to the proof load during the first cycle maintains the stress-strain response in the elastic shakedown with no clear plastic deformation beyond the first cycle, meaning that the cyclic plasticity effects are not evident during fatigue loading in the case study. Therefore, the results of Mono-Rampi and Cyclic-Rampi are similar.

In order to investigate the cyclic plasticity effect, Fig. 9(a) and Fig. 9(b) show the stress-strain responses and equivalent plastic strain, respectively, when the proof load is applied, released, and followed by cyclic loads with an amplitude of 20% MBL in an incremental mean load with an interval of 1% MBL for each progressive cycle. The cyclic stress-strain evolution and the plastic strain accumulation starts to occur at a mean load of 50% MBL, meaning that cyclic plasticity starts to take effect when the cyclic load reaches the proof load level. In contrast, the cyclic plasticity does not take effect when the cyclic load is below 70% MBL. This is because strain hardening, due to the proof load on the first cycle, has a significant effect on maintaining the stress-strain response in elastic shakedown throughout all cycles that are below 70% MBL. Therefore, the cyclic plasticity effect is minor in the case study for all

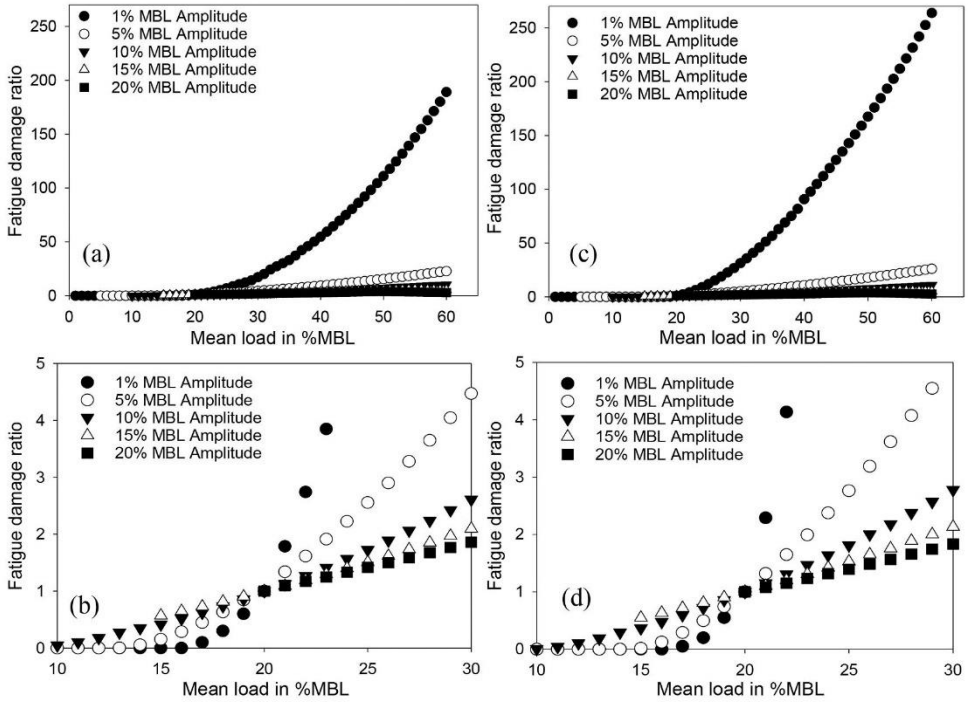

Fig. 8. Mean load effects on the fatigue damage ratio in a range of mean load for Mono-Rampi (a) full range of MBLs 0–60% (b) change in behaviour due to the amplitude at a mean load of 20% MBL, and for Cyclic-Rampi (c) full range of MBLs 0–60% (d) change in behaviour due to the amplitude at a mean load of 20% MBL.

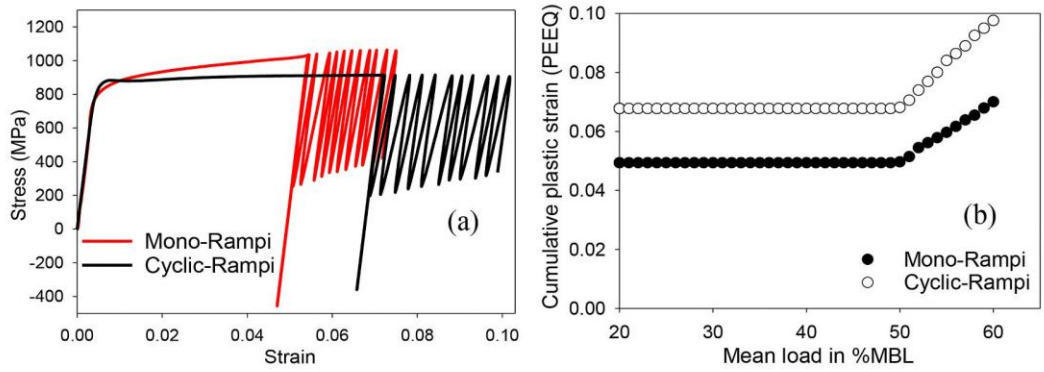

Fig. 9. Fatigue simulation when the proof load is applied, released, and followed by cyclic loads with an amplitude of 20% MBL in an incremental mean load with an interval of 1% MBL for each progressive cycle, showing (a) the stress-strain responses, (b) the plastic strain accumulation.

material models since the individual loading cycles within the tension-spectrum are below 70% MBL. The Mono-Rampi model underestimates the amount of cumulative plastic straining with a mean difference of 28% relative to the Cyclic-Rampi model since the monotonic material model cannot predict the cyclic-softening behaviour, leading to an inaccurate estimation of the fatigue life when cyclic plasticity is involved during fatigue loading in service.

5.3. *Parametric study for fatigue in different sea-states*

Since the mean load is shown to have a significant effect, a parametric study for fatigue in different sea-states is used to assess how often the mean load is above 20% MBL, to identify when the critical plane approach is of significance and to understand the importance of the mean load on fatigue life. The variation of waves over the long-term environment can be described by several representative sea-states, against which the fatigue damage is weighted using the lumped occurrence probability, the proportion of occurrences of a representative sea-state out of the total probability for all sea-states. A typical scatter diagram in the North Sea, consisting of 197 original sea-states, is adopted from Song and Wang [47] which uses the JONSWAP wave spectrum to define the significant wave height, H_s, and up-crossing wave period, T_z. The scatter diagram is partitioned into nine representative sea-state blocks at which the coupled dynamic analysis is simulated for this parametric study, as presented in Appendix B. Only the wave loads are changed in the representative sea-states, while the other assumptions and parameters remain the same as the previous case study described in section 5.1. Table 4 shows the selected representative sea-state blocks based on the highest occurrence rate within each block, with the respective lumped occurrence probability, p.

Fig. 10 shows the mean load distribution in the individual loading cycles of tension-spectrum for each sea-state, separating mean loads at greater than 20% MBL. Sea-states 1, 2, and 3 in Fig. 10(a) are benign, having respectively 0%, 0.3% and 5.3% of the mean load proportion above 20% MBL; therefore, the traditional SN approach can be used. However, sea-states 4, 5 and 6 in Fig. 10(b) have respectively 21.4%, 33.5% and 36.3% of the mean load proportion above 20% MBL, and sea-states 7, 8 and 9 in Fig. 10(c) have respectively 42.4%, 44% and 46.3% of the mean load proportion above 20% MBL. At these higher sea-states, it is important to consider the detrimental effect of the mean load on the fatigue assessment by using the critical plane approach. Similarly, the first case study also has about half of the mean load proportion above 20% MBL. However, the load-amplitude proportions above 5% MBL, that can cause the number of cycles to failure below 10^5 in the low-cycle fatigue regime, are 15.8%, 19.4%, 34.7% for the sea-states 7–9, respectively, while this is 12.9% for the first case study. This shows that in conditions with higher proportions of severe sea-states, the higher the proportion of time the mean load is above 20% MBL and the more important the critical plane approach becomes.

Table 4
The wave parameters for the nine representative partitions of the North Sea.

No.	H_s (m)	T_z (s)	p (%)
1	1.5	7.5	47.976
2	2.5	10.5	20.588
3	5.5	8.5	15.356
4	4.5	11.5	11.067
5	7.5	9.5	2.643
6	8.5	12.5	1.878
7	11.5	10.5	0.167
8	10.5	12.5	0.292
9	13.5	11.5	0.032

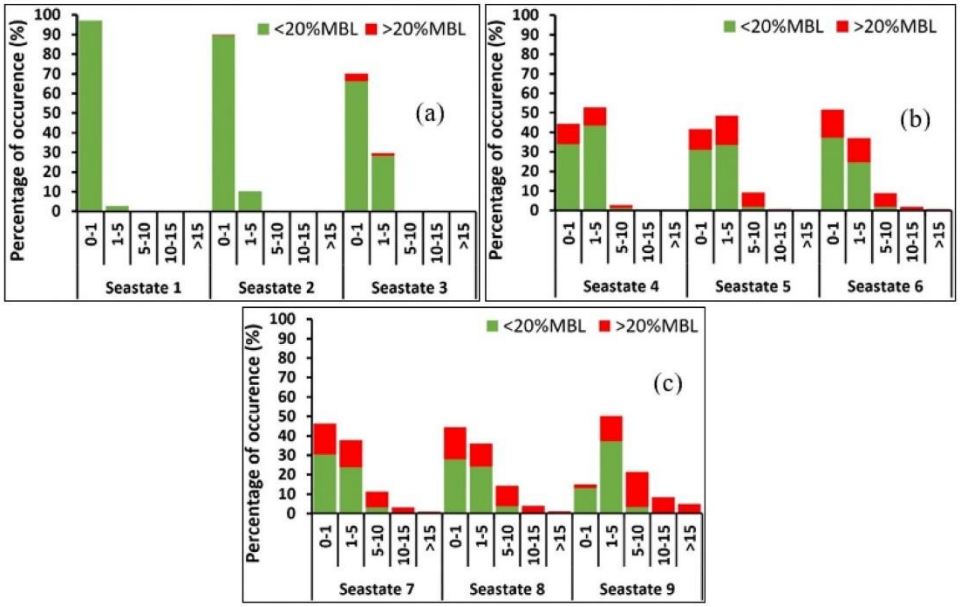

Fig. 10. Mean load distribution in the individual loading cycles of tension-spectrum for (a) sea-states 1–3 (b) sea-states 4–6 (c) sea-states 7–9, where the horizontal axis denotes ranges of load amplitudes in the percentage of the minimum breaking load (% MBL), and the green represents mean load below 20% MBL, and the red represents mean load above 20% MBL.

6. Discussion

The fatigue damage accumulation of the critical plane approach is significantly higher relative to the traditional SN approach, 75% on average for all of the material models used in the case study. This is mainly because the mean load effects are incorporated in the critical plane approach. No cyclic plasticity occurs as the mechanisms are only applied when the tension load exceeds 70% MBL due to the strain hardening effect from the proof load during the first cycle, and therefore the assumption of the Palmgren-Miner's rule can be applied, although the Palmgren-Miner's rule does not account for any load sequence effects [46]. The mean load effect of the critical plane approach shows that fatigue life decreases with an increase in mean load. This is in agreement with full-scale tests in the recent literature [7,9], which found that the fatigue life decreases by a factor of 5–10 as the mean load increases from 6.4% MBL to 20% MBL and found that the fatigue life decreases by a factor of 4 as the mean load increases from 10% MBL to 20% MBL.

When using the standard SN approach, common industry practices suggest using a safety factor of 3 for regularly inspected components and that this safety factor can be increased up to 10 for non-inspected components [6,43]. However, the critical plane approach suggests that these suggested safety factors may be insufficient, indicating that the fatigue life in mooring chain failures can be overpredicted when using the traditional SN approach by factors higher than the suggested safety factors in some cases. The factors are quantified in terms of the fatigue damage ratio in Fig. 8, showing that the higher the mean load, the larger the separation in fatigue damage prediction between the critical plane approach and the traditional SN approach; this can be many times larger when the mean load is above 20% MBL, depending on the mean load and the load amplitude levels. A feature of this critical plane approach is that it predicts lower fatigue damage than the traditional SN approach when the mean load is below 20% MBL, and the difference because of this depends on the load amplitude and the mean load as demonstrated in Fig. 8. This is because the critical plane approach accounts for the compressive residual stress from the proof load during the first cycle.

To show the difference in low-cycle fatigue prediction between both approaches, Fig. 11 shows the demarcation between low-cycle and high-cycle fatigue loading, at the lifetime of 10^5 cycles, predicted by using the different approaches, where the region above each line represents the low-cycle fatigue regime and the region below it indicates the high-cycle fatigue regime. The lines are generated by calculating at which load amplitude level the respective fatigue approach predicts the lifetime of 10^5 cycles across different mean load levels. The traditional SN approach shows this demarcation as a straight line at a load amplitude of just over 6% MBL since it does not consider the mean load effects, while the critical plane approach shows this demarcation as a curve where the higher the mean load, the lower load amplitude to reach the low-cycle fatigue regime. The region on the left-hand side is where the mean load is below 20% MBL and illustrates the conservativeness of the traditional SN approach as it predicts low-cycle fatigue at lower amplitude. However, on the right-hand side, the critical plane approach is more conservative from the mean load level of 20% MBL onwards, predicting low-cycle fatigue at increasingly lower amplitudes and showing a larger proportion of low-cycle fatigue for a given sea-state. The more conservative prediction of the critical plane approach is reflected in the previous case study since about half of the individual loading

Appendix

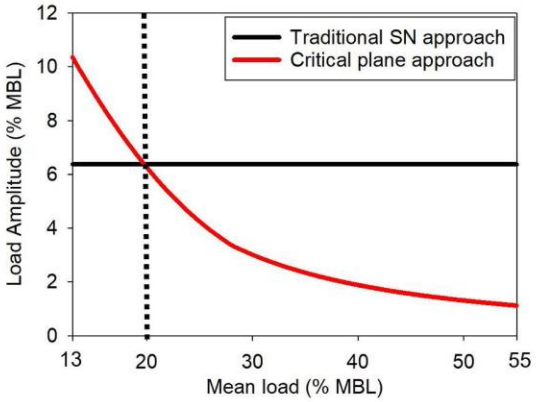

Fig. 11. The separation line between high-cycle and low-cycle fatigue predictions for the traditional SN approach and the critical plane approach.

cycles have mean load levels above 20% MBL, where the critical plane approach predicts 12.9% in the low-cycle fatigue regime, while the traditional SN approach predicts only 7.2%. The result is that the critical plane approach predicts almost twice the proportion of low-cycle fatigue than the traditional SN approach predicts.

The results of the two case studies show the importance of considering low-cycle fatigue contributions in mooring failures. For example, mooring chains are subjected to approximately 15×10^6 total cycles over three years of operation, assuming total individual loading cycles of 1828 for every 3 h of operation based on the case study. The critical plane approach comes closer to explaining why some mooring chain failures are reported as occurring in the first three years [1,3]. This is because it predicts a higher proportion of low-cycle fatigue loading cycles within the total cycles during this period than the traditional SN approach, as demonstrated in Figs. 8 and 11. The pre-tension affects the mean loads as the higher the pre-tension, the higher the mean loads, and mooring systems in the field normally have a pre-tension between 10% and 20% MBL [40], where the pre-tension in the case study is 17% MBL. As the mooring chain failures occurred in harsh sea environments [1,3], it is hypothesised that the pre-tension of the greatest loaded line increases with the mean loads, which leads to an increase in the proportion of low-cycle fatigue causing the reported early failures in the first three years of operation. This is also reflected in the sea-states study, where the more severe the sea-states, the higher the proportion of time the mean load is above 20% MBL and the more accurate the critical plane approach becomes. This implies that in calm sea regions, the traditional SN approach is conservative, but in harsh sea regions, the traditional SN approach can be non-conservative, which is where the most early failures have occurred [1,3].

One common recommendation in industry is to increase the minimum breaking load by increasing the chain diameter, which will decrease the cyclic load magnitude in terms of % MBL experienced; however, this can increase the applied pre-tension to above 20% MBL because the larger the diameter, the heavier the mooring line will be. Another recommendation is to lower the pre-tension by making the mooring line longer; however, this may reduce the mooring line damping, increasing the motions and decreasing the fatigue life [48,49]. Increasing the steel grade to achieve a greater minimum breaking load could be a viable solution to reduce the cyclic load magnitude in terms of % MBL; however, this is not a simple substitution and should be adopted with caution since the higher the strength of steels, the more prone to hydrogen-assisted cracking they may be, bringing in additional failure modes, not accounted for in the fatigue evaluation [5,50]. It should also be noted that the chain can also be corroded or subject to wear, which may reduce the chain fatigue capacity by promoting more detrimental mean load effects, leading to a decrease in the 20% MBL mean load threshold and an increase in the proportion of low-cycle fatigue. This is an important failure mechanism and the combination of low-cycle fatigue and corrosion are likely to form a vicious cycle, with each exacerbating the other, and requires further in-depth analysis.

7. Conclusion

This paper investigates how fatigue damage prediction changes with a more accurate representation of the low-cycle fatigue regime, using a strain-based critical plane approach, under stochastic tension loading in service for intact mooring chains. The critical plane approach is developed based on the multiaxial stress-strain conditions at the hotspot and this is correlated with the fatigue life derived from tests taken from the mooring standards. The fatigue damage accumulation predicted by the critical plane approach is significantly higher than the traditional SN approach, 75% on average for all of the material models considered here. It is found in this case study that the mean load effect is detrimental when it is above 20% of the minimum breaking load, shown to be a high proportion of sea-states 4–9. In addition, it demonstrates that increasing the diameter of the mooring chain may exacerbate this problem, indicating that more explicitly tailored chain design is needed to reduce this issue. The effect of the cyclic plasticity is limited as the mechanisms are only applied when the tension load exceeds 70% of the minimum breaking load due to the strain hardening from the proof load application during the first cycle. The critical plane approach predicts higher proportions of low-cycle fatigue than the traditional SN approach in the mooring line loading when the mean load is above 20% of the minimum breaking load, with the

difference being dependent on the mean loads and the load amplitudes witnessed in operation. The traditional SN approach is conservative when the mean load is below 20% of the minimum breaking load, but after this, it is non-conservative, which is observed in harsh environments where the majority of mooring chain failures were witnessed. The low-cycle fatigue analysis explains why current fatigue assessment in mooring chain applications is non-conservative and demonstrates that the critical plane approach should be accounted for in mooring line design.

Declaration of competing interest

The authors declare that they have no known competing financial interests or personal relationships that could have appeared to influence the work reported in this paper.

Acknowledgement

The authors gratefully acknowledge the funding by the Indonesia Endowment Fund for Education (LPDP) and the support of the Lloyd's Register Foundation (LRF). The authors also acknowledge the support of the University of Southampton for access to its IRIDIS5 High-Performance Computing Facility.

Appendix A

Table A.1 presents the resultant *SWT* damage parameters, according to Eq. (1), and the correlated number of cycles to failure from the fatigue life predictions based on the SN curve of DNVGL-OS-E301 [6] under different load amplitudes, i.e. from 1% to 19% MBL.

Table A.1
Resultant *SWT* fatigue damage parameters for different amplitudes and the correlated number of cycles to failure.

Amplitude (% MBL)	No. of cycles to failure	Mono-Rampi			Cyclic-Rampi			Cyclic-Zarandi		
		$\sigma_{n,max}$ (MPa)	$\Delta\varepsilon_n$	*SWT* (MPa)	$\sigma_{n,max}$ (MPa)	$\Delta\varepsilon_n$	*SWT* (MPa)	$\sigma_{n,max}$ (MPa)	$\Delta\varepsilon_n$	*SWT* (MPa)
19	3778	420.826	0.003694	0.77716	350.278	0.003359	0.58822	362.488	0.003313	0.60048
17	5275	381.147	0.003304	0.62959	314.186	0.003005	0.47205	327.542	0.002962	0.48516
15	7679	341.579	0.002915	0.49791	277.977	0.002651	0.36851	291.943	0.002613	0.38149
13	11796	301.763	0.002526	0.38116	241.775	0.002298	0.27776	256.228	0.002265	0.29014
11	19471	262.004	0.002139	0.28024	205.567	0.001944	0.19983	220.473	0.001916	0.21125
9	35550	222.164	0.001749	0.19427	169.330	0.001591	0.13467	184.743	0.001568	0.14483
7	75556	182.396	0.001361	0.12411	133.120	0.001237	0.08234	149.016	0.001219	0.09085
5	207326	142.544	0.000972	0.06924	96.827	0.000884	0.04278	113.244	0.000871	0.04931
3	959844	102.589	0.000583	0.02992	60.522	0.000530	0.01605	77.445	0.000523	0.02023
1	25915776	62.673	0.000194	0.00609	24.188	0.000177	0.00229	41.600	0.000174	0.00362

The resultant *SWT* damage parameters under different load amplitudes, shown in Table A.1, are used to calibrate the parameters of the fitted curves based on the general formula of Eq. (2) in order to interpolate the number of cycles to failure from the corresponding *SWT* damage parameters during fatigue loading. Table A.2 provides details regarding the calibration of parameters of the fitted curves. Good-match fitting is needed to give an accurate fitted curve between the predicted *SWT* damage parameters across a range of the number of cycles to failure. Therefore, in order to generate a good fit to the data, the fitting curves are separated into lower and upper fitting curves, where the lower fitting curves are used when the number of cycles to failure is below 75556, and the upper fitting curves are used when the number of cycles to failure above 75556. It is seen that using the upper and lower fitting curves, good fits are obtained with R-squared, R^2, above 99.9%.

Table A.2
Details of parameters of fitted curves for predicted *SWT* fatigue damage parameters.

Material		Material constants based on Eq. (2)				R^2
		A_1	a_1	A_2	a_2	
Mono-Rampi	Upper fittings	60.05743	−0.612928	60.05743	−0.612928	99.989%
	Lower fittings	15.32255	−0.500088	15.32255	−0.500088	99.904%
Cyclic-Rampi	Upper fittings	65.53905	−0.656548	65.53905	−0.656548	99.999%
	Lower fittings	33.80939	−0.60351	33.80939	−0.60351	99.961%
Cyclic-Zarandi	Upper fittings	54.05119	−0.631039	54.05119	−0.631039	99.995%
	Lower fittings	17.35095	−0.537771	17.35095	−0.537771	99.930%

Appendix B

Table B.1 presents the scatter diagram in the North Sea where the joint occurrence probabilities of significant wave height, Hs, and up-crossing wave period, Tz, are presented in the wave scatter diagram. The scatter diagram, consisting of 197 original sea-states, is partitioned into nine representative sea-state blocks at which the mooring line simulation is performed.

Table B.1
The wave scatter diagram in the North Sea [47].

H_s (m)	T_z (s) 1.5	2.5	3.5	4.5	5.5	6.5	7.5	8.5	9.5	10.5	11.5	12.5	13.5	14.5	15.5	16.5	17.5	18.5
0.5	0	0	13	1337	8656	11860	6342	1863	369	56	7	1	0	0	0	0	0	0
1.5	0	0	0	293	9860	49760	77380	55697	23757	7035	1607	305	51	8	1	0	0	0
2.5	0	0	0	22	1975	21588	62300	74495	48604	20660	6445	1602	337	63	11	2	0	0
3.5	0	0	0	2	349	6955	32265	56750	50991	28380	11141	3377	843	182	35	6	1	0
4.5	0	0	0	0	60	1961	13543	32885	38575	26855	12752	4551	1309	319	69	13	2	0
5.5	0	0	0	0	10	510	4984	16029	23727	20083	11260	4636	1509	410	97	21	4	1
6.5	0	0	0	0	2	126	1670	6903	12579	12686	8259	3868	1408	422	109	25	5	1
7.5	0	0	0	0	0	30	521	2701	5944	7032	5249	2767	1117	367	102	25	6	1
8.5	0	0	0	0	0	7	154	979	2559	3506	2969	1746	776	277	84	22	5	1
9.5	0	0	0	0	0	2	43	332	1019	1599	1522	992	483	187	61	17	4	1
10.5	0	0	0	0	0	0	12	107	379	675	717	515	273	114	40	12	3	1
11.5	0	0	0	0	0	0	3	33	133	266	314	247	142	64	24	7	2	1
12.5	0	0	0	0	0	0	1	10	44	99	128	110	68	33	13	4	1	0
13.5	0	0	0	0	0	0	0	3	14	35	50	46	31	16	7	2	1	0
14.5	0	0	0	0	0	0	0	1	4	12	18	18	13	7	3	1	0	0
15.5	0	0	0	0	0	0	0	0	1	4	6	7	5	3	1	1	0	0
16.5	0	0	0	0	0	0	0	0	0	1	2	2	2	1	1	0	0	0

References

[1] Fontaine E, Kilner A, Carra C, Washington D, Ma K, Phadke A. Industry survey of past failures, pre-emptive replacements and reported degradation for mooring systems of floating production units. In: Proceeding of Offshore Technology Conference OTC-25273; 2014. p. 14.
[2] Barrera C, Guanche R, Losada IJ. Experimental modelling of mooring systems for floating marine energy concepts. Mar Struct 2019;63:153–80.
[3] Ma K, Duggal A, Smedley P, L'Hostis D, Shu H. A historical review on integrity issues of permanent mooring systems. In: Proceedings of Offshore Technology Conference OTC-24025; 2013. p. 14.
[4] Majhi S, Souza RD. Application of lessons learned from field experience to design, installation and maintenance of FPS moorings. In: Proceedings of Offshore Technology Conference OTC-24181; 2013. p. 15.
[5] Kvitrud A. Lessons learned from Norwegian mooring line failures 2010–2013. Offshore Arctic Eng 2014:10. OMAE2014-23095, ASME 2014 33rd International Conference on ocean.
[6] Det Norske Veritas. "Offshore standard DNVGL-OS-e301 position mooring," *DNV, høvik, Norway*. 2013 [Online]. Available: https://rules.dnvgl.com/docs/pdf/DNV/codes/docs/2013-10/OS-E301.pdf. [Accessed 19 July 2018].
[7] Gabrielsen Ø, Larsen K, Dalane O, Lie H, Reinholdtsen S. Mean load impact on mooring chain fatigue capacity - lessons learned from full scale fatigue testing of used chains. Offshore Arctic Eng 2019:8. OMAE2019-95083, ASME 2019 38th International Conference on ocean.
[8] Gabrielsen Ø, Larsen K, Reinholdtsen SA. Fatigue testing of used mooring chain. Offshore Arctic Eng 2017:11. OMAE2017-61382, ASME 2017 36th International Conference on ocean.
[9] Zhang Y, Smedley P. Fatigue performance of high strength and large diameter. Offshore Arctic Eng 2019:11. OMAE2019-95984, ASME 2019 38th International Conference on ocean.
[10] Suresh S. Fatigue of materials book. second ed. New York: Cambridge University Press; 1998.
[11] Perez IM, Bastid P, Constantinescu A, Venugopal V. "Multiaxial fatigue analysis of mooring chain links under tension loading: influence of mean load and simplified assessment," in *ASME 2018 37th international Conference on ocean*. Offshore Arctic Eng 2018:12. OMAE2018-77552.
[12] Pacheco P, Kenedi P, Jorge J, Savi M, Santos H. Finite element residual stress analysis applied to offshore studless chain links. In *ASME 2004 23rd international Conference on offshore Mechanics and arctic engineering OMAE2004-51508*. 2004. p. 10.
[13] Xue X, Chen NZ, Wu Y, Xiong Y, Guo Y. Mooring system fatigue analysis for a semi-submersible. Ocean Eng 2018;156:550–63.
[14] Pacheco P, Kenedi P, Jorge J, Paiva A. Analysis of the influence of mechanical properties on the residual stress in offshore chain links using the finite element method. In *ASME 2003 22nd international Conference on offshore Mechanics and arctic engineering OMAE2003-37205*. 2003. p. 10.
[15] Palin-Luc T, Pérez-Mora R, Bathias C, Domínguez G, Paris PC, Arana JL. Fatigue crack initiation and growth on a steel in the very high cycle regime with sea water corrosion. Eng Fract Mech 2010;77(11):1953–62.
[16] Pérez-Mora R, Palin-Luc T, Bathias C, Paris PC. Very high cycle fatigue of a high strength steel under sea water corrosion: a strong corrosion and mechanical damage coupling. Int J Fatig 2015;74:156–65.
[17] Benedetti M, Fontanari V, Bandini M. A simplified and fast method to predict plain and notch fatigue of shot peened high-strength aluminium alloys under reverse bending. Surf Coating Technol 2014;243:2–9.
[18] Benedetti M, Fontanari V, Bandini M, Taylor D. Multiaxial fatigue resistance of shot peened high-strength aluminum alloys. Int J Fatig 2014;61:271–82.
[19] Benedetti M, Fontanari V, Santus C, Bandini M. Notch fatigue behaviour of shot peened high-strength aluminium alloys: experiments and predictions using a critical distance method. Int J Fatig 2010;32(10):1600–11.
[20] Liu J, Pang M. Fatigue life prediction of shot-peened steel. Int J Fatig 2012;43:134–41.
[21] Fatemi A, Shamsaei N. Multiaxial fatigue: an overview and some approximation models for life estimation. Int J Fatig 2011;33(8):948–58.
[22] Zarandi EP, Skallerud BH. Cyclic behavior and strain energy-based fatigue damage analysis of mooring chains high strength steel. Mar Struct 2020;70:18.
[23] Zarandi EP, Skallerud BH. Experimental and numerical study of mooring chain residual stresses and implications for fatigue life. Int J Fatig 2020;135.

[24] You C, Achintha M, Soady K, Reed P. "Low cycle fatigue life prediction in shot-peened components of different geometries – part II: life prediction. Fatig Fract Eng Mater Struct 2017;40(5):749–60.
[25] Zhu S, Yu Z, Correia J, De Jesus A, Berto F. Evaluation and comparison of critical plane criteria for multiaxial fatigue analysis of ductile and brittle materials. Int J Fatig 2018;112:279–88.
[26] Li J, Zhang Z, Sun Q, Li C. Multiaxial fatigue life prediction for various metallic materials based on the critical plane approach. Int J Fatig 2011;33(2):90–101.
[27] Pellinghelli D, Riboli M, Spagnoli A. Full-model multiaxial fatigue life calculations with different criteria. Procedia Eng. 2018;213:126–36.
[28] Sum WS, Williams EJ, Leen SB. Finite element, critical-plane, fatigue life prediction of simple and complex contact configurations. Int J Fatig 2005;27(4):403–16.
[29] Dowling NE, Calhoun CA, Arcari A. Mean stress effects in stress-life fatigue and the Walker equation. Fatig Fract Eng Mater Struct 2009;32(3):163–79.
[30] IACS (International Association of Classification Societies). W22 offshore mooring chain. *International Association of Classification Societies*; 2016 [Online]. Available: http://www.iacs.org.uk/publications/unified-requirements/ur-w/ur-w22-rev6-cln/. [Accessed 4 February 2019].
[31] Fernández J, Storesund W, Navas J. Fatigue performance of grade R4 and R5 mooring chains in seawater. In *ASME 2014 33nd international Conference on offshore Mechanics and arctic engineering OMAE2014-23491*. 2014. p. 6.
[32] Gemilang GM, Reed PAS, Sobey AJ. Selection of appropriate numerical models for modelling the operating stresses in mooring chains. Mar Struct 2020;75:102864.
[33] Dassault Systèmes Simulia Corp. "Abaqus analysis user's guide 6.13. " *ABAQUS, Inc.*; 2013 [Online]. Available: http://dsk.ippt.pan.pl/docs/abaqus/v6.13/books/usb/default.htm?startat=pt09ch36s03aus145.html. [Accessed 19 February 2020].
[34] Det Norske Veritas. "DNV-OS-E302 offshore mooring chain," DNV, høvik, Norway [Online]. Available: https://rules.dnvgl.com/docs/pdf/DNV/codes/docs/2009-10/OS-E302.pdf. [Accessed 19 July 2018].
[35] Rampi L, Bignonnet A, Le Cunff C, Bourgin F, Vargas P. "Chain out of plane bending (OPB) fatigue joint industry project (JIP) FEA results and multiaxiality study results," in *ASME 2016 35th international Conference on ocean*. Offshore Arctic Eng 2016:15. OMAE2016-54198.
[36] Chaboche JL. Time-independent constitutive theories for cyclic plasticity. Int J Plast 1986;2(2):149–88.
[37] Lee C, Chang K, Van V. Numerical investigation on the ratcheting behavior of pressurized stainless steel pipes under cyclic in-plane bending. Mar Struct 2016;49:224–38.
[38] Smith KN, Topper T, Watson P. "A stress–strain function for the fatigue of metals (stress-strain function for metal fatigue including mean stress effect). J Mater 1970;5:767–78.
[39] Socie D. Multiaxial fatigue damage models. J Eng Mater Technol 1987;109(4):293–8.
[40] Ma K, Gabrielsen Ø, Li Z, Baker D, Yao A, Vargas P. Fatigue tests on corroded mooring chains retrieved from various fields in offshore west africa and the North sea. In *ASME 2019 38th international Conference on offshore Mechanics and arctic engineering OMAE2019-95618*. 2019. p. 17.
[41] Flexcom Software Documentation, "Flexcom Version 8. 10.2 examples manual." galway. Wood Group Kenny; 2019.
[42] Gao Z, Moan T. Wave-induced fatigue damage of mooring chain under combined non-Gaussian low and wave frequency loads. Offshore Arctic Eng 2006:7. OMAE2006-92389, ASME 2006 25th International Conference on ocean.
[43] American Petroleum Institute. "API rp 2SK: recommended practice for design and analysis of stationkeeping systems for floating structures. 2005. Washington, D. C.
[44] Matsuishi M, Endo T. Fatigue of metals subjected to varying stress. Japan Soc. Mech. Eng. Fukuoka, Japan 1968;68(2):37–40.
[45] Marsh G, Wignall C, Thies PR, Barltrop N, Incecik A, Venugopal V. Review and application of Rainflow residue processing techniques for accurate fatigue damage estimation. Int J Fatig 2016;82:757–65.
[46] Miner MA. Cumulative damage in fatigue. J Appl Mech 1945;12. American Society of Mechanical Engineers-Journal of Applied Mechanics, pp. A159–A164.
[47] Song X, Wang S. A novel spectral moments equivalence based lumping block method for efficient estimation of offshore structural fatigue damage. Int J Fatig 2019;118:162–75.
[48] Yang Y, Chen JX, Huang S. Mooring line damping due to low-frequency superimposed with wave-frequency random line top end motion. Ocean Eng 2016;112:243–52.
[49] Wu Y, Wang T, Eide Ø, Haverty K. Governing factors and locations of fatigue damage on mooring lines of floating structures. Ocean Eng 2015;96:109–24.
[50] Coudreuse L, Renaudin C, Bocquet P, Cadiou L. Evaluation of hydrogen assisted cracking resistance of high strength Jack-up steels. Mar Struct 1997;10(2):85–106.

Appendix

List of References

[1] E. Fontaine, A. Kilner, C. Carra, D. Washington, K. Ma, and A. Phadke, "Industry survey of past failures, pre-emptive replacements and reported degradation for mooring systems of floating production units," in *Proceeding of Offshore Technology Conference OTC-25273*, 2014, p. 14.

[2] C. Barrera, R. Guanche, and I. J. Losada, "Experimental modelling of mooring systems for floating marine energy concepts," *Mar. Struct.*, vol. 63, pp. 153–180, 2019.

[3] J. McCaul, "Projected requirements for FPSOs over the next five years," *International Maritime Associates*, 2014. [Online]. Available: https://www.offshore-mag.com/articles/print/volume-74/issue-5/fpso-outlook/projected-requirements-for-fpsos-over-the-next-five-years.html. [Accessed: 17-Mar-2018].

[4] British Petroleum, "BP Energy Outlook 2018," *February, 2018*, 2018. [Online]. Available: https://www.bp.com/en/global/corporate/news-and-insights/press-releases/energy-outlook-2018.html. [Accessed: 10-Aug-2020].

[5] K. Ma, A. Duggal, P. Smedley, D. L'Hostis, and H. Shu, "A Historical Review on Integrity Issues of Permanent Mooring Systems," in *Proceedings of Offshore Technology Conference OTC-24025*, 2013, p. 14.

[6] S. Majhi and R. D. Souza, "Application of Lessons Learned From Field Experience to Design, Installation and Maintenance of FPS Moorings," in *Proceedings of Offshore Technology Conference OTC-24181*, 2013, p. 15.

[7] Det Norske Veritas, "Offshore Standard DNVGL-OS-E301 Position Mooring," *DNV, Høvik, Norway*, 2013. [Online]. Available: https://rules.dnvgl.com/docs/pdf/DNV/codes/docs/2013-10/OS-E301.pdf. [Accessed: 19-Jul-2018].

[8] Noble Denton Europe Limited, "RR444 - Floating production system: JIP FPS mooring integrity," *Health and Safety Executive*, 2006. [Online]. Available: http://www.hse.gov.uk/research/rrpdf/rr444.pdf. [Accessed: 19-Jul-2018].

[9] A. Ryu, Samsangsoo; Heyl, Caspar; Duggal, "Mooring Cost Sensitivity Study Based on Cost-Optimum Mooring Design," in *Proceedings of Conference 2008 Korean Society of Ocean Engineers*, 2008, p. 5.

[10] R. Crighton, "Gryphon insurance payouts close to £440m," *Energy Voice*, 2013. [Online]. Available: https://www.energyvoice.com/oilandgas/45369/gryphon-insurance-payouts-close-440m/. [Accessed: 04-Feb-2019].

[11] A. Kvitrud, "Lessons Learned From Norwegian Mooring Line Failures 2010–2013," in *ASME 2014 33rd International Conference on Ocean, Offshore and Arctic Engineering OMAE2014-23095*, 2014, p. 10.

[12] R. B. Gordon, M. G. Brown, and E. M. Allen, "Mooring Integrity Management: A State-of-the-Art Review," in *Proceedings of Offshore Technology Conference OTC-25134-MS*, 2014, p. 19.

[13] S. Suresh, *Fatigue of Materials Book*, 2nd ed. New York: Cambridge University Press, 1998.

[14] K. Ma, Y. Luo, T. Kwan, and Y. Wu, "Chapter 4: Mooring design," in *Mooring System Engineering for Offshore Structures*, 2019, pp. 63–83.

[15] A. Yaghin and R. E. Melchers, "Long-term inter-link wear of model mooring chains," *Mar. Struct.*, vol. 44, pp. 61–84, 2015.

[16] B. L. Cafiada and J. Vicinay, "New Mooring Chain Designs," in *Proceedings of Offshore Technology Conference OTC 8148*, 1996, p. 16.

[17] W. K. Lee and C. Z. Jua, "Theoretical and Experimental Stress Analysis to Evaluate the Effect of Loose Studs in Anchor Chain," in *Conference Proceeding Engineering Integrity Assessment, East Kilbride, Glasgow*, 1994, pp. 171–191.

[18] American Petroleum Institute, "API RP 2SK: Recommended Practice for Design and Analysis of Stationkeeping Systems for Floating Structures," Washington, D. C., 2005.

[19] Det Norske Veritas, "DNV-OS-E302 Offshore Mooring Chain," *DNV, Høvik, Norway.*, 2015. [Online]. Available: https://rules.dnvgl.com/docs/pdf/DNV/codes/docs/2009-10/OS-E302.pdf. [Accessed: 19-Jul-2018].

[20] IACS (International Association of Classification Societies), "W22 Offshore Mooring Chain," *International Association of Classification Societies*, 2016. [Online]. Available: http://www.iacs.org.uk/publications/unified-requirements/ur-w/ur-w22-rev6-cln/. [Accessed: 04-Feb-2019].

[21] Petroleum and natural gas industries, "ISO 19901-07:2013 Specific requirements for offshore structures - Part 7: Station keeping systems for floating offshore structures and mobile offshore units," 2013.

[22] American Bureau of Shipping (ABS), *Guide for the Certification of Offshore Mooring Chain*. 2009, p. 47.

[23] I. Perez, P. Bastid, and V. Venugopal, "Prediction of Residual Stresses in Mooring Chains and its Impact on Fatigue Life," in *ASME 2017 36th International Conference on Ocean, Offshore and Arctic Engineering OMAE2017-61720*, 2017, p. 10.

[24] I. Perez, A. Constantinescu, P. Bastid, and Y. Zhang, "Computational fatigue assessment of mooring chains under tension loading," *Eng. Fail. Anal.*, vol. 106, p. 104043, 2019.

[25] P. Bastid and S. D. Smith, "Numerical Analysis of Contact Stresses Between Mooring Chain Links and Potential Consequences for Fatigue

Damage," in *ASME 2013 32nd International Conference on Ocean, Offshore and Arctic Engineering OMAE2013-11360*, 2013, p. 8.

[26] P. Pacheco, P. Kenedi, and J. Jorge, "Elastoplastic Analysis of the Residual Stress in Chain Links," in *ASME 2002 21st International Conference on Offshore Mechanics and Arctic Engineering, OMAE2002-28083*, 2002, p. 8.

[27] P. Pacheco, P. Kenedi, J. Jorge, H. Santos, M. Savi, and A. Paiva, "Modeling Residual Stresses in Offshore Chain Links using Finite Element Method," in *17th International Congress of Mechanical Engineering COBEM2003-0320*, 2003, p. 10.

[28] P. Pacheco, P. Kenedi, J. Jorge, and A. Paiva, "Analysis of the Influence of Mechanical Properties on the Residual Stress in Offshore Chain Links Using the Finite Element Method," in *ASME 2003 22nd International Conference on Offshore Mechanics and Arctic Engineering OMAE2003-37205*, 2003, p. 10.

[29] P. Pacheco, P. Kenedi, J. Jorge, M. Savi, and H. Santos, "Finite Element Residual Stress Analysis Applied to Offshore Studless Chain Links," in *ASME 2004 23rd International Conference on Offshore Mechanics and Arctic Engineering OMAE2004-51508*, 2004, p. 10.

[30] G. J. Shoup, S. M. Tipton, and J. R. Sorem, "The effect of proof loading on the fatigue behaviour of stud link chain," *Int. J. Fatigue*, vol. 14, no. 1, pp. 35–40, 1992.

[31] S. M. Tipton and G. J. Shoup, "The Effect of Proof Loading on the Fatigue Behavior of Open Link Chain," *J. Eng. Mater. Technol.*, vol. 114, no. 1, pp. 27–33, 1992.

[32] G. J. Shoup, S. M. Tipton, and J. R. Sorem, "The Influence of Proof Loading on the Fatigue Life of Anchor Chain," in *Proceedings of Offshore Technology Conference OTC-6905*, 1992.

[33] H. M. Bolt, C. J. Billington, and M. J. Humphries, "Anchor Chain - New Data, New Design Lines and Practical Details," in *Proceedings of Offshore Technology Conference OTC-7707*, 1995.

[34] N. Suzuki, I. Soya, H. Yokota, and S. Sekiguchi, "Estimation of Fatigue Strength of Large Diameter Chain in Air and Sea-water," *Tetsu-to-Hagane*, vol. 74, no. 1, pp. 182–189, 1988.

[35] E. P. Zarandi and B. H. Skallerud, "Experimental and numerical study of mooring chain residual stresses and implications for fatigue life," *Int. J. Fatigue*, vol. 135, 2020.

[36] M. Brown, A. P. Comley, M. Eriksen, I. Williams, P. Smedley, and S. Bhattacharjee, "Phase 2 mooring integrity JIP- summary of findings," in *Proceedings of Offshore Technology Conference OTC-20613*, 2010.

[37] C. Melis, P. Jean, and P. Vargas, "Out-of-Plane Bending Testing of Chain

Links," in *ASME 2005 24th International Conference on Offshore Mechanics and Arctic Engineering OMAE2005-67353*, 2005, no. 41979, pp. 163–172.

[38] A. M. Wang, P. Rong, and S. Zhu, "Recovery And Re-Hookup Of Liu Hua 11-1 FPSO Mooring System," in *Proceedings of Offshore Technology Conference OTC-19922-MS*, 2009.

[39] G. J. Shoup and R. A. Mueller, "Failure Analysis of a Calm Buoy Anchor Chain System," in *Proceedings of Offshore Technology Conference OTC-4764*, 1984, p. 11.

[40] H. Suhara, T.; Koterayama, W.; Tasai, F.; Hiyama, "Dynamic Behavior And Tension Of Oscillating Mooring Chain," in *Proceedings of Offshore Technology Conference OTC-4053-MS*, 1981.

[41] I. Ridge, P. Smedley, and R. Hobbs, "Effects of Twist On Chain Strength and Fatigue Performance: Small Scale Test Results," in *Proceedings of the International Conference on Offshore Mechanics and Arctic Engineering - OMAE2011 49206*, 2011, pp. 1–7.

[42] E. Bjørnsen, "Chains in Mooring Systems," Thesis, NTNU, Dept. Civil Engineering, Trondheim, Norway, 2014.

[43] I. M. Perez, P. Bastid, A. Constantinescu, and V. Venugopal, "Multiaxial Fatigue Analysis of Mooring Chain Links Under Tension Loading: Influence of Mean Load and Simplified Assessment," in *ASME 2018 37th International Conference on Ocean, Offshore and Arctic Engineering OMAE2018-77552*, 2018, p. 12.

[44] J. Fernández, W. Storesund, and J. Navas, "Fatigue Performance of Grade R4 and R5 Mooring Chains in Seawater," in *ASME 2014 33nd International Conference on Offshore Mechanics and Arctic Engineering OMAE2014-23491*, 2014, p. 6.

[45] D. T. Brown and S. Mavrakos, "Comparative study on mooring line dynamic loading," *Mar. Struct.*, vol. 12, no. 3, pp. 131–151, 1999.

[46] Y. Yang, J. X. Chen, and S. Huang, "Mooring line damping due to low-frequency superimposed with wave-frequency random line top end motion," *Ocean Eng.*, vol. 112, pp. 243–252, 2016.

[47] M. Matsuishi and T. Endo, "Fatigue of metals subjected to varying stress," *Japan Soc. Mech. Eng. Fukuoka, Japan*, vol. 68, no. 2, pp. 37–40, 1968.

[48] X. Song and S. Wang, "A novel spectral moments equivalence based lumping block method for efficient estimation of offshore structural fatigue damage," *Int. J. Fatigue*, vol. 118, pp. 162–175, 2019.

[49] J. Du, H. Li, M. Zhang, and S. Wang, "A novel hybrid frequency-time domain method for the fatigue damage assessment of offshore structures," *Ocean Eng.*, vol. 98, pp. 57–65, 2015.

[50] A. O. Vázquez-Hernández, G. B. Ellwanger, and L. V. S. Sagrilo, "Long-term response analysis of FPSO mooring systems," *Appl. Ocean Res.*, vol. 33, no. 4, pp. 375–383, 2011.

[51] D. Stanisic, M. Efthymiou, D. J. White, and M. Kimiaei, "Mooring system reliability in tropical cyclone and North Sea winter storm environments," *Appl. Ocean Res.*, vol. 88, pp. 306–316, 2019.

[52] P. D. Spanos, R. Ghosh, L. D. Finn, and J. Halkyard, "Coupled Analysis of a Spar Structure: Monte Carlo and Statistical Linearization Solutions," *J. Offshore Mech. Arct. Eng.*, vol. 127, no. 1, pp. 11–16, Mar. 2005.

[53] H. C. Karlsen and A. Naess, "Statistical response predictions for a nonlinearly moored large volume structure in random seas," *Appl. Ocean Res.*, vol. 27, no. 6, pp. 273–280, 2005.

[54] A. Naess, O. Gaidai, and P. S. Teigen, "Extreme response prediction for nonlinear floating offshore structures by Monte Carlo simulation," *Appl. Ocean Res.*, vol. 29, no. 4, pp. 221–230, 2007.

[55] I. Felix-Gonzalez and R. S. Mercier, "Optimized design of statically equivalent mooring systems," *Ocean Eng.*, vol. 111, pp. 384–397, 2016.

[56] M. Shafieefar and A. Rezvani, "Mooring optimization of floating platforms using a genetic algorithm," *Ocean Eng.*, vol. 34, no. 10, pp. 1413–1421, 2007.

[57] G. Ma, L. Zhong, H. Wang, Z. Kang, and L. Sun, "Truncation analysis of mooring line based on dynamic similarity with consistent nonlinearity," *Ocean Eng.*, vol. 176, pp. 46–56, 2019.

[58] H. Wei, L. Xiao, X. Tian, and Y. Kou, "Four-level screening method for multi-variable truncation design of deepwater mooring system," *Mar. Struct.*, vol. 51, pp. 40–64, 2017.

[59] Y. M. Low and R. S. Langley, "A hybrid time/frequency domain approach for efficient coupled analysis of vessel/mooring/riser dynamics," *Ocean Eng.*, vol. 35, no. 5, pp. 433–446, 2008.

[60] S. Mazaheri and M. J. Downie, "Response-based method for determining the extreme behaviour of floating offshore platforms," *Ocean Eng.*, vol. 32, no. 3, pp. 363–393, 2005.

[61] C. B. Li, J. Choung, and M. H. Noh, "Wide-banded fatigue damage evaluation of Catenary mooring lines using various Artificial Neural Networks models," *Mar. Struct.*, vol. 60, pp. 186–200, 2018.

[62] R. Guarize, N. A. F. Matos, L. V. S. Sagrilo, and E. C. P. Lima, "Neural networks in the dynamic response analysis of slender marine structures," *Appl. Ocean Res.*, vol. 29, no. 4, pp. 191–198, 2007.

[63] J. Azcona, X. Munduate, L. Gonzalez, and T. A. Nygaard, "Experimental validation of a dynamic mooring lines code with tension and motion

measurements of a submerged chain," *Ocean Eng.*, vol. 129, no. 2016, pp. 415–427, 2017.

[64] B. K. Kim and M. M. Bernitsas, "Nonlinear dynamics and stability of spread mooring with riser," *Appl. Ocean Res.*, vol. 23, no. 2, pp. 111–123, 2001.

[65] Y. A. Hermawan and Y. Furukawa, "Coupled three-dimensional dynamics model of multi-component mooring line for motion analysis of floating offshore structure," *Ocean Eng.*, vol. 200, p. 106928, 2020.

[66] O. A. Montasir, A. Yenduri, and V. J. Kurian, "Effect of mooring line configurations on the dynamic responses of truss spar platforms," *Ocean Eng.*, vol. 96, pp. 161–172, 2015.

[67] Y. Wu, T. Wang, Ø. Eide, and K. Haverty, "Governing factors and locations of fatigue damage on mooring lines of floating structures," *Ocean Eng.*, vol. 96, pp. 109–124, 2015.

[68] J. S. Han, Y. H. Kim, Y. J. Son, and H. S. Choi, "A comparative study on the fatigue life of mooring systems with different composition," *J. Hydrodyn.*, vol. 22, no. 5 SUPPL. 1, pp. 435–439, 2010.

[69] X. Xue, N. Z. Chen, Y. Pu, and X. Gao, "Fracture mechanics analysis for mooring chain links subjected to out-of-plane bending (OPB)," *Mar. Struct.*, vol. 71, no. 135, pp. 1–21, 2020.

[70] X. Xue, N. Z. Chen, Y. Wu, Y. Xiong, and Y. Guo, "Mooring system fatigue analysis for a semi-submersible," *Ocean Eng.*, vol. 156, pp. 550–563, 2018.

[71] X. Xue and N. Chen, "Fracture mechanics analysis for a mooring system subjected to Gaussian load processes," *Eng. Struct.*, vol. 162, pp. 188–197, 2018.

[72] X. Xue, N.-Z. Chen, and Y. Pu, "Fracture Mechanics Based Mooring Fatigue Analysis for a Semi-Submersible Subjected to Triple Narrow-Band Loading Processes," in *ASME 2019 38th International Conference on Ocean, Offshore and Arctic Engineering OMAE2019-95108*, 2019, p. 7.

[73] C. Edward and A. K. Dev, "Numerical Methods for Interlink Stiffness formulations and parameters sensitivity of out-of-plane Bending in Mooring Chains," in *ASME 2019 38th International Conference on Ocean, Offshore and Arctic Engineering OMAE2019-96042*, 2019, p. 11.

[74] Y. Kim, M. S. Kim, and M. J. Park, "Fatigue analysis on the mooring chain of a spread moored FPSO considering the OPB and IPB," *Int. J. Nav. Archit. Ocean Eng.*, vol. 11, no. 1, p. 24, 2018.

[75] L. Rampi, A. Bignonnet, C. Le Cunff, F. Bourgin, and P. Vargas, "Chain Out of Plane Bending (OPB) Fatigue Joint Industry Project (JIP) FEA Results and Multiaxiality Study Results," in *ASME 2016 35th International Conference on Ocean, Offshore and Arctic Engineering OMAE2016-54198*,

2016, p. 15.

[76] J. M. Crapps, H. He, and D. A. Baker, "An FEA-based methodology for assessing the residual strength of degraded mooring chains," *Int. J. Offshore Polar Eng.*, vol. 28, no. 3, pp. 287–293, 2018.

[77] A. Sachan and Y. S. Choo, "Mooring chain strength tests and ductile failure modeling using micromechanics and phenomenology based failure models," *Ocean Eng.*, vol. 195, p. 106663, 2020.

[78] J. Jones, "Finite Element Analysis of The Effect of Twist on Chain Fatigue Performance," in *ASME 2019 38th International Conference on Ocean, Offshore and Arctic Engineering OMAE2019-95276*, 2019, p. 10.

[79] A. Bergara, A. Arredondo, J. Altuzarra, and J. M. Martínez-esnaola, "Calculation of stress intensity factors in offshore mooring chains," *Ocean Eng.*, vol. 214, p. 107762, 2020.

[80] H. M. Hou, T. J. Xu, G. H. Dong, Y. P. Zhao, and C. W. Bi, "Time-dependent reliability analysis of mooring lines for fish cage under corrosion effect," *Aquac. Eng.*, vol. 77, pp. 42–52, 2017.

[81] E. P. Zarandi and B. H. Skallerud, "Cyclic behavior and strain energy-based fatigue damage analysis of mooring chains high strength steel," *Mar. Struct.*, vol. 70, p. 18, 2020.

[82] S. Wang, X. Zhang, T. Kwan, K. E. Service, K. Ma, and C. Corporation, "Assessing Fatigue Life of Corroded Mooring Chains Through Advanced Analysis," in *Proceedings of Offshore Technology Conference OTC-29449-MS*, 2019.

[83] D. A. Baker, Z. Li, S. Wang, and X. Zhang, "Fatigue Assessment of 'Corroded' Mooring chain," in *ASME 2019 38th International Conference on Ocean, Offshore and Arctic Engineering OMAE2019-96191*, 2019, pp. 1–10.

[84] P. M. Vargas, T. M. Hsu, and W. K. Lee, "Stress Concentration Factors for Stud-Less Mooring Chain Links in Fairleads," in *ASME 2004 23rd International Conference on Offshore Mechanics and Arctic Engineering OMAE2004-51376*, 2004, p. 9.

[85] J. S. Sun, K. H. Lee, and H. P. Lee, "Comparison of implicit and explicit finite element methods for dynamic problems," *J. Mater. Process. Technol.*, vol. 105, no. 1, pp. 110–118, 2000.

[86] C. You, "Fatigue lifing approaches for shot peened turbine components," Thesis (Doctoral) - University of Southampton, 2017.

[87] R. S. Ralph, I. Stephens; Ali, Fatemi; Robert, *Metal Fatigue in Engineering*. John Wiley & Sons, 2001.

[88] D. L. McDowell and F. P. E. Dunne, "Microstructure-sensitive computational modeling of fatigue crack formation," *Int. J. Fatigue*, vol.

32, no. 9, pp. 1521–1542, 2010, doi: 10.1016/j.ijfatigue.2010.01.003.

[89] R. Agrawal, "Low Cycle Fatigue Life Prediction," *Int. J. Emerg. Eng. Res. Technol.*, vol. 2, no. 4, pp. 5–15, 2014.

[90] Ø. Gabrielsen, K. Larsen, and S. A. Reinholdtsen, "Fatigue Testing of Used Mooring Chain," in *ASME 2017 36th International Conference on Ocean, Offshore and Arctic Engineering OMAE2017-61382*, 2017, p. 11.

[91] K. Ma, Y. Luo, T. Kwan, and Y. Wu, "Fatigue analysis," in *Mooring System Engineering for Offshore Structures*, 2019, pp. 115–137.

[92] T. Clarke, R. Jacques, A. Bisognin, C. Camerini, S. Damasceno, and T. Strohaecker, "Monitoring the structural integrity of a flexible riser during a full-scale fatigue test," *Eng. Struct.*, vol. 33, no. 4, pp. 1181–1186, 2011.

[93] J. Fernández, A. Arredondo, V. M. Innovación, W. Storesund, and J. Jesús, "Influence of the Mean Load on the Fatigue Performance of Mooring Chains," in *Proceedings of Offshore Technology Conference OTC-29621-MS*, 2019.

[94] Y. Zhang and P. Smedley, "Fatigue Performance of High Strength and Large Diameter," in *ASME 2019 38th International Conference on Ocean, Offshore and Arctic Engineering OMAE2019-95984*, 2019, p. 11.

[95] K. Ma, Ø. Gabrielsen, Z. Li, D. Baker, A. Yao, and P. Vargas, "Fatigue Tests on Corroded Mooring Chains Retrieved From Various Fields in Offshore West Africa and the North Sea," in *ASME 2019 38th International Conference on Offshore Mechanics and Arctic Engineering OMAE2019-95618*, 2019, p. 17.

[96] Ø. Gabrielsen, I. Kulbotten, I. Perez, and L. Haskoll, "Inner Bend Cracks in Mooring Chain : Investigation of Cracks," in *ASME 2019 38th International Conference on Ocean, Offshore and Arctic Engineering OMAE2019-95084*, 2019, p. 11.

[97] Ø. Gabrielsen, T. Liengen, and S. Molid, "Microbiologically Influenced Corrosion on Seabed Chain in the North Sea," in *ASME 2018 37th International Conference on Ocean, Offshore and Arctic Engineering OMAE2018-77460*, 2018, p. 9.

[98] Det Norske Veritas, "DNV-RP-C203 Fatigue Design of Offshore Steel Structures," 2011.

[99] Ø. Gabrielsen, K. Larsen, O. Dalane, H. Lie, and S. Reinholdtsen, "Mean Load Impact on Mooring Chain Fatigue Capacity - Lessons Learned from Full Scale Fatigue Testing of Used Chains," in *ASME 2019 38th International Conference on Ocean, Offshore and Arctic Engineering OMAE2019-95083*, 2019, p. 8.

[100] M. Kamaya and M. Kawakubo, "Mean stress effect on fatigue strength of

stainless steel," *Int. J. Fatigue*, vol. 74, pp. 20–29, 2015.

[101] J. L. Deng, P. Yang, and Y. Chen, "Low-cycle fatigue crack initiation life of hull-notched plate considering short crack effect and accumulative plastic damage," *Appl. Ocean Res.*, vol. 68, pp. 65–76, 2017.

[102] F. Coffin, "The deformation and fracture of a ductile metal under superimposed cyclic and monotonic strain," in *Achievement of High Fatigue Resistance in Metals and Alloys*, 1970, vol. ASTMSTP567, pp. 53–76.

[103] G. Kang, Q. Gao, L. Cai, and Y. Sun, "Experimental study on uniaxial and nonproportionally multiaxial ratcheting of SS304 stainless steel at room and high temperatures," *Nucl. Eng. Des.*, vol. 216, no. 1, pp. 13–26, 2002.

[104] C. B. Lim, K. S. Kim, and J. B. Seong, "Ratcheting and fatigue behavior of a copper alloy under uniaxial cyclic loading with mean stress," *Int. J. Fatigue*, vol. 31, no. 3, pp. 501–507, 2009.

[105] T. Palin-Luc, R. Pérez-Mora, C. Bathias, G. Domínguez, P. C. Paris, and J. L. Arana, "Fatigue crack initiation and growth on a steel in the very high cycle regime with sea water corrosion," *Eng. Fract. Mech.*, vol. 77, no. 11, pp. 1953–1962, 2010.

[106] R. Pérez-Mora, T. Palin-Luc, C. Bathias, and P. C. Paris, "Very high cycle fatigue of a high strength steel under sea water corrosion: A strong corrosion and mechanical damage coupling," *Int. J. Fatigue*, vol. 74, pp. 156–165, 2015.

[107] Y. Zhang, N. Zettlemoyer, and P. Tubby, "Fatigue Crack Growth Rates of Mooring Chain Steels," in *ASME 2012 31st International Conference on Ocean, Offshore and Arctic Engineering OMAE 2012-84223*, 2012.

[108] T. Lassen, J. L. Arana, L. Canada, J. Henriksen, and N. K. Holthe, "Crack Growth in High Strength Chain Steel Subjected to Fatigue Loading in a Corrosive Environment," in *ASME 2005 24th International Conference on Offshore Mechanics and Arctic Engineering OMAE2005-67242*, 2005, pp. 93–101.

[109] J. Lardier, T. Moan, and Z. Gao, "Fatigue Reliability of Catenary Mooring Lines Under Corrosion Effect," in *ASME 2008 27th International Conference on Offshore Mechanics and Arctic Engineering OMAE2008-57360*, 2008, pp. 351–358.

[110] K. Mathisen, Jan. Larsen, "Risk-Based Inspection Planning for Mooring Chain," in *ASME 2002 21st International Conference on Offshore Mechanics and Arctic Engineering OMAE2002-28409*, 2002, pp. 1–10.

[111] H. B. Fredheim, S.; Reinholdtsen, S-A.; Håskoll, L.; Lie, "Corrosion Fatigue Testing of Used, Studless, Offshore Mooring Chain," in *ASME 2013 32nd International Conference on Ocean, Offshore and Arctic Engineering OMAE2013-10609*, 2013.

[112] H. Gerber, *Bestimmung der zulässigen spannungen in eisen-constructionen*. Wolf, 1874.

[113] J. Goodman, *Mechanics Applied to Engineering*, Eight Edit. London: Longmans, Green, 1914.

[114] C. R. Soderberg, "Factor of Safety and Working Stress," *Trans. Am. Soc. Mech. Eng.*, vol. 52, pp. 12–28, 1939.

[115] S. K. Koh and R. I. Stephens, "Mean stress effects on low cycle fatigue for a high strength steel. Fatigue Fract. Engng. Mat. Struct., 14 (4), 413-28," *Fatigue Fract. Eng. Mater. Struct.*, vol. 14, pp. 413–428, Apr. 1991, doi: 10.1111/j.1460-2695.1991.tb00672.x.

[116] S. Foletti, F. Corea, S. Rabbolini, and S. Beretta, "Short cracks growth in low cycle fatigue under multiaxial in-phase loading," *Int. J. Fatigue*, vol. 107, pp. 49–59, 2018.

[117] C. You, M. Achintha, K. Soady, and P. Reed, "Low cycle fatigue life prediction in shot-peened components of different geometries – part II: life prediction," *Fatigue Fract. Eng. Mater. Struct.*, vol. 40, no. 5, pp. 749–760, 2017.

[118] K. S. Kim and J. C. Park, "Shear strain based multiaxial fatigue parameters applied to variable amplitude loading," *Int. J. Fatigue*, vol. 21, no. 5, pp. 475–483, 1999.

[119] C. Han, X. Chen, and K. S. Kim, "Evaluation of multiaxial fatigue criteria under irregular loading," *Int. J. Fatigue*, vol. 24, no. 9, pp. 913–922, 2002.

[120] A. Fatemi and N. Shamsaei, "Multiaxial fatigue: An overview and some approximation models for life estimation," *Int. J. Fatigue*, vol. 33, no. 8, pp. 948–958, 2011.

[121] A. Carpinteri, A. Spagnoli, and S. Vantadori, "Multiaxial fatigue life estimation in welded joints using the critical plane approach," *Int. J. Fatigue*, vol. 31, no. 1, pp. 188–196, 2009.

[122] S. George, "Failure of materials under combined repeated stresses with superimposed static stresses," Los Angeles: California Univ, No. NACA-TN-3495, 2018.

[123] B. Crossland, "Effect of large hydrostatic pressures on the torsional fatigue strength of an alloy steel," in *International conference on fatigue of metals*, 1956, vol. 6, no. 3, p. 12.

[124] D. Van Ky, *Sur la résistance à la fatigue des métaux*. 1973.

[125] W. N. Findley, "A Theory for the Effect of Mean Stress on Fatigue of Metals Under Combined Torsion and Axial Load or Bending," *J. Eng. Ind.*, vol. 81, no. 4, pp. 301–305, 1959.

[126] T. Matake, "An Explanation on Fatigue Limit under Combined Stress," in

Bulletin of JSME, 1977, vol. 20, no. 141, pp. 257–263.

[127] M. Šraml, J. Flašker, and I. Potrč, "Critical plane modelling of fatigue initiation under rolling and sliding contact," *J. Strain Anal. Eng. Des.*, vol. 39, no. 2, pp. 225–236, 2004.

[128] M. Benedetti, V. Fontanari, and M. Bandini, "A simplified and fast method to predict plain and notch fatigue of shot peened high-strength aluminium alloys under reverse bending," *Surf. Coatings Technol.*, vol. 243, pp. 2–9, 2014.

[129] M. Benedetti, V. Fontanari, M. Bandini, and D. Taylor, "Multiaxial fatigue resistance of shot peened high-strength aluminum alloys," *Int. J. Fatigue*, vol. 61, pp. 271–282, 2014.

[130] M. Benedetti, V. Fontanari, C. Santus, and M. Bandini, "Notch fatigue behaviour of shot peened high-strength aluminium alloys: Experiments and predictions using a critical distance method," *Int. J. Fatigue*, vol. 32, no. 10, pp. 1600–1611, 2010.

[131] J. Liu and M. Pang, "Fatigue life prediction of shot-peened steel," *Int. J. Fatigue*, vol. 43, pp. 134–141, 2012.

[132] K. N. Smith, T. Topper, and P. Watson, "A stress–strain function for the fatigue of metals (stress-strain function for metal fatigue including mean stress effect)," *J. Mater.*, vol. 5, pp. 767–778, 1970.

[133] Y. Jiang, O. Hertel, and M. Vormwald, "An experimental evaluation of three critical plane multiaxial fatigue criteria," *Int. J. Fatigue*, vol. 29, no. 8, pp. 1490–1502, 2007.

[134] D. Socie, "Multiaxial Fatigue Damage Models," *J. Eng. Mater. Technol.*, vol. 109, no. 4, pp. 293–298, 1987.

[135] W. J. Qin and C. Y. Guan, "An investigation of contact stresses and crack initiation in spur gears based on finite element dynamics analysis," *Int. J. Mech. Sci.*, vol. 83, pp. 96–103, 2014.

[136] S. Zhu, Z. Yu, J. Correia, A. De Jesus, and F. Berto, "Evaluation and comparison of critical plane criteria for multiaxial fatigue analysis of ductile and brittle materials," *Int. J. Fatigue*, vol. 112, pp. 279–288, 2018.

[137] P. Lopez-crespo, B. Moreno, A. Lopez-moreno, and J. Zapatero, "Study of crack orientation and fatigue life prediction in biaxial fatigue with critical plane models," *Eng. Fract. Mech.*, vol. 136, pp. 115–130, 2015.

[138] J. Li, Z. Zhang, Q. Sun, and C. Li, "Multiaxial fatigue life prediction for various metallic materials based on the critical plane approach," *Int. J. Fatigue*, vol. 33, no. 2, pp. 90–101, 2011.

[139] M. P. Szolwinski and T. N. Farris, "Mechanics of fretting fatigue crack formation," *Wear*, vol. 198, no. 1, pp. 93–107, 1996.

[140] D. Pellinghelli, M. Riboli, and A. Spagnoli, "Full-model Multiaxial Fatigue Life Calculations with Different Criteria," *Procedia Eng.*, vol. 213, pp. 126–136, 2018.

[141] W. S. Sum, E. J. Williams, and S. B. Leen, "Finite element, critical-plane, fatigue life prediction of simple and complex contact configurations," *Int. J. Fatigue*, vol. 27, no. 4, pp. 403–416, 2005.

[142] N. E. Dowling, C. A. Calhoun, and A. Arcari, "Mean stress effects in stress-life fatigue and the Walker equation," *Fatigue Fract. Eng. Mater. Struct.*, vol. 32, no. 3, pp. 163–179, 2009.

[143] V. Fridrici, S. Fouvry, P. Kapsa, and P. Perruchaut, "Prediction of cracking in Ti–6Al–4V alloy under fretting-wear: use of the SWT criterion," *Wear*, vol. 259, no. 1, pp. 300–308, 2005.

[144] R. Hales, S. Holdsworth, M. P. O'Donnell, I. J. Perrin, and R. P. Skelton, "A Code of Practice for the determination of cyclic stress-strain data," *Mater. High Temp.*, vol. 19, pp. 165–185, 2002.

[145] S. Tsutsumi, M. Toyosada, and F. Dunne, "Phenomenological cyclic plasticity model for high cycle fatigue," *Procedia Eng.*, vol. 2, no. 1, pp. 139–146, 2010.

[146] G. B. Broggiato, F. Campana, and L. Cortese, "The Chaboche nonlinear kinematic hardening model: Calibration methodology and validation," *Meccanica*, vol. 43, no. 2, pp. 115–124, 2008.

[147] W. Prager, "A New Method of Analyzing Stresses and Strains in Work-hardening Plastic Solids," *J. Appl. Mech.*, no. 23, pp. 493–496, 1956.

[148] J. Cao, W. Lee, H. Shawn, M. Seniw, and H. Wang, "Experimental and numerical investigation of combined isotropic-kinematic hardening behavior of sheet metals," *Int. J. Plast.*, vol. 25, no. 5, pp. 942–972, 2009.

[149] C. O. Frederick and P. Armstrong, "A Mathematical Representation of the Multiaxial Bauscinger Effect," *Mater. High Temp.*, vol. 24, pp. 1–26, Apr. 2007.

[150] J. L. Chaboche, "Time-independent constitutive theories for cyclic plasticity," *Int. J. Plast.*, vol. 2, no. 2, pp. 149–188, 1986.

[151] C. Lee, K. Chang, and V. Van, "Numerical investigation on the ratcheting behavior of pressurized stainless steel pipes under cyclic in-plane bending," *Mar. Struct.*, vol. 49, pp. 224–238, 2016.

[152] E. T. Brake, J. V. Cammen, and R. Uittenbogaard, "Calculation Methodology of Out of Plane Bending of Mooring Chains," in *Proceedings of the International Conference on Offshore Mechanics and Arctic Engineering OMAE2007-29178*, 2007, pp. 1–9.

[153] I. Perez and Ø. Gabrielsen, "Computational Fatigue Assessment of Chains Working in Twisted," in *ASME 2019 38th International Conference on*

Offshore Mechanics and Arctic Engineering OMAE2019-96000, 2019, pp. 1–9.

[154] M. Hove, "Growth of Fatigue Cracks in Mooring Line Chains," Thesis, NTNU, Norway, 2016.

[155] J. Stiff, D. Smith, and N. Casey, "Fatigue of Mooring Chain in Air and Water - Results and Analysis," in *Proceedings of Offshore Technology Conference OTC-8147-MS*, 1996, p. 7.

[156] P. Sincock and M. Lalani, "Developments in Fatigue Design Guidelines for Anchor Chains as Mooring Lines," in *Proceedings of Offshore Technology Conference OTC-6452*, 1990.

[157] G. de Laval, "Fatigue Tests On Anchor Chain-Cable," in *Proceedings of Offshore Technology Conference OTC1503-MS*, 1971.

[158] L. C. van Helvoirt, "Static and Fatique Tests on Chain Links and Chain Connecting Links," *Proceedings of Offshore Technology Conference OTC-4179-MS*. Offshore Technology Conference, Houston, Texas, p. 8, 1982.

[159] R. E. Melchers, T. Moan, and Z. Gao, "Corrosion of working chains continuously immersed in seawater," *J. Mar. Sci. Technol.*, vol. 12, no. 2, pp. 102–110, 2007.

[160] Z. Gao, T. Moan, and S. E. Heggelund, "Time Variant Reliability of Mooring System Considering Corrosion Deterioration," in *ASME 2005 24th International Conference on Offshore Mechanics and Arctic Engineering OMAE2005-67429*, 2005, no. 41960, pp. 203–210.

[161] D. Witt, K. T. Ma, T. Lee, C. Gaylarde, Z. Makama, and I. Beech, "Field Studies of Microbiologically Influenced Corrosion of Mooring Chains," in *Proceedings of Offshore Technology Conference OTC-27142-MS*, 2016, p. 19.

[162] T. Johan and M. Braut, "Numerical Investigation of 3D Scanned Mooring Chains," Thesis, NTNU, Norway, 2017.

[163] A. Hoel, "3D Scanning of Corroded Mooring Chain," Thesis, NTNU, Norway, 2016.

[164] E. Fontaine, J. Rosen, A. Potts, K. Ma, and R. E. Melchers, "SCORCH JIP - Feedback on MIC and Pitting Corrosion from Field Recovered Mooring Chain Links," in *Proceedings of Offshore Technology Conference OTC-25234*, 2014.

[165] B. J. Leira, K. Larsen, C. A. Holm, and T. Lovstad, "Service life reliability analysis for an anchor system subject to corrosion," in *Proceedings of the International Conference on Offshore Mechanics and Arctic Engineering - OMAE1995*, 1995, vol. 2, pp. 335–341.

[166] A. Arredondo, J. Fernández, E. Silveira, and J. L. Arana, "Corrosion Fatigue Behavior of Mooring Chain Steel in Seawater," in *ASME 2016 35th*

International Conference on Ocean, Offshore and Arctic Engineering OMAE2016-54426, 2016, no. 49927, p. V001T01A006.

[167] F. D. S. Pires, J. Carlos, F. Jorge, L. Felipe, and G. De Souza, "Fatigue Residual Life Assessment Of IACS W22 / 2004 Grade R4 Steel Used In The Manufacturing Of Mooring Chains," in *Proceedings of COBEM 2007 19th International Congress of Mechanical Engineering*, 2007.

[168] R. Nevshupa, I. Martinez, S. Ramos, and A. Arredondo, "The effect of environmental variables on early corrosion of high – strength low – alloy mooring steel immersed in seawater," *Mar. Struct.*, vol. 60, pp. 226–240, 2018.

[169] P. Vargas and P. Jean, "FEA of Out-of-Plane Fatigue Mechanism of Chain Links," *ASME 2005 24th International Conference on Offshore Mechanics and Arctic Engineering OMAE2005-67354*. pp. 173–182, 2005.

[170] T. Lassen, E. Storvoll, and A. Bech, "Fatigue Life Prediction of Mooring Chains Subjected to Tension and Out of Plane Bending," in *ASME 2009 27th International Conference on Ocean, Offshore and Arctic Engineering OMAE2009-79253*, 2009, pp. 229–239.

[171] Bureau Veritas, "Fatigue of Top Chain of Mooring Lines due to In-plane and Out-of-plane Bendings Guidance Note," *Guidance Note NI 604 DT R00*, 2014. [Online]. Available: http://erules.veristar.com/dy/data/bv/pdf/604-NI_2014-10.pdf. [Accessed: 10-Aug-2020].

[172] Y. Lim, K. Kim, J. Choung, and C. Kang, "A Study on Out-of-Plane Bending Mechanism of Mooring Chains for Floating Offshore Plants," *J. Soc. Nav. Archit. Korea*, vol. 47, 2010.

[173] P. Jean, K. Goessens, and D. Hostis, "Failure of Chains by Bending on Deepwater Mooring Systems," in *Proceedings of Offshore Technology Conference OTC-17238*, 2005.

[174] L. Rampi, A. Bignonnet, C. Le Cunff, F. Bourgin, and P. Vargas, "Chain Out of Plane Bending (OPB) Fatigue Joint Industry Project (JIP) Static Test Program And OPB Interlink Stiffness," in *ASME 2016 35th International Conference on Ocean, Offshore and Arctic Engineering OMAE2016-54195*, 2016, p. 15.

[175] L. Rampi, A. Bignonnet, C. Le Cunff, F. Bourgin, and P. Vargas, "Chain Out of Plane Bending (OPB) Fatigue Joint Industry Project (JIP) Fatigue Test Program Results and Methodology," in *ASME 2016 35th International Conference on Ocean, Offshore and Arctic Engineering OMAE2016-54199*, 2016, p. 18.

[176] I. J. Calf, "Multiaxial fatigue criteria for offshore mooring chains subjected to out-of-plane bending," Thesis, Department Maritime & Transport Technology, TU Delft, 2015.

[177] E. Mamiya, F. Castro, L. Malcher, and G. Ferreira, "Grade R4 Steel Mooring Chain Links Under Out-of-Plane Bending: Testing and Fatigue Life Prediction," in *ASME 2019 38th International Conference on Offshore Mechanics and Arctic Engineering OMAE2019-95618*, 2019, pp. 1–6.

[178] E. N. Mamiya, F. C. Castro, and G. V. Ferreira, "Fatigue of mooring chain links subjected to out-of-plane bending: Experiments and modeling," *Eng. Fail. Anal.*, vol. 100, pp. 206–213, 2019.

[179] I. M. L. Ridge, R. E. Hobbs, and J. Fernandez, "Predicting the Torsional Response of Large Mooring Chains," in *Proceedings of Offshore Technology Conference OTC-17789*, 2006, p. 15.

[180] R. E. Hobbs and I. M. L Ridge, "Torque in Mooring Chain. Part 1: Background and Theory," in *The Journal of Strain Analysis for Engineering Design*, 2005, vol. 40, no. 7, pp. 703–713.

[181] I. M. L. Ridge and R. E. Hobbs, "Torque in mooring chain. Part 2: Experimental investigation," in *The Journal of Strain Analysis for Engineering Design*, 2005, vol. 40, no. 7, pp. 715–728.

[182] B. You and S. Lee, "A critical review on multiaxial fatigue assessments of metals," *Int. J. Fatigue*, vol. 18, no. 4, pp. 235–244, 1996.

[183] Flexcom Software Documentation, "Flexcom Version 8.10.2 Examples Manual." Galway: Wood Group Kenny, 2019.

[184] Z. Gao and T. Moan, "Wave-induced fatigue damage of mooring chain under combined non-Gaussian low and wave frequency loads," in *ASME 2006 25th International Conference on Ocean, Offshore and Arctic Engineering OMAE2006-92389*, 2006, p. 7.

[185] M. A. Miner, "Cumulative damage in fatigue," *J. Appl. Mech.*, vol. 12, no. American Society of Mechanical Engineers-Journal of Applied Mechanics, pp. A159–A164, 1945.

[186] G. M. Gemilang, P. A. S. Reed, and A. J. Sobey, "Selection of appropriate numerical models for modelling the operating stresses in mooring chains," *Mar. Struct.*, vol. 75, p. 102864, 2020.

[187] Dassault Systèmes Simulia Corp., "Abaqus Analysis User's Guide 6.13," *ABAQUS, Inc.*, 2013. [Online]. Available: http://dsk.ippt.pan.pl/docs/abaqus/v6.13/books/usb/default.htm?startat=pt09ch36s03aus145.html. [Accessed: 19-Feb-2020].

[188] R. Tian and G. Yagawa, "Generalized nodes and high-performance elements," *Int. J. Numer. Methods Eng.*, vol. 64, pp. 2039–2071, 2005.

[189] S. C. Tadepalli, A. Erdemir, and P. R. Cavanagh, "Comparison of hexahedral and tetrahedral elements in finite element analysis of the foot and footwear," *J. Biomech.*, vol. 44, no. 12, pp. 2337–2343, 2011.

[190] Dassault Systèmes Simulia Corp., "ABAQUS Documentation Version 6.6,"

ABAQUS, Inc., 2006. [Online]. Available: https://classes.engineering.wustl.edu/2009/spring/mase5513/abaqus/docs/v6.6/books/usb/default.htm?startat=pt09ch29s02aus124.html. [Accessed: 07-Mar-2020].

[191] A. M. Prior, "Applications of implicit and explicit finite element techniques to metal forming," *J. Mater. Process. Technol.*, vol. 45, no. 1, pp. 649–656, 1994.

[192] Dassault Systèmes Simulia Corp., *Abaqus/CAE User's Manual, Theory Guide. Version 6.12*. Pawtucket, USA: ABAQUS, Inc., 2012.

[193] J. Ye, Y. Yan, J. Li, Y. Hong, and Z. Tian, "3D explicit finite element analysis of tensile failure behavior in adhesive-bonded composite single-lap joints," *Compos. Struct.*, vol. 201, pp. 261–275, 2018.

[194] P. Liu, X. Cheng, S. Wang, S. Liu, and Y. Cheng, "Numerical analysis of bearing failure in countersunk composite joints using 3D explicit simulation method," *Compos. Struct.*, vol. 138, pp. 30–39, 2016.

[195] F. J. Harewood and P. E. McHugh, "Comparison of the implicit and explicit finite element methods using crystal plasticity," *Comput. Mater. Sci.*, vol. 39, no. 2, pp. 481–494, 2007.

[196] F. Vulliet, M. Ben Ftima, and P. Léger, "Stability of cracked concrete hydraulic structures by nonlinear quasi-static explicit finite element and 3D limit equilibrium methods," *Comput. Struct.*, vol. 184, pp. 25–35, 2017.

[197] F. Li, W. Hu, Q. Meng, Z. Zhan, and F. Shen, "A new damage-mechanics-based model for rolling contact fatigue analysis of cylindrical roller bearing," *Tribol. Int.*, vol. 120, pp. 105–114, 2018.

[198] H. W. Li, H. Yang, and Z. C. Sun, "A robust integration algorithm for implementing rate dependent crystal plasticity into explicit finite element method," *Int. J. Plast.*, vol. 24, no. 2, pp. 267–288, 2008.

[199] Z. Yang, X. Deng, and Z. Li, "Numerical modeling of dynamic frictional rolling contact with an explicit finite element method," *Tribol. Int.*, vol. 129, no. June 2018, pp. 214–231, 2019.

[200] H. Yu, I. W. Burgess, J. B. Davison, and R. J. Plank, "Numerical simulation of bolted steel connections in fire using explicit dynamic analysis," *J. Constr. Steel Res.*, vol. 64, no. 5, pp. 515–525, 2008.

[201] E. M. Gutman, *Mechanochemistry of solid surfaces*. Singapore: World Scientific Publishing Co., Pte. Ltd., 1994.

[202] I. M. Widiyarta, F. J. Franklin, and A. Kapoor, "Modelling thermal effects in ratcheting-led wear and rolling contact fatigue," *Wear*, vol. 265, no. 9, pp. 1325–1331, 2008.

[203] Dassault Systèmes Simulia Corp., "ABAQUS Documentation Version 6.5,"

ABAQUS, Inc., 2004. [Online]. Available: https://classes.engineering.wustl.edu/2009/spring/mase5513/abaqus/docs/v6.5/books/gss/default.htm?startat=ch04s01.html. [Accessed: 09-Feb-2020].

[204] S. Gong, B. Sun, S. Bao, and Y. Bai, "Buckle propagation of offshore pipelines under external pressure," *Mar. Struct.*, vol. 29, no. 1, pp. 115–130, 2012.

[205] M. A. Rabelo, C. P. Pesce, C. C. P. Santos, R. Ramos, G. R. Franzini, and A. Gay Neto, "An investigation on flexible pipes birdcaging triggering," *Mar. Struct.*, vol. 40, pp. 159–182, 2015.

[206] C. C. P. Santos and C. P. Pesce, "An alternative strategy for offshore flexible pipes finite element analysis," *Mar. Struct.*, vol. 65, pp. 376–416, 2019.

[207] G. M. Gemilang, P. A. S. Reed, and A. J. Sobey, "Low-cycle Fatigue Assessment of Offshore Mooring Chains Under Service Loading," *Mar. Struct.*, p. 14, 2020.

[208] J. Araújo and D. Nowell, "The effect of rapidly varying contact stress fields on fretting fatigue," *Int. J. Fatigue*, vol. 24, no. 7, pp. 763–775, 2002.

[209] G. Marsh, C. Wignall, P. R. Thies, N. Barltrop, A. Incecik, and V. Venugopal, "Review and application of Rainflow residue processing techniques for accurate fatigue damage estimation," *Int. J. Fatigue*, vol. 82, pp. 757–765, 2016.

[210] S. Koo, J. Han, K. P. Marimuthu, and H. Lee, "Determination of Chaboche combined hardening parameters with dual backstress for ratcheting evaluation of AISI 52100 bearing steel," *Int. J. Fatigue*, vol. 122, no. November 2018, pp. 152–163, 2019, doi: 10.1016/j.ijfatigue.2019.01.009.

[211] N. Mansor, S. Abdullah, and A. Ariffin, "Effect of loading sequences on fatigue crack growth and crack closure in API X65 steel," *Mar. Struct.*, vol. 65, pp. 181–196, 2019.

[212] M. Reistad, A. K. Magnusson, and S. Haver, "How severe wave conditions are possible on the Norwegian Continental Shelf?," *Mar. Struct.*, vol. 18, pp. 428–450, 2005.

[213] M. Benedetti, V. Fontanari, M. Allahkarami, J. C. Hanan, and M. Bandini, "On the combination of the critical distance theory with a multiaxial fatigue criterion for predicting the fatigue strength of notched and plain shot-peened parts," *Int. J. Fatigue*, vol. 93, pp. 133–147, 2016.

[214] A. Fatemi and D. F. Socie, "A Critical Plane Approach to Multiaxial Fatigue Damage Including out-of-phase Loading," *Fatigue Fract. Eng. Mater. Struct.*, vol. 11, no. 3, pp. 149–165, Mar. 1988.

[215] M. Wall, H. Pugh, and A. Reay, "Information on specific UK and North Sea

FPSO and FSU," *HSE*, 2002. [Online]. Available: https://www.hse.gov.uk/research/otopdf/2001/oto01073c.pdf. [Accessed: 18-Dec-2020].

[216] J. H. S. Johnsen, "Loss of Integrety on Mooring Systems - Causes and Consequences." Master Thesis - Univesity of Stavanger, p. 106, 2016.

[217] L. Coudreuse, C. Renaudin, P. Bocquet, and L. Cadiou, "Evaluation of hydrogen assisted cracking resistance of high strength Jack-up steels," *Mar. Struct.*, vol. 10, no. 2, pp. 85–106, 1997.

[218] X. Y. Cheng, H. X. Zhang, H. Li, and H. P. Shen, "Effect of tempering temperature on the microstructure and mechanical properties in mooring chain steel," *Mater. Sci. Eng. A*, vol. 636, pp. 164–171, 2015.

[219] Standards Norway, *NORSOK: N-003 Actions and action effects*. 2007, p. 60.

[220] N. Co and J. T. Burns, "Effects of macro-scale corrosion damage feature on fatigue crack initiation and fatigue behavior," *Int. J. Fatigue*, vol. 103, pp. 234–247, 2017.